UNIVERSITÀ DEGLI STUDI DI TRIESTE

Facoltà di Scienze Matematiche, Fisiche e Naturali

Dottorato di Ricerca in Fisica - XVI Ciclo

Hydrodynamical Simulations of Galaxy Clusters: Thermodynamics and Chemical Enrichment

DOTTORANDO
Luca Tornatore

COORDINATORE DEL COLLEGIO DEI DOCENTI
Prof. Gaetano Senatore, Università di Trieste

TUTORE
Prof. Stefano Borgani, Università di Trieste

RELATORE
Prof. Stefano Borgani, Università di Trieste

a.a. 2003/20004

Contents

List of Figures

List of Tables

INTRODUCTION

The Universe is currently thought to originate from a singularity in the space–time which began to expand – giving raise to the so–called *Big Bang* – about $\sim 13\,\mathrm{Gyr}$ ago. Theoreticians succeed in conjecturing on the physics of the universe up to 10^{-9} seconds after the time zero; from these speculations we are able to make precise predictions on the pristine abundance of cosmic elements (Burles & Tytler 1998) formed at $t = 3$ minutes. Such a prediction turns out to be in excellent concordance with estimates drawn from the signature left by the recombination of free electrons and nuclei on the Cosmic Microwave Background (CMB) – the relic of the pristine energy bath – , about $4 \times 10^5\,\mathrm{yrs}$ later (Spergel et al. 2003). This is probably one of the most important confirmation of the current Standard Cosmological Model.

After the recombination, baryons – no longer impeded by the radiation pressure of photon which were coupled to them – were able to collapse and rest in the potential well created by an yet unknown form of matter. Since such matter seems to interact only gravitationally with baryons and energy, then not emitting any kind of radiation, it is called *Dark*. Nevertheless, we know it must be there by a number of observations: among others, the rotation curves of spiral galaxies, the mass–over–light ratio for galaxy clusters, the velocity dispersion of galaxies in clusters, the large scale velocity field, the power spectrum of CMB (for recent reviews see e.g. Sellwood (2004), Ellis (2003)).

From that moment on, the Cosmology become the study of structure formation, that is to say the infall of dark matter halos and baryons in those potential wells. It is believed that a pristine field of very tiny fluctuations were superimposed to the otherwise homogeneous density field by some yet uncertain quantum mechanism; in this framework, with the additional assumption of the Cold Dark Matter scenario, the structure formation proceed in a *Bottom-Up* direction, the smallest structures forming first from the peaks of the primordial density fluctuations and then merging as building–blocks for larger ones. The collapse of matter can be described with linear perturbation theory until the contrast with respect to the mean density approaches unity, $(\rho - \bar{\rho})/\bar{\rho} \sim 1$; then, the collapse enters in the *non–linear* regime (see Sec. (1.2)).

At the top of the hierarchy of non–linear structures there are the ***Clusters of Galaxies***, which are the greatest virialized objects in the universe, collecting matter from regions of about $\sim 10\,\mathrm{Mpc}$ ($1\mathrm{pc} \simeq 3.26$ light years). Most of the baryons in

clusters are in the form of a hot, ionized gas which emits by thermal bremsstrahlung in the X–ray band, so that they can be detected at large redshifts, probing the large scale structure in the universe. Originating form the rare high peaks of primordial density perturbations, they probe the high–density tail of the cosmic density field and thereby their evolution is very sensitive to the details of the cosmological model (see Sec. (1.3)).This is the reason why Galaxy Clusters are thought to be very useful cosmological laboratories. Moreover, they can be considered as fair tracers for the baryon's history in the universe, thereby being also invaluable astrophysical laboratories.

Owing to the continuous improvement in both spatial and spectral resolution power of successive generations of X–ray satellites (ROSAT, Beppo–SAX, ASCA, Chandra, XMM–Newton), more and more details on the inner properties of galaxy clusters have been unveiled in the last decade. These objects, that in a first approximation were thought to be virialized and spherically symmetric, have very complex dynamical features – such as strong asymmetries and clumpiness – witnessing for violent processes being acting or having just played a role. They exhibit luminosity and temperature functions which are not trivially related to their mass function, as one would expect for virialized gravitation–driven objects. Moreover, the radial structure of baryons' properties is far to be completely understood: a number of observational facts pose a real challenge to our ability in modeling the physics of the Intra Cluster Medium (ICM). Even the radial profile of both dark and baryonic matter distributions is not yet ascertained; the existence of a universal dark–matter profile, which has been claimed about 10 years ago by Navarro, Frenk and White (1995, 1997, 2004), is nowadays questioned (e.g. Kravtsov et al. 1998, Cen & Ostriker 2000). A number of observational facts clearly point towards an important role of non–gravitational physics in determining the thermodynamical properties of baryons in galaxy clusters. The most important are the slope of the relation between the X–ray luminosity L_X and the temperature (e.g. Arnaud & Evrard 1999), the amplitude of the mass–temperature relation (e.g. Ettori et al. 2002a, Finoguenov et al. 2001b, Nevalainen et al. 2000), the entropy level of gas in the central region of groups of galaxies (e.g. Sanderson et al. 2003).

Galaxy Clusters also harbor a rather large amount of heavy elements – as large as few $10^{11}\,M_\odot$ – both in the hot gas and in the star component. Such elements are synthetized by stars during their evolution; once they are deposited in the Inter Stellar Medium (ISM) by supernovae explosions, stellar winds or other mass losses by stars, some other mechanism is required for them to reach the ICM. Although many possibilities have been considered – the most favored are *galactic winds* and *gas–stripping* by ram pressure or tidal interactions – no firm conclusions have been reached so far about how metals reach the hot gas (e.g. Renzini 2004, Pipino et al. 2002, Aguirre et al. 2001a). Understanding this mechanism would provide us with important clues about the main processes which are driving the galaxy–plasma interaction; moreover, we would also obtain important information on the star formation history, as different ejection mechanisms are likely to act at different epochs. In fact, we have a limited

knowledge of the *Initial Mass Function* (IMF, namely the mass function of a stellar population) which underlines the star formation and whether it is universal or instead environment–dependent and, if so, to what extent (e.g. Finoguenov et al. 2000a, Portinari et al. 2004, Tornatore et al. 2004, Loewenstein 2004, Renzini 2004). As opposed to galaxies, clusters may have been able to retain most, if not all, of the elements that have enriched the ICM; behaving essentially as closed boxes they retain an unbiased memory of the chemistry of the universe. Thus, measuring abundances of the ICM and their evolution provides fundamental hints on the origin of the elements and on mechanisms responsible for their distribution in different environments.

All such topics are of great interest by themselves as they involve the history of a large fraction of baryons in the universe. In addition, understanding the thermodynamical evolution of baryons within clusters is mandatory for these objects to be used as precision tools for cosmology. In fact, the mass of galaxy clusters, which is the predicted quantity, is not a direct observable but must be inferred from other quantities, such as (1) the total X–ray emission, which depends on the total amount of hot gas that is in turn linked to the total mass by the *gas fraction* f_{gas}, namely the ratio $m_{\rm gas}/m_{\rm tot}^{\rm bar}$ and the *baryonic fraction* f_{bar}, namely the ratio $m_{\rm bar}/m_{\rm tot}$; (2) the temperature of the hot gas, which is related to the total mass by the hypothesis of hydrostatic equilibrium. Although other independent methods exist to infer the mass of galaxy clusters – for instance the gravitational lensing or the velocity dispersion of galaxies – a better understanding of the relations between the gas properties and the mass would greatly improve the precision and reliability of clusters as probes in a cosmological context (e.g. Arnaud 2004, Borgani 2004). In fact, the the evolution of their mass function with time is one of the key test to determine both the density parameter Ω_m and the amplitude of the variance of mass fluctuation $(\rho - \bar{\rho})/\bar{\rho}$ on a scale of $8h^{-1}$ Mpc (e.g. Borgani & Guzzo 2001) where h gives the value of the Hubble constant in units of 100 km sec^{-1} Mpc^{-1}.

The aim of this thesis is to investigate the physics of the ICM in many respects by means of advanced numerical methods in order to achieve a deep understanding on the topics mentioned above. Thanks to the enormous increase in the last decade in both the computational power and memory availability, numerical methods are nowadays an invaluable instruments to gain precise clues on the strongly non–linear regime of structure formation and on the highly complex interplay among several physical processes which are acting in galaxy clusters. The Thesis consists basically of two parts. Our first aim is to study in details the thermodynamical properties of the ICM, namely what kind and level of non–gravitational heating is needed to recover the observed scaling relations between X–ray luminosity, temperature and mass as well as the temperature profiles. We also investigate which is the best thermodynamical path, namely the epoch and the mechanism of energy injection. This is reported in **Chap. (2)**. The results reported in this Chapter have been published in Tornatore et al. (2003) and

(2003b).
The second part of our work was aimed at introducing a sophisticated description of the stellar evolution and chemical enrichment in numerical simulations. This is a completely new field, as there are only few previous example of such codes (Lia et al. 2002, Kawata & Gibson 2003). First results have been published in Tornatore et al. (2004); more advanced and complete analysis, as well as a methodology description, will be published in forthcoming papers which are currently in preparation. We have implemented very carefully the stellar evolution and the related production of heavy elements, being also provided with an effective model as for the onset of galactic winds. Moreover, we take take the supernovae energy into account when resolving hydrodynamical equations, as well as other important effects as the metallicity dependence of the radiative cooling and the effect of gas metallicity and supernova energy on star formation. A general introduction on numerical methods in cosmology is given in **Chap. (3)**, whereas we describe our implementation in detail in **Chap. (4)**. Here we also describe the code[1] into which we have inserted our stellar evolutionary code; since this is a far more advanced version than the code used to run simulations performed in the first part of the work, which id described in details by Springel et al. (2001), we choose to postpone such introduction to Chap. (2). Results on the chemical evolution of galaxy clusters are reported and discussed in **Chap. (5)**, along with a discussion on numerical effects. More precisely, we vary a number of numerical parameters and study the effects of such variations; we also let important physical parameters to change in order to achieve some clues about the physics of star formation which is acting in clusters. For instance, we alter the IMF, comparing a 'standard' Salpeter IMF with other two functions which produce more massive stars. This will allow us to follow different patterns of chemical enrichment and different energy injection histories. Furthermore, we also study the effect of altering the velocity of gas taking part in galactic winds. **Chap. (6)** contains the main conclusions from this work and outlines the future directions of investigation.

[1]We use GADGET , kindly provided to us by Volker Springel at Max Planck Institüt für Astrophysik

CHAPTER 1

BASICS OF COSMOLOGY AND GALAXY CLUSTERS

■ *Chapter Outline*

In this chapter we briefly review the Standard Cosmological Model and the Structure Formation. Furthermore, we review the fundamental properties of galaxy clusters as X–Ray Objects and we outline the current knowledge about their chemical enrichment.

1.1 Basics of Cosmology

The basic axiom of modern cosmology is a form of the Copernican idea that human beings – that is to say the Earth – have not a role in the Universe which is special in any respect. This Cosmological Principle states that the Universe is spatially isotropic and homogeneous, meaning that any observer in any place will infer for it the same general properties. Both isotropy and homogeneity are confirmed by observations of the mass distribution on large scale, the Large Scale Structure (LSS), of the Cosmic Microwave Background (CMB), of the cosmic velocity field and of the cosmological X–ray background. In spite of this, it is evident that the Universe is neither homogeneous nor isotropic on small, local scales. This discrepancy is due to a small primeval

perturbation field which is superimposed to an otherwise homogeneous mass distribution. These tiny departures from homogeneity subsequently grow forming the currently observed cosmic structures. Hence, the cosmological theory must solve a twofold problem: the evolution of the Universe as a whole, and the evolution of such perturbations. This latter topic is deferred to Sec. (1.2), while in the rest of this Section we picture the dynamics of cosmological expansion.

1.1.1. Basic Equations

We assume that (1) the Gravitation governs the evolution of the Universe on large scales through the Einstein's Theory of General Relativity and (2) the metric tensor of the Universe is given by the Friedmann–Robertson–Walker (FRW) metric (Weinberg 1972):

$$ds^2 \;=\; dt^2 - a(t)^2 \left[\frac{dr^2}{1-kr^2} + r^2 \left(d\theta^2 + sin^2\theta\phi \right) \right] \tag{1.1}$$

where the *expansion factor* $a(t)$ describes how distances scale with time as a consequence of the Hubble expansion and k is the space *curvature*. We know (Hubble & Humason 1931) that an observer at rest recedes from any other given observer at rest with a velocity, given by $H(t)D$, which increases with the distance D. The *Hubble constant* $H(t)$ at a time t is defined as:

$$H(t) = \frac{\mathrm{d}\, \log a(t)}{\mathrm{d}t} \tag{1.2}$$

and has the units of km s^{-1} Mpc^{-1}; it is commonly parametrized as $H(t) = 100\, h$ km s^{-1} Mpc^{-1} where $h = 0.7$ as for today.
As a consequence of this space expansion, a photon emitted at a time t in the past will be observed at present time $t = 0$ red-shifted by a factor $z = 1/a(t) - 1$ which is exactly called *redshift*; here we set $a(t = 0) \equiv 1$.

The Einstein's field equation

$$G_{\mu\nu} = R_{\mu\nu} - \frac{1}{2}\mathcal{R} g_{\mu\nu} = 8\pi G T_{\mu\nu} + \Lambda g_{\mu\nu} \tag{1.3}$$

relates the geometry of the Universe, with its own energy content, carried by the stress–energy tensor T, for which we assume the form of a perfect fluid:

$$T_{\mu\nu} = p g_{\mu\nu} + (p + \rho) u_\mu u_\nu. \tag{1.4}$$

where p and ρ are related by an equation of state $p = p(\rho)$. The form of such equation for each component is reported in Tab. (1.1).

Component	Eq. of State
Relativistic Matter	$p = 1/3\rho$
Non–Relativistic Matter	$p = 0$
Vacuum energy	$p = -\rho$
Curvature	$p = -1/3\rho$

Table 1.1: Equations of state for different matter–energy components in the Universe.

Substituting the FRW form of metric and the perfect fluid tensor in the field equations gives the *Friedmann's Equations* that describe the expansion of the Universe:

$$\left(\frac{\dot{a}}{a}\right)^2 + \frac{k}{a^2} = \frac{8\pi G}{3}\rho \tag{1.5}$$

$$\frac{\ddot{a}}{a} = -\frac{4\pi G}{3}(\rho + 3p) + \frac{\Lambda}{3} \quad . \tag{1.6}$$

It is useful to define the *critical density* ρ_c as the density needed for $k = 0$; then, it results:

$$\rho_c = \frac{3H^2(t)}{8\pi G} \simeq (1.9 \times 10^{-29}(g\,cm)^{-3})h^2. \tag{1.7}$$

The density ρ_x of a component x of the universe is commonly expressed in units of ρ_c defining the quantity Ω_x as

$$\Omega_x = \rho_x/\rho_c. \tag{1.8}$$

The first of the Friedmann equations can be recasted as:

$$k = a^2H^2(\Omega - 1) \tag{1.9}$$

where Ω accounts for overall the density of the matter–energy density. Hence, the Universe will be spatially *closed*, *flat* or *open* if its means density is respectively smaller, equal or larger than the critical density.
If Ω_r represents the density from the radiation field, Ω_m the density from matter (both baryonic and dark matter), Ω_Λ is due to the Cosmological Constant Λ and we set $\Omega_k = -k/H_0^2 = 1 - \Omega_0$ the second Friedmann equation can be rewritten as:

$$\frac{H(t)}{H_0} = \left[\frac{\Omega_r}{a^4} + \frac{\Omega_m}{a^3} + \frac{\Omega_k}{a^2} + \Omega_\Lambda\right]. \tag{1.10}$$

The Simplest case of $\Omega_k = \Omega_\Lambda \equiv 0$ is called the *Einstein–de Sitter* model; in this case the scaling factor a varies with time as $a(t) \propto t^{2/3}$. It is noteworthing that all models with non–zero Ω_Λ and Ω_k approach the Einstein–de Sitter behaviour when

$$(1+z) \gg max\left[\frac{(1-\Omega_m-\Omega_\Lambda)}{\Omega_m}, \left(\frac{\Omega_\Lambda}{\Omega_m}\right)^{1/3}\right]. \tag{1.11}$$

Finally, we can express $a(t)$ as:

$$a(t) = a_0\left[1 - H_0(t-t_0) - q_0 h_0^2 (t_0-t)^2 + \ldots\right] \tag{1.12}$$

where

$$q_0 = -\frac{\ddot{a}_0 a_0}{\dot{a}_0^2} = \frac{1}{2}\Omega_{0m} - \Omega_\Lambda \tag{1.13}$$

is called *deceleration parameter*.

1.1.2. Key Observations

The Standard Cosmological Model sketched above employs about a tenth of *a priori* free parameters for which theory does not predict preferred values. Hence, deciding if our Universe is flat or open, whether or not there is a Dark Energy at work etc. rest upon observational constraints. The impressive technological improvement of the last twenty years has permitted very precise measures of several parameters with more independent methods; cross–combining these independent estimates leads to more certain conclusions and breaks the degeneracy among linked parameters.

What turns out is that the Model currently favored is the so–called ΛCDM model, having $\Omega = 1$, $\Omega_m = 0.3$, $\Omega_\Lambda = 0.7$.

It is noteworthing that the WMAP experiment (e.g. Bennett et al. 2003) has enormously improved the precision of our knowledge about the values of a number of cosmological parameters: the geometry of the universe, its mean density and baryonic density, the amplitude of density fluctuations, the redshift of decoupling and others have been constrained by measures on CMB of unprecedented precision. Although a number of discrepancies among independent methods are still there, the "concordance model" appears more and more observationally grounded.

■ The Curvature of the Universe

The most powerful technique to measure the curvature of the universe relies on the position of the acoustic peak of the CMB spectrum. Before redshift of decoupling $z_{\rm dec} = 1089 \pm 1$ (Spergel et al. 2003), the Compton scattering tightly couples the photon of CMB and the free electrons, which are in turn coupled with protons. Photon pressure impede the gravitational settling of baryons downto the dark–matter potential well and the "photon–baryon fluid" sets up acoustic oscillations. Once the matter recombines,

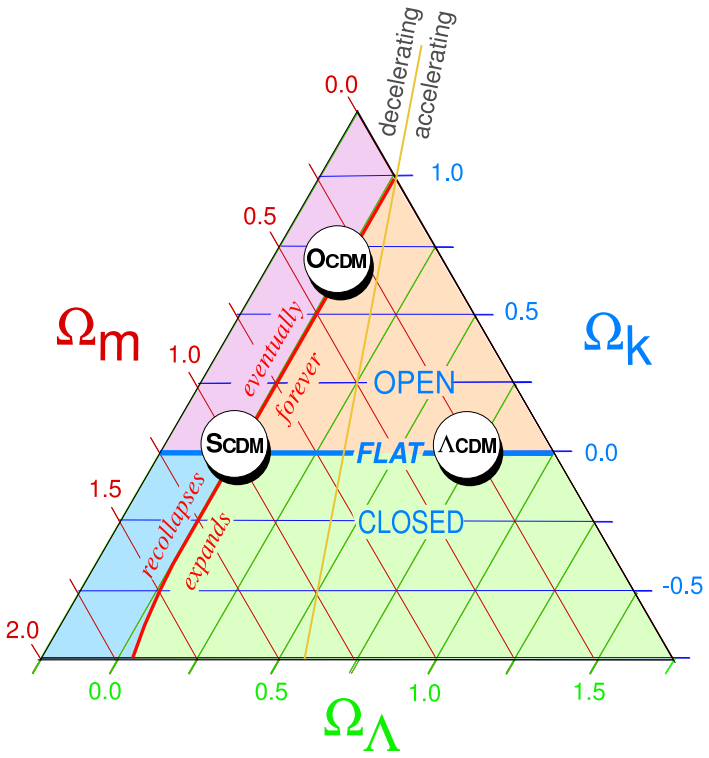

Figure 1.1: A figure from Bahcall et al. (1999) representing the three key cosmological parameters. Each point of the triangle satisfies the rule $\Omega_m + \Omega_\Lambda + \Omega_k = 1$. The horizontal line (marked "FLAT") corresponds to a flat universe ($\Omega_m + \Omega_\Lambda = 1$), separating an open universe from a closed one. The red line, nearly along the $\Lambda = 0$ line, separates a universe that will expand forever (approximately $\Omega_\Lambda > 0$) from one that will eventually recollapse (approximately $\Omega_\Lambda < 0$). And the yellow, nearly vertical line separates a universe with an expansion rate that is currently decelerating from one that is accelerating. The locations of three key models are highlighted: SCDM, dominated by matter ($\Omega_m = 1$) and no curvature or cosmological constant; flat (ΛCDM), with $\Omega_m = 1/3$, $\Omega_\Lambda = 2/3$, and $\Omega_k = 0$; and OCDM, with $\Omega_m = 1/3$, $\Omega_\Lambda = 0$, and $\Omega_k = 2/3$.

at $z = z_{\rm rec}$, photon last scatter on electrons and suffer for gravitational redshift when leaving the potential well of the last scattering surface. The signature of this last scatter is a fluctuation field on the CMB spectrum which appears today as anisotropies on the sky; such fluctuations are called primary anisotropies, whereas secondary anisotropies will be due to later gravitational effects, Sachs–Wolfe effect, Rees–Sciama effects and others. On large scales the fluctuations of CMB must origin from the primordial fluctuation spectrum as no signal can had time to travel long enough distances; instead, at the characteristic scale of the sound horizon at $z_{\rm rec}$ acoustics oscillations mentioned

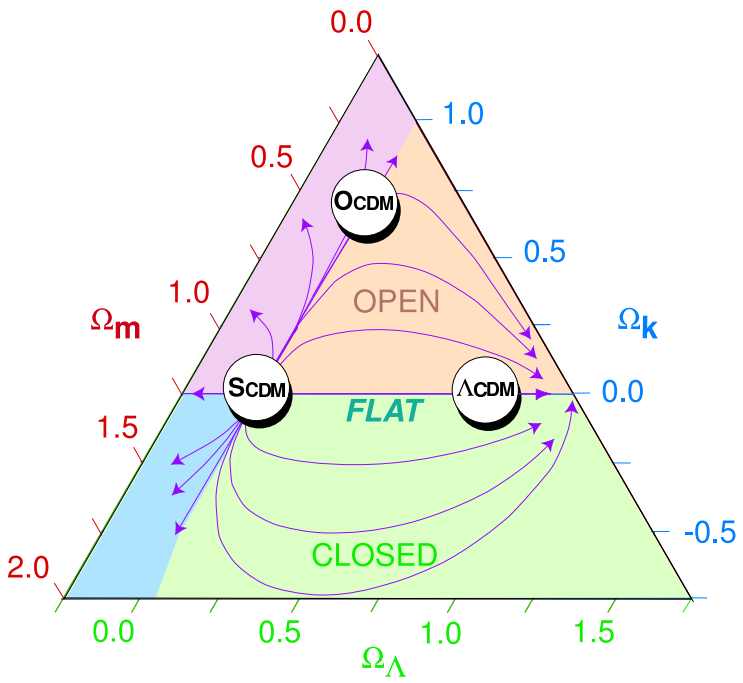

Figure 1.2: A figure from Bahcall et al. (1999) representing the evolution of the universe as "trajectories" in the cosmic triangles. The trajectories, which originate from near $\Omega_m = 1$ (an unstable equilibrium point matching the approximate condition of the universe during early structure formation), indicate the path traversed in the triangle plot as the universe evolves. For the current best fit ΛCDM model, the future represents a flat accelerating universe that expands forever, ultimately reaching $\Omega_m \to 0$ and $\Omega_\Lambda \to 1$.

above can occur and at last scattering the oscillation phase freeze. Therefore, the fluctuation spectrum should exhibit an harmonic series of fluctuation peaks whose distance in the wavenumber space is equal to the critical wavenumber corresponding at the sound horizon. The corresponding anisotropy scale projected on the sky is affected by both the curvature of the universe and the distance of the last scattering surface. Briefly, in the case of a flat space we expect the second acoustic peak at a given angular extent, which will be larger or smaller respectively for positive or negative curvatures. Before WMAP many other experiments (Benoît & coauthors 2003) provided measures of the acoustic peak positions, and all estimates are in perfect agreement with the WMAP result, though its error is much smaller:

$$\Omega_{\rm tot} = 1.02 \pm 0.02. \tag{1.14}$$

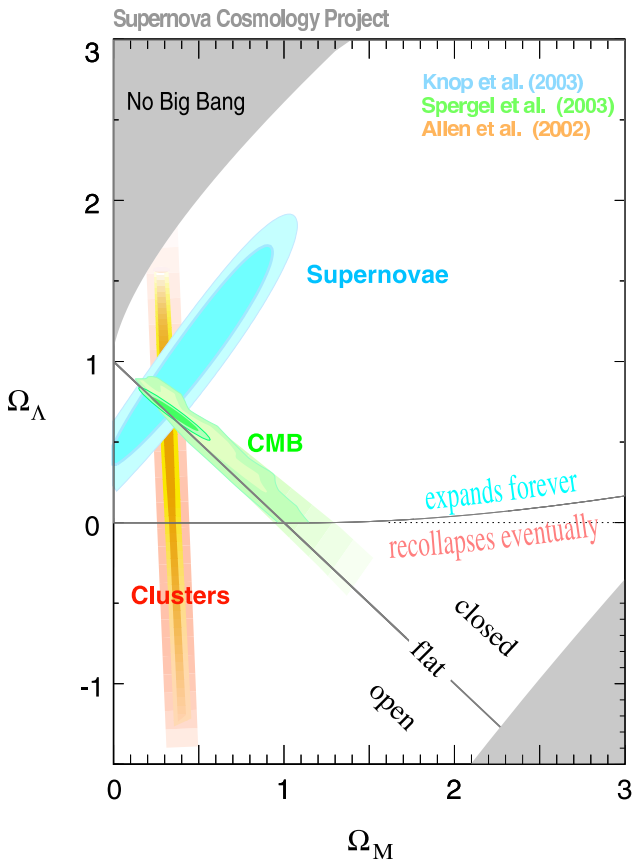

Figure 1.3: Confidence regions for Ω_M and Ω_Λ with the WMAP CMB and galaxy cluster results added on top of the SNIa data from the Supernova Cosmology Project (from Ciardi & Ferrara (2004)).

1.1.3. The Cosmological Acceleration

If an observed object is nearby the observer, its luminosity distance can be well approximated by a linear function of z; otherwise, the dependence on the redshift become important and involves the deceleration parameter. Hence, if we are provided with a set of standard candles which can be found at distances large enough that the luminosity distance is no longer a linear function of z we can infer the past values of the parameter q, then deciding whether the expansion of the universe has been accelerated or not.
Although SnIa are not standard candles in a strict sense, as their luminosity will vary as time elapses from the explosion, they can be calibrated using the characteristic brilliance decaying–time which is instead tightly constant. Hence, we can infer the distance of an observed SnIa from its luminosity and also its receding velocity from

the spectrum. In the case of unaccelerated expansion, a given SnIa at distance d is expected to recede at a velocity $v = H_0 d$, where H_0 is the present value of the Hubble constant. Instead, in case of accelerated or decelerated expansion, the value of $H(t)$ at a given time (redshift) is different than H_0 and the recession velocity will also be different than the expected value. Results on SnIa at $z \gtrsim 3$ from the *Supernova Cosmology Project* (Perlmutter & The Supernova Cosmology Project Team 1999) and the $High - ZSupernovaSearchTeam$ (Riess & coauthors 1998) give a negative value of q_0, indicating the presence of a positive cosmological constant:

$$\Omega_m \sim 0.28 \; ; \; \Omega_\Lambda \sim 0.72. \tag{1.15}$$

■ The Matter and Baryon Density

Both the amplitude of acoustic peaks of the CMB spectrum (Bond & Efstathiou 1984) and the Deuterium abundance $[D/H]$ (Boesgaard & Steigman 1985) are sensitive to the cosmological baryon density. The comparison between the estimates obtained by such independent method provides an important test of the Big Bang model. Using the Baryon–photon ratio inferred from WMAP results $\Omega_b h^2 = 0.0224 \pm 0.0009$ (Spergel et al. 2003), the standard Big Bang nucleosynthesis gives $[D/H] = 2.62^{+0.18}_{-0.20}$. Estimates from $[D/H]$ measures in Lyα clouds and DLA give respectively $\Omega_b h^2 = 0.0214 \pm 0.0020$ and $\Omega_b h^2 = 0.025 \pm 0.001$, with a good agreement which was far to be obvious a priori. Galaxy Clusters observations provide estimates of Ω_m through the evolution with z of their number counts. Fairly different results are obtained by different author: Bahcall et al. (2003) obtain $\sigma_8 = 0.95 \pm 0.1$ for $\Omega_m = 0.25$, Borgani et al. (2001a) obtain $\sigma_8 = 0.66^{+0.05}_{-0.05}$ and $\Omega_m = 0.35^{+0.13}-010$, Reiprich and Böhringer (2002) find $\sigma_8 = 0.96^{+0.15}_{-0.12}$ and $\Omega_m = 0.12^{+0.006}_{-0.004}$. Origins of such significative discrepancy are discussed by Pierpaoli et al. (2003).

1.2 Structure Formation

Besides providing a theory to describe the very early times of the universe and the general framework for the expanding universe, a Cosmological Theory must also provide a model for the formation of cosmological structures and the large scale distribution of matter. To give a comprehensive outline of that matter is far beyond the scope of this brief introduction, so that we address the reader to recent review (e.g. Peebles & Ratra 2003, Coles 2000, Peacock 2001), while in the following we give only few basic ideas.

The Universe shows locally a very rich hierarchical pattern of galaxies, galaxy clusters and clusters of clusters; however, the primeval universe was almost smooth with slight 'ripples' that can be seen as relics in the CMB spectrum. Models of structure

evolution link such initial smoothness to the rich scenario observed nowadays through the effect of gravitation, which causes the initial tiny perturbations to attract more and more mass. If we define the *density contrast* δ with respect to the mean density $\bar{\rho}$ as:

$$\delta \equiv \frac{\rho - \bar{\rho}}{\bar{\rho}}. \tag{1.16}$$

the initial fluctuations in the density field are likely to be a superposition of waves, which can be better expressed by a Fourier transform:

$$\tilde{\delta}(\mathbf{k}) = \frac{1}{(2\pi)^3} \int d^3x \delta(\mathbf{x}) e^{-i\mathbf{k}\cdot\mathbf{x}}. \tag{1.17}$$

For later use, we also define the *Power–Spectrum* P of this field as basically the variance of amplitudes of different waves at a given value of k:

$$\left\langle \tilde{\delta}(\mathbf{k}_1)\tilde{\delta}(\mathbf{k}_2) \right\rangle = P(k_1)\delta_D^3(\mathbf{k}_1 + \mathbf{k}_2). \tag{1.18}$$

where δ_D^3 is the three–dimensional Dirac's *delta* function.
Those initial departures from a complete smoothness are supposed to have been adiabatic and scale invariant. This means (1) that fluctuations in matter and energy are coupled in such a way that the total entropy does not change, and (2) that the power–spectrum of such density fluctuation field looks like $P(k) = Ak^n$ where k has the usual meaning of a wavenumber. The favored value as for the exponent n is $n = 1$. The fact that the universe is isotropic is expressed by $P(\mathbf{k}) = P(k)$.
Currently accepted models predict that Gaussian quantum fluctuations in a scalar field at very early times (e.g. Guth & Pi 1982) has generated the density perturbation field. Since the power–spectrum completely characterizes in a statistical sense the Gaussian stochastic processes, we are provided with a complete statistical description of the initial 'seed' of structure formation once we have the power–spectrum of such pristine perturbation field.
Besides gravitation, other astrophysical process are affecting the growth of perturbations; they are accounted through a *Transfer Function* $T(k)$ which is simply a function of the wavenumber k. The final power spectrum relates to the original one by $P(k) = P_0(k) \times T^2(k)$. For the sake of clarity, here below we just remind some of these non–gravitational effects. As already mentioned, the coupling of baryons with the radiation field or the baryonic pressure can cause the dissipation of perturbation in the baryonic component, as well as the coupling of baryonic and radiation temperature until the time of decoupling, and fast moving ('hot') dark matter particles can lead to kinematic suppression of growth.
This latter effect is mainly important to determine the overall scenario; in fact, hot dark matter particles cancel small–scale structures just by free–streaming across the

small potential wells, so that $T(k)$ vanish for large k. At the opposite, slow moving ('cold') dark matter particles suffer for a smaller dissipation at the horizon size $d_H = c/H$ at matter–radiation equality; nevertheless, a significant signal remains on small scales. Hence, two completely different scenarios results in each case: if the dark matter were 'hot' – which is called HDM scenario – the largest structures form first, and the smallest ones descend by fragmentation. In such scenario, galaxies form at late time, after galaxy clusters. On the other hand, in the CDM scenario – in which the dark matter is 'cold' – the smallest structures, namely the galaxies – are those who form first, becoming the building blocks for the largest ones. These two scenario are also called 'top–down' (the first) and 'bottom–up' (the second). There is no need to say that the HDM scenario has been ruled out by observations, which for instance definitively state, roughly speaking, that galaxies form well before clusters. The net result of perturbation growth in the CDM model is then a Power–Spectrum having a characteristic turn–over at the scale of order the horizon at matter–radiation equality with an asymptotic shape at small scale of $P(k) \propto k^{n-4}$.

In the rest of this Section, we give an outline of the linear theory of growth of structure. An extensive and complete treatment is given e.g. by Peebles (1980).

As we assume that at early times inhomogeneities were small, a perturbative approach can be adopted, at least as a first approximation. Furthermore, if the length scale of perturbations is smaller than the effective cosmological horizon $d_H = c/H$ a Newtonian treatment is physically grounded. If the mean free path of particles is small, matter can be treated as an ideal fluid. Hence, the usual equations (mass conservation, Euler's equation, Poisson's equation – see Sec. (3.1)) must be re–written using comoving coordinates $\mathbf{x} = \mathbf{r}/a(t)$ (spatial coordinates, fixed for an observer moving along with the Hubble expansion), $\mathbf{v} = \dot{\mathbf{r}} - H\mathbf{r} = a\dot{\mathbf{x}}$ (the peculiar velocity field, which represents the proper motions of particles besides the Hubble expansion), $\rho(\mathbf{x}, t)$ (the density field) and $\phi(\mathbf{x}, t)$ (the local value of Newtonian potential, which relates to the fluctuations in the density field). For the exact equations in comoving form see, for instance, Coles & Lucchin (1995).

Expanding ρ, $\mathbf{v}$ and ϕ perturbatively and taking only terms which are linear in δ gives :

$$\ddot{\delta} + 2H\dot{\delta} - \frac{3}{2}\Omega H^2 \delta = 0 \tag{1.19}$$

This linear equations has two independent solutions $\delta_\pm = D_\pm(t)\delta(\mathbf{x})$, where $D_-(t)$ is the *decaying mode* and $D_+(t)$ is the *growing mode* which shortly comes to dominate the evolution of δ. In an Einstein–de Sitter cosmology, for instance, the two modes are $\delta \propto t^{-1}$ and $\delta \propto t^{2/3}$ which also has $D_+(t) \propto a(t)$. The solution for the growth factor $D_+(t)$ in general cosmologies are given by Peebles (1980).
As long as each Fourier mode $\tilde{\delta}(\mathbf{k})$ is small, $\tilde{\delta}(\mathbf{k}) \ll 1$, the linear approximation can be applied and each Fourier mode evolves independently of the others, so that the Power–

Spectrum simply scales as the square of the growth factor. This is what is called the *linear regime* in which larger scales persist longer than the smallest ones, which are those entering first in the *non–linear regime*.

An important difference hold between the collapse of dark and baryonic matter. In fact, baryons suffer for more interactions than dark matter particles; we know, for instance, that the radiation drag prevent it to collapse until the recombination era. At later times, generally, what may impede the baryons to collapse is the pressure support due to baryon–baryon interaction. Jeans (1928) defined, as a function of the local temperature T and the pressure P, a critical length $\lambda_J(T, P)$ below which the pressure waves have times to propagate, then counteracting the gravitational support; his calculations were made in a Newtonian framework, for perturbations in an infinite, uniform and stationary distribution of gas. The mass scale M_J is defined as the mass encompassed in a sphere of radius $\lambda_J/2$, so that perturbation having mass below this limit are not able to undergo the collapse. A similar calculation can be made also in the framework of modern cosmology, accounting for pressure forces in the previous linear equation. The obtained result is just a lower limit to the mass that is able to collapse, since M_J is once more a perturbative result and thus it can only describe the first phases of the process.

It is worthnoting that the Jeans mass represents only a necessary but not a sufficient condition for the collapse of baryons; in addition[1] one has to require that the cooling time (i.e. the characteristic time taken by the gas to loose its internal energy by radiative emission) is shorter than the Hubble Time (i.e. the characteristic expansion time of the universe).
Many competing physical processes – e.g. radiative cooling, molecular cooling, heating from first sources of light, magnetic fields – affect the baryons settling in the potential wells, and the relative importance of them changes with redshift; we address the reader to, e.g., Barkana & Loeb (2001) and Ciardi & Ferrara (2004) and references therein.

Anyway, Dark Matter is made by collisionless particles that interact very weakly with the rest of matter and the radiation field; hence, density contrasts in this component start to collapse at earlier times than the baryonic component. When the perturbation δ becomes of order unity, the full non–linear gravitational problem must be solved; in order to do this, we must resort to numerical N–Body calculations, though a powerful approximation for the mild non–linear regime has been found by Zel'dovich (1970). In such approximation, the first non–linear objects are sheet-like structures, resulting from the contraction along one of the principal axis. As the probability of simultaneous contraction along two (filamentary structures) or three (point–like structures) axis is much less, 'pancakes' dominate the first stage of non–linear evolution.

[1] In fact, the physics of baryonic collapse is not yet fully understood and all recipes are still fairly empirical.

At later times, the prediction of the Zel'dovich model are no longer accurate. Then, the simplest case for which we can find an analytical solution is that of a spherically symmetric perturbation, having a top–hat distribution of uniform density δ_i inside a sphere or radius R_i. Results from this rough model surprisingly comes out to be very useful to gain an accurate description of properties and distribution of halos in the CDM model.
The collapse of such a spherical top–hat is described, in Newtonian formalism, by:

$$\frac{\mathrm{d}^2 r}{\mathrm{d}t^2} = H_0^2 \Omega_\Lambda r - \frac{GM}{r^2} \tag{1.20}$$

where r is the radius in a fixed coordinate frame, H_0 is the present value for the Hubble constant, M is the total mass enclosed in the radius r and the initial velocity field is given by the Hubble flow. Initially, the enclosed δ grows linearly as $\delta_i D(t)/D(t_i)$. We assume that the mass shell at radius r is bound, so that it reaches a maximum expansion and subsequently collapses. The overdensity predicted by the linear theory for the collapse to a point–like structure if (Peebles 1980) $\delta = 1.686$ in an Einstein–de Sitter universe. Thus, a top–hat collapse at redshift z if its linear overdensity extrapolated to the present (the *critical density*) is:

$$\delta_{\mathrm{crit}}(z) = \frac{1.686}{D(z)} \tag{1.21}$$

where $D(z = 0) = 1$. Instead, the halo reaches the virial equilibrium by violent relaxation (which basically means a phase mixing); using the virial theorem we obtain (Peebles 1980) as for the final overdensity at the redshift of collapse:

$$\Delta_c = 18\pi^2 \simeq 178 \tag{1.22}$$

that in a universe having $\Omega_\Lambda + \Omega_m = 1$ becomes (Bryan & Norman 1998):

$$\Delta_c = 18\pi^2 + 82x - 39x^2 \tag{1.23}$$

where $d \equiv \Omega_m^z - 1$ is evaluated at the same collapse redshift:

$$\Omega_m^z - 1 = \frac{\Omega_m (1+z)^3}{\Omega_m (1+z)^3 + \Omega_\Lambda + \Omega_k (1+z)^2}. \tag{1.24}$$

All in all, the following estimates are obtained as for, respectively, the virial radius and the virial temperature for a halo of mass M collapsing at redshift z:

$$r_{\mathrm{vir}} = 0.784 \left(\frac{M}{10^8 h^{-1}\,\mathrm{M}_\odot}\right)^{1/3} \left[\frac{\Omega_m}{\Omega_m^z}\frac{\Delta_c}{18\pi^2}\right]^{-1/3} \left(\frac{1+z}{10}\right)^{-1} h^{-1}\mathrm{kpc} \tag{1.25}$$

$$T_{\mathrm{vir}} = 1.98 \times 10^4 \left(\frac{\mu}{0.6}\right) \left(\frac{M}{10^8 h^{-1}\,\mathrm{M}_\odot}\right)^{2/3} \left[\frac{\Omega_m}{\Omega_m^z}\frac{\Delta_c}{18\pi^2}\right]^{1/3} \left(\frac{1+z}{10}\right) \mathrm{K} \tag{1.26}$$

where μ is the mean molecular weight ($\mu = 0.59$ for a fully ionized primordial gas, $\mu = 0.61$ for primordial gas with fully ionized Hydrogen but neutral Helium, $\mu = 1.22$ for neutral primordial gas).

Since density fluctuations may exist on all scales, in order to determine the formation of objects of a given size or mass it is useful to consider the statistical distribution of the smoothed density field. Using a window function W(y) normalized so that $\int d^3\mathbf{y} W(\mathbf{y}) = 1$, the smoothed density perturbation field, $\int d^3\mathbf{y}\delta(\mathbf{x}+\mathbf{y})W(\mathbf{y})$, itself follows a Gaussian distribution with zero mean. For the particular choice of a spherical top-hat, in which $W = 1$ in a sphere of radius R and is zero outside, the smoothed perturbation field measures the fluctuations in the mass in spheres of radius R. The normalization of the present power spectrum is often specified by the value of $\sigma_8 \equiv \sigma(R = 8\,h^{-1}\mathrm{Mpc})$. For the top–hat, the smoothed perturbation field is denoted δ_R or δ_M, where M is the mass related to the comoving radius R by $M = 4\pi\rho_m R^3/3$ in terms of the current mean matter density ρ_m. The function $\sigma(M)$ plays a crucial role in estimates of the abundance of collapsed objects. This is a critical test for any theory of structure formation, and it is a fundamental step toward inferring the abundances of galaxies and galaxy clusters. A simple analytic model which successfully matches most of the numerical simulations was developed by Press & Schechter (1974). The model is based on the ideas of a Gaussian random field of density perturbations, linear gravitational growth, and spherical collapse. To determine the abundance of halos at a redshift z, we use δ_M, the density field smoothed on a mass scale M, as previously defined. Although the model is based on the initial conditions, it is usually expressed in terms of redshift-zero quantities. Thus, we use the linearly extrapolated density field, i.e., the initial density field at high redshift extrapolated to the present by simple multiplication by the relative growth factor. Similarly, here the present power spectrum refers to the initial power spectrum, linearly extrapolated to the present without including non-linear evolution.

Calculations (see e.g. Press & Schechter 1974, Barkana & Loeb 2001) give the comoving number density $\mathrm{d}n$ of halos with mass between M and $M + \mathrm{d}M$:

$$\frac{\mathrm{d}\,n}{\mathrm{d}M} = \sqrt{\frac{2}{\pi}}\frac{\rho_m}{M}\frac{\mathrm{d}(-\ln\sigma)}{\mathrm{d}M}\nu_c\, e^{-\nu_c^2/2} \tag{1.27}$$

where $\nu_c = \delta_{\mathrm{crit}}(z)/\sigma(M)$ is the number of standard deviations which the critical collapse overdensity represents on mass scale M. Although this distribution function represents fairly well the observations and also the numerical N–Body experiments, a significantly better agreement can be achivied using an ellipsoidal collapse model instead of the simpler spherical one (Sheth & Tormen 2002).

We address the reader to the following references for a more extended discussion

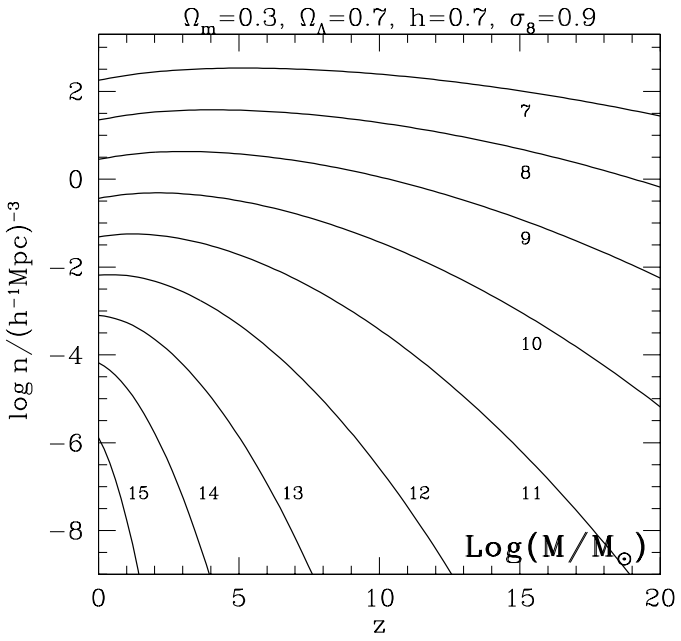

Figure 1.4: The evolution with redshift of the comoving number density of dark matter halos with mass exceeding a specific value in the standard ΛCDM model. For details see Mo & White (2002).

on these topics: see e.g. Peebles (1980, 1993), Coles & Lucchin (1995), Coles (2001), Barkana & Loeb (2001).

1.3 Galaxy Clusters

In this section we briefly summarize the main properties of galaxy clusters and the key observational facts about them. We also give a brief outline of their use to asses the cosmological framework. For further reading, we address the reader to Borgani & Guzzo (2001), Rosati et al. (2002) and to Borgani (2004) for a closer look on numerical simulations.

Clusters of galaxies were first identified as large concentrations in the projected galaxy distribution (Abell 1958, Zwicky et al. 1966, Abell et al. 1989), containing hundreds to thousands galaxies, over a region of the order of ~ 1 Mpc. The first observations showed that such structures are associated with deep gravitational potential wells, containing galaxies with a typical velocity dispersion along the line-of-sight of

$\sigma_v \sim 10^3\,\mathrm{km\,s^{-1}}$. The crossing time for a cluster of size R can be defined as

$$t_{\rm cr} \,=\, \frac{R}{\sigma_v} \simeq 1 \left(\frac{R}{1\mathrm{Mpc}}\right) \left(\frac{\sigma_v}{10^3\,\mathrm{km\,s^{-1}}}\right)^{-1} \mathrm{Gyr}\,. \tag{1.28}$$

Therefore, in a Hubble time, $t_H \simeq 10\,h^{-1}$ Gyr, such a system has enough time in its internal region, $\lesssim 1\,h^{-1}$Mpc, to dynamically relax – a condition that can not be attained in the surrounding, $\sim$10 Mpc, environment. Assuming virial equilibrium, the typical cluster mass is

$$M \,\simeq \frac{R\sigma_v^2}{G} \simeq \left(\frac{R}{1\,h^{-1}\mathrm{Mpc}}\right) \left(\frac{\sigma_v}{10^3\,\mathrm{km\,s^{-1}}}\right)^2 10^{15}\,h^{-1} M_\odot\,. \tag{1.29}$$

Smith (1936) first noticed in his study of the Virgo cluster that the mass implied by cluster galaxy motions was largely exceeding that associated with the optical light component. This was confirmed by Zwicky (1937), and was the first evidence of the presence of dark matter.

1.3.1. X-ray properties of clusters

Observations of galaxy clusters in the X-ray band have revealed a substantial fraction, $\sim$15%, of the cluster mass to be in the form of hot diffuse gas, permeating its potential well. If this gas shares the same dynamics as member galaxies, then it is expected to have a typical temperature

$$k_B T \,\simeq\, \mu m_p \sigma_v^2 \,\simeq 6 \left(\frac{\sigma_v}{10^3\,\mathrm{km\,s^{-1}}}\right)^2 \mathrm{keV}\,, \tag{1.30}$$

where m_p is the proton mass and μ is the mean molecular weight ($\mu = 0.6$ for a primordial composition with a 76% fraction contributed by hydrogen). Observational data for nearby clusters (e.g. Wu et al. 1999) and for distant clusters (see Figure 1.5) actually follow this relation, although with some scatter and with a few outliers. This correlation indicates that the idealized picture of clusters as relaxed structures in which both gas and galaxies feel the same dynamics is a reasonable representation. There are some exceptions that reveal the presence of a more complex dynamics.

At the high energies implied by Eq. (1.30), the ICM behaves as a fully ionized plasma, whose emissivity is dominated by thermal bremsstrahlung. The emissivity for this process at frequency ν scales as

$$\epsilon_\nu \propto\, n_e n_i g(\nu, T)\, T^{-1/2} \exp\left(-h\nu/k_B T\right) \tag{1.31}$$

where n_e and n_i are the number density of electrons and ions, respectively, and $g(\nu, T) \propto \ln(k_B T/h\nu)$ is the Gaunt factor. Whereas the pure bremsstra-hlung emissivity is a good

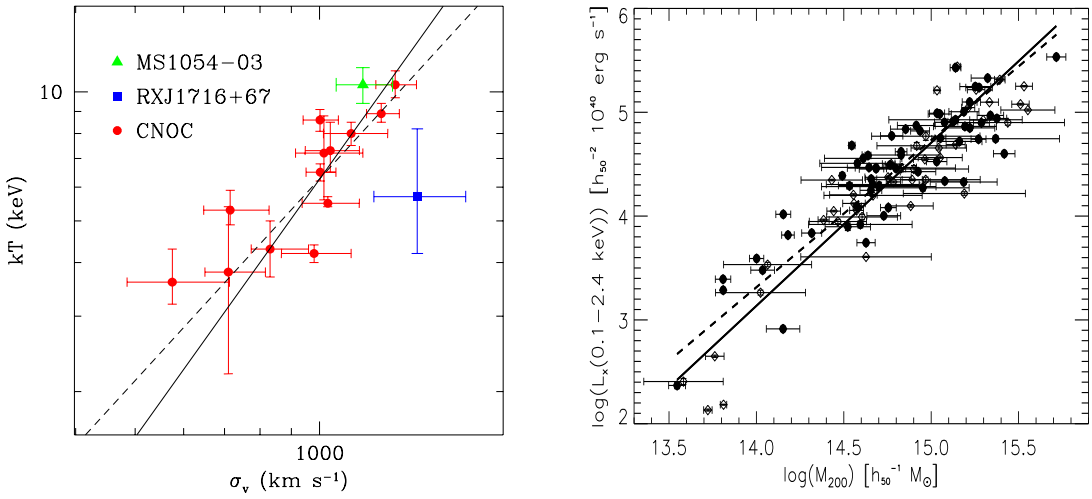

Figure 1.5: *Left* The relation between galaxy velocity dispersion, σ_v, and ICM temperature, T, for distant ($z > 0.15$) galaxy clusters. Velocity dispersions are taken from Carlberg et al. (1997) for CNOC clusters and from Girardi & Mezzetti (2001) for MS1054-03 and RXJ1716+67. Temperatures are taken from Lewis et al. (1999) for CNOC clusters, from Jeltema et al. (2001) for MS1054-03 and from Gioia et al. (1999) for RXJ1716+67. The solid line shows the relation $k_B T = \mu m_p \sigma_v^2$, and the dashed line is the best–fit to the low–z T–σ_v relation from Wu et al. (1999) *Right* The low-z relation between X-ray luminosity and the mass contained within the radius encompassing an average density $200\rho_c$ (from Reiprich & Boehringer 2002). The two lines are the best log–log linear fit to two different data sets indicated with filled and open circles.

approximation for $T \gtrsim 3$ keV clusters, a further contribution from metal emission lines should be taken into account when considering cooler systems (e.g. Raymond & Smith 1977). By integrating the above equation over the energy range of the X-ray emission and over the gas distribution, one obtains X-ray luminosities $L_X \sim 10^{43}$–$10^{45}\,\mathrm{erg\,s^{-1}}$. These powerful luminosities allow clusters to be identified as extended sources out to large cosmological distances.

Assuming spherical symmetry, the condition of hydrostatic equilibrium connects the local gas pressure p to its density $\rho_{\rm gas}$ according to

$$\frac{dp}{dR} = -\frac{GM(<R)\rho_{\rm gas}(R)}{R^2}\,. \tag{1.32}$$

By inserting the equation of state for a perfect gas, $p = \rho_{\rm gas} k_B T/\mu m_p$ into (1.32), one can express, $M(<R)$, the total gravitating mass within R as

$$M(<R) = -\frac{k_B T R}{G\mu m_p}\left(\frac{d\,\log\rho_{\rm gas}}{d\log R} + \frac{d\,\log T}{d\log R}\right)\,. \tag{1.33}$$

If R is the virial radius, then at redshift z we have $M \propto R^3 \bar{\rho}_0 (1+z)^3 \Delta_{vir}(z)$, where $\bar{\rho}_0$ is the mean cosmic density at present time and $\Delta_{vir}(z)$ is the mean overdensity within a virialized region. For an Einstein–de-Sitter cosmology, Δ_{vir} is constant and therefore, for an isothermal gas distribution, Eq. (1.33) implies $T \propto M^{2/3}(1+z)$.

Such relations show how quantities, such as $\rho_{\rm gas}$ and T, which can be measured from X-ray observations, are directly related to the cluster mass. Thus, in addition to providing an efficient method to detect clusters, X-ray studies of the ICM allow one to measure the total gravitating cluster mass, which is the quantity predicted by theoretical models for cosmic structure formation.

A popular description of the gas density profile is the β–model,

$$\rho_g(r) \; = \; \rho_{g,0} \left[1 + \left(\frac{r}{r_c} \right)^2 \right]^{-3\beta/2} , \tag{1.34}$$

which was introduced by Cavaliere & Fusco–Femiano ((1976); see also Sarazin (1988), and references therein) to describe an isothermal gas in hydrostatic equilibrium within the potential well associated with a King dark-matter density profile. The parameter β is the ratio between kinetic dark-matter energy and thermal gas energy (see Eq. (1.30)). This model is a useful guideline for interpreting cluster emissivity, although over limited dynamical ranges. Now, with the *Chandra* and *Newton-XMM* satellites, the X-ray emissivity can be mapped with high angular resolution and over larger scales. These new data have shown that (1.34) with a unique β value cannot always describe the surface brightness profile of clusters (e.g. Allen et al. 2001b).

Kaiser (1986) described the thermodynamics of the ICM by assuming it to be entirely determined by gravitational processes, such as adiabatic compression during the collapse and shocks due to supersonic accretion of the surrounding gas. As long as there are no preferred scales both in the cosmological framework (i.e. $\Omega_m = 1$ and power–law shape for the power spectrum at the cluster scales), and in the physics (i.e. only gravity acting on the gas and pure bremsstrahlung emission), then clusters of different masses are just a scaled version of each other. Because bremsstrahlung emissivity predicts $L_X \propto M \rho_{\rm gas} T^{1/2}$, $L_X \propto T_X^2 (1+z)^{3/2}$ or, equivalently $L_X \propto M^{4/3}(1+z)^{7/2}$. Furthermore, if we define the gas entropy as $S = T/n^{2/3}$, where n is the gas density assumed fully ionized, we obtain $S \propto T(1+z)^{-2}$.

It was soon recognized that X-ray clusters do not follow these scaling relations. As we discuss in Sec. (1.3.4), below, the observed luminosity–temperature relation for clusters is $L_X \propto T^3$ for $T \gtrsim 2$ keV, and possibly even steeper for $T \lesssim 1$ keV groups. This result is consistent with the finding that $L_X \propto M^\alpha$ with $\alpha \simeq 1.8 \pm 0.1$ for the observed mass–luminosity relation (e.g. Reiprich & Böhringer 2002; see right panel of Figure 1.5). Furthermore, the low-temperature systems are observed to have shallower central gas-density profiles than the hotter systems, which turns into an excess of

entropy in low–T systems with respect to the $S \propto T$ predicted scaling (e.g. Ponman et al. (1999), Lloyd–Davies et al. (2000); more recently, Ponman et al. (2003)). Although in the past years there were claims about a clear signature for a breaking in the scaling relations at the groups scale, nowadays a better understanding of intrinsinc scatter and selection effects of observations suggests that a unique slope may instead holds in the whole mass range (2004, 2004, 2003).

A possible interpretation for the breaking of the scaling relations assumes that the gas has been heated at some earlier epoch by feedback from a non-gravitational astrophysical source (Evrard & Henry 1991). This heating would increase the entropy of the ICM, place it on a higher adiabat, prevent it from reaching a high central density during the cluster gravitational collapse and, therefore, decrease the X-ray luminosity (e.g. Balogh et al. 1999, Tozzi & Norman 2001, and references therein). For a fixed amount of extra energy per gas particle, this effect is more prominent for poorer clusters, i.e. for those objects whose virial temperature is comparable with the extra–heating temperature. As a result, the self–similar behavior of the ICM is expected to be preserved in hot systems, whereas it is broken for colder systems. Both semi–analytical works (e.g. Cavaliere et al. 1998, Balogh et al. 1998, Wu et al. 2000, Tozzi et al. 2000) and numerical simulations (e.g. Navarro et al. 1995, Brighenti & Mathews 2001, Borgani et al. 2001a) converge to indicate that ~ 1 keV per gas particle of extra energy is required. We further discuss this point in Chap. (2).

The gas–temperature distributions in the outer regions of clusters are not affected by gas cooling. These temperature distributions have been studied with the *ASCA* and *Beppo–SAX* satellites. General agreement about the shape of the temperature profiles has still to be reached (1998, 2000, 2000). De Grandi & Molendi (2002) analyzed a set of 21 clusters with *Beppo–SAX* data and found the gas to be isothermal out to $\sim 0.2 R_{\rm vir}$, with a significant temperature decline at larger radii. Such results are not consistent with the temperature profiles obtained from cluster hydrodynamical simulations (e.g. Evrard 1997), thus indicating that some physical process is still lacking in current numerical descriptions of the ICM. Deep observations with *Newton–XMM* and *Chandra* will allow the determination of temperature profiles over the whole cluster virialized region.

X-ray spectroscopy is a powerful means for analyzing the metal content of the ICM. Measurements of over 100 nearby clusters have yielded a mean metallicity $Z \sim 1/3 Z_{\odot}$, largely independent of the cluster temperature (e.g. Renzini 1997, and references therein). The spatial distribution of metals has recently been studied in detail with *ASCA* and *Beppo–SAX* data (e.g. White 2000, De Grandi & Molendi 2002). This field has received a major boost over the next few years particularly with *Newton–XMM*, which, with a ten-fold improvement in collecting area and much better angular resolution, is able to map the distribution of different metals in the ICM, such as Fe, S, Si, O (see Sec. (1.4)).

1.3.2. Cooling in the Intra Cluster Medium

In order to characterize the role of cooling in the ICM, it is useful to define the cooling time–scale, which for an emission process characterized by a cooling function $\Lambda_c(T)$, is defined as $t_{cool} = k_B T/(n\Lambda(T))$, n being the number density of gas particles. For a pure bremsstrahlung emission:

$$t_{cool} \simeq 8.5 \times 10^{10}\mathrm{yr}\,(n/10^{-3}\mathrm{cm}^{-3})^{-1}\,(T/10^{8}K)^{1/2}\,. \tag{1.35}$$

Therefore, the cooling time in central cluster regions can be shorter than the age of the Universe. A substantial fraction of gas undergoes cooling in these regions, and consequently drops out of the hot diffuse, X-ray emitting phase. Studies with the *ROSAT* and *ASCA* satellites indicate that the decrease of the ICM temperature in central regions has been recognized as a widespread feature among fairly relaxed clusters (see Fabian (1994), and references therein). The canonical picture of cooling flows predicted that, as the high–density gas in the cluster core cools down, the lack of pressure support causes external gas to flow in, thus creating a superpositions of many gas phases, each one characterized by a different temperature. Our understanding of the ICM cooling structure is now undergoing a revolution thanks to the much improved spatial and spectral resolution provided by *XMM–Newton* . Recent observations have shown the absence of metal lines associated with gas at temperature $\lesssim 3$ keV (e.g. Peterson et al. 2001, Tamura et al. 2001), in stark contrast with the standard cooling flow prediction for the presence of low–temperature gas (e.g. Fabian et al. 2001, Böhringer et al. 2002).

Radiative cooling has been also suggested as an alternative to extra heating to explain the lack of ICM self–similarity (e.g. Bryan 2000, Voit & Bryan (2001), Voit et al. (2003)). When the recently shocked gas residing in external cluster regions leaves the hot phase and flows in, it increases the central entropy level of the remaining gas. The decreased amount of hot gas in the central regions causes a suppression of the X-ray emission (Pearce et al. 2000, Muanwong et al. 2001). This solution has a number of problems. Cooling in itself is a runaway process, leading to a quite large fraction of gas leaving the hot diffuse phase inside clusters. Analytical arguments and numerical simulations have shown that this fraction can be as large as $\sim 50\%$, whereas observational data indicates that only $\lesssim 10\%$ of the cluster baryons are locked into stars (e.g. Bower et al. 2001, Balogh et al. 2001). This calls for the presence of a feedback mechanisms, such as supernova explosions (Menci & Cavaliere 2000, Finoguenov et al. 2000b, Pipino et al. 2002, Kravtsov & Yepes 2000) or Active Galactic Nuclei (e.g. Valageas & Silk 1999a, Wu et al. 2000, Yamada & Fujita 2001), which, given reasonable efficiencies of coupling to the hot ICM, may be able to provide an adequate amount of extra energy to balance overcooling.

1.3.3. Clusters Detection

■ Optical detection

Abell (1958) provided the first extensive, statistically complete sample of galaxy clusters. Based on pure visual inspection, clusters were identified as enhancements in the galaxy surface density on Palomar Observatory Sky Survey (POSS) plates, by requiring that at least 50 galaxies were contained within a metric radius $R_A = 3h_{50}^{-1}$ Mpc and a predefined magnitude range. Clusters were characterized by their *richness* and estimated distance. The Abell catalog has been for decades the prime source for detailed studies of individual clusters and for characterizing the large scale distribution of matter in the nearby Universe. The sample was later extended to the Southern hemisphere by Corwin and Olowin (Abell, Corwin & Olowin, 1989) by using UK Schmidt survey plates. Another comprehensive cluster catalog was compiled by Zwicky and collaborators (Zwicky et al. 1966), who extended the analysis to poorer clusters using criteria less strict than Abell's in defining galaxy overdensities.

Several variations of the Abell criteria defining clusters were used in an automated and objective fashion when digitized optical plates became available. The Edinburgh-Durham Southern Galaxy Catalog, constructed from the COSMOS scans of UK Schmidt plates around the Southern Galactic Pole, was used to compile the first machine-based cluster catalog (Lumsden et al. 1992). In a similar effort, the Automatic Plate Measuring machine galaxy catalog was used to build a sample of ~ 1000 clusters (Maddox et al. 1990, Dalton et al. 1997).

Projection effects in the selection of cluster candidates have been much debated. Filamentary structures and small groups along the line of sight can mimic a moderately rich cluster when projected onto the plane of the sky. In addition, the background galaxy distribution against which two dimensional overdensities are selected, is far from uniform. As a result, the background subtraction process can produce spurious low-richness clusters during searches for clusters in galaxy catalogs. N-body simulations have been extensively used to build mock galaxy catalogs from which the completeness and spurious fraction of Abell-like samples of clusters can be assessed (e.g. van Haarlem et al. 1997).

■ X–ray detection

The X–ray detection of galaxy clusters began several years later, with the *Uhuru* and *Ariel V* satellites (Giacconi et al. 1972, McHardy et al. 1981) and the HEAO-1 A2 experiment (e.g. Henriksen & Mushotzky 1986). Nevertheless, the real era for X–ray observations started with the *Einstein Observatory* (Giacconi et al. 1979) due to its focusing capabilities.

X–ray surveys offer an efficient means of reconstructing samples of galaxy clusters out to cosmological interesting redshifts.
First, the X-ray selection has the advantage of revealing physically-bound systems, because diffuse emission from a hot ICM is the direct manifestation of the existence of a potential well within which the gas is in dynamical equilibrium with the cool baryonic matter (galaxies) and the dark matter. Second, the X-ray luminosity is well correlated with the cluster mass (see right panel of Fig. (1.5)). Third, the X-ray emissivity is proportional to the square of the gas density (Sec. (1.3)), hence cluster emission is more concentrated than the optical bidimensional galaxy distribution. In combination with the relatively low surface density of X-ray sources, this property makes clusters high contrast objects in the X-ray sky, and alleviates problems due to projection effects that affect optical selection. Finally, an inherent fundamental advantage of X-ray selection is the ability to define flux-limited samples with well-understood selection functions. This leads to a simple evaluation of the survey volume and therefore to a straightforward computation of space densities (for an extended discussion see Rosati et al. 2002).

The *ROSAT* satellite had an unprecedented sensitivity and spatial resolution, as well as low instrumental background. With the *ROSAT* All–Sky Survey (RASS; Trümper 1993) was the first X–ray imaging mission to cover the entire sky. Several generations of X–ray satellites has been subsequently launched: *ASCA* , *BeppoSAX* , *Chandra* , Xmm.

■ Other methods

X-ray and optical surveys have been by far the most exploited techniques for studying the distribution and evolution of galaxy clusters. Nevertheless, it is worthmentioning two other methods which rely on important physical properties of clusters. The first is the *Sunyaev-Zeldovich effect*. Clusters are revealed by measuring the distortion of the CMB spectrum owing to the hot ICM. This method does not depend on redshift and provides reliable estimate of cluster masses. It is possibly one of the most powerful methods to find distant clusters in the years to come. At present, serendipitous surveys with interferometric techniques (e.g. Carlstrom et al. 2002) cannot cover large areas (i.e. more than ~ 1 deg^2) and their sensitivity is limited to the most X-ray luminous clusters. The second method relies on the *Gravitational Lensing*; in principle a powerful method to discover mass concentrations in the universe through the statistical distortion of background galaxy images (see Mellier (2002) for a review).

1.3.4. Cosmology with Galaxy Clusters

The mass distribution of dark matter halos undergoing spherical collapse in the framework of hierarchical clustering is described by the Press-Schechter distribution (PS,

Press &Schechter 1974). The number of such halos in the mass range $[M, M + dM]$ can be written as

$$n(M, z)dM \; = \; \frac{\bar{\rho}}{M} \, f(\nu) \, \frac{d\nu}{dM} \, dM \tag{1.36}$$

where $\bar{\rho}$ is the cosmic mean density. The function f depends only on the variable $\nu = \delta_c(z)/\sigma_M$, and is normalized so that $\int f(\nu)\, d\nu = 1$. $\delta_c(z)$ is the linear–theory overdensity extrapolated to the present time for a uniform spherical fluctuation collapsing at redshift z. This quantity conveys information about the dynamics of fluctuation evolution in a generic Friedmann background. The r.m.s. density fluctuation at the mass scale M, σ_M, is connected to the fluctuation power spectrum, $P(k)$, whose normalization is usually expressed in terms of σ_8, the r.m.s. density fluctuation whithin a top–hat sphere of $8\,h^{-1}$ Mpc radius. In their original derivation of the cosmological mass function, Press &Schechter (1974) obtained the expression $f(\nu) = (2\pi)^{-1/2} \exp(-\nu^2/2)$ for Gaussian density fluctuations. Despite its subtle simplicity (e.g., Monaco 1998), the PS mass function has served for more than a decade as a guide to constrain cosmological parameters from the mass function of galaxy clusters. Only with the advent of the last generation of N–body simulations, which are able to span a very large dynamical range, significant deviations of the PS expression from the exact numerical description of gravitational clustering have been noticed (e.g. Gross et al. 1998, Governato et al. 1999, Jenkins et al. 2001, Evrard et al. 2002). Such deviations are interpreted in terms of corrections to the PS approach, e.g. by incorporating the effects of non–spherical collapse (Sheth & Tormen 2002). In the Left Panel of Fig. (1.6) we show that, for a fixed value of the observed cluster mass function, the implid value of σ_8 increases as the density parameter decreases.Determinations of the cluster mass function in the local Universe using a variety of samples and methods indicate that $\sigma_8 \Omega_m^{\alpha} \; = \; 0.4 - 0.6$, where $\alpha \simeq 0.4 - 0.6$, almost independent of the presence of a cosmological constant term providing spatial flatness (egReiprich & Böhringer 2002, Ikebe et al. 2002, Pierpaoli et al. 2003). It is worth pointing out that formal statistical uncertainties in the determination of σ_8 from the different analyses are always far smaller, $\lesssim 5\%$, than the above range of values. This suggests that current discrepancies on σ_8 are likely to be ascribed to systematic effects, such as sample selection and different methods used to infer cluster masses. We comment more on such differences in the following section. Completely independent constraints on a similar combination of σ_8 and Ω_m can be obtained with measurements of the cosmic gravitational lensing shear (e.g. Mellier 1999). The most recent results give $\sigma_8 \Omega_m^{0.6} = 0.45 \pm 0.05$ (van Waerbecke et al. 2001, and references therein).

The growth rate of the density perturbations depends primarily on Ω_m and, to a lesser extent, on Ω_Λ, at least out to $z \sim 1$, where the evolution of the cluster population is currently studied. Therefore, following the evolution of the cluster space density over a large redshift baseline, one can break the degeneracy between σ_8 and Ω_m. This is shown in a pictorial way in Figure 1.7 and quantified in the right panel of Figure 1.6:

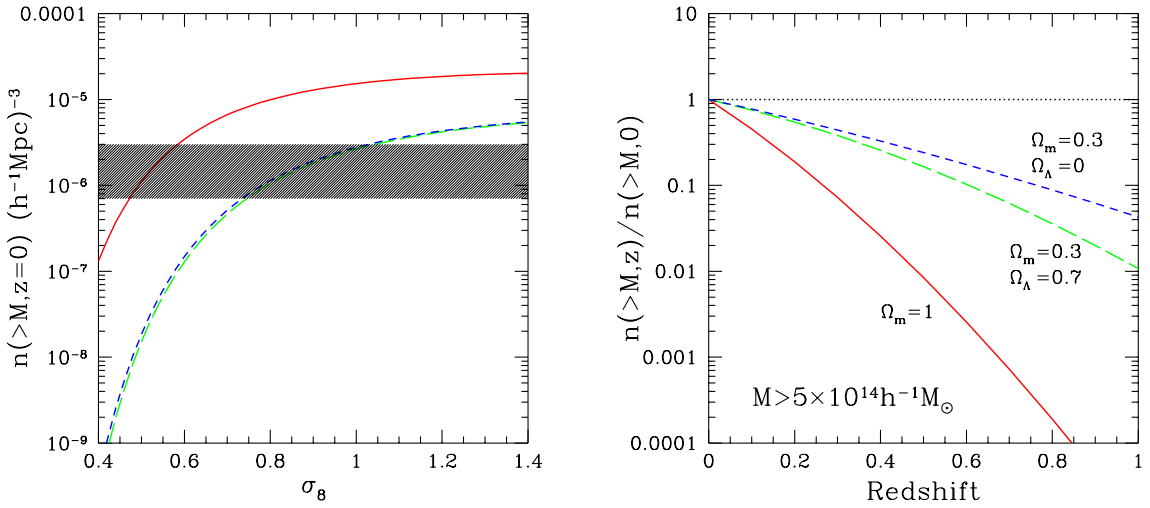

Figure 1.6: The sensitivity of the cluster mass function to cosmological models. (*Left*) The cumulative mass function at $z = 0$ for $M > 5 \times 10^{14} h^{-1} M_\odot$ for three cosmologies, as a function of σ_8, with shape parameter $\Gamma = 0.2$; solid line: $\Omega_m = 1$; short–dashed line: $\Omega_m = 0.3$, $\Omega_\Lambda = 0.7$; long–dashed line: $\Omega_m = 0.3$, $\Omega_\Lambda = 0$. The shaded area indicates the observational uncertainty in the determination of the local cluster space density. (*Right* Evolution of $n(> M, z)$ for the same cosmologies and the same mass–limit, with $\sigma_8 = 0.5$ for the $\Omega_m = 1$ case and $\sigma_8 = 0.8$ for the low–density models. *Taken from Rosati et al. (2002)*

models with different values of Ω_m, which are normalized to yield the same number density of nearby clusters, predict cumulative mass functions that progressively differ by up to orders of magnitude at increasing redshifts.

A common method to estimate cluster masses relies on the measurement of the temperature of the intra–cluster gas. Based on the assumption that gas and dark matter particles share the same dynamics within the cluster potential well, the temperature T and the velocity dispersion σ_v are connected by the relation $k_B T = \beta \mu m_p \sigma_v^2$, where $\beta = 1$ would correspond to the case of a perfectly thermalized gas. If we assume spherical symmetry, hydrostatic equilibrium and isothermality of the gas, the solution of the equation of hydrostatic equilibrium provides the link between the total cluster virial mass, $M_{\rm vir}$, and the ICM temperature: $k_B T \propto \beta^{-1} M_{\rm vir}^{2/3} [\Omega_m \Delta_{\rm vir}(z)]^{1/3} (1+z)\,{\rm keV}$, where $\Delta_{vir}(z)$ is the ratio between the average density within the virial radius and the mean cosmic density at redshift z. The previous expression for the M–T relation is fairly consistent with hydrodynamical cluster simulations with $0.9 \lesssim \beta \lesssim 1.3$ (e.g. Bryan & Norman 1998; see however Voit 2000). Observational data on the $M_{\rm vir}$–T relation show consistency with the $T \propto M_{\rm vir}^{2/3}$ scaling law, at least for $T \gtrsim 3$ keV clusters (e.g. 2001b), but with a $\sim$40% lower normalization. We will discuss in Chap. (2) possible reasons for this difference between the observed and simulated M–T relation. In any case, such uncertainties translate into an uncertain determination of σ_8 (for a fixed value of Ω_m): the higher the normalization of the M–T relation, the larger the mass corresponding to a given temperature, the larger the value of σ_8 required for the predicted mass function to match the observed X–ray temperature function (XRF; e.g. Pierpaoli et al. 2003). Another method to trace the evolution of the cluster number density is based on the XLF. The advantage of using X-ray luminosity as a tracer of the mass is that L_X is measured for a much larger number of clusters within samples well-defined selection properties. The most recent flux–limited cluster samples contain now a large (~ 100) number of objects, which are homogeneously identified over a broad redshift baseline, out to $z \simeq 1.3$. This allows nearby and distant clusters to be compared within the same sample, i.e. with a single selection function. The potential disadvantage of this method is that it relies on the relation between L_X and $M_{\rm vir}$, which is based on additional physical assumptions and hence is more uncertain than the $M_{\rm vir}$–σ_v or the $M_{\rm vir}$–T relations.

A useful parameterization for the relation between temperature and bolometric luminosity is $L_{\rm bol} \propto T_X^{\alpha} (1+z)^A (d_L(z)/d_{L,EdS}(z))^2$, with $d_L(z)$ the luminosity–distance at redshift z for a given cosmology. Independent analyses of nearby clusters with $T_X \gtrsim 2\,{\rm keV}$ consistently show that $\alpha \simeq 2.5 - 3$ (e.g. Arnaud & Evrard 1999 and references therein), with no evidence for a strong evolution out to $z \gtrsim 1$ (e.g. Ettori et al. 2004, Vikhlinin et al. 2002).

In Fig. (1.8) we show the constraints on the σ_8–Ω_m plane obtained from the *ROSAT* Deep Cluster Survey (Borgani et al. 2001b, Rosati et al. 2002). The different panels

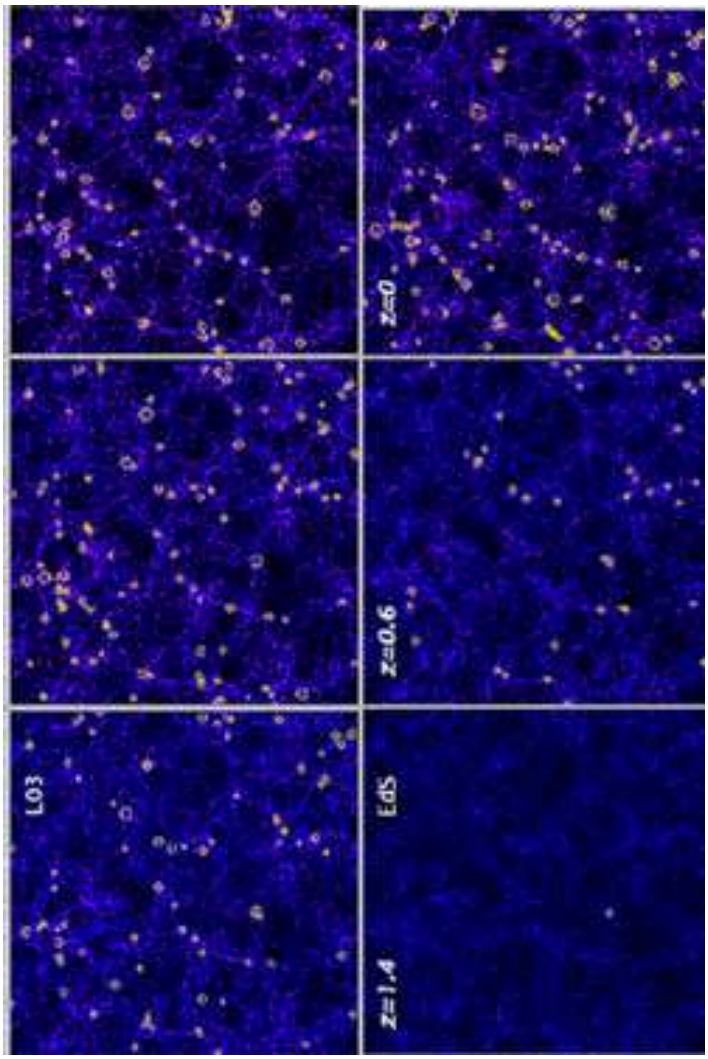

Figure 1.7: The evolution of the cluster population from N–body simulations in two different cosmologies (from Borgani & Guzzo 2001). Left panels describe a flat, low–density model with $\Omega_m = 0.3$ and $\Omega_\Lambda = 0.7$ (L03); right panels are for an Einstein–de-Sitter model (EdS) with $\Omega_m = 1$. Superimposed on the dark matter distribution, the yellow circles mark the positions of galaxy clusters with virial temperature $T > 3$ keV, the size of the circles is proportional to temperature. Model parameters have been chosen to yield a comparable space density of nearby clusters. Each snapshot is $250h^{-1}$ Mpc across and $75h^{-1}$ Mpc thick (comoving with the cosmic expansion). *Taken from Borgani & Guzzo (2001)*

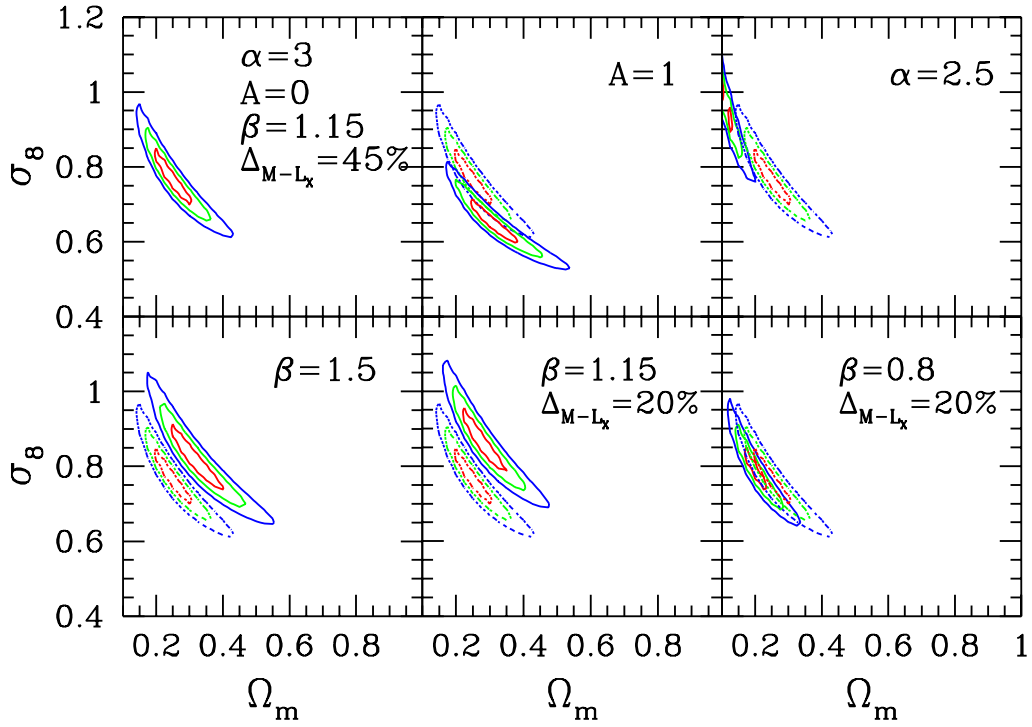

Figure 1.8: Probability contours in the σ_8–Ω_m plane from the evolution of the X–ray luminosity distribution of RDCS clusters. The shape of the power spectrum is fixed to $\Gamma = 0.2$. Different panels refer to different ways of changing the relation between cluster virial mass, M, and X–ray luminosity, L_X, within theoretical and observational uncertainties (see also Borgani et al. 2001b). The upper left panel shows the analysis corresponding to the choice of a reference parameter set. In each panel, we indicate the parameters which are varied, with the dotted contours always showing the reference analysis. *Taken from Borgani (2004)*

report the effect of changing in different ways the T–M–L_X, relation such as the slope α and the evolution A of the L_X–T relation, the normalization β of the M–T relation and the overall scatter ΔM-L_X. Fig. (1.8) demonstrates that firm conclusions about the value of the matter density parameter Ω_m can be drawn from available samples of X–ray clusters. In keeping with most of the analyses in the literature, based on independent methods, a critical density model cannot be reconciled with data. Specifically, $\Omega_m < 0.5$ at 3σ level even within the full range of current uncertainties in the relation between mass and X–ray luminosity. However, Fig. (1.8) results also demonstrate that constraints in the σ_8–Ω_m may change by changing the M–L_X relation within current uncertainties, by an amount which is at least as large as the statistical uncertainties. This emphasizes that the main obstacle toward a precision estimate of cosmological parameter with forthcoming large cluster surveys will lie in the systematic uncertainties in our description of the ICM properties, rather than in the limited statistics of distant clusters.

1.4 Chemical Enrichment of Galaxy Clusters

The ICM in Galaxy Clusters was predicted to harbor a huge amount of heavy elements firstly by Larson & Dinerstein (1975); their prediction was soon supported by the discovery (Mitchell et al. 1976) of a strong emission by the Iron Kα line in the spectrum of the Perseus clusters observed with *Ariel V*, subsequently confirmed by *OSO–8* observations that also detected Iron emission in spectra of Coma and Virgo (Serlemitsos et al. 1977). The analysis of ~ 30 clusters (Mushotzky 1984) found that the presence of Iron in the ICM was a common feature of galaxy clusters and set the abundance at level ~ 0.3–0.5 solar (throughout this work we follow the common notation Z_X as for indicating the abundance of the element X. Eventually, symbol $\odot$ indicate that the reported value is the solar one. See Sec. (1.4.1)).
Prior the launch of the *ASCA* satellite, Fe was the only well–measured element in the ICM; by the 1993, the good spectra resolution and large collecting area of *ASCA* over a broad X–ray band make it possible to realize first relative abundances studies (e.g. Fukazawa et al. 1994). Nevertheless, its limited imaging capability does not allow a precise spatial mapping of elements distribution throughout the ICM. The advent of subsequent X–ray telescopes, such as *BeppoSAX* , *Chandra* and *XMM–Newton* has increased our ability in resolving both spectra and spatial distribution. In particular, both *Chandra* and *XMM–Newton* data have much smaller systematic error and much better signal–to–noise ratios than data from earlier observations; *XMM–Newton* has been built in order to have a much better PSF than *ASCA* , whilst having a smaller field of view, and much more collecting area than *BeppoSAX* and *Chandra* . Unfortunately its background resulted relatively high, what could make results uncertain in some cases.

Despite the huge amount of available observational data on metal abundances in

the ICM, a well–stated picture on the chemical enrichment of galaxy clusters has yet to be drawn. Consensus has been reached only on the very general framework and trends, although several aspects are still debated. It is worthnoting that the large inhomogeneity in the collected data may play a crucial role in driving such interpretative differences.
In the following we discuss in turn the key observational facts.

1.4.1. Units of Measure

Throughout this work, following the standard usage in astronomy, we will refer to elements heavier than Helium as to "metals" or "heavy elements".

The pollution by the element i of a gas having primordial composition is expressed by the relative *abundance by mass* of that element:

$$\text{relative abundance} = \frac{M_i}{(M_{gas} - M^{tot}_{\text{metal}})} \tag{1.37}$$

if $M^{tot}_{\text{metal}} = \sum_j M_j$ is the total mass of all metals. It is common to express abundances in terms of the ratio between the concerned metal and the hydrogen, by number, so that Z^n_i is defined by

$$Z^n_i = N_i/N_H. \tag{1.38}$$

The Above expression defines the *abundance by number* of the element i.
Throughout the text, we will also use the term "metallicity" (by mass or by number) referring to the abundance of a single element, although "metallicity" should be reserved to indicate the abundance of *all* the elements heavier than Helium. Reference abundances are the solar ones, so that normally the metallicity for the element i is given in units of the solar abundance of the same element. The unpleasant drawback of this convention is to make the abundances reported in the literature dependent on the current accepted value for the solar abundances; this continues to make some confusion when results of different groups are compared.
There are two main methods to infer solar abundances; through studying the solar photosphere or analyzing the chemical composition of meteors. Generally, the agreement between meteoritic and photospheric values is now quite good. This was not the same in the past, when there were significative differences for key elements like the Iron. The two most widely used sets of abundance measures are those by Anders & Grevesse (1989) and Grevesse & Sauval (1998). In 1989 the disagreement between values obtained with different methods was not negligible: for instance, the abundance by number of Iron relatively to Hydrogen was $\sim 4 \times 10^{-5}$ and $\sim 3 \times 10^{-5}$ in photospheric and meteoric tables respectively. Mushotzky & Loewestein (1997), Ishimaru & Arimoto

Element	Photospheric	Meteoritic
H	12	-
C	8.52	-
O	8.83	-
Mg	7.58	7.58
Si	7.55	7.56
S	7.33	7.20
Fe	7.5	7.5

Table 1.2: Adopted solar abundances from Grevesse & Sauval (1998).

(1997) and Gibson, Mushotzky & Loewenstein (1997) discussed about implications of such difference.

Solar abundances are generally reported in a logarithmic scale whose "zero" is given by $\log N_H = 12.0$, so that

$$Z_i^{\odot} = \log(N_i/N_H) + 12 \tag{1.39}$$

Values for common elements are given in this units in Tab. (1.2).
Also common is the so–called "bracket notation" to report metallicities. If Z_i^n represent some measured abundance by number relative to hydrogen, then:

$$[Z_i^n] = \log(Z_i^n) - \log(Z_i^n)_{\odot} \tag{1.40}$$

In fact it is more practical and still widely used to report metallicities as mass ratios, though one must be aware to use consistent units (i.e. to refer to the Hydrogen mass). The solar abundance by number for the element i of atomic weight A_i, given in Tab. (1.2), relates to abundances by mass as follows:

$$Z_i^{m,\odot} = 10^{Z_i^{n,\odot}-12} \times A_i. \tag{1.41}$$

so that the abundance by mass ratio in solar units of an element i is given by:

$$Z_i = \frac{m_i/m_H}{(m_i/m_H)_{\odot}} \tag{1.42}$$

Strictly speaking, isotopes should be taken into account; nevertheless, given the uncertainties in the field this is really a minor issue. Throughout the text we will generally refer to mass abundances by mass if not otherwise stated.

1.4.2. The Heavy Elements Abundances

■ Iron

Iron is the most well–studied element and it is widely used as a tracer for the metal content of the ICM; this is due both to its ubiquity and to the fact that its emission lines are the strongest observable in the X–ray spectrum. Clusters having $T \gtrsim 3\,\mathrm{keV}$ show very strong emission from the Kα lines set at 6.97 and 6.67 keV, while lower–temperature systems exhibit Iron emission from the L–shell complex between 0.6 and 2.0 keV. Hwang et al. (Hwang et al. 1999) have shown that *ASCA* determinations of Fe abundances from just the L or K lines are consistent.

The mean Fe abundance of the ICM and its dependence on the temperature of the gas is probably the most well–stated fact on chemical enrichment of galaxy clusters. Fig. (1.9) shows different sets of data on the Fe abundances; the Top Panel report the compilation made by Renzini (2004), whereas the Bottom Panel shows the results from the *ASCA* database (Baumgartner et al. 2003). Data exhibit a remarkable uniformity in rich clusters ($T \gtrsim 3\,\mathrm{keV}$), being constant at $Z_{Fe} \sim 0.3 Z_{Fe}^{\odot}$ with very little scatter. Instead, cooler clusters tend to have much more higher abundances, though the differences in one– and two– temperature fits impose some caution (e.g. Buote 2000, Gastaldello & Molendi 2002). Nevertheless, such trend it is now commonly accepted as a matter of fact (e.g. Mushotzky 2004, Loewenstein 2004), and it is supported by data from *ASCA* shown in Bottom Panel of Fig. (1.9).

Abundances shown in Fig. (1.9) generally refer to the very innermost region of cluster. Nevertheless, detailed spatial analyses for many nearby clusters are available since the first data coming from *ASCA* and *ROSAT* (e.g. Fukazawa et al. 1994, Allen & Fabian 1994, Allen & Fabian 1998, Dupke & White 2000b, Finoguenov et al. 2000b, Finoguenov et al. 2001a). A general result from these works is the evidence of abundance gradients in several clusters, namely those ones identified as *Cooling–Flow* (CF) clusters; however, due to the coarse spatial resolution of *ASCA* , the shape of these gradients is only poorly determined (for instance, A496 has been resolved with only 2 to 5 bins by three successive analyses). Recently, De Grandi & Molendi (2001) have conducted a systematic study of Fe radial distribution using *BeppoSAX* data on 17 rich and nearby ($z \lesssim 0.1$) clusters. The main difference between data from *ASCA* and *BeppoSAX* relies to the different PSF of these two instruments. the *ASCA* PSF is broader (about twice that of *BeppoSAX*), strongly energy dependent and non radially symmetric, whereas the *BeppoSAX* PSF is sharper, almost energy independent and radially symmetric. Findings from De Grandi & Molendi are shown in Fig. (1.10). They confirm that CF clusters (that they call *Cooling Core* (CC) clusters; we adopt this notation hereafter) exhibit a strong radial gradient, having enhanced central abundances. At the opposite, non–CC clusters have fairly flat abundance profiles. Similar

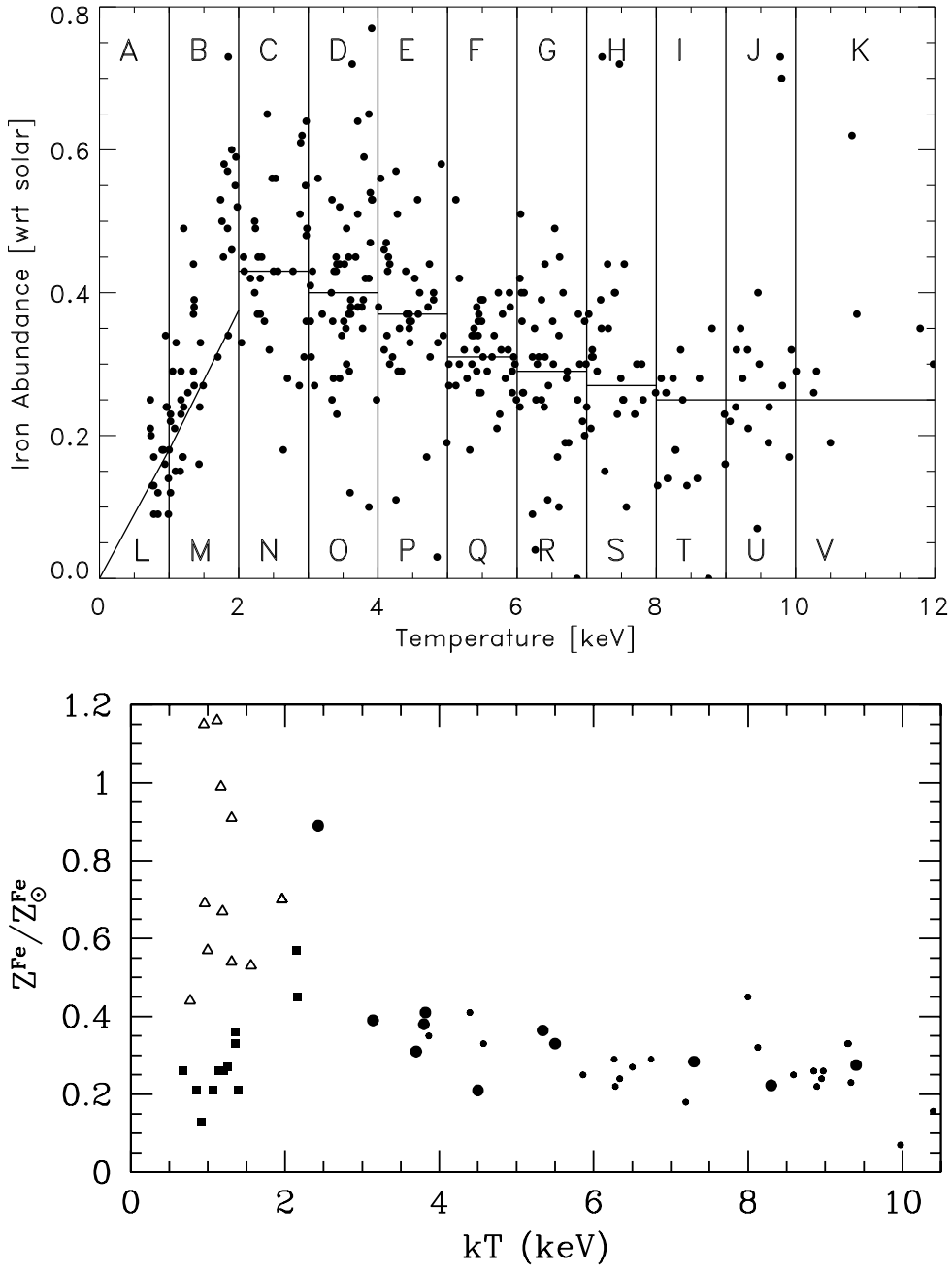

Figure 1.9: The mass dependence of Z_{Fe}^{ICM}. [**Top Panel**] data from Renzini (2004). Circles represent clusters having $T > 2\,\mathrm{keV}$ (smaller circles represent clusters at moderately high redshift, $\langle z \rangle \sim 0.35$). Other symbols (clusters and groups with $T < 2\,\mathrm{keV}$) represent data from Buote (2000) with temperature and abundances determined from one– and two– temperature fits (filled squares and empty triangles, respectively). [**Bottom Panel**] data from the *ASCA* database (Baumgartner et al. 2003).

results have been found by Irwin & Bregman (2001) for 11 clusters observed with *BeppoSAX* . Instead, in analyzing 106 *ASCA* imagings White (2000) find some enhancement in central abundances, particularly in CC clusters, but not a trend which is statistically significant (mainly due to uncertainties in measures).

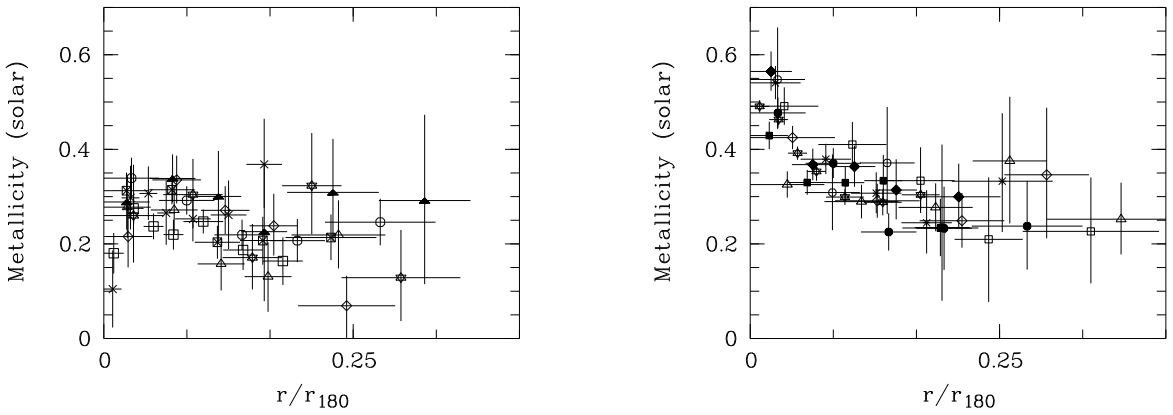

Figure 1.10: Figures from De Grandi & Molendi (2001). Distances are give in units of R_{180}. [**Left Panel**] Non–CC clusters Iron abundance profiles. [**Right Panel**] CC clusters Iron abundance profiles.

Tamura et al. (2004) observed very recently 19 bright, relaxed, nearby (all have $z < 0.1$ except A1835 which has $z = 0.254$) clusters with *XMM–Newton* . Their sample spans the interval 1 keV $\lesssim T \gtrsim$ 8 keV, yet being biased toward medium–temperature clusters. They find a general trend for the Z_{Fe} to increase in the central region in all systems, as shown in Fig. (1.11).

The correlation between an high Fe metallicity and a short cooling time in galaxy clusters is related to the parallel correlation between a radial gradient in the Fe abundance and the presence of a Cooling Core (Allen & Fabian 1998). The X–ray emission depends on the square of the ICM density, and so it is dominated by the innermost densest region; thus, the emission–weighted metallicity would also be determined mostly by the metallicity of the same central region. It is generally thought that non-CC clusters have recently suffered for a major merger event, which will disrupt the inner structure of ICM and re–mixed the gas. Nevertheless, these recent results from *XMM–Newton* not only confirm the known framework, but also suggest an Fe abundance enhancement in hot clusters without a prominent cD galaxy. To what extent this is changing the scenario is yet unclear.

In this respect, we mention that De Grandi & Molendi (2002) performed a detailed analysis of the deprojected spatial distribution of metals and gas for a sample of 22 nearby clusters observed with *BeppoSAX* (De Grandi & Molendi 2001). By directly integrating the deprojected Iron abundance and gas profile, they estimated the Iron mass as a function of radius. It is interesting their finding that the central excess of Iron

in CC clusters of ~ 0.5–$9.5 \times 10^9\,M_\odot$ can be easily accounted for by estimating the Iron mass ejected in the ICM by the stars of central Brigth Galaxy. As well, Fukazawa et al. (1998) analized a sample of 40 clusters extracted from the *ASCA* database; they found, accordingly whith the later suggestion of De Grandi & Molendi, that no appreciable trend with the temperature is shown by the spatially averaged Fe abundance (see Fig. (1.12))

■ Evolution of Fe Abundance

ASCA data have revealed a lack of evolution in the Iron content of galaxy clusters out to redshift 0.4 (Mushotzky & Loewenstein 1997, Matsumoto et al. 2000, Matsumoto et al. 2001) and no evidence od declining at higher redhistfs (Tozzi et al. 2003). *XMM–Newton* and Chandra observations have further expanded the redshift interval back to redshift ~ 1 (e.g. Tozzi et al. 2003) as shown in Fig. (1.13).

The epoch of main ICM enrichment has yet to be identified; in this respect, data on Fe abundance evolution could provide useful constraints on the epoch of Iron production

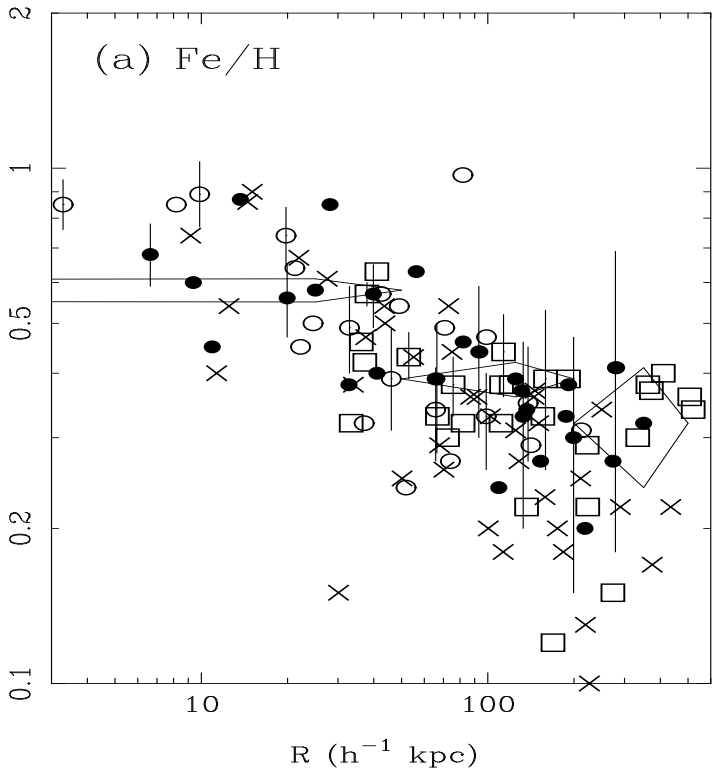

Figure 1.11: From Tamura et al. (2001). Radial profiles for Fe/H for 19 bright nearby clusters observed with *XMM–Newton* . Data are plotted in units of solar photosperic values by Anders & Grevesse (1989).

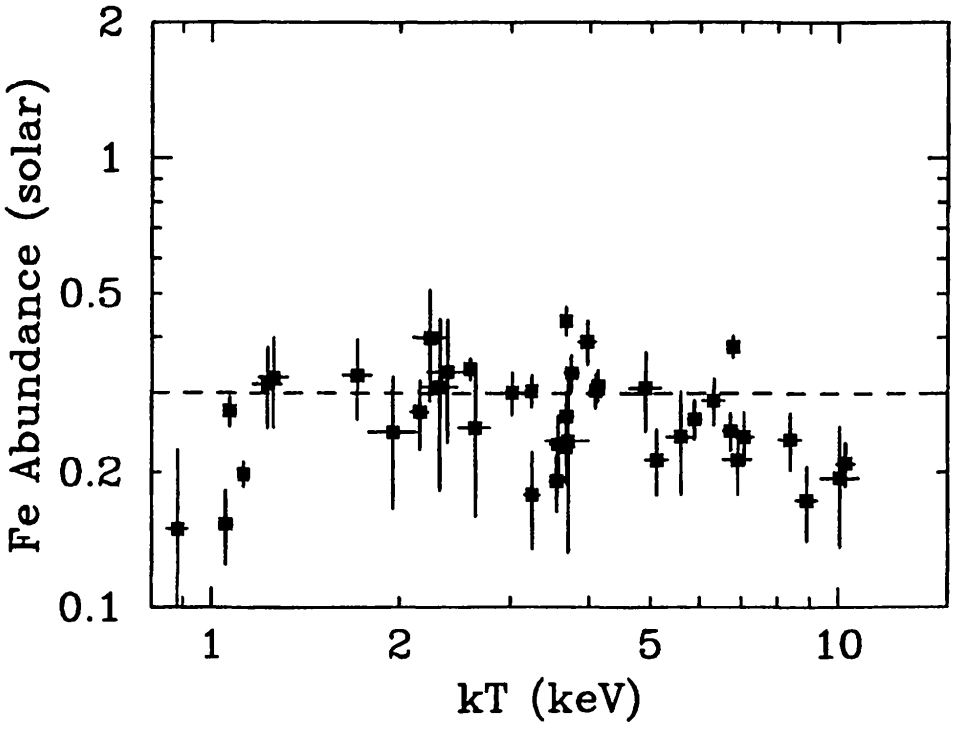

Figure 1.12: From Fukazawa et al. (1998). Spatially averaged Fe abundance obtained from *ASCA* data out to $\sim 0.4h_{50}^{-1}$ Mpc. Inner regions ($R < 0.1h_{50}^{-1}$ Mpc) has been removed. Solar adopted units are those by Anders & Grevesse 1989.

by stellar population as well as on the mechanism of metal ejection. We kown that most of the star formation in the universe occurred prior redshift ~ 1 (e.g. **?**) and the tightness of several correlations, such as the color–magnitude, fundamental plane and Mg_2–σ relations (e.g. Renzini 2004, Renzini 1999) suggests that stars in clusters formed at $z > 2$. As observations puch back the enrichment era, scenarios in which the ICM pollution occurs shortly after the begin of star formation are favoured over those predicting a substantial late enrichment via gas–stripping or SnIa–driven winds (Loewenstein 2004, Renzini 2004).

■ α Elements

In the tipical temperature range of the ICM, most of the elements are almost completely ionized and in collisional equilibrium. Most of them are in H– and He– like ionization states, so that their atomic physics is quite simple and the strength of lines is a direct measure for the abundance (e.g. Kahn et al. 2002).

The abundance of elements with the highest equivalent lines in the temperature

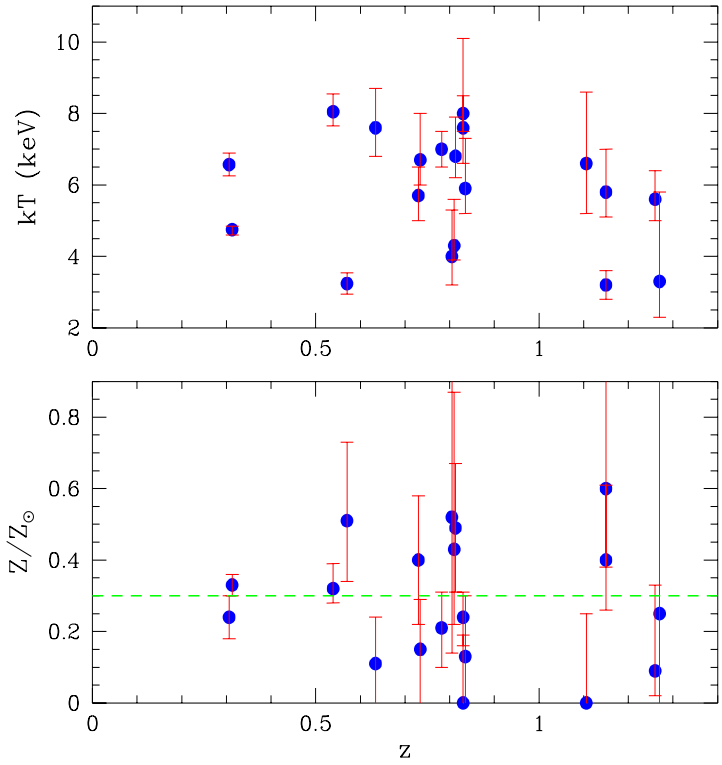

Figure 1.13: From Tozzi et al. (2003). The temperature (**Top Panel**) and averaged Fe abundance (in units of solar abundances given by Anders & Grevesse 1989) (**Bottom Panel**) for a sample of 18 distant clusters observed with *XMM–Newton* .

range 2×10^6–10^8 keV (C, N, O, Ne, Mg, Si, S, Ca, Ar, Fe and Ni) can be determined over a wide range of redshifts and cluster masses, often from one broadband X-ray spectrum. The less abundant elements, like Cr, Zn, Na and Al, are beyond our present capabilities but should be accessible to the next generation of missions (Mushotzky 2002). Besides the Iron, the next most accurate abundances being obtained for O, Si, S and Ni. The ability of X-ray CCDs to derive abundances depends on the temperature of the object, since the equivalent widths of the lines vary strongly with temperature and, when the equivalent width (EW) of the lines is much below the spectral resolution of the instrument, the derived abundances are not robust. For ASCA and Chandra, but not XMM, calibration problems at low energies have prevented accurate oxygen abundances. Ne and Mg are very di cult to measure properly with CCD spectrometers because the H- and He-like lines of these elements are blended with strong Fe L lines. The EWs of Ca and Ar are low and thus somewhat suspect with ASCA data. C and N are not in the ASCA CCD bandwidth and even the best CCDs have low spectral

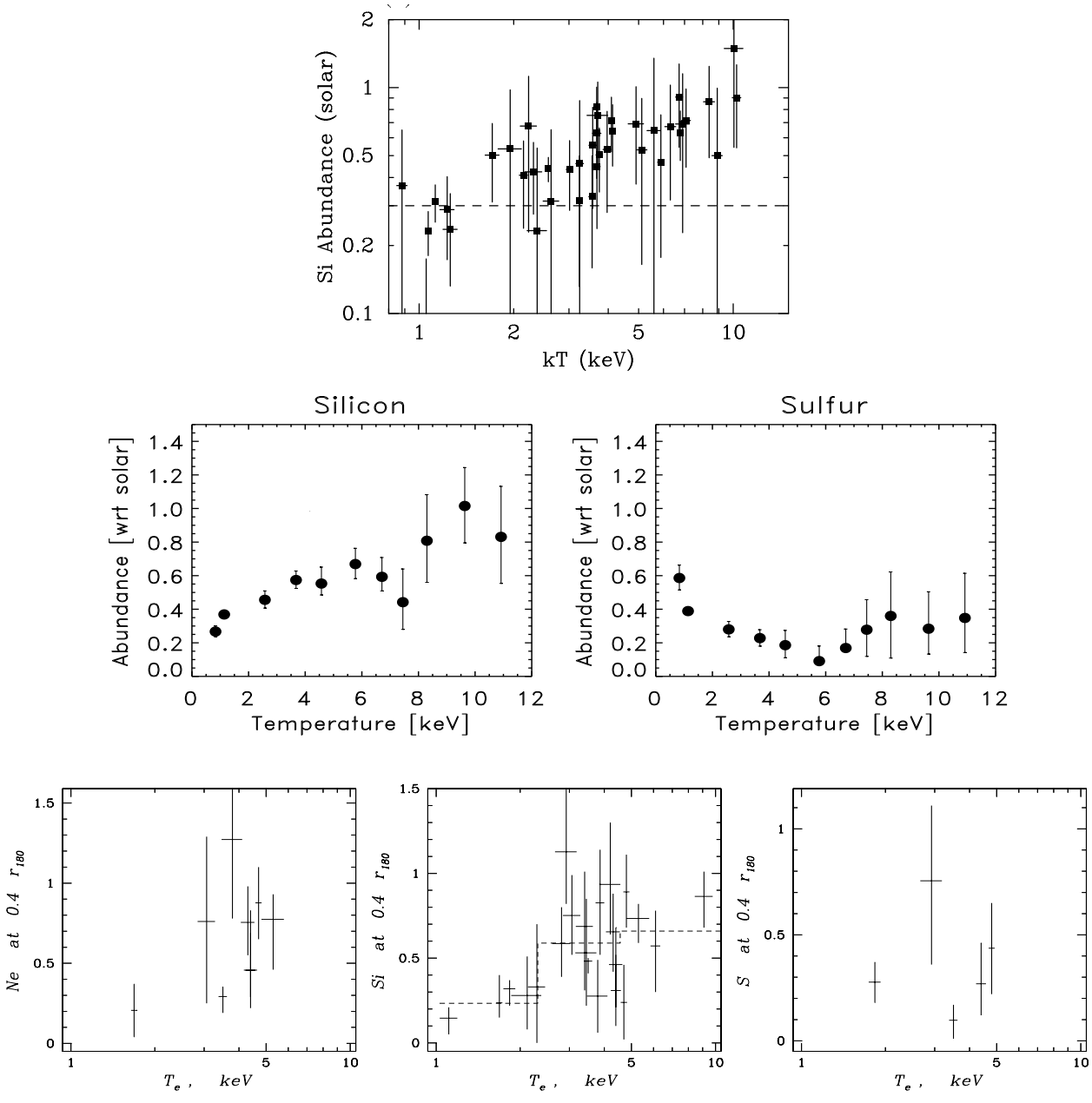

Figure 1.14: The Si abundance of central regions as a function of temperature [**Top Panel**] from Fukazawa et al. (1998) – Solar units by Anders & Grevesse 1989. [**Middle Panel**] From Baumgartner et al. (2003) – Solar units by Grevesse & Sauval 1998. [**Bottom Panel**] from Finoguenov, Arnaud & David (2001) – Solar units by Anders & Grevesse 1989.

resolution at the energies of their strongest lines. In objects with multi-temperature structure there is often not a unique solution for CCD-quality data, particularly for objects with $kT < 1.5$ keV, where the Fe L complex is extremely strong. The difficulty of interpreting these data has resulted in various works reporting rather different abundances. With the higher spatial resolution of Chandra and XMM and the better spectral resolution of the XMM RGS these regions are often resolved out spatially and spectrally and accurate abundances can be derived (Mushotzky 2002, Baumgartner et al. 2003). Elements like O, Mg, C, Ca and S are thought to come almost exclusively from SnII, whereas Ni is supposed to be exclusively produced by SnIa. Also, Fe and Si are mostly produced by SnIaand SnII, respectively. Thus, measuring the abundance of each element may provide us fundamental clues on a number of important topics: which is the IMF of parent stellar populations, what type of supernova is dominating the ICM pollution and at what epoch. Furthermore, the spatial dependence of relative abundance carries information on what is the dominant mechanism for metal ejection from IGM and wheter or not different mechanisms act at different epochs.

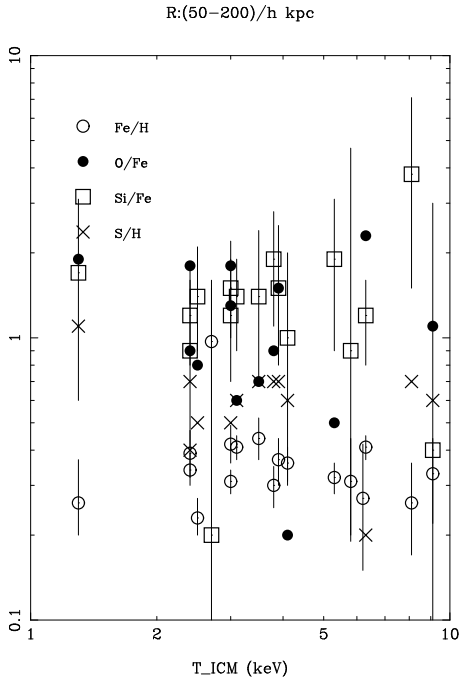

Figure 1.15: *XMM–Newton* data on 19 nearby bright clusters. Abundances have been averaged over the (50-200)h^{-1}kpc bin

The largest homogeneous sample available is that of *ASCA* observations (270 objects), whose data have been worked out by Baumgartner et al (2003). Subsamples have been analized by other groups: Fukazawa et al. (1998), Finoguenov & Ponman (together with *ROSAT* data;1999), Finoguenov, David & Ponman (together with

ROSAT data;2000b), White (2000), Dupke & White (2000a). *XMM–Newton* samples have been recently analized by Tamura et al. (2004), while several single–object observations are available in the literature. Most of the measures relates, besides Fe, to Si and S, whereas while only recently reliable estimates of Oxygen have been obtained. Both overall abundance and spatial distribution of SnII–produced elements constitute an unresolved puzzle. Provided that it is difficult to obtain reliable measures for O abundance, Si is generally treated as a proto–type as for the α group (note that this may be uncorrect to some extent; for instance, we have that the ratio $M_{\rm Si}^{\rm Ia}/M_{\rm Si}^{\rm Ia+II}$ is (0.2, 0.13, 0.19, 0.15) for, respectively, a Salpeter IMF, an Arimoto–Yoshii IMF, a Larson IMF at $2 = 3$ and $z = 5$ (see Sec. (4.5)) – we adopt yields from Woosley & Weaver 1995, Renzini & Voli 1981, Nomoto et al. 1997 model W7). A common finding in *ASCA* data analyses (e.g. Fukazawa et al. 1998, Finoguenov et al. 2000b, Finoguenov et al. 2001a, Baumgartner et al. 2003) is that the Si abundance correlates with the temperature of the cluster (or with $f_{\rm gas}$ as reported by Finoguenov, David & Ponman 2000) since $T \gtrsim 1\,{\rm keV}$. Ne exhibit a similar behaviour, whereas S, which should belong to the same nucleosynthtic channel than Si and Ne, does not suffer for such a variability and instead appears to be equally scattered at all masses (see Fig. (1.14)).

At odds, *XMM–Newton* data reported by Tamura et al. (2004) for clusters with mass in the range $1.3 < kT < 8.7$ show no particular trend with the temperature neither in the Fe abundance nor in α elements abundances (see Fig. (1.15)). As Tamura et al. note, the analized sample is biased towards medium–temperature luminous clusters, so that no striking conclusions can be inferred so far from this apparently stark discrepancy.

As for the spatial distribution, α elements are more widely present in the ICM than Fe, with mild or no radial gradients. Unfortunately, Asca pointing capability is not adequate to make detailed spatial maps of abundance distribution in galaxy clusters, so that the large ASCA database (Baumgartner et al. 2003, Loewenstein 2004) is not suited to obtain insights in this respect. However, in the past year few analyses have been made on a limited number of objects from the *ASCA* database (Finoguenov & Ponman 1999, Dupke & White 2000a, Dupke & White 2000b, Finoguenov et al. 2000b, Finoguenov et al. 2001a, White 2000, Allen et al. 2001a). More recently, spatial analises of *Chandra* (David et al. 2001, Ettori et al. 2002b) and *XMM–Newton* (Tamura et al. 2001, Xu et al. 2002, Peterson et al. 2003, Tamura et al. 2004, de Plaa et al. 2004) have been performed. The fact that α elements do not show appreciable or systematic gradients, on the contrary of SnIa elements, is generally interpreted as the effect of the combination of different epochs of injection for SnII and SnIa products and different physical mechanisms (winds vs gas–stripping) responsible for the transport of element into the ICM. Xmm observation of Abell 496 by Tamura et al. (2001) confirm the peak of Si abundance suggested by Dupke & White(2000b) and Finoguenov, David & Ponman (2000b). As well, they find a significant difference in the radial abundance profiles of O–Ne–Mg as compared to Si–S–Fe–Ni, which is quite

tricky to be explained reminding that both Si and S are α elements like O, Ne and Mg. S is found to exhibit α–abnormal properties also by Finoguenov & Ponman (1999; they even took it aside as they considered S measures unreliables) and by Finoguenov, David & Ponman (2000b) in that S/Fe ratio appears to be of pure SnIa–type (Finoguenov, David & Ponman conjecture that this can arise if the bulk of metals are produced in metal–poor galaxies). Properties of the sample analized by Tamura et al. (2004) can hardly be reconciled with the general results from *ASCA* ; in fact, they found no differences in radial profiles of *both* Si/Fe and S/Fe, while O/Fe ratio strongly increases with radius. In Fig. (1.16) we report the figures from Finoguenov, David & Ponman (200) and Tamura et al. (2004) on Si/Fe and O/Fe ratios.

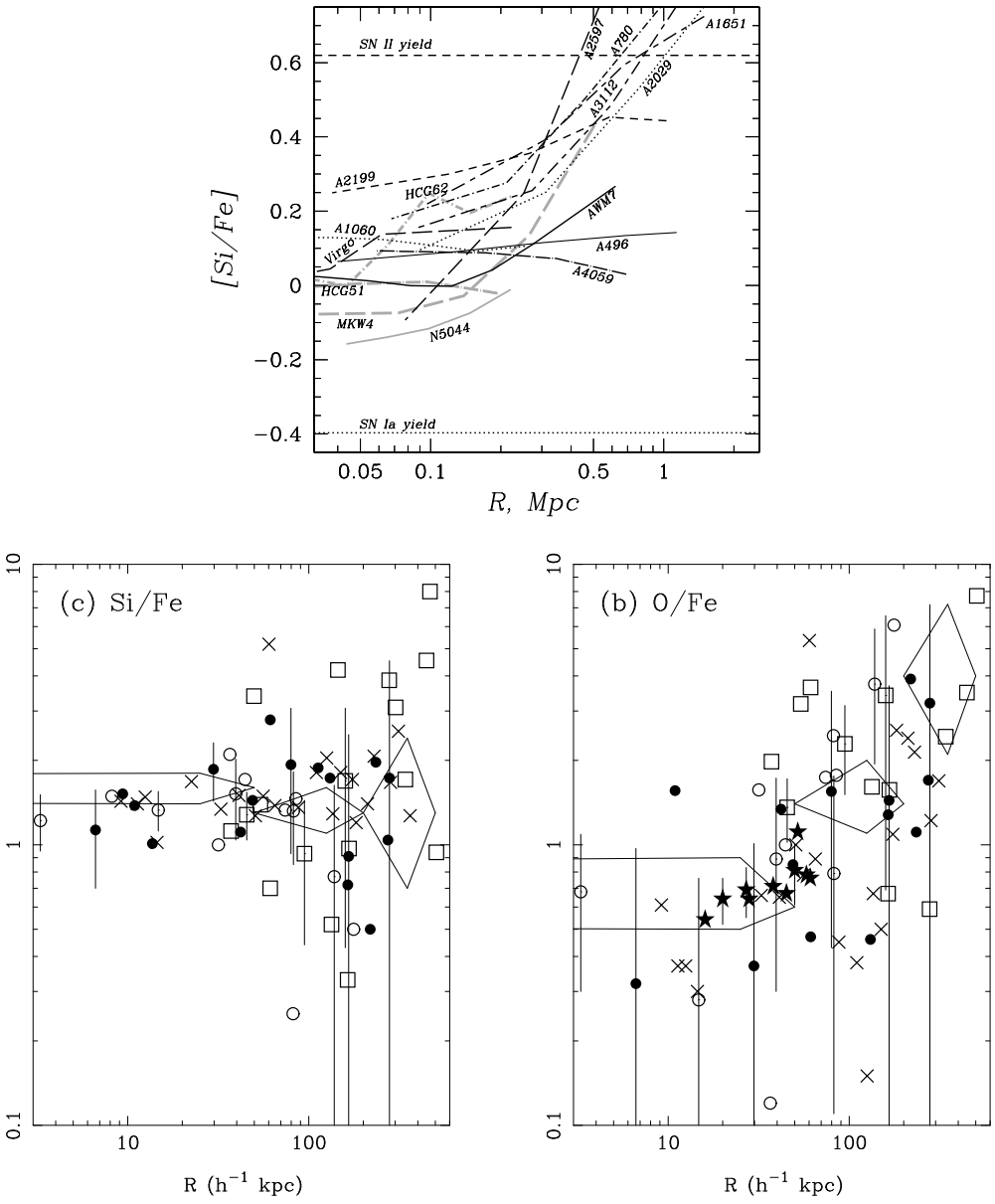

Figure 1.16: [**Top Panel**] Figure from Finoguenov, David & Ponman 2000. [**Bottom Panels**] Figure from Tamura et al. 2004. Best–fit values for cool, medium–temperature, hot and soft–excess clusters are shown with open–circles, filled–circles, opne–square and crosses respectively. Both papers give data in units of photospheric solar abundances by Anders & Grevesse (1989).

CHAPTER 2

THE THERMODYNAMICAL PROPERTIES OF THE ICM

The first part of our Ph.D. work is aimed at inspecting the effect of non–gravitational heating on the thermodynamical properties of the ICM. To this purpose, we insert suitable implementations in the original code by V. Springel, as we discuss in the following. The code used during this part of the work was an earlier version of GADGET that was ready in 2001, when we started this project. Instead, as for implementing the stellar evolution, we use a far more advanced version, as we report in detail in Chap. (4). The content of this chapter largely reflects the results presented in two papers which have already been published (Tornatore et al. 2003, Finoguenov et al. 2003b) and in the proceedings of several conferences.

■ *Chapter Outline*

By means of numerical simulations we discuss the thermodynamics of the ICM, focusing on the scaling relations of its X–ray properties. After a brief review on the observational results, we present and discuss the role of cooling and non–gravitational heating. Different thermodynamical paths and injection epochs are considered for the heating.

Introduction

The simplest picture to describe the thermal properties of the intra–cluster medium (ICM) is based on the assumption that gas heating occurs only by the action of gravitational processes, such as adiabatic compression from gravitational collapse, and by hydrodynamical shocks from supersonic accretion (Kaiser 1986). Since gravity does not have characteristic scales, this model predicts that galaxy systems of different mass look like scaled versions of each other. Under the assumptions of thermal bremsstrahlung emissivity and hydrostatic equilibrium, this model provides precise predictions for X–ray scaling properties of galaxy systems: **(a)** $L_X \propto T^2(1+z)^{3/2}$ for the shape and evolution of the relation between X–ray luminosity and gas temperature; **(b)** $S \propto T(1+z)^{-2}$ for the entropy-temperature relation, where $S = T/n_e^{2/3}$ is the gas entropy and n_e is electron number density; **(c)** $M \propto T^{3/2}$ for the relation between total cluster virial mass and temperature, with normalization determined by the parameter $\beta = \mu m_p \sigma_v^2 / k_B T$ ($\mu = 0.59$ mean molecular weight for primordial composition, namely hydrogen and Helium are 0.76% and 0.24% by mass respectively; m_p: proton mass; and σ_v: line-of-sight velocity dispersion). Numerical simulations that only include gravitational heating showed that $\beta \simeq 1$–1.3 (e.g. Navarro, Frenk & White 1995; Evrard, Metzler & Navarro 1996; Bryan & Norman 1998; Eke et al. 1998b; Borgani, Governato, Wadsley et al. 2002, BGW hereafter).

A number of observational facts demonstrate that this picture is too simplistic, thus calling for the consideration of extra physics in the description of the ICM. The L_X–T relation is found to be steeper than predicted, with $L_X \propto T^{\sim 3}$ at $T_X > 2$ keV (e.g., White, Jones & Forman 1997; Markevitch 1998; Arnaud & Evrard 1999; Ettori, De Grandi & Molendi 2002), possibly approaching the self–similar scaling only for the hottest systems with $T \gtrsim 8$ keV (Allen & Fabian 1998). Evidences also emerged for this relation to further steepen for colder groups, $T \lesssim 1$ keV (e.g., Ponman et al. 1996; Helsdon & Ponman 2000; Mulchaey 2000). Furthermore, no evidence for a strong positive evolution of the L_X–T relation has been found to date out to $z \sim 1$ (e.g., Mushotzky & Scharf 1997; Reichart et al. 1999; Fairley et al. 2000; Borgani et al. 2001a; Holden et al. 2002; Novicki, Sornig & Henry 2002; cf. also Vikhlinin et al. 2002). As for the S–T relation, Ponman, Cannon & Navarro (1999) found from *ROSAT* and *ASCA* data an excess of entropy within the central regions of $T \lesssim 2$ keV systems (see also Lloyd–Davis et al. 2000, Finoguenov et al. 2002a), possibly approaching the value $S \sim 100$ keV cm^2 for the coldest groups. Finally, a series of evidences, based on *ASCA* (e.g., Horner, Mushotzky & Scharf 1999; Nevalainen, Markevitch & Forman 2000; Finoguenov, Reiprich & Böhringer 2001b), *BeppoSAX* (Ettori et al. 2002) and *Chandra* (Allen, Schmidt & Fabian 2001) data, shows that the observed M–T relation has a ~ 40 per cent lower normalization than predicted by simulations that only include gravitational heating.

In the attempt of interpreting these data, theoreticians are currently following two alternative routes, based either on introducing non–gravitational heating of the ICM or on alluding to the effects of radiative cooling.

An episode of non–gravitational heating, occurring before or during the gravitational collapse, has the effect of increasing the entropy of the gas, preventing it from reaching high densities in the central cluster regions and suppressing its X–ray emissivity (e.g., Evrard & Henry 1991, Kaiser 1991; Bower 1997). For a fixed amount of specific heating, the effect is larger for poorer systems, i.e. when the extra energy per gas particle is comparable to the halo virial temperature. This produces both an excess entropy and a steeper L_X–T relation (e.g., Cavaliere, Menci & Tozzi 1998; Balogh, Babul & Patton 1999; Tozzi & Norman 2001). Arguments based on semi–analytical work (e.g., Tozzi & Norman 2001) and numerical simulations (Bialek, Evrard & Mohr 2001; Brighenti & Mathews 2001; Borgani et al. 2001b, 2002) suggest that a specific heating energy of $E_h \sim 1$ keV/part or, equivalently, a pre–collapse entropy floor of $S \sim 100$ keV cm^2, can account for the observed X–ray properties of galaxy systems (cf. also Babul et al. 2002, Finoguenov et al. 2002a for arguments suggesting a stronger pre–heating). Yet, the origin for this energy has still to be determined. Energy release from supernovae feedback has been advocated as a possibility (e.g., Bower et al. 2001; Menci & Cavaliere 2001). Using the abundance of heavy elements of the ICM as a diagnostic for the past history of the star formation within clusters (e.g., Renzini 1997; Kravtsov & Yepes 2000; Pipino et al. 2002; Valdarnini 2002), a number of studies concluded that SN may fall short in providing the required extra–energy budget (cf. also Finoguenov, Arnaud & David 2001a). The other obvious candidate is represented by energy from AGN (e.g., Valageas & Silk 1999; Wu, Fabian & Nulsen 2000; Mc Namara et al. 2000; Nath & Roychowdhury 2002; Cavaliere, Lapi & Menci 2002). In this case, the large amount of energy that is available requires some degree of tuning of the mechanisms responsible for its conversion into thermal energy of the gas. While a suitable amount of non–gravitational heating can account for the observed L_X–T relation and entropy excess, the M–T relation is only marginally affected by extra heating (e.g. BGW), thus leaving the discrepancy between observed and predicted relation unresolved.

As for cooling, its effect is to selectively remove those low–entropy particles from the diffuse X–ray emitting phase which have cooling times shorter than the Hubble time (e.g., Voit & Bryan 2002; Wu & Xue 2002). Conversion of cooled gas into collisionless stars decreases the central gas density and, at the same time, the resulting lack of pressure support causes higher–entropy shocked gas to flow in from the outskirts of the cluster or group. As a result, the X–ray luminosity is suppressed, while the entropy increases, much like in a pre–heating scenario (Pearce et al. 2001; Muanwong et al. 2002; Davé, Katz & Weinberg 2002). However, by its nature, cooling is known to be a runaway process: cooling causes gas to be accumulated into dense structures, and the efficiency of cooling increases with gas density. As a result, most simulations

consistently predict a significant fraction of gas to be converted into cold "stars", $f_{\rm cold} \gtrsim 30$ per cent (e.g., Suginohara & Ostriker 1998; Lewis et al. 2000; Yoshida et al. 2002; BGW), while observations indicate a considerably lower value of $f_{\rm cold} \lesssim 10$ per cent (e.g., Balogh et al. 2001; Wu & Xue 2002).

This suggests that in real clusters some source of extra heating is increasing the entropy of the gas, preventing overcooling. Voit et al (2002) have developed a semi–analytical approach to derive X–ray observable properties of the ICM in the presence of both cooling and extra heating. Based on this approach, these authors found that cooling and a modest amount of extra heating are able to account for basically all the X–ray ICM observables. Oh & Benson (2002) pointed out that pre–heating is needed to increase the cooling time and prevent overcooling, by suppressing the gas supply to galaxies (see also Finoguenov et al. 2002b). It is however clear that, as for any analytical approach, suitable assumptions and approximations are needed to choose criteria for removing cooled gas from the hot diffuse phase, and to follow the complex dynamics of cooling/heating of gas during the process of cluster formation.

Muanwong et al. (2002) and Kay, Thomas & Theuns (2002) used hydrodynamical simulations within a cosmological box to study the interplay of gas cooling and a few prescriptions for non–gravitational heating. As a general result, they found that increasing the heating can suppress the amount of cooled gas. While the choice of simulating a whole cosmological box has the advantage of providing a large statistics of groups and clusters, it also severely limits the available mass and force resolution. On the other hand, by the very nature of cooling, increasing the mass resolution allows to follow the formation of smaller halos at progressively larger redshift, where cooling and, potentially, star formation are particularly efficient. As a consequence, unless very high mass resolution is achieved, cooling in simulations can be significantly underestimated (e.g., Balogh et al. 2001).

We follow the alternative approach of simulating at very high resolution a limited number of group– and cluster–sized halos selected from a cosmological box, and we widen the explored range of possible patterns for non–gravitational heating (see also BGW). While this limits our ability to precisely calibrate shape and scatter of X–ray scaling relations, we are able to increase the resolution in the most interesting regions of the gas distribution. Indeed, the simulations presented in this Chapter are among the highest resolution attempts realized so far to follow the structure of gas cooling within groups and clusters in the presence of a variety of schemes for extra gas heating. Furthermore, we also investigate how the cooling efficiency depends both on numerical resolution and on details of the SPH implementation.

The structure of this Chapter is as follows. After providing a short description of the code, we present in Section 2 the procedure to simulate individual halos at high resolution and discuss the main characteristics of the four selected halos. In Section 3, we discuss the results on the cold fraction. Here we will concentrate on showing how this fraction depends on numerical resolution, integration scheme and removal of cold dense

particles from the SPH computation (star formation). Finally, we present the adopted schemes for non–gravitational gas heating and discuss their impact on the resulting cold fraction and pattern of star formation. In Section 4, we present the predictions on X–ray properties of clusters and groups from our simulations, namely the entropy–temperature, the luminosity–temperature and the mass–temperature relations. Finally, we discuss our main results and draw conclusions in Section 5.

2.1 The simulations

2.1.1. The code

We realized the simulations presented in this Chapter using the former version of GADGET [1], a parallel tree N–body/SPH code (for a complete reference, see Springel, Yoshida & White 2001), with fully adaptive time–step integration. Gas cooling in the SPH part of the code is implemented following Katz, Weinberg & Hernquist (1996, KWH hereafter). Specifically, the abundances of ionic species are computed by assuming collisional equilibrium for a gas of primordial composition (mass–fraction $X = 0.76$ of hydrogen and $1 - X = 0.24$ of helium). No metal content is accounted as for calculating the gas emissivity. We include the effect of a time–dependent uniform UV background (e.g., Haardt & Madau 1999), although its effect is only very small for the massive objects we focus on in this study. We set the number of neighbors for SPH computations to 32, allowing the SPH smoothing length to drop at most to the value of the gravitational softening length of the gas particles. In this first part of our work, we not implement the metal production from star–formation. We provide a complete description of the most advanced version of the GADGET code in Chap. (3), as well as a detailed description of the implementation of stellar evolution in Chap. (4).

2.1.2. The simulated structures

We simulate four halos at high resolution, which are extracted from a low–resolution DM only simulation within a box of $70\,h^{-1}$Mpc on a side, for a cosmological model with $\Omega_m = 0.3$, $\Omega_\Lambda = 0.7$, Hubble constant $H_0 = 70$ km s^{-1} Mpc^{-1} and normalization $\sigma_8 = 0.8$, consistent with recent determinations of the number density of nearby clusters (Pierpaoli et al. 2002, and references therein). As for the baryon content, we assume $\Omega_{\rm bar} = 0.019\,h^{-2}$ (e.g., Burles & Tytler 1998). This choice of $\Omega_{\rm bar}$ corresponds to $f_{\rm bar} \simeq 0.13$ for the cosmic baryon fraction, which, for the assumed cosmology, is consistent with the value measured from cluster observations (e.g., Ettori 2002, and references therein).

[1] `http://www.mpa-garching.mpg.de/gadget`

The most massive halo we selected corresponds to a Virgo–like cluster, with virial mass of about $4 \times 10^{14} M_{\odot}$ (as usual, we call "virial" the mass within the radius encompassing the virial overdensity computed for the simulated cosmology; e.g. Eke et al. 1998a). This turns out to be the most massive system extracted from the simulation box. In the following, we will refer to this system as the "Virgo" cluster. The other three halos, which have been extracted from a single Lagrangian region, correspond to groups in the mass range $(2–6) \times 10^{13} M_{\odot}$. In the following, we will refer to these three structures as "Group-1", "Group-2" and "Group-3". We provide in Table 2.1 the main characteristics of the simulated structures.

We follow the technique originally presented by Katz & White (1993) to increase the mass resolution and to add short wavelength modes within Lagrangian regions that contain the structures of interest. In these high–resolution regions, particles are split into a dark matter and a gaseous part, with mass ratio reflecting the value of the cosmic baryon fraction. Force and mass resolution are then gradually degraded in the outer regions, so as to limit the computational cost, while providing a correct representation of the large–scale tidal field. The size of the regions selected at $z = 0$, to be resimulated at high resolution, typically corresponds to 10-20 Mpc in Lagrangian space, and is always chosen to be large enough that no low-resolution heavy particles contaminate the virial region of the simulated halos.

In order to assess numerical effects, structures have been simulated at different mass and force resolutions. We fix three different mass resolutions, which correspond to $m_{\rm gas} \simeq 2.5 \times 10^9 M_{\odot}$, $3.2 \times 10^8 M_{\odot}$ and $3.9 \times 10^7 M_{\odot}$ for the mass of the gas particles, respectively. In the following, the group runs with the smallest (intermediate) value of $m_{\rm gas}$, and the Virgo runs with the intermediate (largest) $m_{\rm gas}$ will be indicated as high–resolution (low–resolution) runs and labeled with HR (LR). We do not discuss Virgo runs with the smallest $m_{\rm gas}$ and Group runs with the largest $m_{\rm gas}$ among this list of three mass resolutions. With these choices for the mass resolution, the HR runs resolve the virial regions of the simulated structures with a number of gas particles ranging from about 70,000 to about 185,000 (see Table 2.1). The redshift z_i at which initial conditions are generated is chosen such that the r.m.s. fluctuation in the density field of the high–resolution region is $\sigma = 0.1$ (on the scale of the smallest resolved masses). With this requirement, we have $z_i \simeq 65$. As for the choice of the softening scale for the computation of the gravitational force, we assume it to have a constant value in comoving units down to $z = 2$, and a constant value in physical units at later epochs. The corresponding values of the Plummer–equivalent softening scale at $z = 0$ are $\epsilon_{\rm Pl} = 10$, 5 and 2.5 kpc for the three different choices of $m_{\rm gas}$. This choice has been dictated by the requirement of resolving halos down to scales of about one percent of their virial radii, so as to correctly follow the gas clumpiness and, therefore, to have convergent estimates of the X–ray luminosity (e.g., Borgani et al. 2002).

We show in Figure 2.1 the gas density and entropy maps for the HR runs of the cluster and of the group regions at $z = 0$ for the runs including cooling and star

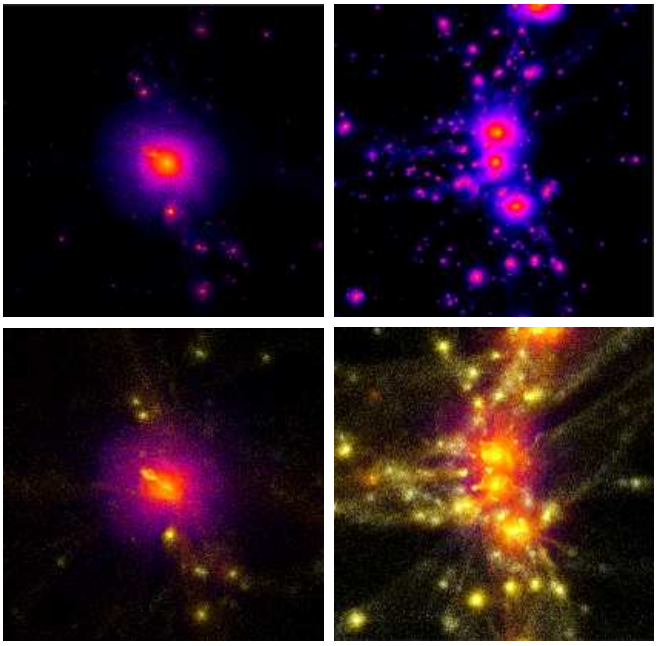

Figure 2.1: Maps of the gas density (upper panels) and of the gas entropy (lower panels) for the Virgo run (left panels) and for the region containing the groups (right panel), for the HR runs including cooling and star formation (see text). The size of each box is 10 Mpc, so as to show the environment of the simulated systems. Brighter regions indicate higher gas density and lower entropy in the upper and lower panels, respectively.

Table 2.1: Physical characteristics and numerical parameters of the simulated halos in the HR runs. Column 2: total mass within the virial radius at $z = 0$ ($10^{13} M_\odot$); Column 3: virial radius (Mpc); Column 4: total mass within R_{500}; Column 5: radius containing an average density $\bar{\rho} = 500\rho_{\rm crit}$. Column 6: number of gas particles within $R_{\rm vir}$; Column 7: Plummer-equivalent softening parameter at $z = 0$ (h^{-1}kpc).

Run	$M_{\rm vir}$	$R_{\rm vir}$	M_{500}	R_{500}	$N_{\rm gas}$	ϵ
Cluster	39.4	1.90	23.3	0.94	1.5e5	5.0
Group-1	5.98	1.01	3.43	0.49	1.8e5	2.5
Group-2	2.52	0.76	1.60	0.38	7.8e4	2.5
Group-3	2.35	0.74	1.35	0.36	7.1e4	2.5

formation (see below). In the entropy map of the Virgo cluster (lower left panel), we note a tail of low entropy gas pointing toward the center. This feature is generated by a merging sub-group, whose gas has been tidally stripped during the first passage through the cluster virial region. The persistence of low entropy for this gas indicates that it has been only recently stripped and has still to thermalize within the cluster environment. As apparent from the gas–density map (upper left panel), this merging sub-halo gives rise only to a minor disturbance of the gas density, thus marginally disturbing the relaxed dynamical status of the cluster. As for the simulation of the region containing the three groups, we note that they are placed along a filamentary structure. Although they are still relatively isolated and separated from each other by a few virial radii, their motion shows that they are approaching each other and will merge to form a cluster–sized structure in a few Gyrs. In general, these maps witness that a rich variety of structures, emerging when high resolution is achieved, are naturally expected to characterize the ICM, much like shown by high resolution *Chandra* observations.

2.2 Computing the collapsed gas fraction in cluster simulations

2.2.1. Introducing radiative cooling

An important aspect when dealing with simulations that include cooling concerns the detailed scheme of SPH implementation. Most standard implementations integrate the specific thermal energy as an independent variable, differing however in the detailed method used for symmetrizing the pairwise hydrodynamic forces between gas particle pairs, where either a simple arithmetic or a geometric mean form the most common choices (e.g., Weinberg, Hernquist & Katz 1997; Davè et al. 1999; White, Hernquist & Springel 2001). While these SPH implementations conserve energy and momentum, Springel & Hernquist (2002, SH02 hereafter) have shown that several of the commonly used SPH implementations are characterized by a spurious loss of specific entropy in strongly cooling regions, an effect which can be particularly severe at low resolution, and which is stronger when the geometrical scheme for hydrodynamical force symmetrization is adopted. This problem is essentially due to spurious coupling between cool dense particles, which should have virtually left the collisional phase, and neighboring hot gas particles, which still belong to the diffuse phase. In order to avoid the resulting spurious overcooling, different techniques have been suggested by several authors (e.g., Pearce et al. 2001; Marri et al. 2002).

SH02 proposed a new SPH implementation based on integrating the specific entropy as an independent thermodynamic variable, an approach which explicitly conserves

entropy in non–shock regions. Using a variational principle to derive the SPH equations of motion, they also showed that this new formulation removes any ambiguity in the choice of symmetrization and conserves energy, even when adaptive smoothing lengths are used.

Since one of the main purposes of this Chapter is to investigate the properties of gas cooling in galaxy clusters, we will study below by how much differences in the SPH implementation can change the resulting fraction of cold gas. Adopting the naming convention of SH02, we refer to a standard SPH implementation with geometric symmetrization as "geometrical", and to one with arithmetic symmetrization as "arithmetic", while the new formulation of SH02 will be referred to as "entropy–conserving" (see Chap. (3)).

2.2.2. Introducing star formation

Star formation is introduced as an algorithm to remove dense cold gas particles from the SPH computation, treating them as collisionless "stars". We follow the recipe originally proposed by KWH. According to this recipe, a gas particle is eligible to form stars if the following conditions are met: *(i)* locally convergent flow, $\nabla \cdot \mathbf{v} < 0$; *(ii)* Jeans unstable, i.e. locally determined sound crossing time longer than dynamical crossing time; *(iii)* gas overdensity exceeding a critical overdensity value, $\delta_g > 55$; *(iv)* local number density of hydrogen atoms $n_H > 0.1$ cm^{-3}.

Once a particle is eligible to form stars, its star formation rate (SFR) is given by $\mathrm{d}\ln\rho_g/\mathrm{d}t = -c_*/t_g$, where t_g is the minimum between the local gas–dynamical time–scale, $t_{\rm dyn} = (4\pi G\rho_g)^{-1/2}$, and the local cooling time–scale. We assumed $c_* = 0.1$ for the parameter regulating the rate of conversion of cold gas into stars, and verified with a low–resolution simulation of the Virgo cluster that basic results are left essentially unchanged by taking instead $c_* = 0.01$. A gas particle eligible for star formation is assumed to be gradually converted into a star particle, according to the above SFR. Instead of creating a new star particle for every star–formation (SF) instance, each gas particle undergoing SF behaves in a "schizophrenic" way, with its stellar part feeling only gravity (see, e.g., Mihos & Hernquist 1994). Once the SPH mass fraction decreases to 10 per cent, it is dissolved into SPH neighbors, thus leaving a purely stellar particle.

We also follow the recipe by KWH to compute the energy feedback from the SN associated with the star–formation produced in the simulations. Assuming a Miller–Scalo (1979) initial mass function (IMF), we compute the number of stars with mass $> 8\,M_\odot$, which we identify with instantaneously exploding SN. After assuming that each SN releases 10^{51} ergs, the resulting amount of energy per formed stellar mass turns out to be 7×10^{48} ergs $M_\odot^{-1}$. While the approximation of instantaneous explosion can be justified for type-II SN, due to the short life–time of their progenitor stars, it is not valid for type-Ia SN, which have stellar progenitors of smaller masses and much longer

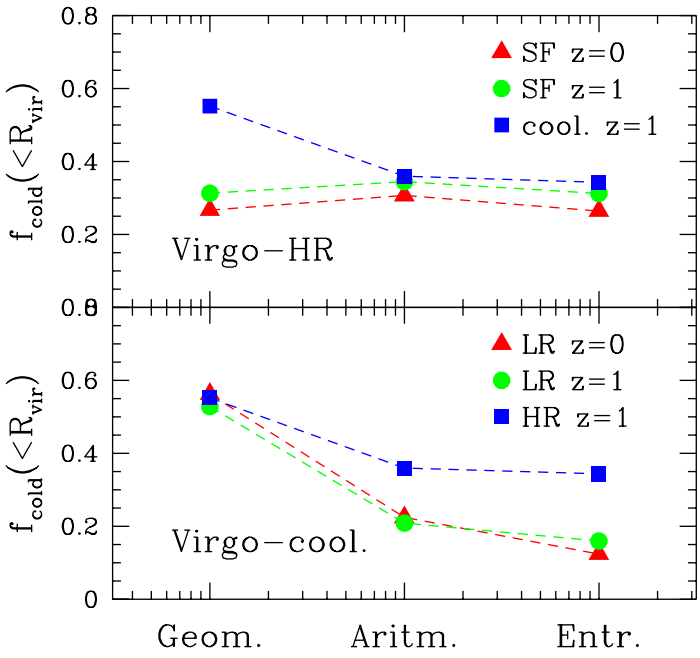

Figure 2.2: The fraction of collapsed gas within the virial radius for the Virgo run, for the three different schemes of SPH implementation. The lower panel refers to runs including cooling but not star formation. The upper panel shows the effect of introducing star formation for the HR runs.

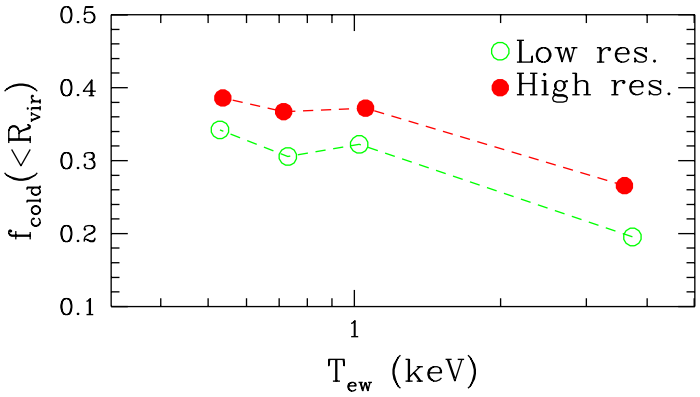

Figure 2.3: The fraction of cold gas as a function of the emission–weighted temperature, $T_{\rm ew}$, of the simulated structures. Results at two different resolutions are shown for the simulations of the groups.

life–times (e.g. Lia, Portinari & Carraro 2001; Pipino et al. 2002; Valdarnini 2002). The resulting feedback energy is assigned as thermal energy to the star–forming gas particles. This scheme for SN feedback is known to thermalize a negligible amount of energy in the diffuse medium, since it acts mostly on cold dense particles which rapidly radiate away the feedback energy as a consequence of their short cooling time. In the following, we show results based on including this scheme for SN feedback while bearing in mind that it causes only negligible differences compared to simulations that lack any stellar feedback. In Section 3.3 we shall discuss a different SN feedback scheme, based on the predictions of semi–analytical modelling of galaxy formation. In Chap. (3) we will extensively discuss a more sophisticated feedback scheme for SN, that is far more effcient in preventing overcooling and in regulating the star formation.

The effect of including star formation on the fraction of collapsed gas in the Virgo cluster run is shown in Figure 2.2. Besides the population of collisionless star particles, we also define as belonging to the cold phase all the SPH particles which have over-density $\delta_{\rm gas} > 500$ and temperature $T < 3 \times 10^4$ K (see also Croft et al. 2001, Borgani et al. 2002). At $z = 1$, the star formation simulation produce $f_{\rm cold} \simeq 25$–35 per cent of collapsed gas, with a weak dependence on the integration scheme. However, in the cooling-only simulations, where collapsed gas is not converted to stars, the "geometric" scheme leads to substantially larger values, indicating a numerical overcooling problem in this method. This effect is absent in the entropy–conserving scheme, which proves effective in suppressing spurious cooling in the absence of an explicit SF scheme. Note that $f_{\rm cold}$ is seen to slightly decrease at later epochs, which is as a consequence of a reduction of the rate at which cooling and star formation proceeds with respect to diffuse gas accretion.

In Figure 2.3 we show the trend of $f_{\rm cold}$ against the emission–weighted temperature,

which is defined here as

$$T_{ew} = \frac{\sum_i \rho_i T_i^{3/2}}{\sum_i \rho_i T_i^{1/2}}, \tag{2.1}$$

where ρ_i is the gas density carried by the i-th SPH particle. This definition is valid only for bremsstrahlung emissivity, although final values of T_{ew} are left essentially unchanged if we account for the contribution from metal lines.

For the groups, we plot results for both the LR and the HR runs. The trend toward a higher $f_{\rm cold}$ in colder systems is a consequence of the shorter cooling times of the associated DM halos, which makes cooling to proceed faster in lower–mass systems. Quite apparently, increasing the resolution causes a ~ 20 per cent or a ~ 50 per cent increase of $f_{\rm cold}$ at the group and at the cluster scales, respectively. The effect of numerical resolution is also shown in the left panel of Figure 2.4. In this figure we plot the density of star–formation rate (SFR) within the virial region of the Virgo cluster and of the Group-1. Once the same mass resolution is used for the simulation of these two structures, the resulting SFRs are quite similar. Increasing the resolution of the group simulation allows to resolve smaller halos forming at higher z, where additional star formation can take place. As a result, the peak in the SFR moves from $z \simeq 2$ to $z \simeq 3$ and then declines more gently, while recovering the same shape at lower redshift. Note that the integrated star formation rate is dominated by the contribution from these low redshifts, where most of the physical time is being spent. The resolution achieved in the HR runs is sufficient to resolve "galaxy" halos well below L_*. Therefore, we are confident that we are obtaining nearly converged estimates of the collapsed gas fraction, at least when the highest mass resolution is used. At the same time, our results should be considered as a warning on the interpretation of simulations that lack the resolution to adequately follow gas cooling.

In summary, our simulations demonstrate that cold fractions as large as $f_{\rm cold} = 25$–35 per cent should be expected when radiative cooling and star formation are considered. These values are larger than the observed $\sim 10\%$ fraction of cold gas in clusters (e.g., Balogh et al. 2001). This calls for the need to introduce a suitable scheme of non–gravitational energy injection, allowing a regulation of the runaway cooling process.

2.2.3. Introducing extra heating

The SN feedback recipe that we discussed so far, where thermal energy is deposited into cold gas, does not produce any sizable effect. In order to overcome this problem, many different schemes have been proposed. All these schemes attempt to prevent feedback energy from being quickly radiated away, for example by suitably parameterizing "sub–grid" physics, such as the multi-phase structure of the interstellar medium or galactic winds (e.g., Kay et al. 2000; Springel & Hernquist 2002; Marri & White 2002).

Here we present different phenomenological approaches for non–gravitational heating. Rather than predicting feedback from the star formation actually produced in the simulations, these schemes are designed to shed light on how much extra energy is required and how it should be distributed in redshift and as a function of the local gas density, to prevent overcooling and, at the same time, to reproduce X–ray observables of galaxy clusters and groups. A summary of the characteristics of the heating recipes that we explore here is provided in Table 2.2. In the rest of the Chapter we will present results based only on the high–resolution (HR) runs.

■ Impulsive heating

In our first class of heating schemes, we assume that all the energy is dumped into the diffuse baryons in an impulsive way, with a single heating episode occurring at some redshift z_h.

(a) Entropy floors $S_{\rm fl} = 50$ keV cm^2 at redshift $z_h = 9$ (S50-9 runs) and at $z_h = 3$ (S50-3 runs), and $S_{\rm fl} = 25$ keV cm^2 at $z_h = 9$. In this scheme, the entropy associated with each gas particle, $s = T/n_e^{2/3}$ (T: temperature in keV; n_e electron number density in cm^{-3}), is either increased to the value $S_{\rm fl}$ if smaller than that, or otherwise left unchanged (see also Navarro et al. 1995; Bialek et al. 2001; BGW). The choice of $z_h = 9$ corresponds to a heating epoch well before a substantial amount of gas in simulations cools and forms stars and, therefore, heavily suppresses star formation. The existence of a pristine SN generation (from the so–called Pop III stars) has been invoked to account for the IGM metal enrichment (e.g., Madau, Ferrara & Rees 2001). However, were this heating able to rise the entropy to the above levels, it would prevent the later formation of the Ly-α forest, which is known to have about one order of magnitude lower entropy. Furthermore, the amount of heating energy would also correspond to a too high production of heavy elements. For these reasons, we consider this choice for $S_{\rm fl}$ to be motivated by the phenomenology of X–ray ICM properties alone, rather than by expectations from star formation processes at high redshift.

(b) A fixed amount of heating energy per particle, $E_h = 0.75$ keV/particle at $z_h = 3$. This amount of energy is roughly the same as the average specific energy dumped by the S50-3 scheme within the halo virial radius (see Table 2.2). Therefore, it allows to check for differences induced in the final results by distributing the same energy budget in a different way as a function of gas density. The $z_h = 3$ heating epoch is close to that at which the star-formation rate within a proto–cluster region peaks (e.g., Menci & Cavaliere 2000; Bower et al. 2001; BGW). An energy budget $E_h \sim 0.6$–0.8 keV/part has been also suggested by Finoguenov et al. (2001a) to be consistent with the Si abundance detected in groups and clusters.

Table 2.2: Prescriptions for non–gravitational heating. We give in Column 1 name of the runs. For the impulsive heating schemes we give in Column 2: the quantity which is modified by the heating; Column 3: the heating redshift z_h. For the SAM–predicted SN feedback we give in Column 2: the number of SN per unit $M_\odot$; Column 3: the limiting density contrast for the gas particles to be heated. Column 4 gives the mean specific energy assigned to the gas particles falling within $R_{\rm vir}$ by $z = 0$. The asterisks indicate those runs which have been realized only for the "Virgo" cluster.

Impulsive heating

Name of run	Scheme	z_h	$E_h(< R_{\rm vir})$
S25-9*	$S_{\rm fl} = 25$ keV cm^2	9	0.5
S50-9	$S_{\rm fl} = 50$ keV cm^2	9	0.9
S50-3	$S_{\rm fl} = 50$ keV cm^2	3	0.8
K75-3	$E_h = 0.75$ keV/part	3	0.75

SAM-predicted SN feedback

Name of run	η_0	δ_g	$E_h(< R_{\rm vir})$
SN03$_L$	$3.2\,10^{-3}$	50	0.15
SN07$_L$*	$7.0\,10^{-3}$	50	0.32
SN15$_L$*	$1.5\,10^{-2}$	50	0.43
SN07$_H$	$7.0\,10^{-3}$	500	0.36

■ SAM–predicted SN feedback

This heating scheme is based on computing the star–formation rate (SFR) within clusters using a semi–analytic model (SAM) of galaxy formation (e.g., Kauffmann, White & Guiderdoni 1993, Somerville & Primack 1999, Cole et al. 2000, and references therein). Here we employ a variation of the scheme described by Menci & Cavaliere (2000, see also Bower et al. 2001), and we refer to their paper for a detailed description of the method, while we refer to BGW for further details on the its implementation in cluster simulations.

The hierarchical merging of DM halos is followed by means of the extended Press–Schechter formalism (e.g. Lacey & Cole 1993), while model parameters describing the gas physics, such as cooling, star formation and stellar feedback, are chosen so as to reproduce observed properties of the local galaxy population, such as the Tully–Fisher relation, or optical luminosity functions and disk–sizes (e.g. Poli et al. 2001). The model prediction we are interested in here is the integrated star formation history, $\dot{m}_*(z, M_0)$,of all the condensations which are incorporated into a structure of total mass M_0 by the present time. For a halo of size similar to our Virgo–like cluster, the SFR peaks at $z \simeq 4$ in this semi-analytic model, while it is $z \simeq 2.5$–3 for the group–sized halos (see BGW, for a plot of the M_0–dependence of the cluster SFR).

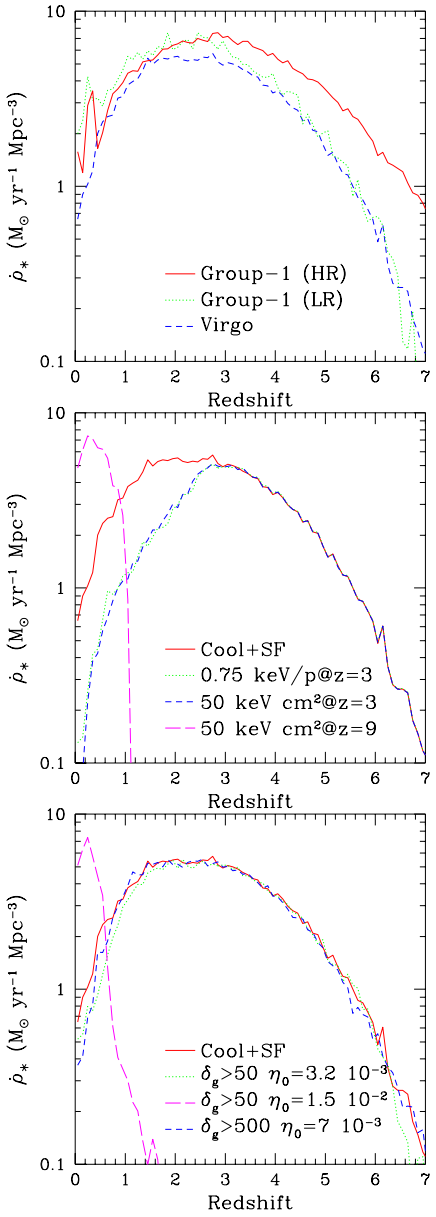

Figure 2.4: The density of the star–formation rate, $\dot{\rho}_*(t)$, computed for the Lagrangian volume of the object that corresponds to the $z = 0$ virial region of the simulated systems. Left panel: $\dot{\rho}_*(t)$ for the Virgo simulation (dashed curve), and for both the LR and HR runs of Group-1 (dotted and solid curves, respectively), when no extra heating is included. Central and right panels: results for the Virgo cluster, simulated with impulsive heating and SAM–predicted SN heating, respectively.

The rate of total energy feedback released by type-II SN is then computed as

$$\frac{\mathrm{d}E_{SN}}{\mathrm{d}t} = 10^{51}\mathrm{ergs}\ \eta_0\, \dot{m}_*(z, M_0)\,, \tag{2.2}$$

where η_0 is the number of SN per solar mass of formed stars. This value depends on the assumed initial mass function (IMF), and is obtained by integrating over the IMF for stellar masses $> 8M_\odot$. In the following, we will use the values $\eta_0 = 3.2 \times 10^{-3} M_\odot^{-1}$, which follows from a Scalo IMF (Scalo 1986), $\eta_0 = 7 \times 10^{-3} M_\odot^{-1}$, from the Salpeter IMF (Salpeter 1955) and $\eta_0 = 1.5 \times 10^{-2} M_\odot^{-1}$, as an extreme case.

Since our simulations include cooling, radiative losses of SN energy do not need to be assumed a priori, rather they are self–consistently computed by the code. However, we need to specify the gas overdensity, δ_g, at which the SN heating energy is assigned to the gas. In the following we take $\delta_g = 50$ or 500, and assume that $E_{\rm SN}$ is shared in equal parts among all the gas particles at overdensity larger than δ_g. The choice $\delta_g = 50$ corresponds to assuming that the virial region of the whole halo is heated and, therefore, that physical processes like galactic winds, for example, are rather efficiently transferring energy to the IGM. Increasing δ_g implies two competitive effects: on one hand, it decreases the number of heated gas particles, therefore it increases the amount of extra energy assigned to each of them; on the other hand, the energy is assigned to denser particles, which have shorter cooling time and, therefore, larger radiative losses.

2.2.4. The effect of extra heating on the cold fraction

As we have already discussed, introducing cooling causes a too large fraction of gas to be converted into stars. This is a well known feature of hydrodynamical simulations, which has been widely discussed in the literature (e.g., Suginohara & Ostriker 1998, BGW). Even worse, the runaway nature of the cooling process causes its efficiency to be highly sensitive to numerical resolution (see Fig.2.3, see also Balogh et al. 2001). Therefore, one should be very cautious in the interpretation of results from simulations that do not resolve halos with luminosity well below L_*.

In Figure 2.5, we show the effect of the different heating schemes on the resulting cold fraction within the virial radius of our simulated structures. As expected, we find a decrease of $f_{\rm cold}$ when non–gravitational heating is included. However, the efficiency of this suppression of star–formation does not exclusively depend on the amount of dumped energy. For instance, imposing an entropy floor of 50 keV cm^2 at $z_h = 9$ (left panel of Fig.2.5) is far more efficient than at $z_h = 3$. The reason for this is illustrated by the different patterns of SFR history, that we show in Figure 2.4. The impulsive heating at $z_h = 3$ causes a suppression of the SFR at later epochs, but a fair amount of stars are already in place at z_h (central panel of Fig. 2.4). Quite interestingly, the results for the two runs with heating at $z_h = 3$ produce quite similar SFR. This indicates that, once the heating epoch is fixed, the degree of SFR suppression depends only on

the amount of heating energy, while being largely independent on its distribution as a function of the local gas density.

However, heating at $z = 9$ with a comparable amount of energy does not allow gas to reach high densities within DM halos and to cool before $z \simeq 1$. Once cooling takes place, it converts less than 10 per cent of the gas into stars, within a short episode of star formation. The resulting SFR peaks at very low redshift, $z \simeq 0.3$, which is highly discrepant with observational determinations of the SFR history in clusters (e.g., Kodama & Bower 2001). Of course, this is not the only feature which rules out the picture of a strong heating occurring at such a high redshift. For instance, at $z = 0$, stars are all concentrated in one single object located at the center, a cD–like galaxy, while no other galaxy–sized DM halos contains significant amounts of collapsed gas.

As for the SN heating (right panel of Fig. 2.4), suppressing the star fraction below the 10 per cent level requires a high, probably unrealistic value for η_0. Also, taking $\eta_0 = 1.5 \times 10^{-2} M_{\odot}^{-1}$ generates an implausible SFR history, resembling that found for the runs based on setting the entropy floor at $z_h = 9$: the large amount of extra heating at high redshift prevents the occurrence of star formation down to $z \simeq 1.5$. Taking η_0 in the range 3–7$\times 10^{-3}$ predicts more realistic SFRs, but it is not able to suppress $f_{\rm cold}$ below the $\simeq 20$ per cent level.

A general conclusion of our analysis is that heating schemes producing plausible SFR histories are not efficient in suppressing the fraction of cold gas below the 20 and 25 per cent values at the cluster and group scales, respectively. Vice-versa, a more efficient suppression is obtained by preventing gas to cool at high redshift, at the expense of delaying star formation to unreasonably low redshifts.

2.3 X–RAY PROPERTIES OF SIMULATED CLUSTERS

2.3.1. The entropy of the ICM

Measurements of the excess entropy in central regions of poor clusters and groups are considered to provide direct evidence for the lack of self–similarity of the ICM properties (e.g., Ponman et al. 1999; Finoguenov et al. 2002a). In a separate paper (Finoguenov et al. 2002b), a self–consistent comparison is realized between the entropy properties of the simulations with impulsive heating, that we present here, and the observational data for groups and clusters by Finoguenov et al. (2002a). The main result of this comparison is that, although cooling and star formation tend to somewhat increase entropy in central cluster regions, they still fall short in producing the entropy excess which is observed at the group scale. While preheating at $z_h = 3$ is shown to increase the entropy to the observed values, runs with $z_h = 9$ are characterized by a low entropy level in central regions of clusters and groups.

Instead of attempting any further comparison with observations, we want to discuss

here the dynamical reasons for such a behavior. To this end, we show in Figure 2.6 the effect of cooling and non–gravitational heating on the entropy profiles for our whole set of "Virgo" simulations. As expected, when cooling and SF are included, low entropy gas is selectively removed in central cluster regions, thus inducing a flattening of the profile. This is explicitly shown in Figure 2.7: while the run including only gravitational heating has a population of high–density low entropy gas particles, such particles are removed from the diffuse phase once cooling and star formation are introduced. This result is consistent with the expectation from analytical arguments based on the comparison between cooling time–scale and typical cluster age (e.g., Voit et al. 2002, Wu & Xue 2002). The inclusion of extra heating has a non–trivial effect on the efficiency of cooling in removing particles from the lower left side of the S–δ_g phase diagram. For instance, imposing the same entropy floor at $z_h = 9$ and at $z_h = 3$ has quite different effects on the entropy pattern (see lower panels of Fig. 2.7). Heating at $z_h = 9$ has the effect of increasing the cooling time for most of the gas particles, so as to allow star formation to take place only quite recently (see Fig. 2.4). The increased time-scale for cooling causes this process to proceed in a more gradual way. For this reason, the entropy of gas particles undergoing cooling decreases slowly, thus making their removal from the hot diffuse phase less efficient.

2.3.2. The luminosity–temperature and luminosity–mass relations

The slope of the L_X–T relation also provides important observational evidence for the lack of self–similar behaviour of the ICM. Since the first measurements of ICM temperatures for sizable sets of clusters, it has been recognised that $L_X \propto T^\alpha$ with $\alpha \simeq 3$, although with a considerable scatter (e.g., White et al. 1998, and references therein). Better quality observations established that a significant contribution to this scatter is associated with the different strength of cooling flows detected in different clusters. Either excluding clusters with pronounced signatures of cooling flows or correcting for their effect (e.g., Markevitch 1998; Allen & Fabian 1998; Arnaud & Evrard 1999; Ettori et al. 2002) results in a much tighter L_X–T relation, albeit still with a rather steep slope. At the same time, hints have also been found for a further steepening of this relation at $T \lesssim 1$ keV (e.g., Helsdon & Ponman 2000, and references therein), possibly indicating that the mechanism responsible for the L_X–T scaling should act in a different way for clusters and groups.

Simulations that allow for non–gravitational heating (e.g., Bialek et al. 2001; BGW) and radiative cooling (e.g. Pearce et al. 2001; Davè et al. 2002; Muanwong et al. 2002) have been shown to be able to account for the observed L_X–T relation. However, a sometimes overlooked issue in determining the X–ray luminosity of clusters in simulations concerns the contribution of metal lines to the emissivity. While this contribution is negligible above 2 keV, it becomes relevant at the scale of groups. For instance, ne-

glecting the contribution from line emissivity for an ICM enriched to a metallicity of $Z = 0.3Z_\odot$ leads to an underestimate of the X–ray luminosity by almost 50 per cent at 1 keV, and by more than a factor 2 at 0.5 keV (e.g. BGW).

A correct procedure would require simulations that include a treatment of metal enrichment and a self–consistent estimate of the contribution of line cooling to the X–ray emissivity. However, only preliminary attempts have been realized so far to include the treatment of ICM metal enrichment from SN ejecta (Lia et al. 2002; Valdarnini 2002). Pearce et al. (2001) include the contribution of metals to the cooling function adopted in their simulation by assuming $Z = 0.3\,Z_\odot$ at the present epoch, linearly decreasing with time towards the past. Davé et al. (2002) did not include the metal contribution in their cooling function, but estimated X–ray luminosities by assuming a phenomenological relation between metal abundance and temperature of the galaxy system. However, while the ICM metallicity at the scale of rich clusters is quite well established from observations, the situation is less clear for poor clusters and groups (e.g., Davis, Mulchaey & Mushotzky 1999; Renzini 2000, and references therein).

The cooling function used in our simulations assumes zero metallicity, but we compute the X–ray luminosity by adding to the bremsstrahlung emissivity the contribution from lines for a $Z = 0.3\,Z_\odot$ plasma. This represents a reasonable approximation as long as gas spends most of the time at low metallicity, being enriched to high metallicity only recently. Owing to the uncertainties connected to these assumptions, the reliability of L_X values at $T \lesssim 1$ keV is unclear, however. Precise predictions will require a fully self–consistent treatment of metal enrichment of the ICM from star formation activity.

In Figure 2.8, we show the profiles of emissivity (energy released per unit time and unit volume) for the different Virgo runs. As expected, including only cooling and star formation has the effect of flattening the profiles in the central cluster regions as a consequence of gas removal from the hot phase. When extra heating is included, the profiles change according to the amount of gas left at relatively low entropy in the central cluster regions. For instance, the fairly large population of low entropy particles in the run with $S_{\rm fl} = 50$ keV cm^2 at $z_h = 9$ (see Fig.2.7) is responsible for the spike in the X–ray emissivity. In the same way, the efficient removal of low–entropy gas for the run where an entropy floor was imposed at $z_h = 3$ explains the flattening of the luminosity profile in the central cluster region. These results confirm the existence of a non–trivial interplay between the effects of cooling and extra heating. In some cases, one reaches the apparently paradoxical conclusion that combining heating and cooling increases the X–ray luminosity, although their separate effects are that of suppressing L_X.

Figure 2.9 shows the comparison between the simulated and the observed L_X–T relation for clusters and groups. As expected, cooling causes a sizeable suppression of the X–ray luminosity. At the same time, the emission–weighted temperature is increased as a consequence of the steepening of the temperature profiles in the central

halo regions (see below). While the mere introduction of cooling and star–formation brings the "Virgo" cluster into agreement with observations, the simulated groups are somewhat overluminous with respect to data. The inclusion of pre–heating at $z_h = 3$ has a smaller effect on the Virgo cluster, consistent with the result from the luminosity profile, while it further suppresses L_X at the scale of groups. A similar result is also found for the runs with SAM–predicted SN feedback.

Quite interestingly, the L_X value for Group-2 in the runs with no extra heating appears to be systematically in excess with respect to that inferred from the L_X–T scaling of the other three simulated structures. This deviation is due to the occurrence of a recent merger shock in the Group-2 run, which produced a sudden increase in the X–ray emission. When extra heating is included, its effect is that of decreasing the strength of the shock, thus also reducing the jump in luminosity.

A similar constraint is provided by the relation between X–ray luminosity and mass. Reiprich & Böhringer (2002) have estimated this relation by applying the equation of hydrostatic equilibrium to a fairly large ensemble of clusters and groups, under the assumption of isothermal gas. They used ICM temperatures based on *ASCA* data, in combination with *ROSAT* -PSPC data for the surface brightness profile. Ettori, De Grandi & Molendi (2002) used the better quality data from *BeppoSAX* observations to resolve the temperature profiles for a smaller ensemble of clusters. Although the analysis by Ettori et al. explicitly includes temperature gradients when solving the equation of hydrostatic equilibrium, it is restricted to clusters with $T \gtrsim 3$ keV, thus hotter than those simulated here.

For this reason, we here compare our simulation results to the data by Reiprich & Böhringer (see Figure 2.10). In this analysis, the cluster masses, M_{500}, are computed within the radius encompassing an average density $\bar{\rho} = 500\rho_{\rm crit}$, while observed luminosities are provided in the 0.1–2.4 keV *ROSAT* energy band. We use the MEKAL spectral model to correct bolometric luminosities from simulations by assuming $Z = 0.3\,Z_\odot$ for the global ICM metallicity. Consistent with the results from the analysis of the L_X–T relation, we find that the runs with heating at $z_h = 3$ and that with SN feedback, based on a Salpeter IMF, are able to follow the steep slope of the observed $L_{0.1-2.4}$–M_{500} relation.

In principle, the L_X–T and the L_X–M relations do not provide independent information, since masses are anyway estimated using temperature data. Still, both relations are obtained by using largely different observational data sets and analysis procedures. Therefore, the fact that the same simulations are able to account for both scalings lends support to the robustness of our results and indicates that our conclusions are not affected by observational biases or systematics.

Owing to the uncertainties mentioned above in modelling the luminosities of groups, it appears prudent not to make strong claims about how much extra heating is needed to reproduce the observations. Overall, we note that all the runs that produce a delayed star formation, such as those with $z_h = 9$ and the one with SN–feedback and

large $\eta_0 = 1.5 \times 10^{-2} M_\odot^{-1}$ (see Fig.2.4), are quite inefficient in suppressing L_X. On the contrary, runs with pre–heating at $z_h = 3$ or with SN–feedback combined with more reasonable values for η_0 succeed to account for the steep slopes of the L_X–T and L_X–M relations.

Having warned about the reliability of the emissivity modeling for gas at $T < 1$ keV, a word of caution should also be spent on the reliability of the interpretation of current observational data. Estimating temperature and luminosity for small groups from pre–*Chandra* and pre–XMM data is not a trivial task, mostly due to the difficulty of separating the contribution of the diffuse intra–group medium from that of member galaxies, and of detecting X–ray emission out to a significant fraction of the virial radius (see, e.g., Mulchaey 2000, for a review on the X–ray properties of groups). The situation is likely to improve as newer and better quality data will be accumulated, although we will probably have to wait for a few more years before a critical amount of *Chandra* and *XMM–Newton* observations of groups will be available.

2.3.3. The mass–temperature relation

Under the assumptions of spherical symmetry and an isothermal gas distribution, the condition of hydrostatic equilibrium predicts a precise relationship between the virial mass of a cluster and its temperature:
$k_B T = 1.38 \beta^{-1} M_{15}^{2/3} [\Omega_m \Delta_{\rm vir}(z)]^{1/3} (1+z)$ keV for a gas of primordial composition, with M_{15} being the virial mass in units of $10^{15} h^{-1} M_\odot$ and $\Delta_{\rm vir}$ being the ratio between the virial density and the average cosmic matter density at redshift z. Under the above assumptions, the β parameter gives the ratio between the specific kinetic energy of dark matter particles and the thermal energy of the gas. Simulations including only gravitational heating demonstrated that this relation is reproduced quite well, with $\beta \simeq 1$–1.2 (e.g., Evrard et al. 1996; Bryan & Norman 1998; Frenk et al. 1999; BGW). For these reasons, the M–T relation has been considered for several years as a fairly robust prediction of hydrostatic equilibrium: gas temperature, unlike X–ray emissivity, is primarily determined by the action of gravity and, as such, depends on global cluster properties, and only weakly on local structure of the ICM.

However, data based on *ASCA* and *ROSAT* observations show an M–T relation which is about 40 per cent lower than predicted (Horner et al. 1999; Nevalainen et al. 1999; Finoguenov et al. 2001b), a result which has been confirmed by *BeppoSAX* (Ettori, De Grandi & Molendi 2002) and *Chandra* (Allen et al. 2001) data for relatively hot systems ($T \gtrsim 4$ keV).

Non–gravitational heating could be naively expected to solve this discrepancy by increasing the ICM temperature at fixed cluster mass. However, BGW have shown that for a broad class of pre–heating models similar to those discussed here the M–T relation is left almost unchanged by the injection of extra–energy (cf. also Lin et

al. 2002). In fact, as long as gas has time after being heated to settle back into hydrostatic equilibrium within the gravitational potential well, its temperature is mainly determined by the amount of collapsed dark matter, which is unaffected by the heating process.

An alternative explanation for the observed low amplitude of the M–T relation, based on the effect of radiative cooling, has been shown by Thomas et al. (2002) to be much more promising. In this case, gas left in the diffuse phase flows towards the central cluster region, where it is compressed, thus increasing its temperature. As a result, the overall mass–weighted temperature remains almost unchanged, but the emission weighted temperature significantly increases. Our results, as shown in Figure 2.11, actually confirm this picture and generalise it to a large range of schemes for extra heating: while the value of M_{500} is left unchanged by the cooling/heating processes, $T_{\rm ew}$ increases as a consequence of the temperature increase in the central cluster regions.

In order to better understand the effect of cooling on the central temperature structure of the ICM, we plot in Figure 2.12 the gas pressure, $P = \rho_{\rm gas} k_B T/(\mu m_p)$, as a function of gas density for the simulations of the "Virgo" cluster. We introduce here the effective polytropic index $\gamma = {\rm d}\log P/{\rm d}\log\rho_{\rm gas}$ to describe the run of pressure as a function of gas density. In the external cluster region the gas is characterised by $\gamma \gtrsim 1$, thus consistent with the slowly outward-declining temperature profiles, almost independent of the presence of cooling and extra heating. However, cooling leads to a loss of pressure in central high–density regions. As cooling partially removes low–entropy gas from the diffuse phase, gas of higher entropy flows in from more external regions. As long as this gas has sufficiently long cooling time, its entropy is conserved and the gas is adiabatically compressed during the inflow. In this regime, the effective polytropic index increases towards $\gamma = 5/3$, thus indicating an adiabatic behaviour of the ICM. This result is essentially independent of whether gas is preheated. The only effect of imposing an entropy floor at $z_h = 9$ is that of making the cooling process more gradual. This allows a larger amount of gas to remain in the diffuse phase, so as to reach higher density and higher pressure in central regions (see also Fig. 2.8).

2.3.4. The temperature profiles

The way in which cooling acts in reconciling the observed and the simulated M–T relations implies that temperature profiles should steepen in central cluster regions. From an observational viewpoint, the possibility of realizing spatially resolved spectroscopy has recently opened the possibility to determine temperature profiles for fairly large samples of clusters. Interestingly, observations based on the *ASCA* (e.g., Markevitch et al. 1998) and *BeppoSAX* (De Grandi & Molendi 2002) satellites show *declining* temperature profiles in the outer regions, at cluster-centric distances $\gtrsim 0.2$–$0.3 R_{\rm vir}$ (cf. also Irwin & Bregman 2000). This behaviour is generally reproduced by simulations

that do not include cooling (e.g., BGW). Furthermore, both *BeppoSAX* (De Grandi & Molendi 2002), *Chandra* (e.g., Ettori et al. 2002; Allen et al. 2001; Johnstone et al. 2002) and *XMM–Newton* (e.g., Tamura et al. 2001) data for fairly hot systems, $T_X \gtrsim 4$ keV, show temperature profiles declining towards the very central regions of clusters, thus indicating the presence of cooling cores. Indeed, all *XMM–Newton* profiles are consistent (Mushotzky 2004) with an isothermal profile out to $R/R_{\rm vir} \sim 0.5$, with the exception of Kaastra et al. (2001) and, more recently, of Piffaretti et al. (2004); they report, for 13 nearby cooling–flow clusters, mild gradients in outer regions ($R \gtrsim 0.3R_{\rm vir}$) and strong decreasing within $\sim 0.1R_{\rm vir}$, quite in agreement with results by De Grandi & Molendi. Similar results are obtained by (Vikhlinin et al. 2004) from
Chandra observations. This behaviour is grossly at variance with respect to that found for the "Virgo" runs, as reported in Figure 2.13: the only case where a somewhat declining profile is produced is the one with gravitational heating, while cooling always gives rise to steeply increasing profiles with no evidence for any decline, independent of the presence of extra heating.

A more comprehensive comparison with the observations would require simulations to be realized for a set of clusters with higher temperature. On the other hand, our simulated Virgo cluster has been chosen as a fairly relaxed system. Therefore, as long as observations suggest profiles to be universal for such systems (Allen et al. 2001), such a discrepancy should be taken quite seriously. A steepening of the temperature profiles caused by cooling has been already noticed by Lewis et al. (2000), Muanwong et al. (2002) and Valdarnini (2002). The temperature profiles in Fig. 2.13 generalise this result also in the presence of a variety of extra–heating mechanisms.

We also note that the steep temperature profiles predicted by simulations are also at variance with respect to those predicted by the semi–analytical model for ICM heating/cooling by Voit et al. (2002). A detailed comparison between the predictions of semi–analytical models and simulations is beyond the scope of this Chapter. However, a full understanding of the physical processes taking place in the ICM will only be obtained if the reasons for such differences can be understood and eventually sorted out.

If the discrepancy between observed and simulated temperature profiles will be confirmed, it may indicate that we are missing some basic physical mechanism which affects the thermal properties of the gas in the high density cooling regions. For instance, thermal conduction has been advocated by some authors as a mechanisms that, in combination with central heating, may regulate gas cooling (e.g. Voigt et al. 2002) while providing acceptable temperature profiles for a suitable choice of the conductivity parameter (e.g., Zakamska & Narayan 2002; Ruszkowski & Begelman 2002). In this scenario, one expects the outer layers to heat gas in the innermost regions, so as to increase its cooling time, allowing it to stay in the diffuse phase at a relatively low temperature. However, the detection of sharp features in the temperature map of several clusters, as observed by the *Chandra* satellite, led some authors to suggest that

thermal conduction is suppressed in the ICM (e.g., Ettori & Fabian 2000). Magnetic fields are naturally expected to produce such a suppression (e.g., Sarazin 1988). Still, it is not clear whether this mechanism can act in an ubiquitous way inside clusters or whether the turbulence associated with the presence of magnetic fields is actually able to maintain a relatively efficient thermal conduction (e.g., Narayan & Medvedev 2001).

2.4 Discussion and conclusions

In this Chapter, we presented results from high resolution Tree+SPH simulations of a moderately poor "Virgo"–like cluster and of three group–sized halos, including the effects of radiative cooling and non–gravitational gas heating. The numerical accuracy reached in these simulations was aimed at following in detail the pattern of gas cooling and its effect on the X–ray properties of groups and clusters of galaxies. The main results that we obtained can be summarised as follows.

(a) Including cooling and star formation causes a fraction $f_* \simeq 0.25$ of baryons to be converted into a collisionless "stellar" phase in the Virgo cluster and $f_* \simeq 0.35$–0.40 in the simulated groups. Given the sensitivity of cooling on numerical resolution, it is likely that the result for the "Virgo" run should still be interpreted as a lower limit on f_*.

(b) The cold fraction is reduced by including non–gravitational heating. The degree to which overcooling is suppressed depends not only on the amount of feedback energy, but also on the redshift and on the gas overdensity at which it is released into the diffuse medium. For instance, heating at $z_h = 9$ is very efficient in decreasing f_* below the 10 per cent level, at the expense of delaying the bulk of star formation to $z \lesssim 1$. A more realistic star formation history, peaking at $z \simeq 3$, consistently requires that most of the non–gravitational heating takes place at a similar redshift, with at least 20 per cent of the baryons still being converted into stars.

(c) Heating at $z_h = 3$ with $E_h \simeq 0.75$ keV/part is shown to produce scalings of X–ray luminosity, mass and entropy vs. temperature which agree in general with observational data. This result holds independent of whether an equal amount of energy is assigned to all gas particles or whether an entropy floor is created. A similar agreement is also found for the SAM–predicted SN feedback, once realistic models for the IMF are used. Both, heating at $z_h = 9$, or using an IMF which produces a large number of SN, are not efficient in suppressing the X–ray luminosity, which is a consequence of the fairly large amount of gas that, while avoiding cooling, is concentrated in central cluster regions.

(d) Including cooling and star formation increases the ICM temperature in the central regions. While this helps in reconciling simulations with the observed M–T relation, it steepens the temperature profiles, which show no evidence for any decline at small cluster-centric distances. This result, which holds independent of the scheme for non–gravitational heating, is discrepant with recent observations.

Over the last couple of years, different groups have presented simulations aimed at studying the effect of radiative cooling and feedback on the X–ray properties of the ICM (e.g. Brighenti & Mathews 2001, Muanwong et al. 2002, Davé et al. 2002, Kay et al. 2002, Kay et al. 2003, Borgani et al. 2002, Borgani et al. 2004, Tornatore et al. 2003). Most of these studies are based on simulations which follow the gas hydrodynamics within the full volume of a cosmological box (e.g., Muanwong et al. 2002; Davé et al. 2002; Kay et al. 2002; Borgani et al. 2002, 2004). One common result of these simulations, which agrees with what we find in our analysis, is that the effect of cooling is able to alleviate or even solve the discrepancy between simulated and observed X–ray scaling properties of clusters and groups, but the fraction of baryons converted into stars is too large. To remedy this problem, Muanwong et al. (2002) pre–heated the gas by adding 1.5 keV thermal energy to all the gas particles at $z_h = 4$. As a result, they found that the cold fraction in groups and clusters is decreased from 15 per cent to 0.4 per cent, which is somewhat smaller than the values found in our simulations. Kay et al. (2002) implemented a feedback mechanism in their simulations, which accounts for the rate of both type Ia and type II SN. By assuming an energetics twice as large as that provided by standard supernova computations, they were able to reproduce the observed X–ray scaling properties, while obtaining only 3 per cent of the gas to be converted into stars. The main limitation of this type of simulations is that one is restricted to relatively poor numerical resolution in order to limit the computational cost. For instance, the simulations by Muanwong et al. (2002) have a mass resolution which is about one order of magnitude worse than that of our "Virgo" runs and almost two orders of magnitude worse than that of our group runs. A better mass resolution within a smaller box was used by Kay et al. (2002), for which the mass of gas particles are a factor 2.8 and 22 smaller than for our Virgo and Group runs, respectively.

The results that we presented in Section 3 demonstrate that the cooling efficiency is quite sensitive to mass resolution. For this reason, one has to be careful in drawing conclusions about overcooling and how it is suppressed by extra heating, in the presence of limited numerical resolution. In fact, our simulations demonstrate that the two main problems caused by the introduction of radiative cooling, namely the overproduction of stars and the steeply increasing temperature profiles in central cluster regions, may not be easily solved by the introduction of non–gravitational heating.

Does this imply that none of our heating schemes is a realistic approximation to what happens in real clusters? The energy release in all these schemes misses, although

to different degrees, to faithfully follow the simulated rate of star production. A realistic scheme for SN feedback should dump thermal energy with a rate that accurately follows the star formation rate, properly accounting for the typical life–times of different stellar populations. Furthermore, our schemes for energy release demonstrate that for feedback to have a sizeable effect on the ICM thermodynamics, it has to act in a non–local way, so as to assign most of the energy on gas particles which have a sufficiently long cooling time. Such non–local feedback mechanisms may arise from AGN activity, cosmic rays or galactic winds, for example.

However, as a word of caution, we must remind that while in the last years the break in L_X–T relation seemed established, very recent observations question such result. many conjectures of systematic biases have been discussed very recently and improved observations have been presented (Mulchaey & Zabludoff 1998, Osmond & Ponman 2004). What results is that early detections of a steepening of $L_X - T$ relation at the groups scale was possibly due to the large scatter observed in this mass range (Mushotzky 2004) and to selection effect of previous samples (Ponman et al. 2003); also, the 'entropy floor' detected by the pioneering works of Ponman et al. (1999) and Lloyd–Davies et al. (2000) has become an 'entropy ramp', possibly with entropy scaling $S \propto T^{2/3}$.

As for the M–T relation, Borgani et al. (2004) found that if masses of simulated clusters are estimated with the same procedure used with observations (i.e. under the assumptions of a βmodel in hydrostatic equilibrium with a polytropic equation of state), they are found to be biased low by just the amount required to recover the agreement with the observed M-T relation. Quite interestingly, a good agreement is in fact found by comparing simulation results to the M_{2500}-T_{2500} relation based on the *Chandra* data by Allen et al. (2001), which does not rely on the assumption of a specific gas density profile. This suggests that the problem of the M-T normalization may be solved by a better data treatment.

While further work is clearly needed to study such feedback mechanisms self-consistently in simulations, a better understanding is also required as to whether optical/X–ray data really implies a stellar fraction as small as $\lesssim 10$ per cent within clusters and groups. Balogh et al. (2001) used the 2MASS results on the K–band luminosity function by Cole et al. (2001) to estimate the cosmic fraction of baryons converted into stars. After assuming a Kennicutt IMF (Kennicutt 1983), they find $f_* \simeq 0.05$ for our choice of Ω_m and h, and argued that no much evidence exists for f_* to increase inside clusters, or to depend on the cluster mass (cf. also Bryan 2000). However, this estimate of the cosmic value of f_* increases by about a factor 2 if a Salpeter IMF (Salpeter 1955) were used instead. Furthermore, it is worth reminding that the estimate inside clusters relies to some degree of extrapolation. For instance, Balogh et a. (2001) obtained the stellar mass in clusters from the B–band luminosity data by Roussel et al. (2000), using $M/L_B = 4.5$, and correcting for undetected galaxies by extrapolating the luminosity function to the faint end slope. It is clear

that a more robust determination of f_* in clusters should rather rely on K– or H–band luminosity, which is more directly related to stellar mass (e.g., Gavazzi et al. 1996), rather than to B–band luminosity whose conversion to stellar mass is quite sensitive to galaxy morphology. More recently, Huang et al. (2002) used the Hawaii-AAO K-band redshift survey to estimate the K-band luminosity function in the local Universe. They found that the K–band luminosity density is twice as large as that from 2MASS, thus implying a twice as large f_* value. In light of this discussion, a f_* value somewhat larger than 10 per cent, possibly as large as 20 per cent, may still be viable at present, which would tend to alleviate the problem of ICM overcooling.

As for the temperature profile, our results indicate that the discrepancy between observations and simulations is unlikely to be solved by the inclusion of feedback mechanisms that are similar to the ones explored here. If this is the case, it would demonstrate that our simulations are missing some basic physical mechanisms. For instance, as we discussed, thermal conduction has been proposed to be an important effect in clusters. Another piece of physics which is currently missing from most simulation work is the effect of magnetic fields (e.g., Dolag, Bartelmann & Lesch 2002). Their introduction might give rise to non–trivial structures in the gas distribution if they can locally suppress thermal conduction, or it they provide a non–thermal contribution to the gas pressure.

There is little doubt that including such more complex physics will represent a significant, non-trivial challenge for cluster simulations of the next generation. Most of the processes involved require both, a rather sophisticated numerical method, and a treatment of sub-grid physics. Still, the inclusion of more physics in numerical codes is mandatory if the reliability and the predictive power of cluster simulations want to keep pace with the increasing quality of observational data.

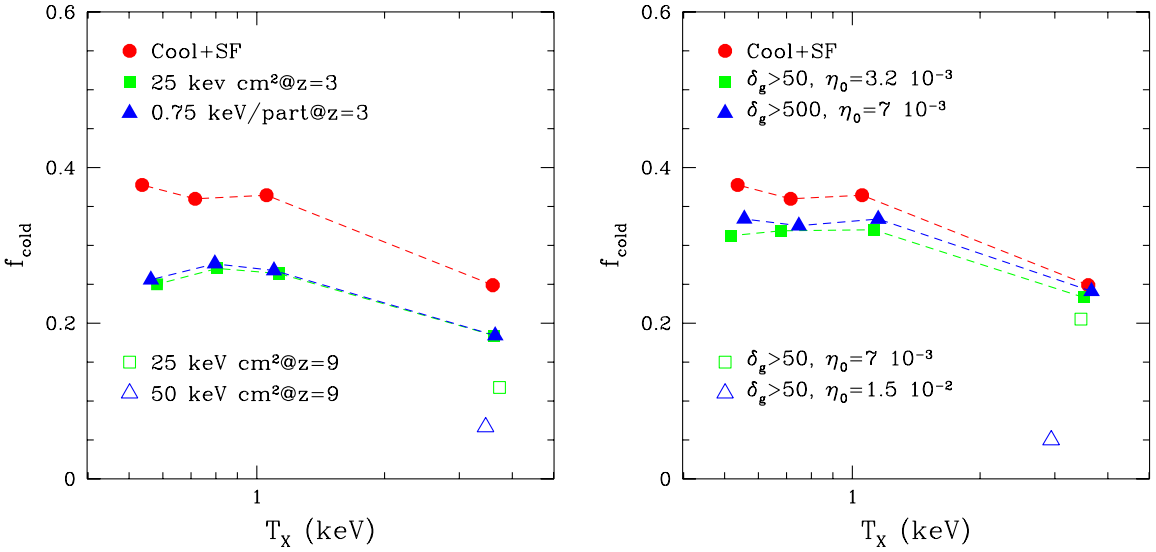

Figure 2.5: The fraction of cold gas within the virial region of the simulated structures at $z = 0$. Left and right panels show the effect of impulsive heating and of SAM-predicted SN feedback, respectively.

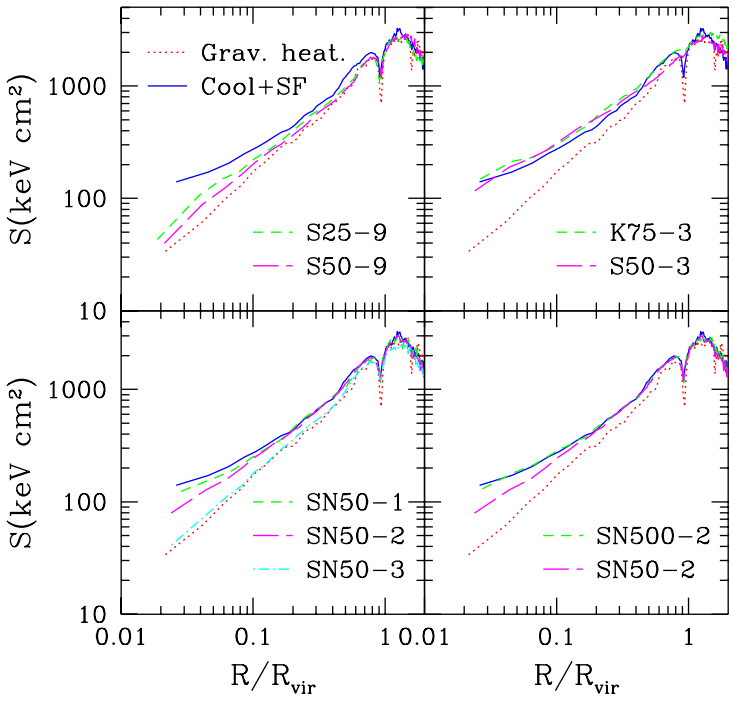

Figure 2.6: The entropy profiles of the "Virgo" cluster simulations. The upper panels show the effect of impulsive heating at $z = 9$ (on the left) and $z = 3$ (on the right), while the lower panels show the effect of SN feedback from the SAM–predicted SFR history, after changing η_0 (on the left) and the density threshold for gas heating (on the right). For reference, the entropy profiles for the run with gravitational heating and for the run including only cooling and star formation are shown in all the panels with the dotted and the solid lines, respectively.

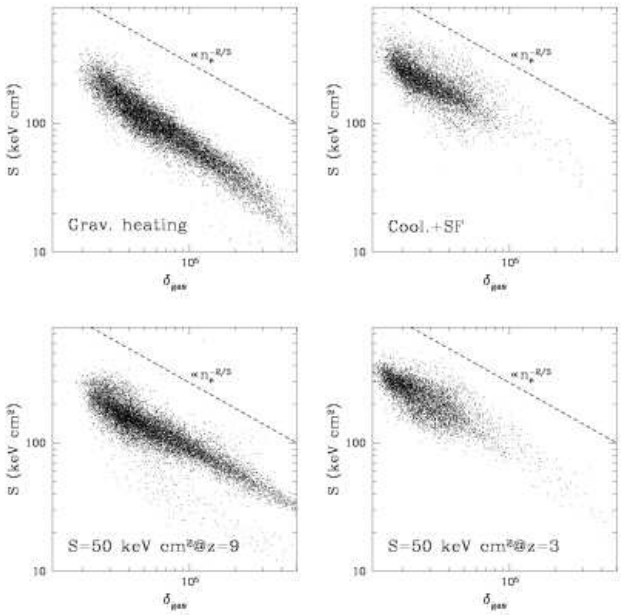

Figure 2.7: The entropy–overdensity phase–diagram for the gas particles falling within $0.1\,R_{\rm vir}$ at $z = 0$, for different runs of the "Virgo" cluster. In each panel, the dashed line shows the scaling $S \propto n_e^{2/3}$ expected for isothermal gas.

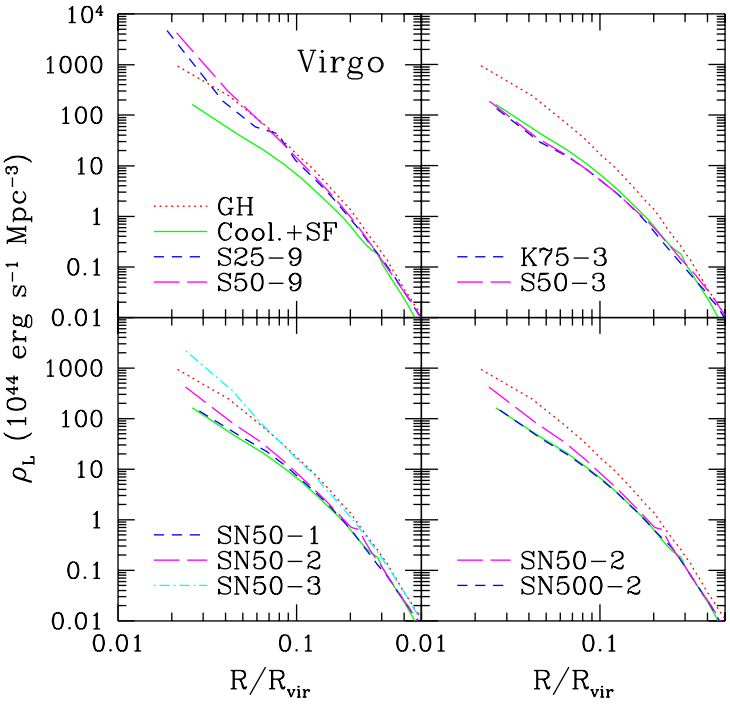

Figure 2.8: The profiles of X–ray luminosity density for the "Virgo" runs. The sequence of panels is the same as in Figure 2.6.

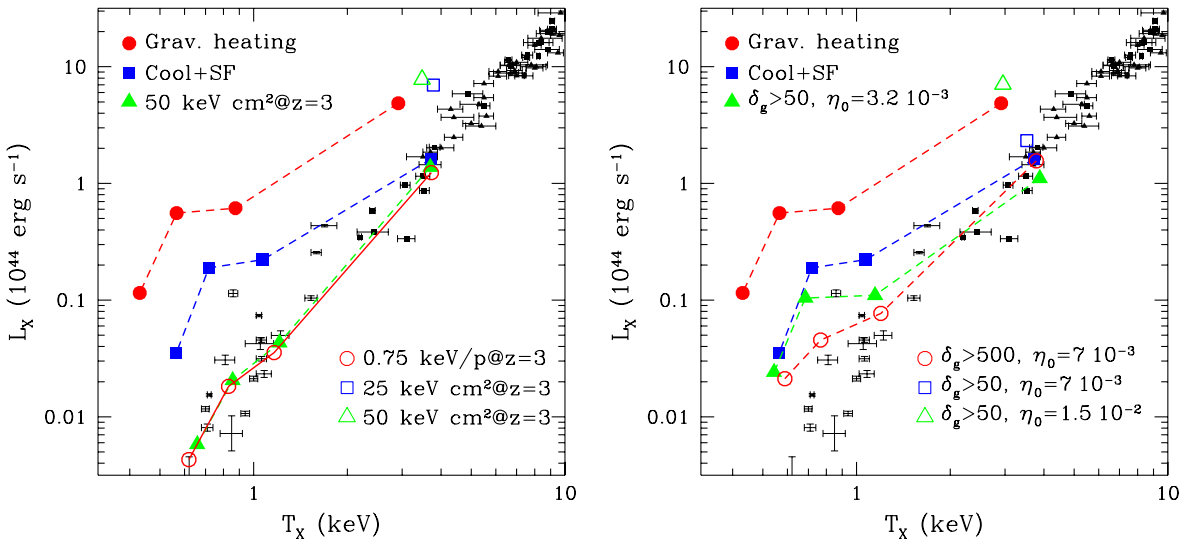

Figure 2.9: The relation between bolometric luminosity and emission weighted–temperature for the simulations and for observational data at $z = 0$. The right and the left panel are for the effects of impulsive heating and SN feedback, respectively. Data points at the cluster scale are from Markevitch (1988, small triangles) and from Arnaud & Evrard (2000, small squares), while data for groups (crosses) are from Helsdon & Ponman (2000).

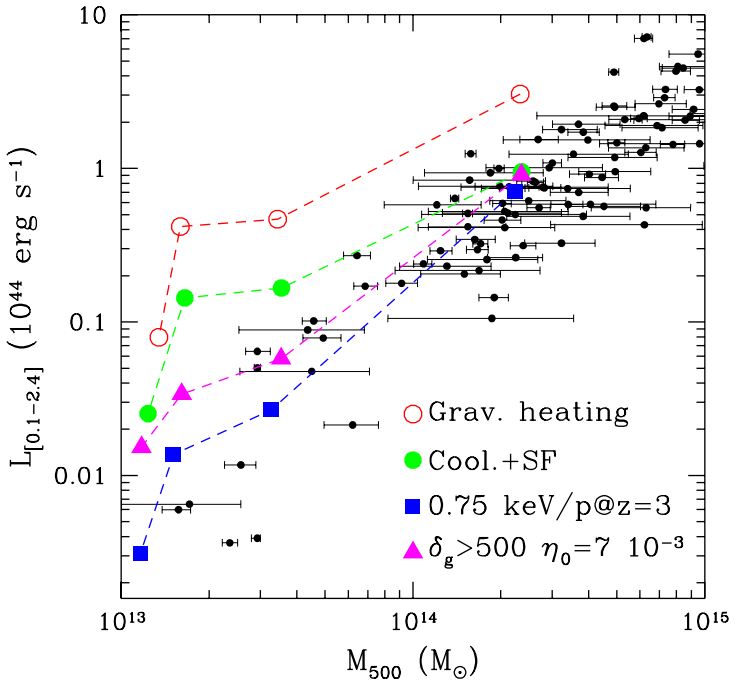

Figure 2.10: Comparison of simulations and observational results for the relation between X–ray luminosity in the 0.1–2.4 keV energy band and the mass at an overdensity $\bar{\rho}/\rho_{\rm crit} = 500$. Small circles with errorbars are the observational data points from Reiprich & Böhringer (2002).

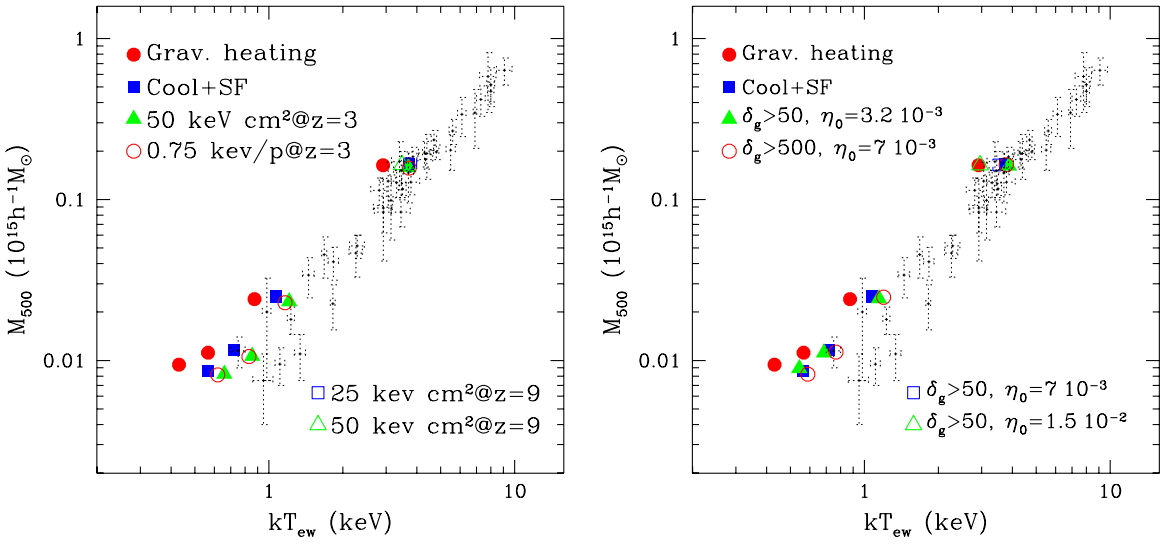

Figure 2.11: The relation between the mass at overdensity $\rho/\rho_{\rm crit} = 500$ and the emission weighted–temperature. The right and the left panels are for the effects of impulsive heating and SN feedback, respectively. Data points are from Finoguenov et al. (2001b).

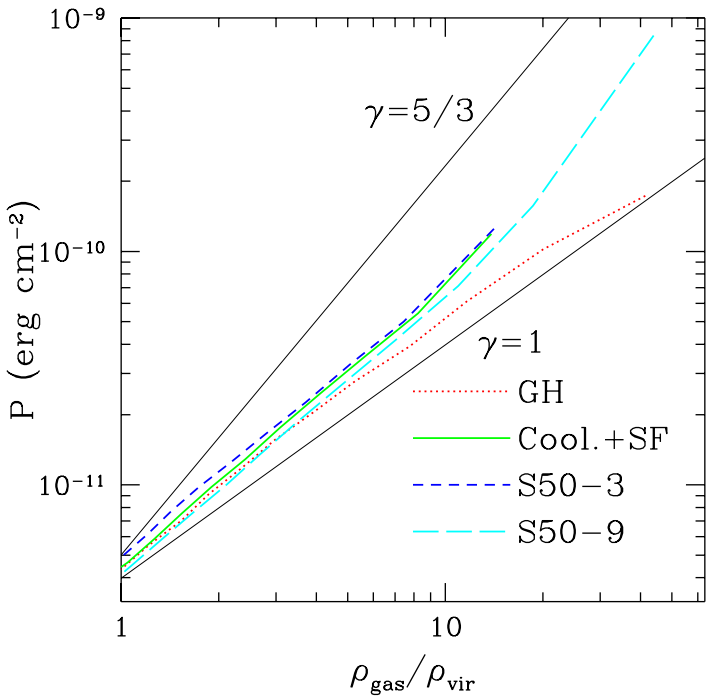

Figure 2.12: The relation between gas pressure (cgs units) and density (in units of the average total density within the virial radius), computed within spherical shells. The two thin solid lines correspond to effective polytropic indices $\gamma = \mathrm{d}\log P/\mathrm{d}\log\rho_{gas} = 1$ (isothermal model) and $\gamma = 5/3$ (adiabatic model).

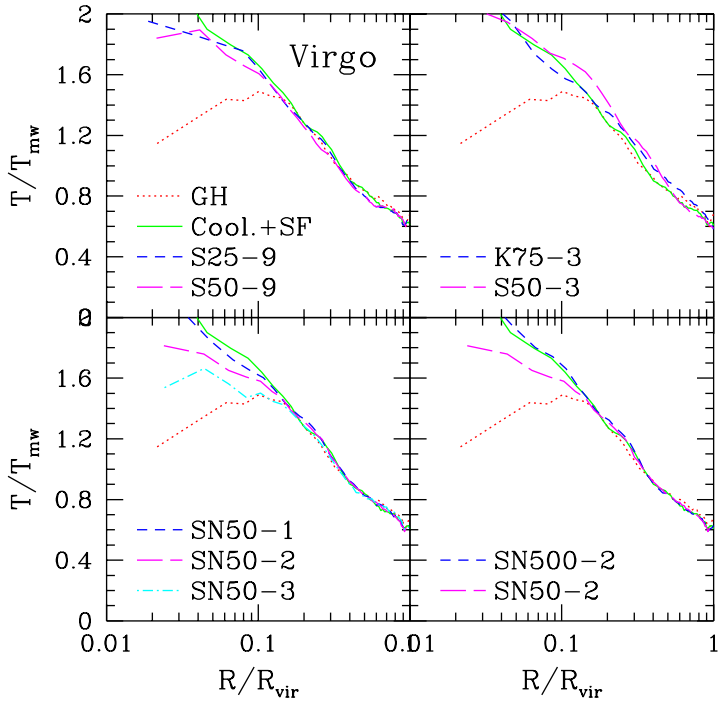

Figure 2.13: Temperature profiles of the "Virgo" runs, in units of the mass–weighted temperature. The sequence of panels is the same as in Figure 2.6.

CHAPTER 3

NUMERICAL APPROACHES TO COSMOLOGY

■ *Chapter Outline*

This Chapter sketches the basics of numerical techniques involved in cosmological hydrodynamical simulations. The focus is on describing the SPH algorithms and the features of the GADGET code.

3.1 Basic Hydrodynamics

The ICM has an atomic density of about $n \sim 10^{-3}\,\mathrm{cm}^{-3}$, so that we can model him in the dilute gas approximation. This means that the occupation number in the phase–space is small so that the exclusion principle is unimportant. Hence the gas is thought as an ensemble of classical point–like ballistical particles which collide with each other. If we consider the phase–space density $f(\mathbf{r}, \mathbf{v})$, which live in the 6-*th* dimensional volume with $d^6w = d^3x d^3v$, balancing the flux of particles across the boundaries of a given volume gives

$$\frac{\mathrm{d}}{\mathrm{d}t}\int_V d^6w f \;=\; -\int_S dS\; \mathbf{n}\cdot(f\dot{w})$$

the Boltzmann equation for the phase-space density $f(\mathbf{r}, \mathbf{v})$ in non–relativistic case is easily derived and reads

$$\frac{\mathrm{d}\, f}{\mathrm{d}t} = \left(\frac{\partial}{\partial t} + \dot{\mathbf{x}} \cdot \nabla_X + \dot{\mathbf{v}} \cdot \nabla_V \right) f = 0. \tag{3.1}$$

In other words, along the paths of particles the space–density and the momentum–density must vary so that their product remains constant. This does not hold if we take into account the effect of collisions which will scatter particles in and out of a phase–space region:

$$\frac{\mathrm{d}\, f}{\mathrm{d}t} = \left(\frac{\partial}{\partial t} + \dot{\mathbf{x}} \cdot \nabla_X + \dot{\mathbf{v}} \cdot \nabla_V \right) f = \left(\frac{\partial\, f}{\partial t} \right)_{coll}. \tag{3.2}$$

Defining the velocity average of some function $\mathcal{F}$ as

$$\langle \mathcal{F} \rangle = \frac{\int d^3v\ f\mathcal{F}}{\int d^3v\ f} = \frac{1}{n} \int d^3v\ f\mathcal{F}$$

the conservation of $\mathcal{F}$ during collisions gives

$$\int d^3v \mathcal{F}(\mathbf{v}) \left(\frac{\partial\, f}{\partial t} \right)_{coll} \ = \ 0$$

and results in

$$\frac{\partial\, n \langle \mathcal{F} \rangle}{\partial t} + \frac{\partial\, n \langle \mathcal{F}\mathbf{v} \rangle}{\partial \mathbf{x}} + n \frac{\partial\, \Phi}{\partial \mathbf{x}} \cdot \left\langle \frac{\mathrm{d}\, \mathcal{F}}{\mathrm{d}\mathbf{v}} \right\rangle \ = \ 0. \tag{3.3}$$

where Φ is the gravitational potential. Using the previous equation we can derive the conservation of mass, momentum and energy. In the following we report their final form, addressing the reader to reference text on hydrodynamics or statistical physics for a more proper derivation (see e.g. Landau&Lifshitz (1959, 1969)).

Conservation of Mass

Setting $\mathcal{F} = m$ in Eq. (3.3) we obtain

$$\frac{\partial\, \rho}{\partial t} + \nabla \cdot (\rho \mathbf{u}) \ = \ 0 \tag{3.4}$$

where $\rho = nm$ and

$$\mathbf{u} \ = \ \frac{\int d^3v\ f\mathbf{v}}{\int d^3v f}$$

is the bulk velocity. Equation Eq. (3.4) is known as the *continuity equation* and tells us that the mass variation within a volume must be equal to the mass flux across the surface defining the same volume.

If the observer is moving along with the stream, it will observe

$$\frac{D\,\rho}{Dt} \;=\; -\rho\nabla\cdot\mathbf{u} \tag{3.5}$$

being $D/Dt = \partial/\partial t + \mathbf{u}\cdot\nabla$ the *Lagrangian derivative*.

Conservation of Momentum

If $\mathcal{F} = m\mathbf{v}$ Eq. (3.3) yields to

$$\frac{\partial\,\rho u_i}{\partial t} + \frac{\partial\,\rho\,\langle v_i v_k\rangle}{\partial x_k} + \rho\frac{\partial\,\Phi}{\partial x_i} \;=\; 0.$$

Writing the velocity $\mathbf{v}$ as $\mathbf{v} = \mathbf{u} + \mathbf{w}$ where $\mathbf{w}$ is the velocity of 'random' motions with respect to the mean velocity $\mathbf{u}$ and having $\rho\,\langle v_i v_k\rangle \;=\; P\delta_{ik} - \pi_{ik}$ with the gas pressure

$$P \equiv \rho\left\langle|\mathbf{w}|^2\right\rangle/3 \tag{3.6}$$

and the viscous stress tensor

$$\pi_{ik} \equiv \rho\left\langle|\mathbf{w}|^2\,\delta_{ik}/3 - w_i w_k\right\rangle. \tag{3.7}$$

equation Eq. (3.3) now reads

$$\frac{\partial\,\rho u_i}{\partial t} + \frac{\partial}{\partial x_k}\left(\rho u_i u_k + P\delta_{ik} - \pi_{ik}\right) \;=\; -\rho\frac{\partial\,\Phi}{\partial x_i}$$

and using Eq. (3.4) we obtain the *force equation*

$$\rho\frac{D\mathbf{u}}{Dt} \;=\; -\rho\nabla\Phi - \nabla P + \nabla\cdot\boldsymbol{\pi} \tag{3.8}$$

being $(\nabla\cdot\boldsymbol{\pi})_i \;\equiv\; \partial\,\pi_{ik}/\partial x_k$.

Conservation of Energy

Equation Eq. (3.3) becomes the law of energy conservation if $\mathcal{F} = 1/2mv^2 = 1/2mu^2 + 1/2mw^2 + m\mathbf{w}\cdot\mathbf{u}$. To derive it, let us define the *specific internal energy* as

$$\rho\epsilon \;=\; \rho\left\langle w^2/2\right\rangle \;=\; 3P/2 \tag{3.9}$$

and the *heat conduction flux* $\mathbf{F}$ as

$$F_k \;=\; \frac{1}{2}\rho\left\langle w_k w^2\right\rangle \tag{3.10}$$

so that we obtain the *total energy conservation law*

$$\frac{\partial}{\partial t}\left(\frac{1}{2}\rho u^2+\rho\epsilon\right)+\frac{\partial}{\partial x_k}\left(\frac{1}{2}\rho u_k u^2+u_i\left(P\delta_{ik}-\pi_{ik}\right)+\rho\epsilon u_k+F_k\right) \;=\; -\rho u_k\frac{\partial\,\Phi}{\partial x_k} \tag{3.11}$$

which can be rewritten as the following *internal energy equation*

$$\frac{\partial\,\rho\epsilon}{\partial t}+\frac{\partial\,\rho\epsilon u_k}{\partial x_k}=-P\frac{\partial\,u_k}{\partial x_k}-\frac{\partial\,F_k}{\partial x_k}+\Psi \tag{3.12}$$

where the *rate of viscous dissipation* Ψ is defined as

$$\Psi \;=\; \pi_{ik}\frac{\partial\,u_i}{\partial x_k} \;=\; \frac{1}{2}\pi_{ik}\left(\frac{\partial\,u_i}{\partial x_k}+\frac{\partial\,u_k}{\partial x_i}\right). \tag{3.13}$$

Using the continuity equation we have at the end

$$\rho\frac{D\epsilon}{Dt} \;=\; P\nabla\cdot\boldsymbol{u}-\nabla\cdot\mathbf{F}+\Psi. \tag{3.14}$$

Navier–Stokes Equations

Collecting together Eq. (3.4), Eq. (3.8) and Eq. (3.14), which represent the moments of the Boltzmann' transport equation, we can have all the *Navier–Stokes equations*:

$$\begin{aligned}
\left(\frac{\partial}{\partial t}+\mathbf{u}\cdot\nabla\right)\rho &= -\rho\nabla\cdot\mathbf{u}\\
\rho\left(\frac{\partial}{\partial t}+\mathbf{u}\cdot\nabla\right)\mathbf{u} &= -\rho\nabla\Phi-\nabla P+\nabla\cdot\boldsymbol{\pi}\\
\rho\left(\frac{\partial}{\partial t}+\mathbf{u}\cdot\nabla\right)\epsilon &= -P\nabla\cdot\mathbf{u}-\nabla\cdot\mathbf{F}+\Psi
\end{aligned}$$

being

$$\begin{aligned}
\rho &= m \int d^3v f(\mathbf{x}, \mathbf{v}, t) \\
\mathbf{u} &= \langle \mathbf{v} \rangle \\
\epsilon &= \frac{3}{2} P/\rho \;=\; \frac{1}{2} \left\langle w^2 \right\rangle \\
\pi_{ik} &\equiv \rho \left\langle |\mathbf{w}|^2 \, \delta_{ik}/3 - w_i w_k \right\rangle \\
F_k &= \frac{1}{2} \rho \left\langle w_k w^2 \right\rangle \\
\Psi &= \pi_{ik} \frac{\partial \, u_i}{\partial x_k}.
\end{aligned}$$

Note that previous equations have been written in their *non conservation form*, i.e. from the point of view of a particle moving in the fluid, which is the Lagrangian approach that we use in simulations. It is also worthwhile to note that $\nabla\Phi$ should be substituted by a more general term $\mathbf{f}$, which stands for a general external force per unit mass exerted on a gas volume, when accounting for some other fields than gravitation, e.g. magnetic fields (Dolag et al. 2002).

So far we have written three equations: the continuity equation, the Euler (or momentum) equation and the energy equation. To close the system we also need a fourth relation, namely the equation of state which relates the thermodynamical variables with each other. This is:

$$P = (\gamma - 1)\rho u \tag{3.15}$$

where $\gamma = 5/3$ is the adiabatic exponent for a monoatomic ideal gas and ϵ is the energy per unit mass. Note that in this notation the sound speed of a pressure wave is

$$c^2 = \gamma P/\rho. \tag{3.16}$$

The form we use in numerical simulation we run is quite different from Eqs. (3.4), (3.8) and (3.14) because, as it is usual in cosmological simulations, we ignore the viscous stress tensor and thermal flux terms, then considering the ICM as a perfect gas. Then the governing equations are:

$$\left(\frac{\partial}{\partial t} + \mathbf{u} \cdot \nabla\right) \rho = -\rho \nabla \cdot \mathbf{u} \tag{3.17}$$

$$\left(\frac{\partial}{\partial t} + \mathbf{u} \cdot \nabla\right) \mathbf{u} = -\nabla\Phi - \frac{\nabla P}{\rho} \tag{3.18}$$

$$\left(\frac{\partial}{\partial t} + \mathbf{u} \cdot \nabla\right) \epsilon = -\frac{P}{\rho} \nabla \cdot \mathbf{u} - \frac{\mathcal{L}(\epsilon, \rho)}{\rho} \tag{3.19}$$

neglecting other terms than gravity as for the external forces and accounting for non–hydrodynamical heating and cooling with the $\mathcal{L}$ function.

3.2 Different Approaches to Computational Fluid Dynamics

Considering Eq. (3.5) one can infer the existence of two different approaches to describe the motion of fluids, namely the *Eulerian* and the *Lagrangian* "philosophy".

As for the former, the fluid is studied considering the properties of a fixed volume in space and studying their variations with space and time. This is what the left–hand term in Eq. (3.5) refers to. In the second approach, the fundamental object of our analysis is a volume of fluid whose properties are studied along its trajectory: then, the derivative in the left–hand side (l.h.s) of mentioned Eq. (3.5) will be for the density

$$\frac{\mathrm{d}\,\rho(x,y,z,t)}{\mathrm{d}t} = \frac{\partial\,\rho}{\partial t} + \frac{\partial\,\rho}{\partial x}\frac{\mathrm{d}\,x}{\mathrm{d}t} + \frac{\partial\,\rho}{\partial y}\frac{\mathrm{d}\,y}{\mathrm{d}t} + \frac{\partial\,\rho}{\partial z}\frac{\mathrm{d}\,z}{\mathrm{d}t}$$

leading to the right–hand side (r.h.s) of equation Eq. (3.5). Less formally, we can say that the first term ($\partial/\partial t$) of the Lagrangian derivative carries informations about the "local" or "intrinsic" variation whereas the second one ($\mathbf{v}\cdot\nabla$, the *convective derivative*) describe the variation due to the surrounding environment.

Both Eulerian and Lagrangian methods present advantages and disadvantages. A comprehensive review is beyond the scope of this work, so we will summarize them reminding that Eulerian approaches are best suited as shock–capturing methods and resolve better underdense regions and arbitrarily large gradients, while Lagrangian codes are not locked to a pre–defined geometry and can adapt the resolution to the local needs allowing for wide spatial and dynamical ranges. Modern Eulerian codes (e.g. Bryan 1996, Quilis 2004) make use of more refined algorithm to adapt the underlying basic grid to the typical scale of the problem, for instance in resolving shocks, both having more grid–levels or a dynamic mesh refinement algorithm. Depending on the problem one is dealing with, one choice or another is preferable: for a while Lagrangian methods have been the ones used for the bulk of works in computational cosmology since they are free of fixed geometries and the ability in managing the huge dynamical ranges that a typical problem in this field present, e.g. with three or more order of magnitude as for the density contrast. Recently, also AMR codes have proven to be robust and practical in many similar problems, offering also a good capability to capture and resolve hydrodynamical shocks. As a final, quite obvious, note, it is worth to mention that Eulerian codes are better suited to easily calculate fluxes and quantity exchanges, e.g. mass fluxes (and then diffusion equation), radiative transport etc, while a particle description is useful when dealing with well–separated phases, e.g. in studying the star formation.

Moreover, equations derived considering infinitesimal moving fluid elements have the so–called *non–conservation* form, whereas one would obtain the *conservation* one starting from a space–fixed volume. The two forms differ essentially in using flux variables $(\rho\mathbf{u}, (p + \rho u^2))$ as independent variables (the latter) or the primitive $(\rho, \mathbf{u}, p)$ ones (the former). Because it is every time possible to derive one from the other, from a theoretical point of view it is unimportant which one we choose to deal with. On the contrary it arise to be quite different in the computational hydrodynamics. Let we explain this with an example. The continuity equation in conservation form reads as

$$\frac{\partial \rho}{\partial t} + \nabla \cdot (\rho \mathbf{v}) = 0 \tag{3.20}$$

while in non–conservation form it appears slightly different

$$\frac{\mathrm{d} \rho}{\mathrm{d} t} + \rho \nabla \cdot \mathbf{v} = 0. \tag{3.21}$$

Now, when a shock occurs there are some constraints on the values of thermodynamical quantities at the left and at the right of the shock edge, namely the *Rankine–Hugoniot conditions* (e.g. Landau & Lifshitz 1959). The one for the specific energy reads as

$$\rho_1 u_1 = \rho_2 u_2$$

(subscripts 1 and 2 refer to left and right sides respectively). Clearly the product ρu will not suffer of any discontinuity while the separate thermodynamical variables will do. All the same, the Eq. (3.20) will not suffer for severe discontinuities in its primary independent variable while the other one will do. Although this example is somewhat simplistic it can clarify why using the conservation form would make easier to make a high–quality shock–capturing scheme. [1].

3.3 A Lagrangian View: the Smoothed Particle Hydrodynamics

> "Many of the most interesting problems in astrophysics involve systems with large departures from spherical symmetry. [..] the standard *finite difference* representations of the continuum equations are of limited use, because of the very large number of grid points required [..]. A better method is to make use of the *Lagrangian* description of the fluid flow which automatically focuses attention on fluid elements."

[1] The *shock–capturing* schemes are those which are designed to have shock waves appearing naturally as a result of the overall hydrodynamics. The case for an explicit, exact insertion of Rankine–Hugoniot relations is that of *Shock–fitting* methods. Clearly, the formers are best suited for complex problems involving shocks without any knowledge in advance of their position or number

Gingold and Monaghan (1977)

> "We wanted a method that was easy to work with and could give a reasonable accuracy. The SPH method satisfied these requirements. As a bonus we found the SPH was rugged, gave sensible answers in difficult situations, and could be extended to complicated physics without much trouble."

J. J. Monaghan (1992)

3.3.1. SPH Code Basics

Real fluids consist of an infinite number of infinitesimally–extended elements which move obeying the Newtonian equations under the influence of pressure gradients and other, if any, external forces like gravity, magnetic fields, inertial forces from rotating systems etc. For obvious reasons it is definitely impractical to model such real fluids in the computational realm, so that the standard approach is to select a set of N finite elements, representing them by particles, and assume that their mass density is proportional to the mass density of the fluid so that the latter can be inferred given the former if the system is evolving following the laws of thermodynamics. In recovering the density ρ of the fluid from the distribution of particles we are basically recovering a probability distribution from a sample. To do this we have to smear out the local statistical fluctuations due to the finite number of used elements. In the SPH technique, this task is accomplished using the smoothing kernel method as first presented by Lucy (1977) and Gingold and Monaghan (1977).

It is worth to mention that while in the earliest formulations of SPH the particles were thought to have equal masses, later derivations (e.gMonaghan & Lattanzio 1985, Hernquist & Katz 1989) of equations as well as numerical experiments (Monaghan & Pongracic 1984) definitely showed that this is not mandatory.

Following the original discussion of Gingold and Monaghan (1977), the heart of the SPH technique is the evaluation of a smoothed scalar or vector field f

$$\langle f(\mathbf{r})\rangle := \int f(\mathbf{r}')W(\mathbf{r},\mathbf{r}',h)d\mathbf{r}' \tag{3.22}$$

by a Monte Carlo method from a set of N points at coordinates $\mathbf{r}_1,\ldots,\mathbf{r}_N$:

$$\langle f(\mathbf{r})\rangle_N := \sum_{j=1}^{N}\frac{f_j}{n_j}W(\mathbf{r}-\mathbf{r}_j,h) \tag{3.23}$$

where $W(\mathbf{r},\mathbf{r}',h)$ is an interpolant kernel that is assumed to have the form $W(\mathbf{r}-\mathbf{r}',h)$ which is sufficient general and simplify the analysis, n_j is the local number density of

points at the point $\mathbf{r}_j$ and h is a sort of *resolution* in the sense that every property with length scale $l \ll h$ is strongly smoothed: for kernel with compact support, h is about the size of the support itself.
The kernel W must satisfy the condition

$$\int W(\mathbf{r}, h) d\mathbf{r} = 1. \tag{3.24}$$

over the all space. Furthermore, we must ensure that

$$\langle f(\mathbf{r}) \rangle \rightarrow f(\mathbf{r}) \tag{3.25}$$
$$\langle f(\mathbf{r}) \rangle_N \rightarrow \langle f(\mathbf{r}) \rangle \tag{3.26}$$

the former being true in the limit

$$\lim_{h \to 0} W(\mathbf{r} - \mathbf{r}', h) = \delta(\mathbf{r} - \mathbf{r}') \tag{3.27}$$

which ensures the locality of estimates, and the latter being true as the parameter h is linked to the number N of sampling particles such as $h \rightarrow 0$ as $N \rightarrow \infty$. The best choice of h depends on the problem being analyzed and is yet a debated issue (e.g. Lombardi et al. 1999): as a general assert, a relation like $h \propto n^{-1/3}$ should be met for constant smoothing length, and $\delta h_i / h_i \propto -\frac{1}{3} \delta \rho_i / \rho_i$ is expected for spatially varying resolution. Quoting the original discussion of Gingold and Monaghan, we state that the condition

$$\langle f(\mathbf{r}) \rangle_N \rightarrow f(\mathbf{r}) \tag{3.28}$$

is met if the kernel W has the form

$$W(\mathbf{r}, h) = \frac{1}{h^3} K(\mathbf{r}/h). \tag{3.29}$$

If $h \rightarrow 0$ as $N \rightarrow \infty$ and if $K(\mathbf{u})$ is a Borel function satisfying

$$\int K(\mathbf{u}) d\mathbf{u} = 1, \quad \left| \mathbf{u}^2 K(\mathbf{u}) \right| \rightarrow 0 \text{ as } |\mathbf{u}^2| \rightarrow \infty, \quad \int |K\mathbf{u}| d\mathbf{u} < \infty \tag{3.30}$$

then our request Eq. (3.28) is satisfied. Although the original paper of SPH used a Gaussian kernel, to day it is more common to use spline–kernels Sec. (3.3.4).
It is worth to mention that the error in using Eq. (3.23) instead of Eq. (3.22) depends on the disorder of the particles and is normally $O(h^2)$ or better (and references thereinMonaghan & Lattanzio 1985, Monaghan 1992).
In the following we drop the subscript N since it will be clear whether we refer to the summation interpolant or the actual function.

By using a differentiable kernel our estimates are also differentiable and the derivatives of the interpolant are constructed just using derivatives of the kernel, so that

$$\langle \nabla f(\mathbf{r}) \rangle \equiv \int W(-\mathbf{r}', h) \nabla f(\mathbf{r}') d\mathbf{r}' \tag{3.31}$$

become, after integrating by part,

$$\langle \nabla f(\mathbf{r}) \rangle = \int f(\mathbf{r}') \nabla W(\mathbf{r} - \mathbf{r}', h) d\mathbf{r}' \tag{3.32}$$

as long as we can ignore surface terms, which we are allowed to if $fW \to 0$ on the boundary. This hypothesis is satisfied because generally the kernel vanishes rapidly for $|\mathbf{r} - \mathbf{r}'| \to \infty$, and is always true for kernel with compact support.

In the discrete approximation the previous equation become

$$\langle \nabla f(\mathbf{r}) \rangle = \sum_{j=1}^{N} \frac{f_j}{n_j} \nabla W(\mathbf{r} - \mathbf{r}_j, h). \tag{3.33}$$

In other words, W must be differentiable up to the same order as that of terms present in the equations to be integrated: for instance, ∇W must exist for non–pressureless medium and $\nabla^2 W$ must exist if we introduce the diffusion equation (e.g. to calculate heat conduction or describe diffusive phenomena).

3.3.2. Fundamental Equations of Hydrodynamics in SPH

The mass density $\rho(\mathbf{r})$ can be estimated using Eq. (3.23) with $n_j = \rho_j / m_j$ so that

$$\langle \rho(\mathbf{r}) \rangle = \sum_{j=1}^{N} m_j W(\mathbf{r} - \mathbf{r}_j, h) \tag{3.34}$$

and therefore the density of the particle i is estimated as

$$\rho_i = \sum_{j=1}^{N} m_j W(\mathbf{r}_{ij}, h) \tag{3.35}$$

where from now on $\mathbf{r}_{ij} \equiv \mathbf{r}_i - \mathbf{r}_j$.

Following Hernquist and Katz (1989), we note that the previous definition is susceptible of two different interpretation: by the former, the so–called *scatter* interpretation, at each point $\mathbf{x}$ the density is contributed by each neighboring particle with its own profile, where "neighbor" means a particle j whose distance satisfy $|\mathbf{r}_j - \mathbf{r}_x| < h$ if the kernel has a compact support. This relation reads $|\mathbf{r}_j - \mathbf{r}_x| < h_j$ if the parameter h

differs from particle to particle (so far we wrote equations as if it were constant for all particles).

The second interpretation, known as *gather* one, assign at the point $\mathbf{x}$ a density that is the sum of all neighboring particles each weighted according to $W(\mathbf{r}_j - \mathbf{r}_x, h)$. In the case of variable h we have to assign h_x to the point. As is evident, this distinction is relevant only if h varies from point to point. We shall return on this later on.

A direct translation of the continuity equation Eq. (3.4) in the SPH language using Eq. (3.34) and Eq. (3.33) would read as

$$\frac{\mathrm{d}\,\rho(\mathbf{r})}{\mathrm{d}t} = -\rho(\mathbf{r}) \sum_{j=1}^{N} \frac{m_j}{\rho_j} \mathbf{v}_j \nabla_i W_{ij} \tag{3.36}$$

where ∇_i stands for the gradient taken with respect to the coordinates of particle i and $W_{ij} = W(\mathbf{r}_i - \mathbf{r}_j, h)$. Nevertheless, using the estimate for ρ given by Eq. (3.34) we would introduce an error greater than the second order truncation (Monaghan 1982): for that reason it is better to rewrite equations with density inside operators. In this case we have

$$\rho \nabla \cdot \mathbf{v} = \nabla \cdot (\rho \mathbf{v}) - \mathbf{v} \cdot \nabla \rho \tag{3.37}$$

and the equation of continuity become

$$\frac{\mathrm{d}\,\rho_i}{\mathrm{d}t} = \sum_{j=1}^{N} m_j (\mathbf{v}_i - \mathbf{v}_j) \cdot \nabla_i W_{ij}. \tag{3.38}$$

In a similar way we can derive the standard form of the momentum equation using the identity

$$\frac{\nabla P}{\rho} = \nabla \frac{P}{\rho} + \frac{P}{\rho^2} \nabla \rho \tag{3.39}$$

so that

$$\frac{\mathrm{d}\,\mathbf{v}_i}{\mathrm{d}t} = -\sum_{j=1}^{N} m_j \left(\frac{P_j}{\rho_j^2} + \frac{P_i}{\rho_i^2} \right) \nabla_i W_{ij}. \tag{3.40}$$

If we interpret the kernel as being Gaussian, we can write down the force on particle a due to particle b as (Monaghan 1992)

$$\frac{2 m_a m_b}{h^2} \left(\frac{P_a}{\rho_a^2} + \frac{P_b}{\rho_b^2} \right) (\mathbf{r}_a - \mathbf{r}_b) W_{ab} \tag{3.41}$$

so that pressure force between particle pairs is symmetric central, then conserving both linear and angular momenta. It is worth to note that this symmetric form would arise quite naturally if equations were derived form the Lagrangian. Such a result would not

be assured with a non–symmetric formulation and does not hold for a non–symmetric kernel.

The energy equation becomes

$$\frac{\mathrm{d}\, u_i}{\mathrm{d}t} = \left(\frac{P_i^2}{\rho_i^2}\right) \sum_{j=1}^{N} m_j \mathbf{v}_{ij} \cdot \nabla_i W_{ij} \tag{3.42}$$

but reminding that

$$-\frac{P}{\rho}\nabla \cdot \mathbf{v} = -\nabla \cdot \left(\frac{P\mathbf{v}}{\rho}\right) + \mathbf{v} \cdot \nabla \left(\frac{P}{\rho}\right) \tag{3.43}$$

we can also write it as

$$\frac{\mathrm{d}\, u_i}{\mathrm{d}t} = \sum_{j=1}^{N} m_j \left(\frac{P_j}{\rho_j^2}\right) \mathbf{v}_{ij} \cdot \nabla_i W_{ij} \tag{3.44}$$

and taking the average of them we end up with

$$\frac{\mathrm{d}\, u_i}{\mathrm{d}t} = \frac{1}{2} \sum_{j=1}^{N} m_j \left(\frac{P_j}{\rho_j^2} + \frac{P_i}{\rho_i^2}\right) \mathbf{v}_{ij} \cdot \nabla_i W_{ij} \tag{3.45}$$

which shows the same symmetrization as Eq. (3.40).

The equations that GADGET actually integrates are quite different from those shown above in many aspects: (1) it fully account for the Lagrangian nature of the SPH letting the spatial resolution being spatial–dependent; (2) consequently from point 1, it implement a symmetrized formulation with respect to h; (3) so far we have ignored the artificial viscosity term, necessary to avoid particle interpenetration at shock fronts; (4) following suggestions from Hernquist (1993) GADGET choose to integrate entropy instead of energy. We discuss all these points in the following sections.

3.3.3. Non–Constant Spatial Resolution

As already outlined, the h parameter plays the role of "resolution" in estimating hydrodynamical and thermodynamical quantities and their variations, in the sense that all characteristic scales $l \ll h$ will be smoothed out. There is no theoretical reason to assume, as done in the early implementations of SPH scheme, a resolution that is time–dependent but constant in space, because, as long as the kernel is symmetric in h, the momentum can be conserved. Rather, allowing each particle to have its own resolution, depending on the local conditions, will fully retain the Lagrangian nature of SPH. In fact, the statistical fluctuations from kernel estimates arise from the "noise" associated to the variable number N of particles inside the smoothing volume: with a

constant h estimates in underdense regions would be less accurate than in overdense ones because the relative sampling error of the discrete approximation grow as N decreases, approaching unity for $N = 1$. Indeed, it would be far more preferable to maintain the same computational accuracy all over the space. Furthermore we would not get full profit from the distribution of particles to resolve local structures and we would smooth over even more particles or even unresolve shocks that otherwise we had better described.

In other words, letting h varying over the space arise quite naturally from the Lagrangian approach.

To accomplish this task we have to rewrite all the above SPH equations in order to symmetrize them with respect to h.

Clearly now, as already anticipated, scatter and gather interpretations differ: Eq. (3.22) become

$$\langle f(\mathbf{r})\rangle = \int W(\mathbf{r}-\mathbf{r}', h(\mathbf{r}'))f(\mathbf{r}')\ d\mathbf{r}' \tag{3.46}$$

$$\langle f(\mathbf{r})\rangle = \int W(\mathbf{r}-\mathbf{r}', h(\mathbf{r}))f(\mathbf{r}')\ d\mathbf{r}' \tag{3.47}$$

respectively so that Eq. (3.23) is computed for the density as

$$\langle \rho(\mathbf{r}_i)\rangle = \sum_{j=1}^{N} m_j W(r_{ij}, h_j) \tag{3.48}$$

$$\langle \rho(\mathbf{r}_i)\rangle = \sum_{j=1}^{N} m_j W(r_{ij}, h_i). \tag{3.49}$$

Since errors are of the order $\sim O(h^2)$ in both cases (Hernquist & Katz 1989), there are no apparent reasons to prefer one or another form: nevertheless a key point to consider is that, in both cases, when the particles of a pair exchange the role they will play differently in the same definition then introducing a violation of Newton's third law. To avoid this drawback the equations of motion must be symmetrized in h_i and h_j.

Although for an isoentropic nondissipative gas, dynamical equations can be derived in either gather or scatter formulation in a momentum–conservative form (Gingold & Monaghan 1982), this cannot be easily generalized so that two possible solutions are: (1) to substitute $(h_i + h_j)/2$ for h_i and h_j, bearing in mind that Hernquist and Katz (1989) found errors on system integration; (2) symmetrize the kernel itself as

$$W_{ij} = \frac{1}{2}\left[W(r_{ij}, h_i) + [W(r_{ij}, h_j)\right] \tag{3.50}$$

where errors are again $\sim O(h^2)$ because this expression is a linear combination of gather and scatter approaches.

As we allow h to depend on the space position and time, it might be that severe errors arise in entropy and energy conservation in the case equations had not been derived consistently. This is due essentially to the fact that the change in particles' smoothing length acts as a non–adiabatic source of energy (Hernquist 1993). As a consequence, when using the expression Eq. (3.34), if we integrate the energy or the entropy equation, the total entropy or energy of the system will not be conserved, respectively. To overcome this problem, density could be calculated following Eq. (3.45) so that entropy (for an ideal isoentropic gas) will be conserved as long as we integrate energy with one of the above formulae. In this case the drawback would be the non–conservation of the mass (Monaghan 1992), provided that errors would scale as $\sim O(h^2)$ (Hernquist 1993). Furthermore it this lack in conservation violation is independent of the limit $N \to \infty$, since the amount of conservation errors does not decrease when the system is approximated by a larger number of particles (e.g. Serna et al. 1996). Rather, it depends on the incorrect derivation of the basic equations that need to be derived from the true Hamiltonian with h included as a canonical variable (Springel & Hernquist 2002, Monaghan 2002).

As a final remark, it is worth mentioning an interesting result on cosmological simulations from Alimi et al. (2003): neglecting the so–called ∇h terms turns in to an overestimate of density peaks associated with shocks, which, in turn, leads to an overestimated efficiency of star formation process.

Deep inspections have been performed by Nelson and Papaloizu (1993, 1994), Serna et al. (1996), Alimi et al. (2003). Because a detailed discussion of this issue is outside the scope of this work, we address the reader to the above papers for further details.

3.3.4. The Kernel Choice

Under the general requests Eq. (3.30), many kernels can be found to work in SPH. Although a Gaussian kernel $1/(h_{ij}^2\pi)^{3/2}e^{-r_{ij}^2/h^2}$ would provide the easiest interpretation of the physical meaning of equations, it has the disadvantage of a slow fall off with the r_{ij}/h ratio, so that virtually all particles will contribute to the properties of each one. This is a disadvantage for two reasons. Firstly, it involves an higher computational effort, especially in parallel environments where it translates mainly in a large amount of communications among processors. Secondly, the local nature of the physical properties will be also smoothed while it would be better to retain it at best as long as possible. To avoid these drawbacks, other kernels have been proposed, mainly based on spline functions with compact support as they ensure continuity of derivatives and good interpolation properties.

Some discussion on the kernel choice can be found in the literature (e.gMonaghan & Lattanzio 1985): a widely used kernel is the B-spline based kernel

$$W(\mathbf{r},h)=\frac{3}{4\pi h^2}\begin{cases}\frac{10}{3}-7u^2+4u^3; & 0\le u\le 1\\ (2-u)^2\left(\frac{5-4u}{3}\right); & 1\le u\le 2\\ 0; & u>2\end{cases} \tag{3.51}$$

3.3.5. Artificial Viscosity

Due to the intrinsic limitation in spatial resolution, every numerical methods will lead to some piling of high frequency waves up to the extreme numerical mode: this could result in more or less severe numerical instability when high wave numbers are intrinsically present as is in case of discontinuities, for instance when a shock occurs. Furthermore, as for the "classic" SPH derivation, a method is needed to prevent particles' interpenetration, which would make the fluid properties multivalued. Besides this genuinely "numerical" issue, one also has to mimic the true physical viscosity that is neglected in the ideal gas approach.

To this purpose, a Von Neumman–Richtmeyer approach of adding an *Artificial Viscosity* (AV) is commonly followed. Many forms of AV have been proposed so far but the symmetrized form of the classic AV suggested by Monaghan (1992) has probably been the most widely used:

$$\Pi_{ij}=\frac{-\alpha\mu_{ij}c_{ij}+b\mu_{ij}}{\rho_i j} \tag{3.52}$$

where α and β are constants, $c_{ij}=(c_i+c_j)/2$ ($c=(\gamma p/\rho)^{1/2}$ is the sound speed), and

$$\mu_{ij}=\begin{cases}\frac{\mathbf{v}_{ij}\cdot\mathbf{r}_{ij}}{h_{ij}(|\mathbf{r}_i-\mathbf{r}_j|^2/h_{ij}^2+\eta^2)} & \text{if } \mathbf{v}_{ij}\cdot\mathbf{r}_{ij}<0\\ 0 & \text{if } \mathbf{v}_{ij}\cdot\mathbf{r}_{ij}>=0\end{cases} \tag{3.53}$$

having, as usual, $\mathbf{v}_{ij}=\mathbf{v}_i-\mathbf{v}_j$ and $\mathbf{r}_{ij}=\mathbf{r}_i-\mathbf{r}_j$. This is a combination of a bulk viscosity and a Von Neumann–Richtmeyer viscosity, respectively linear and quadratic in μ_{ij}. This form is very effective in preventing particles' interpenetration in strong compression regions due to its dependence on pairwise products $\mathbf{v}_{ij}\cdot\mathbf{r}_{ij}$. For the same reason, when this terms are non–null but the particles are not getting a head–head collision (as in shear flows), the resulting viscosity does not vanish, becoming a shear viscosity which is a side–effect.

Balsara (1995) suggested a shear–correcting factor that Steinmetz (1996) and Navarro and Steinmetz (1997) have implemented in the form

$$\Pi_{ij}\rightarrow\bar{\Pi}_{ij}=\Pi_{ij}\,\bar{f}_{ij} \tag{3.54}$$

where

$$\bar{f}_{ij} = \frac{f_i + f_j}{2} \tag{3.55}$$

and

$$f_i = \frac{| < \nabla \cdot \mathbf{v} >_i |}{| < \nabla \cdot \mathbf{v} >_i | + | < \nabla \times \mathbf{v} >_i | + a c_i / h_i} \tag{3.56}$$

having added $a \ll 1$ to prevent numerical divergence. In the SPH formalism the divergence and the curl of the velocity are calculated as

$$\nabla \cdot \mathbf{v}_i = \frac{1}{\rho_i} \sum_{j=1}^{N} m_j \mathbf{v}_{ij} \cdot \nabla_i W_{ij} \tag{3.57}$$

$$\nabla \times \mathbf{v}_i = \frac{1}{\rho_i} \sum_{j=1}^{N} m_j \mathbf{v}_{ij} \times \nabla_i W_{ij} \tag{3.58}$$

where W_{ij} is the evaluation of the kernel in the chosen symmetrization. This factor acts like a switch vanishing when the vorticity become strong and approaching unity for strong compressional flows.

3.3.6. Energy vs. Entropy

In order to describe the changes in the specific energy of gas, equation the Eq. (3.14) provide a quite natural option and is, in fact, commonly used. Nevertheless, we can rewrite it in terms of specific entropy s, as originally proposed by Lucy (1977). Defining the specific entropy as

$$s = \frac{ln(P/\rho^\gamma)}{\gamma - 1} \tag{3.59}$$

we can also define the specific entropy function $a(s)$ so that

$$P = a(s)\rho^\gamma. \tag{3.60}$$

We can now write the energy equation using the function $a(s)$ as

$$\frac{\partial\, a(s)}{\partial t} + (\mathbf{v} \cdot \nabla) a(s) = -\frac{\gamma - 1}{\rho^\gamma} \mathcal{L}. \tag{3.61}$$

In absence of sources or wells, entropy can change only due to shocks: to allow this possibility, the standard SPH formulation of the previous equation account for the AV and is given by (Springel & Hernquist 2002)

$$\frac{\mathrm{d}\, a_i(s)}{\mathrm{d}t} = -\frac{\gamma-1}{\rho_i^{\gamma}}\mathcal{L}(\rho_i,\epsilon_i) + \frac{1}{2}\frac{\gamma-1}{\rho_i^{\gamma-1}}\sum_{j=1}^{N} m_j \Pi_{ij}\mathbf{v}_{ij}\cdot\nabla_i \bar{W}_{ij} \tag{3.62}$$

where the derivative in the left–hand side is the Lagrangian derivative. Note that this equation supply a far better control on sources of entropy. In particular, it ensures that entropy will only grow with time (considering adiabatic evolution, so neglecting the term $\mathcal{L}$) and that its change is only due to shocks, external heating or energy losses due to some specific physical process, like radiative cooling, brought by term $\mathcal{L}$.

Springel and Hernquist (2002) have shown that this approach makes the difference with respect to other "classical" formulations of SPH, providing a very accurate conservation of both energy *and* entropy when coupled with their elegant fully–consistent derivation of SPH with fully–adaptive local resolution. This is all the more important under conditions particularly severe but of strong astrophysical interest, as point–like explosions, or cooling in poorly resolved halos. In both cases the SPH formulation *entropy conservative* of Springel and Hernquist has proven to give very good results. In the explosion test it succeed in conserving the energy and accurately describing the wave propagation. Also, it show a fairly good ability in handle adiabatic compression and cooling when halos are poorly resolved, so significantly reducing the amount of condensed matter within cosmological simulations (see also Sec. (3.4.5)).

3.4 GADGET

GADGET is a State–of–the–Art code to simulate self–gravitating fluids allowed to interact with collision–less matter in cosmological context. Besides gravitational and hydrodynamical treatment of the gas in an expanding background, the code also implements several physical processes: radiative cooling, ionizing effect of the UV background, star formation process for multi–phase gas, Magnetic Fields etc. We have substantially improved the code adding a full treatment of stellar evolution and a detailed accounting for the supernova energy in the thermodynamics of the gas. An exhaustive description of such improvements is given in Chap. (4).
A comprehensive review of its features is given in a number of articles by its Author, Volker Springel (Springel et al. 2001, Springel & Hernquist 2002, Springel & Hernquist 2003a, Jubelgas et al. 2004, Springel 2004), so we refer to them for all the details about the code. Springel et al. (2001) give a complete reference for the earlier version of GADGET . The current version (Springel 2004) contains substantial improvements. In the following we summarize the main features of GADGET which are of interest for this work.

3.4.1. Gravity

Baryons and dark–matter particles are both subject to the self–gravitational field: in this respect they can be modeled as a collisionless fluid obeying the Boltzmann equation (Eq. (3.1)) for the mass phase–space density distribution function $f(\mathbf{x}, \mathbf{v}, t)$

$$\frac{\mathrm{d}\, f}{\mathrm{d}t} \equiv \frac{\partial\, f}{\partial t} + \mathbf{v}\frac{\partial\, f}{\partial \mathbf{x}} - \frac{\partial\, \Phi}{\partial \mathbf{r}}\frac{\partial\, f}{\partial \mathbf{v}}, \tag{3.63}$$

having defined the gravitational potential Φ through the equation

$$\nabla^2\Phi(\mathbf{r}, t) = 4\pi G \int f(\mathbf{x}, \mathbf{v}, t) d\mathbf{v}. \tag{3.64}$$

The analytical solution of this problem for more than two bodies is notoriously impossible, so we have to resort to numerical methods. The most obvious one is the **particle–particle** (PP) method. As it exploits exact pairwise calculations, it gives the best accuracy in force estimates, yet its computational cost is intrinsically of the order $\sim O(N^2)$ for N particles, so it becomes highly impractical as N become larger and larger. Two far more effective algorithms are the so–called **particle–mesh** (PM) and **particle–particle particle–mesh** (P3M). Both rely on the fact that we can resume the continuous density distribution field starting from its discrete representation smearing the latter on a mesh. Then the Poisson' equation, Eq. (3.64), can be resolved on the mesh and the contributions from all mesh–points are added to each particle. The computational cost is now of the order $\sim O(N \log N)$, so that the speed–up with respect of the PP scheme is very high. PM entirely resolve the system this way: clearly it is a reliable method as long as the mesh spacing is lower than the shorter wavelength of interest and the number of particles which fall inside a mesh–cell is high enough to maintain low the fluctuation level (Hockney & Eastwood 1981). However it provides a poor representation of the *local* potential and force field, i.e. for those particles whose separation is of the order of the mesh spacing.
P3M try to combine the computational advantages of PM with the more accurate force representation of PP as for the local field: in fact it considers the force on a single particle i as the sum $\mathbf{F}_i = \sum_{local} \mathbf{F}_{ij}^{direct} + \mathbf{F}^{mesh}$ of a *short–range* term (the first one) due to particles js which live within a given distance which define "locality" and a *long–range* term due to the evaluation of Eq. (3.64) on the mesh. The first term describes basically the rapidly varying field due to the very local mass distribution, while the second one accounts for the slow varying field resulting from the large–scale structure. Excellent works on this topic are the reference book by Hockney & Eastwood (1981) and the classic paper of Efstathiou et al. (1985).

A further effective algorithm, of order $\sim O(N \log N)$ that is reduced to $\sim O(N)$ in most refined codings, is the **hierarchical TREE code** (e.g. Hernquist & Katz 1989). This kind of approach is fully Lagrangian as it decomposes the entire simulated space

in a hierarchy of cells, each containing a single particle or further sub–hierarchies, with no restrictions on the global geometry or on the local resolution. While building the tree, multipole moments of each cell are calculated and propagated upward in the hierarchy so that each cell either contains a single particle or carries the monopole and quadrupole moments of all the particles which live inside it.
Then, the force on each particle is contributed by direct summation from nearby particles or by evaluating the multipole expansions of distant cells (single particles or groups of particles) at the particle location. Whether a cell is considered distant is decided by the *opening criterion*. The standard choice in the algorithm by Barnes & Hut (1986) implemented in GADGET is that a node of size l has to be "opened" and "walked" (i.e. the cells inside it must contribute separately to the force summation) if

$$r > \frac{l}{\theta} \tag{3.65}$$

where r is the distance of the cell's centre of mass from the particle and θ is an accuracy parameter which plays the role of an angle of view. Clearly, the accuracy in the force calculation depends also on the criterion used to decide whether or not a multipole estimate is a good approximation at the point of interest. A particularly delicate issue is the force resulting from an almost homogeneous mass distribution, for instance from the density field at high redshifts; in this case single contributions tends to cancel each other and a relative small error can end up in a significant relative error in the final results. The criterion shown above does not guarantee a sufficient accuracy, so that other conditions must be fulfilled. We leave a complete discussion to Springel et al. (2001), Springel (2004).

As a final note, we remind that GADGET leaves to the user the choice whether to use a PM+TREE or a pure TREE code evaluation of the gravity force (note that in the earlier versions of the code only the second choice was allowed as described in Springel et al. (2001)).

3.4.2. Hydrodynamics

GADGET use the SPH technique to account for the ideal gas physics, so that we will refer to the equations given in Sec. (3.3). GADGET implements SPH in its fully–Lagrangian form, thus allowing each particle to have its own resolution through an individual h_i parameter and its own time–step as for the time integration. The early versions of the code neglected the ∇h terms (see Sec. (3.3.3)) in the SPH equations, while the current advanced version fully include them by using equations derived from the Lagrangian

$$L(\mathbf{q}, \dot{\mathbf{q}}) = \frac{1}{2}\sum_{i=1}^{N} m_i \dot{\mathbf{r}}_i^2 - \frac{1}{\gamma - 1}\sum_{i=1}^{N} m_i A_i \rho_i^{\gamma - 1} \tag{3.66}$$

where the independent variables are $\mathbf{q} = (\mathbf{r}_1, \ldots, \mathbf{r}_N, h_1, \ldots, h_N)$, the thermal energy acts as a potential driving the motion of SPH particles and density is a function of $\mathbf{q}$s following equation Eq. (3.34) (see Springel & Hernquist 2002). The fully conservative nature of this approach also relies upon a fixed mass being contained in the smoothing volume of particles, i.e. $(4\pi/3)h_i^3\rho_i = M_{SPH}$ where $M_{SPH} = \bar{m}N_{SPH}$ roughly relates M_{SPH} to the average mass of particles and to the desired number of neighbours. The equation of motion, having adopted the kernel symmetrization as in Hernquist & Katz (1989), results in

$$\frac{\mathrm{d}\,\mathbf{v}_i}{\mathrm{d}t} = -\sum_{j=1}^{N} m_j \left[f_i \frac{P_i}{\rho_i^2} \nabla_i W_{ij}(r_{ij}, h_i) + f_j \frac{P_j}{\rho_j^2} \nabla_i W_{ij}(r_{ij}, h_j) \right] \tag{3.67}$$

where the factors f account for the h variation effects. From the above equation Springel and Hernquist (2003a) derive the form

$$f_i = \left(1 + \frac{h_i}{3\rho_i} \frac{\partial\,\rho_i}{\partial h_i} \right)^{-1}. \tag{3.68}$$

As for the description of the shocks, an artificial viscosity is then added (Navarro & Steinmetz 1997), with the corrections suggested by Balsara (1995) in order to strongly reduce the undesired shear viscosity (see also section 3.3.5).

GADGET also offers the possibility to activate an artificial viscosity which varies with local environmental conditions (e.g. Morris & Monaghan 1997) through a parametrical time–varying factor α which grows when the particle enters a shock and decays otherwise. We refer the reader to cited papers on GADGET for further details.

3.4.3. Time Integration

When in the 1980's accelerator–physicists were integrating equations over 10^9 orbits, numerical violations of phase–space volume conservation became a delicate issue, as well as in studies about the long–term stability of the solar system (Shadwick et al. 2000). This is related to the Hamiltonian nature of the system which is studied and the existence of a "non–trivial *structure* that embodies important physical properties which can affect the *qualitative* behaviour of the system" (quoted from Shadwick et al. (2000)). Here "structure" must be interpreted in a broad sense: for instance it could be the conservation of phase–space volume for Hamiltonian systems, the existence of some constant of motions like energy, momentum etc.

As for these systems, we can think that a given real solution live on a n–surface: then, numerical errors can be thought to be a *tangent* or a *normal* deviation to this surface. Errors from the normal deviations will violate the structure of the system then representing a *qualitative* error as the found solution does not lie anymore on the

correct n–surface. Tangent deviations, instead, just represent a *quantitative* error in the integration of he system equations.

in order to suppress the first kind of errors ('normal' errors), one resorts to the so–called symplectic integration schemes. A integration scheme is said to be symplectic when it preserves the phase–space structure of the system, or, in other words, represents a canonical transformation, so that the calculated solution live on the same surface at every time.

A second–order symplectic scheme commonly used, due to its simple implementation and low computational cost, is the Leap–Frog integrator (Quinn et al. 1997, Preto & Tremaine 1999). From a numerical point of view, a "symplectic integrator is an exact solution to a discrete Hamiltonian system that is close to the continuum Hamiltonian of interest" (quoted from Quinn et al.). Then, the integration will conserve an energy that is an approximation to the true energy of the system: if the difference is small, almost all the orbits that are stable in the real system will continue to be stable in the discrete representation.

Building a leap–frog scheme which allows each particle to have its variable timestep is a rather challenging task, since this breaks the fundamental requirement of time reversibility. With such a scheme, bouncing forward a step and then stepping backward will not end up to the same point. Nevertheless, some techniques to build a variable–stepping full reflexible leap–frog integrator have been introduced by (Quinn et al. 1997). They make use of a decomposition of the overall integration time in power–of–two subdivisions, then restricting the choice for the time step of the particle i at the step n to

$$\tau_i^n = \frac{\tau_{total}}{2^{k_i^n}}. \tag{3.69}$$

for some integer $k_i^n < K$ where $\tau_{total}/2^K$ is the minimum step allowed.

GADGET perform a symplectic leap–frog integrator; for further discussion and implementation details we refer to the various papers on the code mentioned above.

3.4.4. Additional Physics: I - Cooling

As the gas of the ICM is assumed to be in collisional ionization equilibrium (Cox & Tucker 1969, Cen 1992, Abel et al. 1997), we have at hand the possibility to estimate a *cooling function* which only depends on the temperature and density of a particle. The one used in GADGET model the emission from atom's excitations and de-excitations, ionizations and recombinations due to two–body collisions, bremsstrahlung and inverse Compton for a gas of primordial composition, i.e. made by Hydrogen and Helium with by–mass weights 0.76 and 0.24 respectively. This cooling curve has been calculated by several authors (e.g. Abel et al. 1997, Cen 1992).

The only difficulty that arises in including radiative cooling is that it could lead to extremely short cooling–times, namely the characteristic time required for the gas

to entirely radiate its internal energy at a given cooling rate. In this case of a cooling time shorter than the time–step, the energy of a very dense particle would become negative over the particle timestep. To obviate to this problem, the energy loss is treated semi–implicitly in an isochoric approximation and then added to the rate of change of internal energy due to adiabatic gas physics. The maximum cooling rate is restricted to half of the energy being lost in a single timestep (Katz & Gunn 1991).

3.4.5. Additional Physics: II - Multi–Phase ICM & Star Formation

Although today we are able to reproduce the large–scale ($\gtrsim 10\,\mathrm{Mpc}$) gravity–dominated structure of the Universe with a considerable high precision, modelling the local gasdynamical processes related to star formation (SF henceforth) remains a challenge. Our difficulties are due to a yet missing understanding both of the ISM complex structure and of the feedback mechanisms. For the time being computational resources do not enable us to have a dynamical range that allows a well–resolved ISM and a large volume to live in the same simulation. Therefore we are led either to explore some refined modelling of the ISM or to rely on a phenomenological model of the sub–resolution physics.

The common way to deal with such a model is to treat the gas as a single–phase fluid converted into stars with a given time–scale $t_\star$, usually a function of the local density through the local dynamical time–scale. Provided that, assuming an IMF, the expected energy feedback per formed star mass is easily obtained, it is not clear how this energy should be returned to the gas. Simply adding the energy to the internal energy of the gas has proven to be completely ineffective in regulating the SF for the energy being promptly dissipated by radiative cooling which is mostly effective in high–density regions. As a consequence simulations continue to suffer for an overcooling problem, namely the overlocking of baryons in a cold dense phase, which end up in too many stars being formed. Such and effect arise owing to the fact that cooling is a run–away process; when the gas cools it loose pressure support and tend to become denser; as the cooling roughly depends on the square of the density, this calls for a more efficient cooling and thus to a further lowering of the pressure support until the temperature reaches the $10^4\,\mathrm{K}$ limit of null ionization at which the cooling function set to zero (provided that we are not modelling further molecular cooling).

Several refinements or even different approaches have been tempted so far for (see e.g. Kay et al. 2002), but no one has proven to be resolutive. Highly artificial recipes, like constraining an adiabatic phase or a density lowering after the energy injection as well as extreme "blow–out" models with instantly redistribution of cold gas around the centre of gas clumps, have had the merit to point out how some physical processes could deserve a particular attention when a sub–grid model is implemented in a cosmological code.

Several attempts to make multi–phase models have been realize at the end of 90s, following the key theoretical work of McKee & Ostriker (1977). Springel & Hernquist (2003a) report about the model currently implemented in GADGET . We address the reader to this work as the ultimate reference for what we describe in the following. They started from few assumptions about the ISM in order to make an effective sub–resolution "hybrid" model that use spatially–averaged properties to describe the medium.

The fundamental step is to describe the ISM as an ambient "hot" gas with condensed cold clouds living therein. Pressure equilibrium is assumed to hold between these two components. The clouds represent as the reservoir supplying matter to the stars' birth. This reservoir is continuously fueled by gas cooling from the hot phase. Therefore the baryons are thought to be in one of the three allowed phases: the gas, the clouds and the stars whose densities are addressed respectively as ρ_h, ρ_c, and $\rho_\star$. These densities represent an average over small regions of the ISM as individual molecular clouds cannot be resolved.

The total gas density is $\rho = \rho_h + \rho_c$ since it is assumed that the regions used to define the averages are of constant volume. Therefore, writing the energy per unit mass of gas and clouds as u_h and u_c, the specific energy of the gas is $\epsilon = \rho_h u_h + \rho_c u_c$.

The three phases interact with each other exchanging mass by three mechanisms: the gas cools down to clouds, the clouds form stars and are evaporated by supernovae explosions due to the stars more massive than M_{up} threshold value (see Sec. 5.4) which restore mass and energy in the ambient gas. A pictorial view of the interplay among the phases is given in Fig. (3.1).

■ Star Formation

Clouds are expected to form stars over a characteristic time–scale $t_\star$ with basically a Schmidt (Schmidt 1959) law which reads:

$$\frac{\mathrm{d}\,\rho_\star}{\mathrm{d}t} = \frac{\rho_c}{t_\star}. \tag{3.70}$$

where ρ_c is the density of the cold phase from which star originate. If we assume that a mass fraction β of these stars will instantly explode (see sec. 3.4.5) as supernovae we can write

$$\frac{\mathrm{d}\,\rho_\star}{\mathrm{d}t} = \frac{\rho_c}{t_\star} - \beta\frac{\rho_c}{t_\star} = (1-\beta)\frac{\rho_c}{t_\star} \tag{3.71}$$

in this way SF depletes the reservoir of clouds and increase the mass of ambient gas with a rate $\beta\rho_c/t_\star$, because it is assumed that ejecta from supernovae are entirely accounted as hot gas. A discussion about the values of the parameter β (about 0.1 for a Salpeter IMF normalized in the mass range 0.1–100 $\mathrm{M}_\odot$) is left to section 5.4. If ϵ_{SN}

is the energy released by supernovae explosion per solar mass of formed stars, the gas heating results in

$$\left.\frac{\mathrm{d}}{\mathrm{d}t}(\rho_h u_h)\right|_{SN} = \epsilon_{SN}\frac{\mathrm{d}\,\rho_\star}{\mathrm{d}t_\star} = \beta u_{SN}\frac{\rho_c}{t_\star}. \tag{3.72}$$

where $u_{SN} = \epsilon_n\,(1-\beta)/\beta$. For a Salpeter IMF normalized in the mass range 0.1–$100\,\mathrm{M}_\odot$ and assuming that each supernova explosion provide 10^{51} erg, ϵ_n takes is about $3 \times 10^{1}5\,\mathrm{erg}$ per g per solar mass of formed stars.

■ Evaporation

The model assumes that at the surface of cold clouds the condensed gas evaporates when interacting with hot bubbles which inflate after the supernovae explosions. The total mass of clouds which undergoes a phase change is taken to be proportional to the mass in the supernovae:

$$\left.\frac{\mathrm{d}\,\rho_c}{\mathrm{d}t}\right|_{EV} = A\beta\frac{\rho_c}{t_\star}. \tag{3.73}$$

The evaporation efficiency A is a model parameter, with functional dependence on the density like $A = A_0\rho^{-4/5}$ (McKee & Ostriker 1977). The determination of th parameter A_0 is discussed in Sec. (5.5).

■ Cooling

Cooling is taken into account as we described in sec. 3.4.4. Furthermore, the model also includes the effect of thermal instability which operates in such a way that the mass flux between the hot and the cold phase is

$$\left.\frac{\mathrm{d}\,\rho_c}{\mathrm{d}t}\right|_{TI} = -\left.\frac{\mathrm{d}\,\rho_h}{\mathrm{d}t}\right|_{TI} = \frac{\Lambda(\rho_h, u_h)}{u_h - u_c}; \tag{3.74}$$

if the temperature and the total volume are kept constant during the cloud growth. As long as $u_h \gg u_c$, the internal energy of the clouds is unimportant for the model: typically a temperature $T_c \sim 1000\mathrm{K}$ is assumed but Springel & Hernquist (2003) report that results are not affected by this choice as long as $T_c \ll 10^4\mathrm{K}$, which is the minimum temperature allowed for the gas. This is the minimum temperature allowed for the gas since further cooling would require molecular modelling.
In general gas is expected to be thermally unstable if the cooling rate is a declining function of the temperature: in a primordial gas this is the case for $T \gtrsim 10^5\mathrm{K}$. For the onset of the thermal instability itself, a density threshold criterion introduced, thus requiring that $\rho > \rho_{th}$ for the gas at density ρ to become thermally unstable.

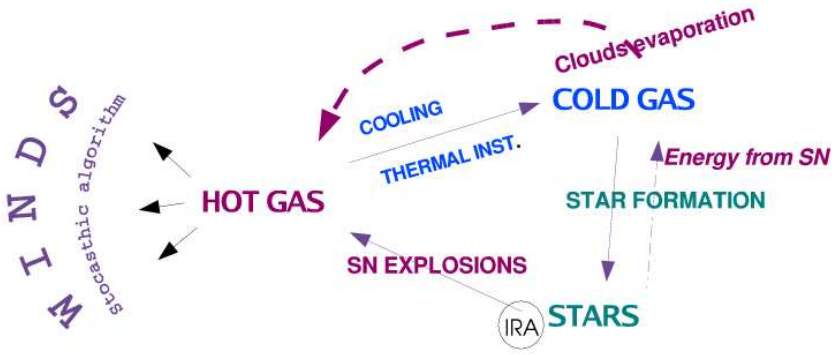

Figure 3.1: A pictorial view of the effective SF model described in Springel & Hernquist (2003).

Finally, if f is a switch between normal cooling ($f = 1$) and thermal instable regime ($f = 0$), the evolving rates of hot and cold masses can be written as:

$$\frac{\mathrm{d}\,\rho_c}{\mathrm{d}t} = -\frac{\rho_c}{t_\star} - A\beta\frac{\rho_c}{t_\star} + \frac{1-f}{u_h - u_c}\Lambda(\rho_h, u_h), \tag{3.75}$$

$$\frac{\mathrm{d}\,\rho_h}{\mathrm{d}t} = \beta\frac{\rho_c}{t_\star} + A\beta\frac{\rho_c}{t_\star} - \frac{1-f}{u_h - u_c}\Lambda(\rho_h, u_h). \tag{3.76}$$

where $\Lambda(\rho, u)$ is the cooling function. We define Λ_{net} function as the sum of the radiative cooling function and the heating due to UV background, and u_{SN} as $(1-\beta)/\beta\epsilon_{SN}$, or, otherwise, as a "supernova temperature" $T_{SN} = 2\mu u_{SN}/3k$ ($\sim 10^8$K for a Salpeter IMF and a supernova energy equal to 10^{51} erg). Thus, the energy budget of the gas is written as

$$\frac{\mathrm{d}}{\mathrm{d}t}(\rho_h u_h + \rho_c u_c) = -\Lambda_{net}(\rho_h, u_h) + \beta\frac{\rho_c}{t_\star}u_{SN} - (1-\beta)\frac{\rho_c}{t_\star}u_c, \tag{3.77}$$

Summing up all the contributions, two separate equations can be written for the energy of the hot and cold phase:

$$\frac{\mathrm{d}}{\mathrm{d}t}(\rho_c u_c) = -\frac{\rho_c}{t_\star}u_c - A\beta\frac{\rho_c}{t_\star}u_c + \frac{(1-f)u_c}{u_h-u_c}\Lambda_{net}(\rho_h,u_h) \tag{3.78}$$

$$\frac{\mathrm{d}}{\mathrm{d}t}(\rho_h u_h) = \beta\frac{\rho_c}{t_\star}(u_{SN}+u_c) + A\beta\frac{\rho_c}{t_\star}u_c - \frac{u_h-fu_c}{u_h-u_c}\Lambda_{net}(\rho_h,u_h). \tag{3.79}$$

Since the first of the two is dropped out by the assumption that u_c is constant, it remains only to integrate the second one which now reads

$$\frac{\mathrm{d}\,u_h}{\mathrm{d}t} = -\frac{\beta}{t_\star}\frac{\rho_c}{\rho_h}(A+1)u_h + \frac{\beta}{t_\star}\frac{\rho_c}{\rho_h}(u_{SN}+(A+1)u_c). \tag{3.80}$$

It is easy to show the from the previous equation that u_h will tend to the equilibrium solution

$$u_h = \frac{u_{SN}}{(A+1)} + u_c \tag{3.81}$$

with deviations decaying over a time–scale

$$\tau_h = \frac{t_\star}{\beta(A+1)}\frac{\rho_h}{\rho_c}. \tag{3.82}$$

Thus if SF if rapid enough with respect to adiabatic heating or cooling the specific energy of the hot phase is retained to the value of Eq. (3.81), independent of $t_\star$. This value is $\sim u_{SN}/A$ if $A \gg 1$ and $u_{SN}/A \gg u_c$ as found usually.

A further interesting feature of this model is that it leads to a self–regulated cycle of SF when the growth of clouds is balanced by their evaporation owing to supernovae feedback. In such a regime the effective pressure of the medium

$$P_{eff} = (\gamma-1)(\rho_h u_h + \rho_c u_c) \tag{3.83}$$

is expected to be constant. This imply

$$\frac{\rho_c}{t_\star} = \frac{\Lambda_{net}(\rho_h,u_h)}{\beta u_{SN} - (1-\beta)u_c}. \tag{3.84}$$

Since $\Lambda_{net}(\rho_h,u_h) = (\rho_h/\rho)^2\Lambda_{net}(\rho,u_h)$ the ratio of masses in the two phases is

$$\frac{\rho_c}{\rho_h} = \frac{\rho_h}{\rho}y \tag{3.85}$$

having defined

$$y = \frac{t_\star\Lambda_{net}(\rho,u_h)}{\rho\,[\beta u_{SN} - (1-\beta)u_c]}. \tag{3.86}$$

The mass fraction locked in clouds turns out to be

$$x = \frac{\rho_c}{\rho} = 1 + \frac{1}{2y} - \sqrt{\frac{1}{y} + \frac{1}{4y^2}} \tag{3.87}$$

so that the effective pressure of the gas will be

$$P_{eff} = (\gamma - 1)\rho \left[(1 - x)u_h + xu_c\right]. \tag{3.88}$$

The time–scale provided by Eq. (3.82) is short compared to the SF characteristic time. This means that the conditions for self–regulation are met quite rapidly.

As for the numerical implementation, it is convenient to assume that conditions for the self–regulation of SF are always satisfied, so that the codings is greatly simplified. In fact it will not be necessary to store values for different phases and mass exchanges will not be explicitly stated. Moreover, the SF process is not described for each singular star but instead stochastically with expectation values consistent with the actual SF rate $\dot{M}_\star = (1 - \beta)xm/t_\star$ where m is the mass of the star–forming gas particle. If the timestep is Δt, a new "star" particle is created with mass $m_\star = m/N_g$ in the case a randomly generated number is lower than

$$p_\star = \frac{m}{m_\star}\left\{1 - exp\left[-\frac{(1 - \beta)x\Delta t}{t_\star}\right]\right\}. \tag{3.89}$$

N_g is an integer parameter which define the number of stellar population that a gas particle is allowed to spawn. If a star–forming gas particle has already formed $N_g - 1$ stars, it will entirely turn into a star particle.

This approach is quite mandatory to avoid an uncontrolled proliferation of particles that will take place if the star–particle creation of whatever mass were permitted. Also, this approach avoids an artificial dynamical coupling of the gas with the stars. Furthermore, allows us to trace the actual SF ages straightforwardly.

We refer the reader to the paper by Springel & Hernquist (2003a) for more details and discussions.

3.4.6. Additional Physics: III - Winds' Model

Along with the SF model reported in the previous section, Springel & Hernquist modeled the onset of winds due to injection of SN energy. Their phenomenology–cal recipe intends to mimic the mechanism of galactic outflows in analogy with Aguirre et al. (Aguirre et al. 2001b), but it serves also to account for the mass–loss of galaxies within simulations of clusterized halos although they are much less resolved than in

dedicated galaxy–forming simulations. It has proven to be very effective in extracting the gas which lie in the star–forming regions harbored in very dense clumps of particles..

The model for galactic winds can be summarized as follows. First, the disc mass-loss rate that goes into the winds is proportional to the SF rate, $\dot{M}_w = \eta \dot{M}_\star$. This assumption is based on the observational evidence ($\eta = 1$–5; (e.g. Martin 1999)) and tells nothing about the ability of this mass to escape from the potential well. Second, a fixed fraction χ of the feedback energy is used to kick out the mass, $1/2 \dot{m}_w v_w^2 = \chi \epsilon_{SN} \dot{M}_\star$. The value for χ ranges in the interval 0–1, although in the model it can be set to value larger than 1. In fact, this is just a phenomenological model and a precise energetic balance is neglected. Clearly this will lead to a violation of the energy budget, for the energy $\chi \epsilon_{SN}$ being used twice, once to ensure the pressure support to the hot gas and again to power winds. Owing to the uncertainties on the true value of ϵ_{SN}, this appears as venial sin in front of the complexity of re-adjust the parameters A_0 and $t_0^\star$. All in all, the velocity of winds is given by:

$$v_w^2 = 2 \frac{\chi}{\eta} \epsilon_{SN} \dot{M}_\star. \tag{3.90}$$

For the numerical implementation, a probabilistic method is exploited also in this case. A gas particle joins the wind during the time–step Δt if a random number is to be lower than

$$p_w = 1 - exp \left[- \frac{\eta (1 - \beta) x \Delta t}{t_\star} \right]. \tag{3.91}$$

The velocity vector of the gas particle then becomes

$$\mathbf{v}' = \mathbf{v} + v_w \mathbf{n}. \tag{3.92}$$

The direction n can be either a randomly chosen vector on the unit sphere, or the vector $\mathbf{v} \times \nabla \phi$, where ϕ is the potential field, so as to mimic the raising of fountains orthogonal to the galactic plane in spiral galaxies.
When wind particles depart from the inner parts of a star–forming regions, their kinetic energy is likely to be thermalized inside the region itself due to hydrodynamical interactions. To avoid this undesirable effect and let the wind particles freely escape from star–forming dense phase, a "decoupling" mechanism of the wind particles from hydrodynamical interactions is provided; a wind particle is then only included in gravity and density computation until either its density has fallen below $0.1 \rho_{th}$ or a time of 50 Myr has elapsed.

As described in Chap. (4), we insert in this model the contribution from the SnIIwhich are below the threshold mass M_{up} and from SnIa. In order to account for such energy, we basically add it to ϵ_{SN} in the previous equation.

3.4.7. Additional Physics: IV - Thermal Conduction

Jubelgas et al. (2004) report about their implementation of thermal conduction in GADGET , which is now a stable feature of the code.
As it is well–known, the problem is to describe the energy transfer by free electrons ought to the local heat flux given by

$$\mathbf{j} = -\kappa \nabla T \tag{3.93}$$

were $T(\mathbf{r})$ is the temperature field and κ is the heat conduction coefficient. In other terms, if u stands for the specific energy, the equation of interest reads

$$\frac{\mathrm{d}\, u}{\mathrm{d}t} = -\frac{1}{\rho}\nabla \cdot \mathbf{j} = \frac{1}{\rho}\nabla \cdot (\|\nabla T). \tag{3.94}$$

Spitzer, in his key book (1962), derived a classical result about the heat conductivity due to electrons in a fully ionised plasma in absence of magnetic fields: it reads

$$\kappa_{sp} = 1.31 \lambda_e n_e k \left(\frac{kT_e}{m_e}\right)^{1/2}. \tag{3.95}$$

In the previous equation, λ_e and n_e are the mean free path and density of electrons respectively. Since it is

$$\lambda_e n_e = \frac{3^{3/2}(kT_e)^2}{4\sqrt{\pi} e^4 \ln \Lambda} \tag{3.96}$$

approximating the Coulomb logarithm as in Sarazin (1988), one can write the relation

$$\kappa_{sp} = 8.2 \times 10^{20} \left(\frac{K_B T_e}{10\mathrm{keV}}\right)^{5/2} m_e \ \frac{\mathrm{erg}}{\mathrm{cm\ s\ keV}} \tag{3.97}$$

This expression for the Spitzer conductivity exhibits a strong dependence on the temperature. We just quote in the following the SPH equations found by Jubelgas et al., while addressing the reader to the references therein as for the effect of magnetic fields, observations and further discussions.

The straightforward SPH implementation of Eq. (3.94) – the one that is derived by differentiating the gradient of interpolated T multiplied by κ – demonstrates to be highly sensitive to the fluctuations in particle distribution. So that it is far better to follow the approach described by Brookshaw (1985, 1994) leading to the equation

$$\frac{\mathrm{d}\, u_i}{\mathrm{d}t} = \sum_j \frac{m_j}{\rho_j \rho_i} \frac{(k_j + k_i)(T_j - T_i)}{|\mathbf{x}_{ij}|^2} \mathbf{x}_{ij} \nabla_i W_{ij}. \tag{3.98}$$

For a recent application of this algorithm to simulations of galaxy clusters, see Dolag et al. (2004).

CHAPTER 4

THE NUMERICAL IMPLEMENTATION OF CHEMICAL ENRICHMENT

Chapter Outline

In this Chapter we give the details of our implementation of the stellar evolution, the supernova explosions and the production of energy and heavy elements. Before that, we review the SF algorithm of GADGET and the adopted stellar evolution model.

Introduction

Accounting for the effects of the stellar evolution will provide alternative ways to better understand and/or to constrain both the history of the star formation and the thermodynamical history of the ICM, so that the main aim of our work is to include a detailed description of the chemical enrichment process in simulations of galaxy clusters.

We choose to include such physics into the publicly–available state–of–the–art TREE–SPH code GADGET , that have been kindly provided in its most advanced

version to us by the author, Volker Springel; in Sec. (3.4) the main features of this code that are of interest for our work have been described and briefly discussed.

The GADGET original implementation only performs an "overall" production of metals by SnII with no delayed releasing of elements; as well no dependence of SF process on the metal content of the gas is included.

Instead, we implement a complete treatment of stellar evolution, fully accounting for the delayed production of elements and making the star formation process itself dependent on the energetics of supernovae explosions and gas metal content. A detailed description is given in the following sections.

In Sec. (4.1) we review how the SF is treated in GADGET ; in Sec. (4.2) we summarize the key assumptions of our implementations, which concern the stellar evolution model to which we refer, the IMF and how the formed metals reach the ICM. In the following sections, Sec. (4.3), Sec. (4.4), Sec. (4.5) and Sec. (4.6), we exactly review the stellar evolution, the adopted Initial Mass Functions and the spreading of supernoave ejecta on the gas particles surrounding the star particles. In particular, all the equations needed to compute the metal and energy production as a function of time are given in Sec. (4.4). We also have modified the cooling function and made the effective model for star formation dependent on the star formation energetics in a different way than in the original code; a full description is given in Sec. (4.7), Sec. (4.8) and Sec. (4.9). Finally, we account for the energy of SnIa in the wind model, as reported in Sec. (4.9).

The implementation of accurate stellar evolutionary models and chemical enrichment in the GADGET code discussed in this Chapter represents a further refinement of what discussed in the paper (Tornatore et al. 2004) and reported in several international workshops (e.g. **?**, **?**, **?**). All the details will appear in a paper (Tornatore et al. 2005) now in preparation.

4.1 Star Formation in Gadget

As we mentioned in Sec. (3.4), the star formation is not described "smoothly" but instead treated probabilistically as pioneered by Katz, Weinberg & Hernquist (1996). This means that we do not keep trace of the continuous star formation rate of each Gas Particle creating a Star Particle each time a star formation activity occurs. This would lead to an unmanageable large number of new particles. Furthermore, severe effects of two–body heating and mass segregation will arise because most of them would also have a mass much smaller than the mass of gas or dark matter particles. Instead, the code "spawn" a collisionless star from a Gas Particle each time some conditions are fulfilled. At the end of a large number of star formation events, the "true" star formation rate and history will be recovered by the creation of Star Particles. In the following, we will refer to particle representing "stars" in our simulations as "Star Particles" or "Stars",

whereas we will refer to real stellar object as "stars".

In the effective model for a multi–phase ISM implemented in GADGET , the star are formed from the cold gas of the cloud phase. The rate of gas locking in stars is estimated as

$$\dot{m}_\star = (1-\beta)\, xm/t_\star \tag{4.1}$$

where β is the fraction immediately returned to the hot–gas phase by the explosion of SnII, m is the mass of a Gas Particle, that comprise both the hot gas and the cold clouds (see Sec. (3.4.5) as for the definitions of both), x is the fraction of mass that is in the cold phase, so that xm is the mass of the reservoir for star formation. Furthermore $t_\star$ is the characteristic time for the cloud consumption, calculated as

$$t_\star(\rho) = t_0^\star \left(\rho/\rho_{th}\right)^{-1/2} \tag{4.2}$$

where ρ is the density of the Gas Particle, being $\rho = \rho_{cold}+\rho_{hot}$, ρ_{th} is a density threshold for star formation that acts as a physical cut–off threshold, and $t_0^\star$ is a parameter which give an overall star–formation time–scale as found by Kennicutt (1998). Both $\rho_t h$ and t_0^* have been introduced in Sec. (3.4.5). Constraints on both ρ_{th} and $t_0^\star$ have been discussed in 3.4.

This leads to a Schmidt–type law (Schmidt 1959) for the star formation rate

$$\dot{\rho}_\star \propto \rho^n \tag{4.3}$$

which with $n = 1.5$ has been widely used since the '50s as a gross estimate of the rate of star formation phenomenon in very different environments. Note that this functional form has also been commonly used in numerical simulations, with $t_\star$ estimated as the local dynamical time of the gas, $t_{dyn} = (G\rho)^{-1/2}$. From Eq. (4.1), we have $\dot{m}_\star = \alpha m/t_\star$ whose integration gives

$$m_\star = m\frac{\Delta t}{t_\star} \tag{4.4}$$

that would imply an unphysical result for $\Delta t \geq t_\star$. Instead, writing

$$\dot{\rho}_\star = -\dot{\rho}_g = \alpha\rho_g \tag{4.5}$$

with α having the dimension of a inverse of the time, this results in

$$\rho_\star(t) = \Delta\rho_g = \rho_g(t_0) * (1 - e^{-\alpha\Delta t}) \tag{4.6}$$

which can be read as the "probability" that a star mass density $\rho_\star$ were formed from a gas mass density ρ_g in the time interval Δt, equal to $(1 - e^{-\alpha\Delta t})$. Here α accounts here both for the local characteristic time of the star formation and for the fraction of density ρ_g prompt to be locked in stars, if any. So that, recovering the notation of Eq.

(4.1), the expected mass $m_\star$ to be formed from a star–forming Gas Particle of mass m is

$$m_\star = m \left\{ 1 - exp\left(-\frac{(1-\beta)x\Delta t}{t_\star} \right) \right\}. \tag{4.7}$$

Then, a Gas Particle is converted into a Star Particle when a random number, drawn in the interval $[0,1]$ with uniform probability, falls below

$$p = \left[1 - exp\left(-\frac{(1-\beta)x\Delta t}{t_\star} \right) \right]. \tag{4.8}$$

At the end of a reasonable number of star formation events, the Star Particle formation rate would recover stochastically the "true" star formation rate. The main advantage is that this will not lead to an uncontrolled proliferation of new particles and will keep constant the mass resolution of both Star and Gas Particles. Moreover, every artificial coupling of the collisionless star dynamics with the collisional dynamics of gas is avoided. This is not the case in the "hybrid scheme" (e.g.Katz et al. 1996) in which every Gas Particle carries on its own star fraction. What is also remarkable, is that it is straightforward to provide each Star Particle with its own formation time, so that the distribution of them directly relates to the star formation history.

In order to increase the mass resolution in following the star formation history, the above scheme has been slightly modified in the original GADGET code. This will also have some advantages as for the chemical enrichment as will be discussed. Instead of converting a whole Gas Particle of mass m into a Star Particle of equal mass, a finer representation can be obtained by converting a given fraction of gas: then, if $N_g^\star$ is the number of "stellar generations" that arises from each Gas Particles of mass m_0, then a Star Particle of mass $m_0^\star = m_0/N_g^\star$ is spawned from an eligible Gas Particle if a random number in the interval $[0,1]$ falls below

$$p = \frac{m}{m_0^\star} \left[1 - exp\left(-\frac{(1-\beta)x\Delta t}{t_\star} \right) \right]. \tag{4.9}$$

If a Gas Particle has a mass $m < (3/2)m_0^*$ or if it has already spawned $N_g^\star - 1$ stars, then it will be turned into a Star should it become eligible for. If $N_g^\star \gtrsim 1$ the total number of particles will of course grow, still it will be kept under control, while a reasonable constant mass resolution holds for the gas phase.

4.2 Implementing the Stellar Evolution

Given the scheme described above, we are provided with Stars each with its own mass and formation time, so that conceptually it appears straightforward to add the stellar evolution features to the code. We choosed a different approach than the fully stochastic

one by Lia et al. (2002), as we would like to describe in the most accurate way also the local evolution of metal enrichment along with its global properties. Hence, we choose to calculate exactly the evolution of each Star at each time and to restore the ejecta from supernovae into the gaseous phase as properly as possible. This approach should better ensure that the metal enrichment is described at a constant "metal resolution" even in stellar regions which are poorly resolved or as for the diffuse stars which are scattered outside "galaxies".

This task requires three assumptions about the pattern of star formation and evolution: the first one is the IMF with which the stars form, the second concerns the choice of a specific *stellar model* and the third one about the *spreading*, i.e. the mechanism with which the ejecta are returned to surrounding Gas Particles. In turn, the stellar model involves assumptions about the lifetime of a star, which is a function of its mass, and about the metal it produces during its life, basically a function of its mass and initial abundances of heavy elements. Each of these assumptions can be considered as a "free parameter" of the code, in the sense that to some degree we are allowed to change them to make our simulations fitting the observational data. In turn this provides constraints on each assumption, or even rule out some of them, what can be called a "backward approach". Alternatively, we can take some or all of them as firmly stated by physically grounded arguments from other fields of the (e.g. stellar evolutionary studies, chemical enrichment of the solar neighborhood etc.), taking out some conclusions about the ones left as "free" or, more likely, on our modelling of the physics, to improve it or to add other neglected physical effects that instead turn out to be important.

In the following sections we describe each one of the assumptions we made and the technique used to implement them.

4.3 The Stellar Evolution Model

In the framework of the standard Big Bang model we know that nucleosynthetic channels were acting during the primeval explosion so that the pristine gas were made up by a huge amount of Hydrogen (about 0.76 as for the mass fraction) and Helium (about 0.24) and traces of D, ^3He, ^4He and slightly heavier elements up to ^6Li, ^7Li. Due to Coulomb barriers and the lack of stable nuclei with mass 5 and 8 further nucleosynthesis has been prevented. This is what we refer to when talking about the "cosmological abundance".

Whereby, as far as we move within this picture, all the elements whom signatures we actually observe, and by whom we are made, must have been built by stellar nucleosynthetic activity. Therefore, at the heart of the study of the chemical enrichment of galaxy cluster are stellar evolution models and metal production networks from which we can derive the 'yields' for every single element. The term *stellar yield* is commonly

used to indicate the masses of elements produced and ejected by a star of initial mass m and metallicity Z.

Being this field not so well–known to people usually dealing with cosmology, in this section we briefly review the stellar evolution and nucleosynthesis, addressing the reader to cited references for a deeper glance of the matter.

We proceed by sketching the evolution of a single stars, then describing our adopted model as for both Supernovae (SNe) Type II and Type Ia (respectively SnII and SnIa hereafter). Then we introduce basic concepts as the Initial Mass Function (IMF) and the Star Formation Rate (SFR).

The history of a star is the history of the quest for equilibrium between the pressure supplied by its own internal energy and the gravitational force, which tends to collapse the gas. The internal energy of a star originates from nuclear reactions ignited when high enough density and temperature are reached.
Accordingly to their initial mass, stars evolve quite differently and have very different lifetimes. The "lifetime" of a star is defined as the time spent in the Main Sequence (MS) phase, i.e. when the hydrogen is burned in helium. Such a phase last for about 90% of the lifetime of each star (where lifetime is intended in strict sense). The lifetime of a star decreases with the initial mass, owing to the luminosity scaling as the fourth power of the mass:

$$L_{MS} \propto M^4. \tag{4.10}$$

Since the nuclear energy E_N is roughly proportional to the mass, the 'energetic' lifetime can be estimated by writing

$$t_{MS} \propto E_N / L_{MS} \propto M^{-3}. \tag{4.11}$$

As the initial mass increases, also the temperature and pressure in the inner regions increase and the star become able to proceed along successive nucleosynthetic channels, and ignite all the six main hydrostatic nuclear burnings (H–, He–, C–, Ne–, O– and Si–burning). After this, an inert Fe core is formed, owing to the well–known fact that the binding energy per nucleon reaches the maximum with the Iron nucleus. This limit is reached starting from massive stars ($M > 10 - 12\,\mathrm{M}_\odot$). Following (Iben & Renzini 1983) we individuate the following crucial mass ranges:

- *Low mass stars,* namely stars having mass $m \leq M_{HeF}$, where M_{HeF} is the limiting mass for the formation of an electron–degenerate He–core.
- *Intermediate mass stars,* namely the stars in the range $M_{HeF} \leq m \leq M_{up}$. M_{up} is the limiting mass for the formation of an electron degenerate C–O core.
- *Massive stars*, all stars with masses $m > M_{up}$

Other important limiting masses are M_L, the lowest mass needed as to ignite the H core, M_w, the limiting mass for the formation of a C-O white dwarf and M_{SnII}, the limiting mass for the occurrence of SnII Beyond this mass, a star either become a Wolf–Rayet star or implode as a black hole.

4.3.1. Low Mass Stars

Stars having $\mathbf{m < M_L}$ never ignite and, once they have radiated the energy stored during the slow gravitational collapse, stand as dark objects. A value for M_L which is commonly adopted by most models is $M_L \sim 0.08 - 0.09\,\mathrm{M}_\odot$. Stars in the range $\mathbf{M_L \leq m \leq 0.5}\,\mathrm{M}_\odot$ end their life as He–dwarfs, as they never become as much hot as necessary to ignite the Helium core. Finally, stars in the range $\mathbf{0.5}\,\mathrm{M}_\odot \leq \mathbf{m \leq M_{HeF}}$ evolve after the MS phase burning the Helium and becoming C-O dwarfs after passing along a series of intermediate phases. During these steps, the stars loose a fraction of their mass (a $\sim 1\,\mathrm{M}_\odot$ star becomes a C-O white dwarf of $\sim 0.6\,\mathrm{M}_\odot$) and this is the way they restore processed and unprocessed material into the Inter Stellar Medium (ISM).

4.3.2. Intermediate Mass Stars

Describing the complicate life of these stars is beyond the scope of this work, then we address the reader to, e.g. Matteucci (2003) and references therein for further reading. Here we only remind that the value of M_{up} is still strongly debated, as it is highly sensitive to the treatment of convection within the star. Classical stellar models give $M_{up} \simeq 7 - 9\,\mathrm{M}_\odot$, while other models indicate $M_{up} \simeq 5 - 6\,\mathrm{M}_\odot$. The value of M_{up} is also a non–monotonic function of the initial metal content of the star. In this work we choose the fiducial value $M_{up} = 8\,\mathrm{M}_\odot$.

4.3.3. Massive Stars

We defined above the massive stars as those which ignite Carbon non–degenerately. Stars in the range $\mathbf{M_{up} < m < (10 - 12)}\,\mathrm{M}_\odot$ ignite their cores and end as SNe of type II leaving a neutron star of $\sim 1.3\,\mathrm{M}_\odot$. Their final state is still debated. Stars in range $\mathbf{(10 - 12)}\,\mathrm{M}_\odot < \mathbf{m \leq M_{WR}}$ evolve through all the six main hydrostatic nuclear burnings and form an Fe-core, then exploding as *iron–core collapse Sn.* Here M_{WR} is the limiting mass for a Wolf–Rayet star, which is basically a star that has lost its H–He envelope. The explosion mechanism is still unclear, and is based on the principle of a core–bounce that occurs when the Fe-core, which is not burning, reaches the density of atomic nuclei. Stars having $\mathbf{M_{WR} < m \leq 100}\,\mathrm{M}_\odot$ can end as SNe but not of Type II as they are missing the H–He envelope, whereas SnII are characterized by H lines in

the spectrum. The limiting mass M_{RW} is not known exactly. For a solar metallicity, $M_{WR} \geq 40\,\mathrm{M}_{\odot}$.

4.3.4. Supernovae

We mentioned above that SnII arise from massive stars, namely from stars having mass $m \geq M_{up}$, where our choice is $M_{up} = 8\,\mathrm{M}_{\odot}$. Nevertheless, we never mentioned so far how Supernovae are classified. Basically, SNe are called *Type II* if they show strong Hydrogen emission lines in their spectra and *Type I* otherwise. In turn, SnIa are sub–classified as being *Ia, Ib* and *Ic*; such sub–types are defined by the properties of the early time photospheric spectra. Also SnII are sub–classified. Depending on the shape of their light curve, they are named SnII–L (linear), SnII–BL (bright linear) and SnII–P (plateau). We address the reader to the literature for further reading on this topic. From the viewpoint of the chemical enrichment, roughly speaking the SnIa are the main producers of Iron whereas the SnII produce the bulk of ^{14}N, ^{12}C (stars in range $M_{up} < m < 10 - 12\,\mathrm{M}_{\odot}$) and of the so–called α elements ^{16}O, ^{24}Mg, ^{28}Si, ^{32}S, ^{40}Ca etc.

SnIa represent a class of very homogeneous objects, so that they are good standard cosmic candles. They are thought to originate from white dwarfs in binary systems exploding by C–deflagration once they achieve the Chandrasekar mass by accretion from the companion. In spite of various debated details and uncertainties, there is a common consensus that SnIa originate from the thermonuclear disruption of a C-O white–dwarfs accreting H–rich material from a companion, such a disruption occurring when the C-O dwarf reach the Chandrasekar limit and ignite the Carbon.

■ Details on the Model for Supernovae Type Ia

As we have outlined above, the main spectroscopical features of SnIa are the lack of hydrogen lines and the presence of Si II lines together with a number of intermediate mass elements (Ca II, S II, O I) which dominates the spectra near the time of maximum light. In later phases the spectra are dominated by Iron. A general consensus has been reached on the general picture about the progenitor of SnIa; they are thought to origin from the thermonuclear disruption of a white dwarf (WD) which accreted material from a companion in binary systems. Actually, no firm conclusions have instead been reached about the nature of the companion (MS star, Red Giant star or another WD), the nature of the WD (C-O–, He–, O-Ne-Mg– WD), the mass reached by the exploding WD (Chandrasekar or sub–Chandrasekar) and the details of the explosion mechanism itself (delayed–detonation, detonation or deflagration). Nevertheless, it is commonly assumed that the best representation consists in a Carbon deflagration in a C-O WD of Chandrasekar mass. Among models which relates on such a representation, the most

common are the followings (for more details and references see e.g. the discussion by (Matteucci & Recchi 2001)):

a) *double–degenerate* The explosion is due to the merging of two C-O WDs; they approach owing to the energy loss by gravitational waves and then reach the Chandrasekar mass.

b) *single–degenerate* A WD reach the Chandrasekar mass after accretion from a nondegenerate companion. Only a narrow range of mass accretion rate leads to a stable accretion; otherwise, a nova explosion will occur and the Chandrasekar limit will not be reached.

c) A C-O WD explodes after accreting Helium from an He–star companion.

d) A recent model, based on the single–degenerate scenario, predicts metal-licity–dependent effects that stabilize the mass transfer. Nevertheless, it has to be yet tested.

In this work we assume the single–degenerate model, in whose framework the explosion timescale is given by the lifetime of the secondary. We choose the formulation by (Greggio & Renzini 1983) as for the characteristic masses of the system. The maximum allowed mass to form a C-O WD is $8\,\mathrm{M}_\odot$ (as for classic stellar model; ones whit overshooting predict lower values) and the smallest permitted secondary is $0.8\,\mathrm{M}_\odot$. Therefore the explosion timescales vary from $\sim 3 \times 10^7$ yrs to about the present age of the universe. The minimum mass of the whole binary system is $3\,\mathrm{M}_\odot$, to ensure that the WD and the companion are large enough to allow the WD with the minimum possible mass ($\sim 0.5\,\mathrm{M}_\odot$).
Hence, the explosion rate of SnIa is given by:

$$A \int_{M_{B,\mathrm{inf}}}^{M_{B,\mathrm{sup}}} \varphi(m) \left[\int_{\mu_{\min}}^{0.5} f(\mu)\psi(t-\tau_{m_2})\, d\mu \right] dm \tag{4.12}$$

The extremes of the outer integral are the minimum (M_{Bm}) and maximum (M_{BM}) mass of the binary system at a given time. We mentioned that the M_{Bm} lower limit is $3\,\mathrm{M}_\odot$. As for the upper limit of M_{BM} it is twice the maximum mass which form a C-O WD, thus $16\,\mathrm{M}_\odot$. At a given time, the limits of outer integral are given by:

$$\begin{aligned} M_{B,\mathrm{inf}} &= \max[2M_2(t), M_{Bm}] \\ M_{B,\mathrm{sup}} &= \tfrac{1}{2}M_{BM} + M_2(t), \end{aligned} \tag{4.13}$$

where $M_2(t)$ is the mass of those secondaries which are exploding at time t. We define $\mu = M_2/M_B$ as the ratio of the secondary mass over the total mass of the system and $f(\mu)$ as its distribution function, so that at each time the limit $\mu_{\min}$ of the inner integral

is set accordingly to the value of $M_2(t)$. Statistical studies (see (Matteucci & Recchi 2001) and references therein) indicate that mass ratios closed to 1 are preferred; the commonly adopted form for the distribution function $f(\mu)$ is then:

$$f(\mu) = 2^{1+\gamma}(1+\gamma)\mu^{\gamma} \tag{4.14}$$

where γ is a free parameter commonly set to $\gamma = 2$. As for the adopted lifetime function, we report it in Sec. (4.4).

4.3.5. The Star Formation

Despite the fact that most of the physics of the star formation process is still uncertain, a general framework has been drawn. Basically, once a cold clouds of gas is in place, having a large enough density, the formation of low mass stars proceed by fragmentation of those clouds and subsequent collapse of each piece. This is thought to be a self–propagating process; when the first star appears, they immediately produce a surrounding HII region, i.e. a volume within which the hydrogen is heated and ionized by the emitted photons. Then, the HII region starts expanding in the colder and less dense environment, thus inducing gravitational instability of gas in surrounding regions, thereby triggering the formation of new stars. Instead, the formation of massive stars is thought to be a secondary process as it implies a slow accretion in dense environments.

■ The stellar BirthRate and the Initial Mass Function

Once the star formation process begin, stars of different masses start to form. The number of stars whose mass lives in the interval m, $m + dm$ and formed in the time interval t, $t + dt$ gives the so–called birthrate function $B(m, t)$. Usually this function is written as the product of two independent function; the first, namely the Initial Mass Function $\varphi(m)$ (IMF) depends only on the mass m, and the second one, the Star Formation Rate $\psi(t)$ (SFR) is a function of time. Thus, the birthrate is written as

$$B(m, t) = \varphi(m)\psi(t)\, dmdt. \tag{4.15}$$

The current mass distribution of MS stars per unit sky area (the present day mass distribution, PDMF) in the solar neighbourhood, indicated with $n(m)$, can be written for stars having lifetime equal or larger than the age t_G of the Galaxy as:

$$n(m) = \int_0^{t_G} \varphi(m)\psi(t)\, dt. \tag{4.16}$$

Usually, $\varphi(m)$ is assumed to independent of time and thus:

$$n(m) = \varphi(m)\,\langle\psi\rangle\,t_G \tag{4.17}$$

where $\langle\psi\rangle$ is the average star formation rate in the past. For stars having lifetimes τ_m much shorter than t_G (i.e. $m \gtrsim 2\,\mathrm{M}_\odot$) we can write instead:

$$n(m) = \int_{t_G-\tau_m}^{t_G} \varphi(m)\psi(t)\,dt. \tag{4.18}$$

Supposing again that $\varphi(m)$ does not change with time, we derive:

$$n(m) = \varphi(m)\psi(t_G)\tau_m \tag{4.19}$$

if the assumption that the star formation rate at present time $\psi(t_G) = \psi(t_G - \tau_m)$ is valid. Stars with masses in range $1 - 2\,\mathrm{M}_\odot$ have lifetimes comparable with t_G so that we can apply neither of the two previous approximations. Therefore, the IMF in this mass range depends on the ratio between the present time SFR and the average mass of stars ever formed in the galaxy life, which is written as:

$$b(t_G) = \frac{\psi(t_G)}{\langle\psi(t_G)\rangle\,t_G} \tag{4.20}$$

Once the PDMF has been obtained from observations, one can derive the IMF using the previous equations and assuming a form for the SFR:

$$IMF = \begin{cases} PDMF/\left(\langle\psi\rangle\,t_G\right) & m_\star \leq 1\,\mathrm{M}_\odot \\ PDMF/\tau_m\psi(t_G) & m_\star \geq 2\,\mathrm{M}_\odot \\ PDMF/\int_{t_G-\tau_m}^{t_G}\psi(t)\,dt & 1\,\mathrm{M}_\odot < m_\star < 2\,\mathrm{M}_\odot \end{cases} \tag{4.21}$$

Many authors have shown that the best approximation of the IMF in the solar neighbourhood is given by a power law:

$$\varphi(m) = A_\varphi m^{-(1+x)} \tag{4.22}$$

which is supposed constant in time and space. The normalization constant A_φ is obtained imposing the following normalization condition:

$$\int_0^\infty m\varphi(m)\,dm = 1. \tag{4.23}$$

The most popular and widely used IMF is that by Salpeter (1955), having the exponent $x = 1.35$. This IMF had been derived for masses in range $0.4\,\mathrm{M}_\odot \geq m \leq 10\,\mathrm{M}_\odot$ though it is generally employed in the range $0.1\,\mathrm{M}_\odot - 100\,\mathrm{M}_\odot$; the low mass limit

is imposed by the faintness of low mass stars, while the high mass limit is still uncertain. Spectroscopic analysis seems to indicate a limit of $100\,M_{\odot}$ (Matteucci 2003). Nevertheless, Scalo (1986) showed that a single power law is not a good approximation of the IMF and since his work power laws with mass–dependent exponents were preferred. The low mass tail is the main source of disagreement among different authors, as the observations are highly uncertain due to the faintness of these stars owing to the rapidly declining of their mass–luminosity relation. Discussion mainly concerns whether the IMF in this mass interval increases, flattens or even decreases.
Anyway, all the proposed IMFs have been derived from data coming from the solar neighbourhood and we do not know whether the IMF is universal or instead it does depends on the surrounding environment or even on time. Such dependences are highly unclear and no firm conclusions have been reached so far. Since in metal–poor environments the cooling efficiency is much smaller (see Sec. (4.7)), the temperature in such regions will be larger; therefore, the basic idea is that the formation of massive stars should be preferred as the Jeans' Mass should also be larger. A number of observational facts seem also to suggest that the IMF has suffered for variations with time (Larson 1998); among the others:

[**1**] the standard cosmological model predicts that the first stars formed in a non–enriched environment; nevertheless,no metal–free stars have been detected yet.

[**2**] Chemo–photometric calculations suggest that the ICM has been enriched by stellar populations composed by a larger fraction of massive stars than the local one.

[**3**] Simple models of chemical evolution predict an excess of metal–poor stars with respect to the observed number ("G–Dwarfs" problem).

We note that Larson (Larson 1998) has proposed recently an IMF which maintains the Salpeter shape at the high–mass end, while flattening below a characteristic mass which can also be made time–dependent to account for the evolution of the Jeans' Mass. We report this IMF in Sec. (4.3.5) as we have adopted it in some of our simulations (see Sec. (5.8)).

4.3.6. The Basic Equations of the Chemical Evolution

In this Section we briefly report the main equations for the stellar evolution and the chemical enrichment. We divide the discussion in two parts; in the first one we describe the *Simple Model* by Tinsley (1980), while in the second one we report our adopted equations.

■ The IRA Assumption

Basically, the Simple Model for the chemical evolution with a constant $\varphi(m)$ is valid for a volume in which the gas is homogeneous and the mass flux is null ("closed–box model"). Moreover, a key assumption is that at every time the produced elements are well–mixed. In the followings we use the notations defined here below; the mass fraction of gas is labelled by $\mu = M_{gas}/M_{tot}$, the total mass is defined as $M_{tot} = M_{gas} + M_\star$ and the metallicity is defined by $Z = M_Z/M_{gas}$ if M_Z is the mass in metals. The basic equation for the gas evolution is then given by:

$$\frac{\mathrm{d}\, M_{gas}}{\mathrm{d}t} = -\psi(t) + E(t) \tag{4.24}$$

where $E(t)$ is the rate at which enriched and non–enriched material is restored into the ISM; such quantity is given by:

$$E(t) = \int_{m(t)}^{\infty} (m - M_R(m))\, \psi(t - \tau_m)\varphi(m)\, dm \tag{4.25}$$

where $m(t)$ is the mass born at $t = 0$ and dying at time t, $M_R(m)$ is the mass of the remnant of a star of mass m and τ_m is the lifetime of the same star. Substituting Eq. (4.25) into Eq. (4.24) provide an integro–differential equation which can straightforwardly solved neglecting the stellar lifetimes in Eq. (4.25). Such assumption is named Instantaneous Reciclying Approximation (IRA).
The total mass fraction which is restored in the ISM by a stellar generation s defined by:

$$R = \int_1^{\infty} (m - M_R)\varphi(m)\, dm. \tag{4.26}$$

The mass of element i produced by a stellar generation *per solar mass of formed stars*, namely the *effective yield*, is defined by the following equations if $p_{Z_i(m)}$ is the mass fraction which ends in the newly produced and ejected element i by a star of mass m:

$$Y_{Z_i} = \frac{1}{1 - R} \int_1^{\infty} m p_{Z_i(m)} \varphi(m)\, dm. \tag{4.27}$$

Hence, we can rewrite Eqs. (Eq. (4.24), Eq. (4.25)) as:

$$\frac{M_{gas}}{t} = -\psi(t)(1 - R) \tag{4.28}$$

and

$$E(t) = \psi(t)R \tag{4.29}$$

so that we can write the equation of metals:

$$\frac{(ZM_{gas})}{t} - Z\psi(t) + E_Z(t) \tag{4.30}$$

having defined

$$E_{Z_i}(t) = \int_{m(t)}^{\infty} \left[(m - M_R)\, Z(t - \tau_m) + m p_{Z_i(m)}\right] \psi(t - \tau_m)\varphi(m)\, dm. \tag{4.31}$$

Note that the first term in square bracket accounts for the non–processed gas whereas the second term represents the newly formed elements. When neglecting the stellar lifetime τ_m, this equation become:

$$E_{Z_i(t)} = \psi(t)RZ(t) + y_{Z_i}(1 - R)\psi(t) \tag{4.32}$$

which admits the following analytical solution:

$$Z_i = y_{Z_i} \ln\left(\frac{1}{\mu}\right). \tag{4.33}$$

■ Numerical Models for Metal Enrichment

The Simple Model that we have presented in the previous Section has the serious drawback of neglecting the stellar lifetimes; as this hypothesis may be acceptable when dealing with massive stars, whose lifetime is in fact negligible compared with the evolution time of the system, it is no longer a good approximation approaching stars of intermediate mass, whose lifetimes are of the order of tenth or hundred of million years. Hence, to better describe the releasing of heavy elements, one must solve the following complete equation (Matteucci 2003) for each chemical specie, where σ_i is the surface mass density of element i in the gas and $X_i = \sigma_i/\sigma_{gas}$ is the abundance by mass:

$$\begin{aligned}
\dot{\sigma}_i(t) = -\psi(t)X_i(t) + \textstyle\int_{M_L}^{M_{Bm}} \psi(t - \tau(m))Q_{mi}(t - \tau_m)\varphi(m)\, dm + \\
A \textstyle\int_{M_{B,\mathrm{inf}}}^{M_{B,\mathrm{sup}}} \phi(m) \left[\int_{\mu_{min}}^{0.5} f(\mu)\psi(t - \tau_{m_2})Q_{mi}(t - \tau_{m_2})\, d\mu\right] dm + \\
(1 - A) \textstyle\int_{M_{Bm}}^{M_{BM}} \psi(t - \tau(m))Q_{mi}(t - \tau_m)\varphi(m)\, dm + \\
\textstyle\int_{M_{BM}}^{M_U} \psi(t - \tau(m))Q_{mi}(t - \tau_m)\varphi(m)\, dm.
\end{aligned} \tag{4.34}$$

Here below we give a short description of the meaning of each term. The quantity $Q_{mi}(t)$ is defined as $Q_{mi}(t - \tau_m) = Q_{ij}(m)X_j(t - \tau_m)$ is basically the same quantity

as $p_{Z_i(m)}$, though it accounts for the chemical composition of star to calculate the produced elements. This dependence is brought by Q_{ij} terms that are the entries of the *production matrix* which relates the production of element i to the presence of element j. The information on initial composition of stars dying now is contained in the factors $X_j(t-\tau_m)$ that describe the abundances of gas at the formation time of those stars.

$\boxed{-\psi(t)X_i(t)}$ This represents the locking of metals in stars, which are more and more enriched when subsequently forming in star–forming regions.

$\boxed{\int_{M_L}^{M_{Bm}} \psi(t-\tau_m)\ldots\, dm}$ This integral represents the enrichment due to the mass loss by low mass stars.

$\boxed{A\int_{M_{B,\mathrm{inf}}}^{M_{B,\mathrm{sup}}} \varphi(m)[\ldots\, d\mu]\, dm}$ This term accounts for the materials ejected by SnIa.

$\boxed{(1-A)\int_{M_Bm}^{M_{BM}} \psi(t-\tau_m)\ldots\, dm}$ This term gives the mass of metal restored by single stars ($m < 8\,\mathrm{M}_\odot$) not ending in SnIa–like binary systems or SnII ($m > 8\,\mathrm{M}_\odot$).

$\boxed{\int_{M_BM}^{M_U} \psi(t-\tau_m)\ldots\, dm}$ This last term accounts for the SnII explosions.

4.4 Detailed Equations for Metal Production

As we discussed above, our Star Particles are the stochastic representation of the star formation process, i.e. they depict the stars that formed over a time interval over a number of gas particles, or in other words within a space–time volume. Hence, we loose some information about the exact mass with which they formed at what exact time. This loss will define the resolution that we have in such a representation. As an example the left panel of Fig. (4.1) shows the time that elapse between subsequent samplings of star formation, as a function of the time of simulation, while the right panel of the same figure shows the ratio between the true star mass and the sampled one (solid line) and the same quantities integrated over time (dashed line), both again as a function of time. The graphview are taken from one of the simulations we present in Sec. (5.1), but can be considered as representative of the average case.

Then, the stochastic model of star formation "samples" the process in average each few million years and estimate the underlying stellar mass fairly well, as all along the simulation we have a scatter no larger than few percent. Only at the very beginning the sampling is relatively poor, due to the low number of star formation event at high

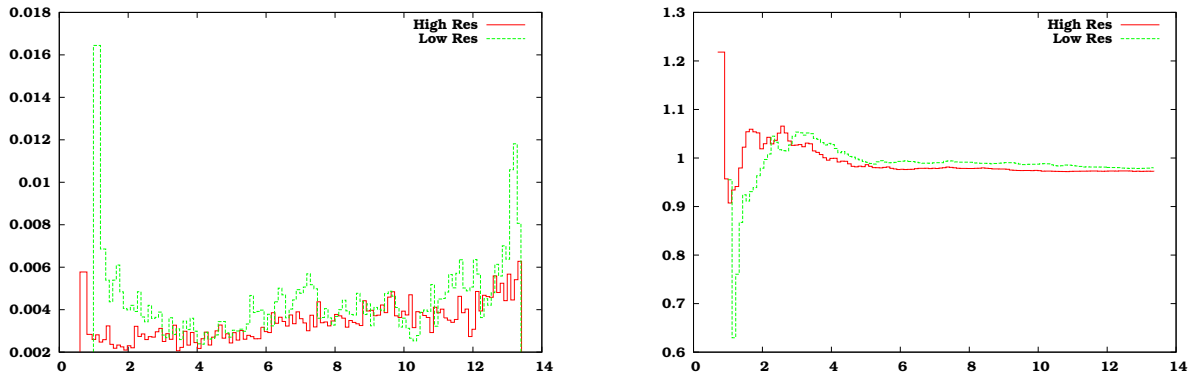

Figure 4.1: [**Left Panel**] The average time, in Million Years, that elapses between subsequent events of Star Particle creation. [**Right Panel**] The average ratio between the "true" stellar mass and the stochastic one ever formed at a given time. The x-axis for both panels indicate the Gyr elapsed from the birth of the universe, so that today is at the extreme right.

redshifts. For the same reason, the "time resolution" is a bit worse also at late times, the star formation rate is strongly decreasing.

In order to calculate the evolution of each Star Particle, we need to know the star formation rate underlying its creation. Since from the above discussion it descend that we cannot recover the real rate, we assume an impulsive SFR $\Psi(t) = \delta(t)$ for each Star Particle, that is equivalent to assume that all the considered stars which live into that particle are exactly coeval. Such an ensemble of stars is named a Single Stellar Population (SSP).

Here below we derive the form of the rate for both SnII and SnIa under this assumption, given that the Stellar Model we refer to is the one described in Sec. (4.4).

The last ingredient that we must provide is the stellar lifetime. This is a function of the star mass, the more massive stars having the shortest life. Several lifetimes have been proposed in the literature. Following (Matteucci & Recchi 2001) we choose to adopt the lifetimes given by (Matteucci & Padovani 1993). The analytical formula to calculate them is the following:

$$\tau(m) = \begin{cases} 10^{((1.338-\sqrt{1.790-0.2232*(7.764-log10(m))})/0.1116)-9} & m \leq 6.6\,\mathrm{M}_{\odot} \\ 1.2 \times m^{-1.85} + 0.003 & otherwise \end{cases} \tag{4.35}$$

Since the lifetime function affects both the rate of supernovae and the time–scale of stellar evolution, we expect the results to be sensitive to this choice. Therefore, we have also run simulations with a different lifetime function in order to check this sensitivity. As an alternative, we choose the lifetime function provided by Maeder & Meynet (1989):

$$\tau(m) = \begin{cases} 10^{-0.6545\log m+1} & m \leq 1.3\,\mathrm{M}_\odot \\ 10^{-3.7\log m+1.351} & 1.3 < m \leq 3\,\mathrm{M}_\odot \\ 10^{-2.51\log m+0.77} & 3 < m \leq 7\,\mathrm{M}_\odot \\ 10^{-1.78\log m+0.17} & 7 < m \leq 15\,\mathrm{M}_\odot \\ 10^{-0.86\log m-0.94} & 15 < m \leq 53\,\mathrm{M}_\odot \\ 1.2 \times m^{-1.85} + 0.003 & otherwise \end{cases} \tag{4.36}$$

As this equation predicts lifetimes for low–mass shorter than those from the formula by Padovani & Matteucci, we expect then to maximize the differences in the production of Iron–peak elements, that are the most direct indicators of the ICM metal enrichment.

In the following all calculations are made using the lifetime function given by Padovani and Matteucci, if not otherwise stated. We refer to their lifetime as "PM", whereas the lifetime from Maeder & Meynet is referred as "MM".

4.4.1. Computing the Supernova Type II Rates

Because the SnII originates from stars which are more massive than $8\,\mathrm{M}_\odot$ the rate with which they explode at the time t is simply given by the integral

$$R_{SnII} = -\int_{\tau^{-1}(M_U)}^{\tau^{-1}(M_{BM})} \varphi\left[m(t)\right] \Psi\left\{t - \tau[m(t)]\right\} \frac{d\,m(t)}{dt} dt \tag{4.37}$$

Here $\tau(m)$ is the lifetime function, so that $m(t) = \tau^{-1}(t)$ is the mass of stars exploding as supernova at time t. Because we are considering impulsive star formation rate, this becomes

$$R_{SnII} = \varphi\left(m(t)\right) \times \left(-\frac{d\,m(t)}{dt}\right). \tag{4.38}$$

4.4.2. Computing the Supernova Type Ia Rates

We remind that the number of SnIa exploding at time t is given by

$$R_{Ia}(t) = A \int_{M_{B,\mathrm{inf}}}^{M_{B,\mathrm{sup}}} \varphi(m_B) \int_{\mu_{min}}^{\mu_{sup}} f(\mu)\Psi(t - \tau_{m_2}) d\,\mu d\,m_B \tag{4.39}$$

where m_B is the mass of the binary system ranging in $M_{B,inf}$–$M_{B,sup}$, $f(\mu)$ is the distribution of the mass fraction of the secondary star in the binary system function for the secondary star, namely $\mu = M_2/(M_1 + M_2)$. A is the fraction in the IMF of

binary systems with the right properties to give rise to SnIa (see Sec. (4.3.4)); m_2 is the mass of the secondary star such that $\mu = m_2/m_B$ and τ_m is the lifetime for a star of mass m.

At a time t elapsed since the birth of the SSP, stars of mass m die having a lifetime τ that matches $\tau(m) = t$.

The inner integral

$$\int_{\mu_{\rm inf}}^{\mu_{\rm sup}} f(\mu)\Psi(t-\tau_{m_2})d\,\mu$$

gives how many binary systems of mass m_B have secondary stars of mass $m = \mu\, m_B = \tau^{-1}(t)$ so that we re–write it as

$$-\int_{\tau(\mu_{\rm sup})}^{\tau(\mu_{\rm inf})} f\left(\mu(t)\right)\delta(t-\tau_{m_2})\frac{\mathrm{d}\,\mu(t)}{\mathrm{d}t}dt \tag{4.40}$$

Taking into account the impulsive nature of Ψ, it results into

$$-f(\mu_{m_2})\frac{\mathrm{d}\,\mu_{m_2}}{\mathrm{d}t}, \tag{4.41}$$

that using $\mu = 2^{1+\gamma}(1+\gamma)\mu^\gamma$ with $\gamma = 2$ (e.g. Matteucci & Recchi 2001) finally gives

$$-24\left(\frac{m_2}{m_B}\right)^2\frac{1}{m_b}\frac{\mathrm{d}\,m_2(t)}{\mathrm{d}t}. \tag{4.42}$$

The rate of SnIanow reads

$$R_{SnIa}(t) = -\frac{\mathrm{d}\,m(t)}{\mathrm{d}t}\bigg|_{m_2\equiv\tau^{-1}(t)} 24\,m_2^2\,A\int_{M_{B,inf}}^{M_{B,sup}}\varphi(m_B)\frac{1}{m_B^3}dm_B. \tag{4.43}$$

For a power–law IMF of the type $\varphi(m) = A_\varphi\cdot\, m^{-(1+x)}$ the rate of Supernovae Ia is

$$R_{SnIa}(t) = -\frac{\mathrm{d}\,m(t)}{\mathrm{d}t}\bigg|_{m_2} 24\,m_2^2\,A\,A_\varphi\frac{1}{3+x}\left[M_{B,\mathrm{inf}^{-(3+x)}} - M_{B,\mathrm{sup}^{-(3+x)}}\right] \tag{4.44}$$

while for a Larson IMF, $\varphi(m) = A_\varphi\cdot 1/m\cdot(1+m/m_s)^{-x}$, the result is

$$R_{SnIa}(t) = -\frac{\mathrm{d}\,m(t)}{\mathrm{d}t}\bigg|_{m_2} 24\,m_2^2\,A\,A_\varphi\int_{M_{B,inf}}^{M_{B,sup}}\left(1+\frac{m_B}{m_s}\right)^{-x}\frac{d\,m_B}{m_B^4}. \tag{4.45}$$

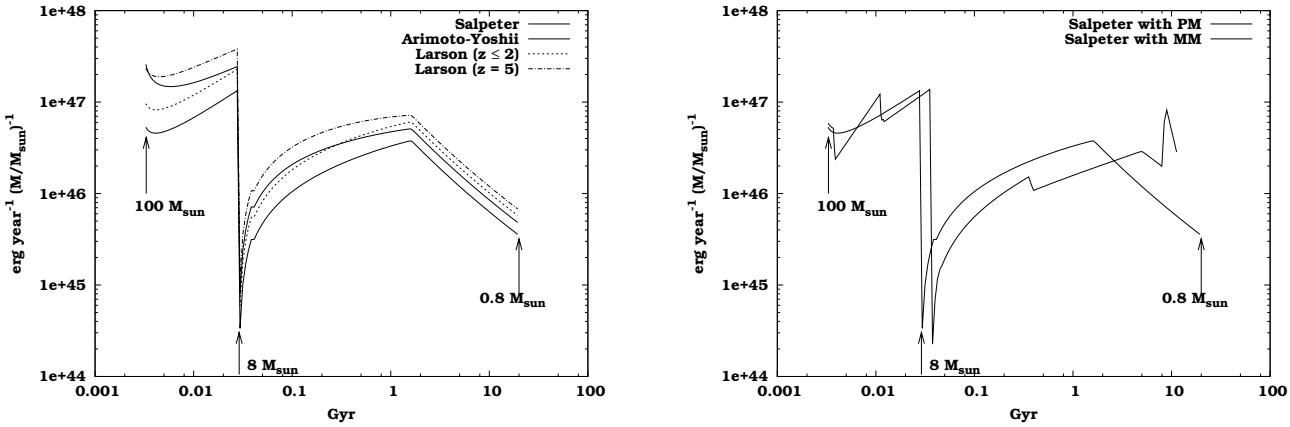

Figure 4.2: [**Left Panel**] The energy ejection rate for different IMFs due to both SnII (time range $[\sim 3 - \sim 28] \times 10^6$yr) and SnIa as a function of time. Arrows indicate the lifetime of labelled masses. [**Right Panel**] The energy ejection rate for a Salpeter IMF, using different lifetime functions; bold line indicates the rate given by using PM lifetimes and thin line that given by using MM lifetimes.

4.4.3. The Energy Ejection Rate

The above results (Eq. (4.39) and Eq. (4.43)) give the *number* of SnII and SnIa, exploding at the time t, per unit time for a stellar population of mass m. Then the energy ejection rate is immediately calculated as

$$R^e_{Sn} = e_{SnII} \times R_{SnII} + e_{SnIa} \times R_{SnIa} = e_{Sn} \times (R_{SnII} + R_{SnIa}), \tag{4.46}$$

once we assume that all supernovae eject the same amount $e_{Sn} = 10^{51}$erg of energy. In Fig. (4.2) we show this rate for different IMFs in the left panel and for the Salpeter IMF using the lifetime function given by PM and the one given by Maeder & Meynet ("MM" henceforth) (1989).

4.4.4. The Low–Mass Stars

Stars with mass below $8\,\mathrm{M}_\odot$ does not explode as SnII, and, if not exploding as SnIa, they terminate their life progressively fading. In the late stage of their evolution these stars loose their external envelope, then diffusing in the ISM the heavy elements that were in this region. Because this loss happens at the end of their evolution, one can calculate the rate of events in the same way as for the SnII. The only difference is that we have to multiply by a factor $(1 - A)$ in order to account for the fact that a fraction A ends up in binary systems from which the SnIa arise. Then, the rate is expressed by

$$R_{LM=}(1 - A) \times \varphi\left(m(t)\right) \times \left(-\frac{d\,m(t)}{dt}\right). \tag{4.47}$$

Since the fraction A usually amounts to few percent, the common usage is to ignore it in the previous equation.

4.4.5. The Ejection Rate of Metals

The "fallout" of heavy elements in the ICM is the consequence of the explosion of a supernova or of the mass–loss by a low-mass star. Therefore, in order to calculate the rate of pollution due to a stellar population we have to multiply the integrand in the previous rate–defining equations by the yields related to the element of interest. In this way, if we consider the element Z_i that is produced with a yield $y^X_{Z_i}(m)$, which is function of the star mass, the production rate of this element by each considered source X is given by

$$\begin{aligned} R^{Z_i}_{SnII}(t) &= y^{II}_{Z_i}(m(t)) \times \varphi(m(t)) \times \left(-\tfrac{d\,m(t)}{dt}\right) \\ R^{Z_i}_{SnIa}(t) &= -\tfrac{\mathrm{d}\,m(t)}{\mathrm{dt}}\Big|_{m_2 \equiv \tau^{-1}(t)} 24\, m_2^2\, A \int_{M_{B,inf}}^{M_{B,sup}} y^{Ia}_{Z_i}(m(t))\, \varphi(m_B) \tfrac{1}{m_B^3} dm_B \\ R^{Z_i}_{LM}(t) &= y^{LM}_{Z_i}(m(t)) \times \varphi(m(t)) \times \left(-\tfrac{d\,m(t)}{dt}\right). \end{aligned} \tag{4.48}$$

In Tab. (4.1) and Tab. (4.2) we list the yields adopted in this work for SnIa and SnII respectively. The yields for SnIa Tab. (4.1) are taken from the model W7 of Nomoto et al. (1997), the yields for SnII Tab. (4.2) are taken from the lowest–metallicity model of Woosley & Weaver (1995) and the effective yields for the low–mass stars are taken from Renzini & Voli (1981). As the latter yields stops at $m = 1$, we didn't extrapolate it down to $m = 0.8$, so that the minimum mass that give raise to SnIa progenitors is slightly different from standard assumption in our reference model (see Sec. 4.4). Nevertheless, the difference has a negligible impact on the final results.

As for masses beyond $40\,\mathrm{M}_\odot$ we choosed again to not extrapolate up to $100\,\mathrm{M}_\odot$ but to keep the $40\,\mathrm{M}_\odot$ yields also for larger masses. This could make some difference in final results, though this mass range account only for the high–mass tail where the IMF is rapidly declining. Considering a Salpeter IMF, stars with mass $m > 40\,\mathrm{M}_\odot$ represent a fraction as large as 2.2×10^{-4} and 0.037 respectively in number and in mass, while for an Arimoto–Yoshii these fractions amount to 1.96×10^{-3} and 0.15 respectively. As for the heavy elements production (see the right panel of Fig. (4.3)),

Remn	H	He	others	C	N	O	Mg	Si	Fe
1.4E+00	0.00E+0	0.00E+0	4.299E-1	4.83E-02	1.16E-06	1.43E-01	1.58E-02	1.50E-01	6.13E-01

Table 4.1: Yields for SnIa from Nomoto et al. (1997). Values are expressed in units of solar masses.

mass	$\sum M_{Z_i}$	H	He	others	C	N	O	Mg	Si	Fe
1	0.426	0.291	0.126	0.001921	0.000991	0.000873	0.00409	0.000281	0.000303	0.000541
2	1.188	0.814	0.345	0.002611	0.0093	0.00265	0.0113	0.000784	0.000845	0.00151
3	1.988	1.34	0.59	0.00246	0.0274	0.0043	0.0186	0.00131	0.00141	0.00252
4	2.794	1.82	0.864	0.01039	0.06	0.00583	0.0264	0.00184	0.00199	0.00355
5	3.6	2.23	1.2	0.01458	0.103	0.00821	0.0347	0.00238	0.00256	0.00457
6	4.6	2.79	1.63	0.00775	0.105	0.0123	0.0428	0.00304	0.00327	0.00584
8	6.6	4.08	2.31	0.00197	0.11	0.0173	0.0633	0.00436	0.00469	0.00838
10	8.7	5.4	2.95	0.10697	0.107	0.0255	0.0876	0.00574	0.00619	0.011
11	9.7	5.59	3.73	0.103	0.0532	0.0367	0.139	0.0121	0.0231	0.0129
12	10.7	5.96	4.11	0.1729	0.0815	0.036	0.218	0.0111	0.0927	0.0178
13	11.6	6.32	4.51	0.2309	0.115	0.0468	0.274	0.0228	0.0619	0.0186
15	13.6	6.98	5.24	0.33541	0.162	0.0541	0.684	0.00399	0.116	0.0245
18	16.3	7.89	6.28	0.4422	0.249	0.0569	1.13	0.0771	0.146	0.0288
19	17.1	8.08	6.46	0.412	0.285	0.0572	1.44	0.0459	0.285	0.0349
20	18	8.24	6.72	0.4317	0.214	0.0599	1.95	0.0495	0.3	0.0349
22	20.1	8.79	7.51	0.6262	0.242	0.0674	2.38	0.0624	0.382	0.04
25	23.1	9.4	8.64	0.8642	0.323	0.0795	3.25	0.162	0.339	0.0423
30	26.95	10.5	10.4	0	0.292	0.104	4.88	0.347	0.385	0.0446
35	31.3	11.5	11.9	1.0453	0.322	0.125	5.82	0.391	0.166	0.0307
38	31.8	11.3	12.4	1.1801	0.343	0.132	5.91	0.379	0.124	0.0319
40	32.5	11.1	13	1.3865	0.365	0.141	6.03	0.364	0.0801	0.0334

Table 4.2: Yields for SnII ($m \geq 8\,\mathrm{M}_\odot$) and Low–Mass stars ($m < 8\,\mathrm{M}_\odot$) from Woosley & Weaver (1995) and Renzini & Voli (1981). Values are expressed in units of solar masses.

in the considered mass range a Salpeter IMF will produce about the 22% of the total amount, while an Arimoto–Yoshii IMF will produce the 33% of the total amount.

Oxygen accounts for most of the metals produced, especially in the high–mass tail (see Fig. (4.3)); stars with $m \geq 40\,\mathrm{M}_\odot$ synthetize about 30% of the overall amount of Oxygen for a Salpeter IMF and an even larger fraction for a top–heavier IMF. Since these stars burn their nuclear fuel very quickly, exploding within few million years, this huge amount of Oxygen is promptly returned to the surrounding gas. Uncertainties on the yields in this mass range will also reflect on the ratio between the $\alpha-$elements and the Iron abundances in regions of recent or on–going star formation.

A natural way to extrapolate the yields for masses $> 40\,\mathrm{M}_\odot$ would be to keep them fixed at the value for $40\,\mathrm{M}_\odot$ stars. Using such extrapolated yields would increase the importance of very massive stars: the mass of Oxygen released grows up to 50% of the total oxygen produced and the overall fraction of metals raises up to 30%.

In summary, since our adopted yields do not extend beyond a given upper mass m_{th}, we prefer to assume their value to be constant for $m > m_{th}$ as this appears to be the least arbitrary procedure.

In Fig. (4.5) the ejection rates of both Oxygen and Iron are shown. Left panel shows the comparison between Salpeter and Arimoto–Yoshii IMFs, whereas the right

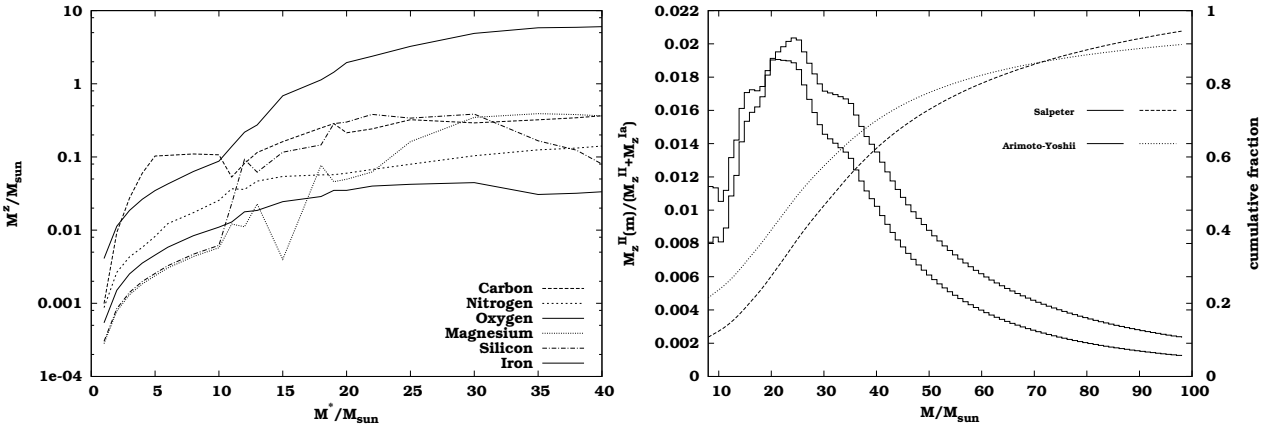

Figure 4.3: [**Left Panel**] The yields presented in Tab. (4.2). Note that the Oxygen dominate by an order of magnitude among the considered metals, and the negligible Iron production. [**Right Panel**] Continuous lines show the fraction of heavy elements provided by SnII as a function of mass both for a Salpeter (*bold*) and an Arimoto-Yoshii IMF (*light*), comparatively with all the elements provided by all SnII and SnIa; dotted and dashed lines show the cumulative contribution for a Salpeter and an Arimoto-Yoshii IMF respectively.

panel shows the effect of assuming different lifetime functions.

The effect of assuming the Arimoto–Yoshii IMF is evident most of all at high masses (which correspond to shortest time–scales to the left of the x–axis), but it is also significant as for the enrichment due to SnIa. In fact, as shown in Fig. (4.6), the Arimoto–Yoshii IMF falls below the Salpeter one only for $m \sim 1.8\,\mathrm{M}_\odot$, becoming the 26% lower at $m = 1\,\mathrm{M}_\odot$ while being two times higher for $m \geq 10\,\mathrm{M}_\odot$. Therefore the mass range where the Salpeter IMF dominates is essentially the one of dwarf stars that never explode. The net effect is a much higher metal ejection of the Arimoto–Yoshii IMF.

The same effect can be seen in Fig. (4.5), where the Salpeter IMF is compared to our adopted Larson IMF computed for $z \leq 2$ (Left Panel) and at $z = 5$ (Right Panel). Since this Larson IMF is heavier at higher redshift, the described effect is even enhanced, also owing the fact that the Larson IMF dominates over the Salpeter IMF down to very low masses (see the Right Panel of Fig. (4.6)).

As for the effect of using the lifetime function from MM, the variation is mainly important for SnIa, where the MM lifetimes for stars of $\sim 1\,\mathrm{M}_\odot$ are few Gyr shorter than the PM lifetimes do, and to concentrate the death of these stars in range $1\,\mathrm{M}_\odot \leq m \lesssim 1.3\,\mathrm{M}_\odot$ in a very narrow time interval around 9 Gyr.

If we account for stars in the mass range $0.8\,\mathrm{M}_\odot \leq m < 1\,\mathrm{M}_\odot$ and, at the same time, we use MM lifetimes, would maximize the amount of elements produced by SnIa. Instead, by using the PM lifetimes we miss all the elements produced by recently formed low–mass stars. Moreover, if we neglect stars with $m < 1\,\mathrm{M}_\odot$, we miss an additional

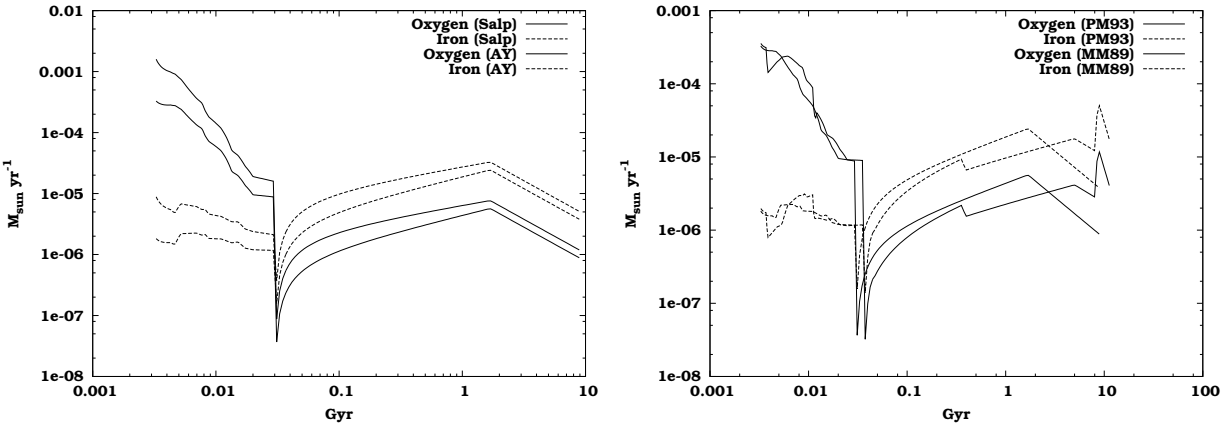

Figure 4.4: The ejection rate of Iron (*dashed lines*) and Oxygen (*solid lines*). **Left Panel** shows the comparison between a Salpeter (*bold lines/dashes*) and an Arimoto–Yoshii (*light lines/dashes*) IMFs and **Right Panel** the comparison between using PM and MM lifetimes.

fraction of Iron–peak elements. Still, the total mass of these missed metals turns is only about $2 - 2.5\%$ both for a Salpeter and for an Arimoto–Yoshii IMFs.

4.5 The IMF

As we outlined in Sec. (4.3.5), the IMF is defined as the number of stars ever formed per unit area per unit mass. In practical usage different than observations of projected quantities, the "area factor" will drop so that the IMF become the number of stars ever formed per unit mass interval, *in units of mass of the considered stellar population*, so that given a functional form

$$\varphi(m) = A\phi(m) \tag{4.49}$$

the following relation must be satisfied:

$$\int_0^\infty A\, m\phi(m)\, dm = 1. \tag{4.50}$$

This defines the normalization constant A *by mass*. As already stated, the most common form for $\phi(m)$ is a power–law like form $\phi(m) = m^{-(1+x)}$. Within this family of IMFs, the most common is the Salpeter (Salpeter 1955) one that has $x = 1.35$. As other slopes have not been yet ruled out, we treat the IMF as a parameter. In the following we will also consider more top–heavier IMFs like the Arimoto–Yoshii ($x = 0.95$) or other IMFs with a different functional form, like the one proposed by Larson (Larson 1998), having a time–dependent shape, as proposed by Finoguenov et al. (2003b).

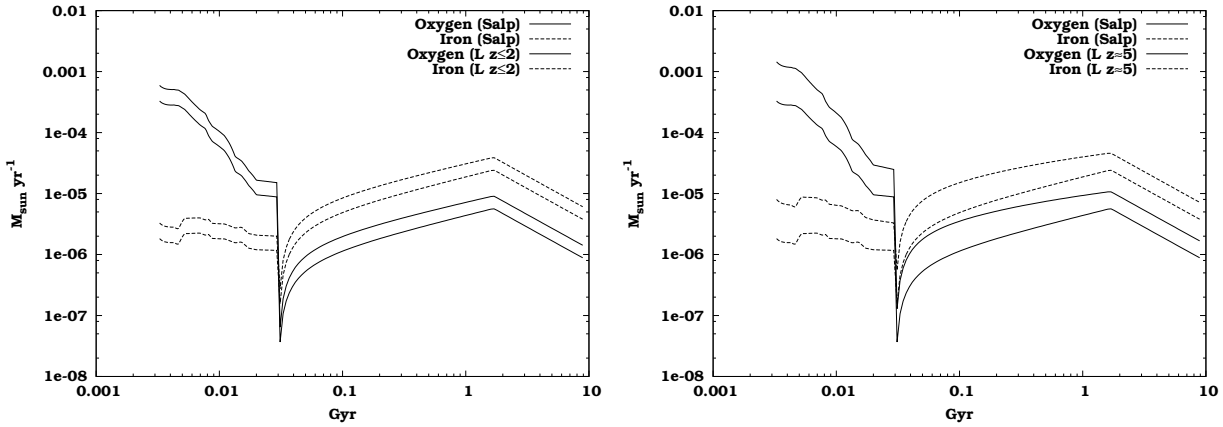

Figure 4.5: The ejection rate of Iron (*dashed lines*) and Oxygen (*solid lines*) for different IMFs. In both Left and Right Panels Salpeter/Larson IMFs are drawn in bold/light lines and dashes. In **Left Panel** the Larson parameter m_s is 0.35 ($z \leq 2$), in **Right Panel** it is set to 3.52 ($z = 5$).

Changing the IMF results significant differences in final results, for both the abundances of single elements and the ratios of abundances among different ones. Such variations are due to the different fraction of stars which lie in a given mass interval M–$M + dM$ when the IMF varies. In Fig. (4.6) we plot the IMFs used to run our simulations.

Finoguenov et al. (2003b) argued about the need of a strong IMF evolution at $z \gtrsim 4$ in order to reconcile the element ratios between groups and clusters of galaxies. Following Ferrara and Hernandez (2001), they take a Larson IMF

$$d\,\phi(m)/d\log m \propto (1 + m/m_s)^{-1.35} \tag{4.51}$$

and identify the characteristic mass scale m_s with the Jeans mass of the star–forming clouds, then making it dependent on the redshift at which the clouds are considered. They found that it is necessary to keep $m_s = 0.35$ constant below redshift 2 and impose a linear growth of $\log m_s$ from that epoch on. We take their results as an example of time–varying IMF, making m_s changing as

$$\log_{10}(m_s(z)) = \begin{cases} \log_{10}(m_{s,\,inf}) & z \leq z_{inf} \\ \dfrac{z - z_{inf}}{z_{sup} - z_{inf}} \times (\log_{10} m_{s,\,sup} - \log_{10} m_{s,\,inf}) & z_{inf} < z < z_{sup} \\ \log_{10}(m_{s,\,sup}) & z \geq z_{sup} \end{cases} \tag{4.52}$$

with

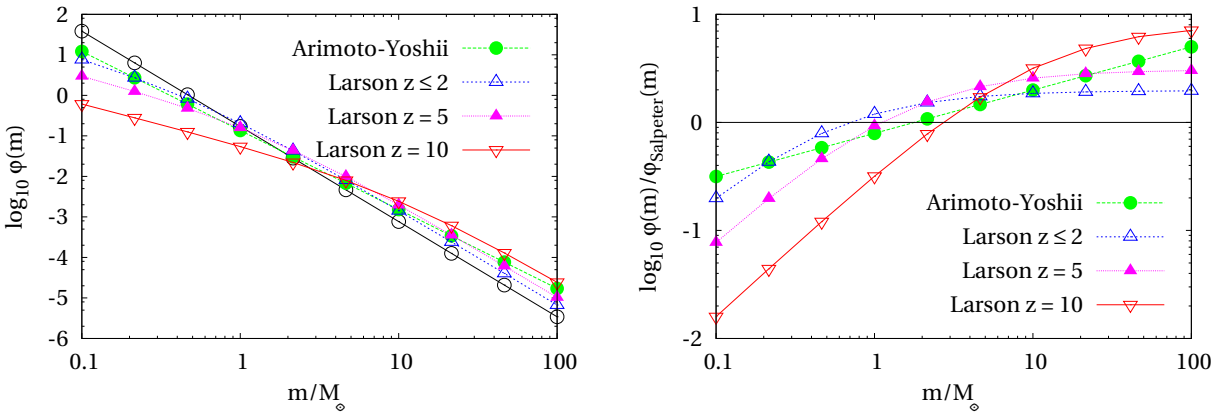

Figure 4.6: [**Left Panel**] Salpeter IMF is plotted (*solid line*) along with an Arymoto–Yoshii IMF and the Larson IMF of Eq. (4.52) for different redshifts. Note that the plot is by *number fraction*. [**Right Panel**] $\varphi_{\rm Larson}(m,z)/\varphi_{\rm Salpeter}(m)$ and $\varphi_{\rm AY}(m,z)/\varphi_{\rm Salpeter}(m)$ are plotted. It is clear how much the high–mass tail of the Larson IMF becomes more and more important at high redshifts.

$$
\begin{aligned}
z_{inf} &= 2 \\
z_{sup} &= 10 \\
m_{s,\,inf} &= 0.35 \\
m_{s,\,sup} &= 10
\end{aligned}
$$

In this way m_s is constant and equal to 0.35 and 10 respectively below $z = 2$ and beyond $z = 10$, and $\log_{10}(m_s)$ linearly varies at intermediate redshifts. Fig. (4.6) shows the obtained functions $\varphi(m)$ at some redshifts in the left panel, while the right panel shows how the number of stars falling the low–mass and high–mass tails changes with redshifts, with respect to the Salpeter IMF (straight line).

4.6 Metal–Enriching the Gas Particles

Once a Star Particle has been created, it starts to evolve accordingly with the model we have described above. Because each Star Particle is considered as a Single Stellar Population, we can straightforwardly apply the evolutionary equations presented in Sec. (4.2) for the metal production as well as for the energy ejection.

We outline here again that a Star Particles is a stochastic representation of the local star formation process surrounding the Gas Particle from which it originates. Hence, each of them "contains" the stars born in some volume during a typical interval of few million years (see Fig. (4.1)). We remind that the mean mass of a Star is $m_0^\star = m_0/N_g^\star$, being m_0 the mean initial mass of Gas Particles and $N_g^\star$ the number of Stars that each Gas Particle is allowed to form.
Therefore, at the typical resolution of our simulations, for $N_g^\star = 3$ each star particle has

an average mass of $\sim 10^{6.5-7}\,M_\odot$. Hence, we deal with object as massive as a very rich globular clusters or more, and have to distribute their products over the surrounding gas.

What is exact the meaning of "surrounding" remains fairly arbitrary. The most common and, to some extent, natural answer would be to translate it in the language of SPH. This means (1) to consider as "surrounding" all the Gas Particles which would contribute to the definition of the hydrodynamic properties of a Gas Particle that were in place of the considered Star, and (2) to make each neighbour Gas receiving a fraction of ejecta as large as its SPH weight, calculated using the same SPH kernel used for hydrodynamics.
This approach was suggested by Katz et al. (1996) and followed by later works. Obviously, this amounts to define some characteristic gas mass that receives the ejecta from Stars. This mass will be roughly equal to $N_n \times m_0$ if N_n is the number of neighbours. Using N_n equal to the neighbours number used for SPH calculations is in turn a natural choice in this framework.
In fact, N_n gives the mass–scale for the accuracy of lagrangian treatment of hydrodynamics. Still this has little or none to do with the "deposition" of supernovae ejecta for several reasons.
(1) Our Stars are not exactly the stars related to the star formation that is physically dependent on the hydrodynamics of the surrounding.
(2) How far the blast wave will penetrate the gas is more a matter of insterstellar medium physics than ICM physics. In other words, it involves length–scales that are about two orders of magnitude below the better spatial resolution of typical cosmological simulations. The extent of penetration, and then of deposition, is not immediately related to the SPH resolution.
(3) The SPH kernel assigns much more weight to very close neighbours than to the more distant ones, so that few Gas Particles receive most of the metals and of the energy. We expect this situation to take place in real Sn explosions, with nearby gas being more heated and enriched. However, in the stochastic representation of star formation we are somehow loosing information on the locality this process. For this reason, an equal weighting of all neighbors, independent of their distance from the SP, may be more consistent with our stochastic representation.

As at present there are no comprehensive studies about this topic, and it is unclear how and how far the results depend on the choice made. In the following we outline a discussion of this dependence.

■ The Theoretical Kernel's Weight Distribution

We show in Fig. (4.7) the SPH kernel that we use to run our simulations, as described in Sec. (3.3.1). The equal–weighting of the particles that we mentioned right above would be obtained by a Top–Hat (TH) Kernel, which assigns to all neighbour particles

a constant weight equal to $1/N_n$. Given the explicit expression of the TH kernel, in Fig. (4.7) it would be represented by a straight line at weight value of 1.

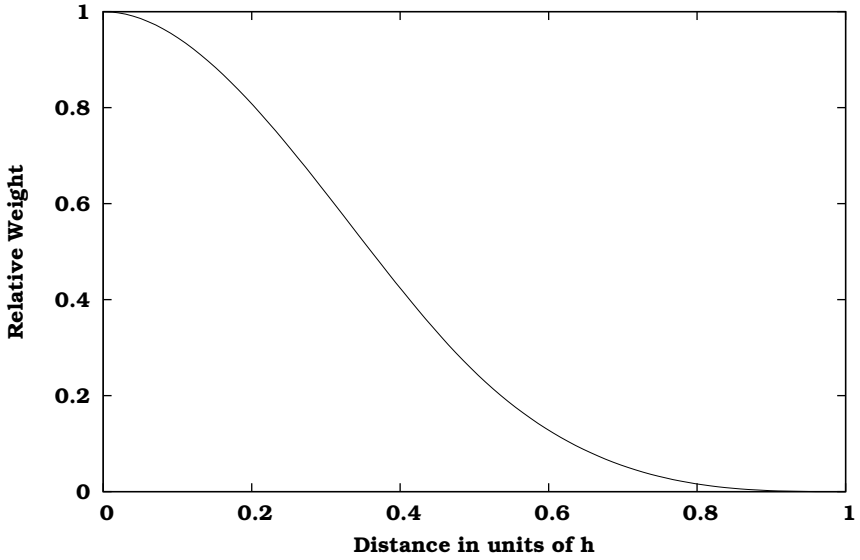

Figure 4.7: The cubic–spline SPH kernel used in simulations.

In order to assign its relative weight to a particle i that falls within the radius R_n enclosing the N_n neighbours, we have to calculate first the sum of absolute weights of all the neighbours, so that the relative weight is given by

$$w_i = \frac{K(r_i, h)}{\sum_{j=1}^{N_n} K(r_j, h)} \tag{4.53}$$

where $K(r, h)$ is the value of the Kernel function at the distance r and h is the measure of the Kernel support, i.e. roughly the distance of the most distant Gas Particle. Hence the relative weight of a particle is a function only of its distance from the Star. If we want to study how the relative weights distribute with respect to the relative distance of the particles, or with respect the relative mass enclosed within this relative distance, we must assume a distribution function for the Gas Particles. Assuming that each Particle has the same mass, or that no segregation effects are in place and Particles of different masses are well–mixed, this is equivalent to assume a density function for the gas. For the purpose of this discussion, we will model the density of gas around Stars simply as a power–law

$$\rho(r) = r^{\alpha} \tag{4.54}$$

so that $\alpha > 0$ will hold for Particles that tends to distribute over spheres around Stars, $\alpha = 0$ means a uniform distribution and $\alpha < 0$ for gas particles concentrated around Stars.

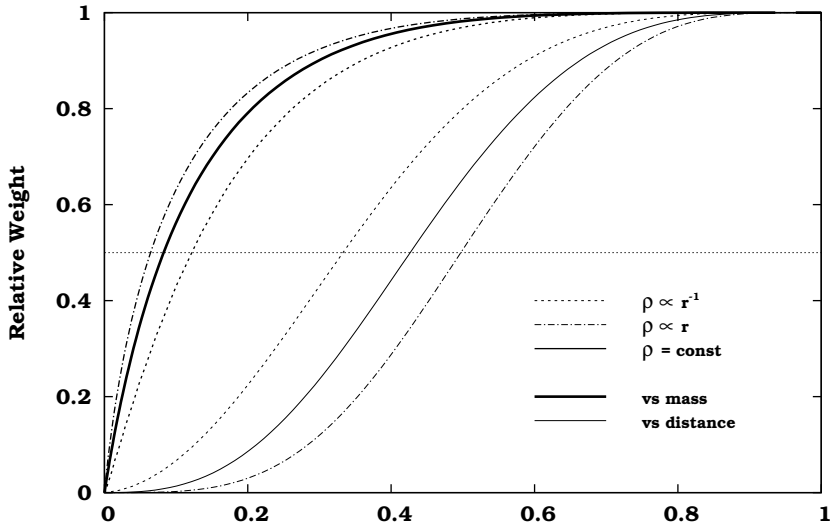

Figure 4.8: The relative weight distribution. Thick lines give the mass fraction which is receiving a given relative weight. Thin lines indicate instead the number fraction.

In Fig. (4.8) the three cases $\alpha = 1$, $\alpha = 0$ and $\alpha = -1$ are shown. The bold curves are the functions

$$f(\alpha, m/m_{Tot}, h) = \int_0^{r(m)/h} K(r,h) \cdot \rho(x) \cdot 4\pi r^2 dr = \int_0^{r(m)/h} K(r,h) \cdot 4\pi r^{\alpha+2} dr$$

where $r(m)$ is the radius which encompasses the mass m. It is convenient to deal with normalized quantities, so that hereafter we call r and m the fractions of radius and mass and, hence, h is identically equal to 1. Bold lines in Fig. (4.8) give the relative weight assigned to a given mass fraction. The thin lines are given by

$$f(\alpha, r, h) = \int_0^{r} K(r,h) \cdot \rho(x) \cdot 4\pi r^2 dr = \int_0^{r} K(r,h) \cdot 4\pi r^{\alpha+2} dr$$

and then give the relative weight falling within the radius r.

What can be immediately inferred is that the more concentrated is the gas, the larger is the mass fraction which receives a given fraction of metals (in what follows we

will use "weight", "ejecta" and "metals" as synonym). As the gas is more and more concentrated around the Star, the radius at which the integral of relative weights reach a fixed value decreases. On the contrary, for $\alpha > 0$, the mass which receives the same amount of metals is lower while the radius is larger. For instance, as α grows from -1 to 1, 50% of the weight is assigned to about 12% ($\alpha = -1$), to the $\sim 8\%$ ($\alpha = 0$) and finally to the $\sim 6\%$ ($\alpha = 1$) of the mass. Though the absolute values do not changes so much, the relative ratios are as large as a factor of two, and can become larger if gas become more concentrated. This does matter as we must reason in terms of particles, namely discrete numbers.

So far we used $\rho_{gas}(r)$ as a tracer of the Particle density $\rho_{pp}(r)$ under the assumption that all Particles have the same mass (or that different masses are well–mixed). It is worth to mention that, since we are interested precisely on the final effect about using SPH Kernel to spread over *particles*, we must take care to use $\rho(r)$ properly, that is rescaling h (i.e. the radius enclosing all the mass and then all the particles) in such a way that the total mass inside this radius be always the same as α changes; in fact we would take a given fixed number N_n of particles independently of $\rho_{pp}(r)$.

■ The Distribution of Weights in Simulations

We run few simulations in order to check to what extent the results on metal distribution are sensitive to the adopted spreading scheme. We address the reader to Chap. (5) for details about the runs; here it is sufficient to know that all simulations are homogeneous as for the implied physics, the only difference being the number of neighbours N_n (4, 32 and 128) and the Kernel used for the spreading (SPH or TH). The test simulations have been also run using two different mass resolutions, the higher being height times better than the lower. We will refer to such simulations using letters L and H for low and high resolutions respectively. The pedix will remind the value of N_n and apex the kernel used, so that L_4^S is a low–resolution simulation using $N_n = 4$ and the SPH Kernel, while H_{32}^T stands for an high–resolution run with $N_n = 32$ and the TH Kernel.

The resulting Iron profiles are reported in Fig. (4.9). The first line shows the lower–resolution results and the second line the higher–resolution ones. While the formers exhibit a remarkable instability as N_n and Kernel are changed, the H–results are instead stable and seem to have achieved a good numerical convergence.

Therefore, we are confident that our high–resolution results are not biased by the choice made as for the spreading.

If we consider the distribution of Gas Particles with the Iron abundance, as shown in Fig. (4.10), this conjecture is strongly supported. In fact, the distribution in high–resolution runs is basically independent of the choice made as for the spreading, while the abundances in low–resolution simulations are strongly affected by both changes of N_n and of the Kernel, in such a way that increasing N_n tends to flatten the distribution

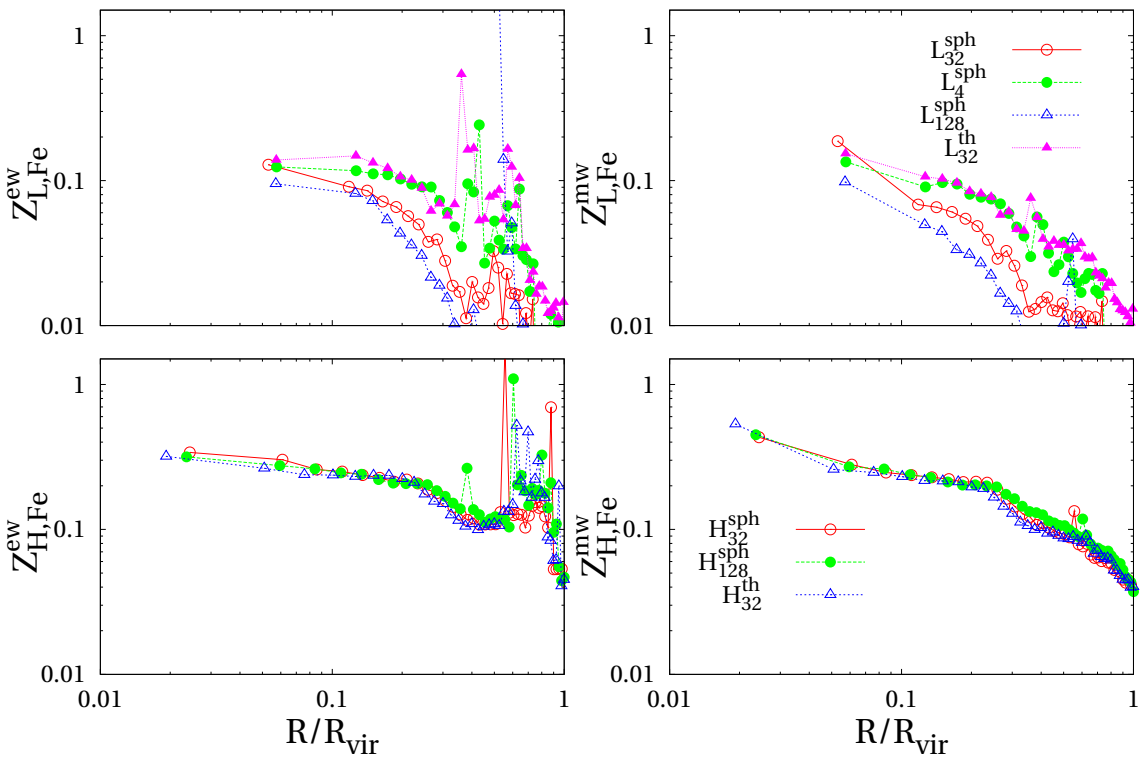

Figure 4.9: Profiles for Iron abundance (in solar units). The radius is in units of the virial radius. [**Top Panels**] show the *Low Resolution Runs*, and [**Bottom Panels**] show the *High Resolution Runs*. Profiles shown in [**Left Panels**] are emission weighted while the ones on [**Right Panels**] are mass weighted.

while stretching it towards low abundances and suppressing the high–Z tail.

When the TH Kernel is used instead of the SPH one, the mean Iron metallicity of the gas increases, and the very–low abundance tail is greatly reduced while the population with low and mean metallicity grows. The very–high abundance bins are rather stable as they lie in regions of very strong star–formation and high gas density, where the star–number to gas–number ratio is quite high.

A comprehensive analysis of such features are much less simple, and we do not go further in the matter. From the results shown here, we assume that our high–resolution results are not biased by the choice made as for the number of neighbours and the spreading. We defer a more detailed discussion to a forthcoming paper.

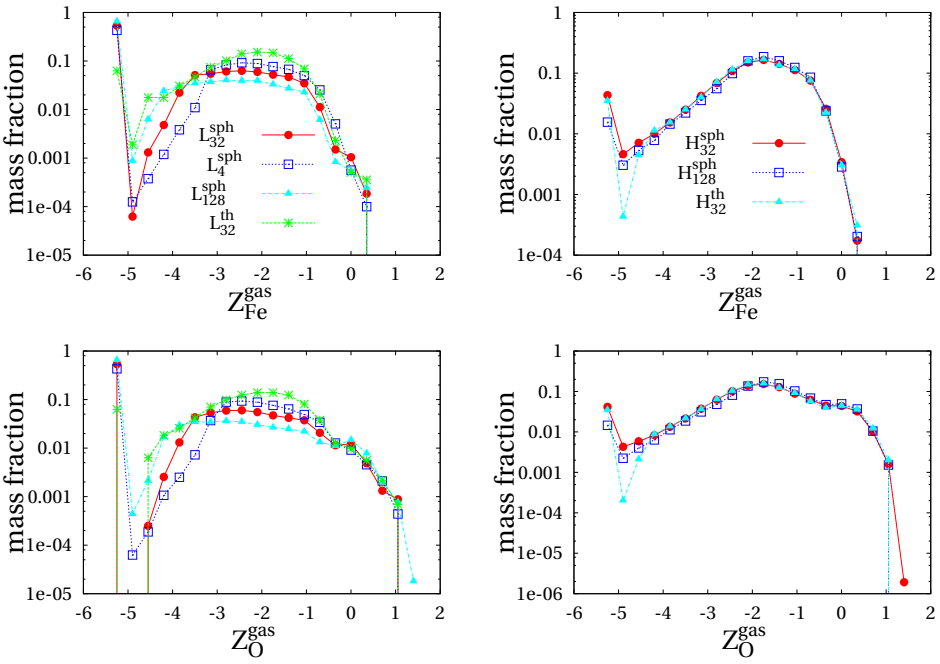

Figure 4.10: The gas mass distribution vs Fe (*Upper Row*) and O abundances (*Bottom Row*). Low resolution results are shown on the *Left Hand Side* whereas High resolution results are shown on the *Right Hand Side*.

4.7 The Metallicity–Dependent Cooling Function

Once the Gas Particles have been metal enriched, the physics governing their evolution will also change, basically for the net energy emission being far more efficient due to the line emission of heavy elements. The exact accounting of this effect would require to model the gas chemistry with as many elements as possible; nevertheless, using only few does not allow a proper modelling of the line emission and, on the other hand, increasing too much the number of traced metals would be unpractical as for the memory consumption. Hence, we decided to make use of the cooling curves modelled by Sutherland & Dopita (1993). An alternative would be to use the code mekal to calculate the emissivity due to 14 metals with real relative abundances, but we did not yet implemented it.

They calculated, as a function of the temperature, the bolometric emission for an enriched gas of solar composition, and indexed it with the Iron abundance. Then, in order to calculate the cooling of an enriched Gas Particle, we linearly interpolate the two curves referring to values of $[Fe/H]$ that include the value for the particle so that to obtain a fiducial value of its energy emissivity. The curves are shown in Fig.

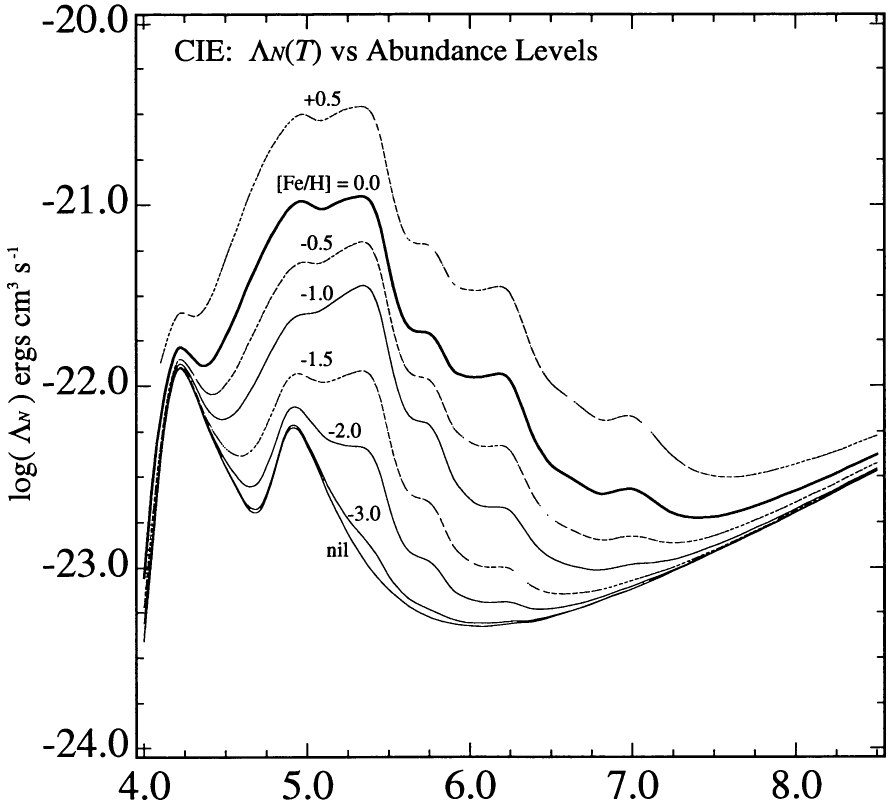

Figure 4.11: Figure from Sutherland & Dopita (1993). The emissivity curves of a low–density ionized plasma as function of temperature for different gas metallicities. Values for [Fe] are indicated by labels on curves.

(4.11). The cooling in presence of metals differs considerably from the cooling of a pristine non–enriched gas. As it has been shown, this turns out to be fairly important in removing low–entropy gas in the inner regions of clusters (see Chap. (2)).

One further important implication of using the metallicity-dependent cooling is that the density threshold for the onset of star formation is strongly decreased if the gas is metal–enriched, as a consequence of the higher efficiency with which the energy is radiated. To model this effect, we store in an array the values of the density threshold ρ_{th} for different metallicities of the gas, in the range $[-4{:}0.5]$ as for $[Fe]$. Values are calculated as in the standard effective–model. Then, during the simulation, each Gas Particle will form stars accordingly to the threshold pertaining to its own metallicity. The threshold is linearly interpolated using the array calculated ad the begin of run. A detailed description is given in Sec. (5.5).

4.8 The IRA Threshold

Having implemented what we have discussed in detail in Sec. (4.2), it would be straightforward to calculate exactly the evolution of each one of the Star Particles once all the ingredient of stellar model are given. Nevertheless, as we described in Sec. (3.4), the star–formation effective–model as implemented in GADGET requires an amount of energy to be promptly thermalized in the hot gas phase in order to achieve the self–regulation of this process. We note that something similar is likely to happen within real galaxies; since the star formation process is not instantaneous, the energy ejected by the first–born most massive stars will affect the ongoing process few million years after the first star formation episode. Furthermore, our Star formation has a limited time resolution (see Fig. (4.1)) then we do not describe the very early stages of stellar evolution.

Finally we choosed to consider some fraction of the stellar population being formed as istantaneously exploding. Namely the most massive, or short–living, stars are treated as in IRA assumption. That is to say that we allow the energy of those stars, as well as the metals they synthetized, to be promptly available in the Effective Model.

In more formal terms, let M_{th}^{IRA} be the threshold mass above which the stars are considered short–living and $\tau_{th}^{IRA} = \tau\left(M_{th}^{IRA}\right)$ the corresponding lifetime.

Depending on M_{th}^{IRA} a different amount of energy and metals are released at the epoch at which a Star Particle is created.
This could make significative differences as for the locking of metals in stars (see Sec. (5.4)).

The number of stars in the mass range $[8\,\mathrm{M}_{\odot} < M_{th}^{IRA} : M_{UP}]$ is easily calculated as

$$N_{th} = \int_{M_{th}^{IRA}}^{M_{UP}} \varphi(m)\, dm$$

Therefore, under our assumption of constant energy e_{Sn} per supernova, the energy released is

$$e_{th} = e_{Sn} \times N_{th}.$$

If $y_i(m)$ is the yield for the element i, the mass of that metal per solar mass of stars formed is given by

$$m_{Z_i}^{th} = \int_{M_{th}^{IRA}}^{M_{UP}} m\, y_i(m)\, \varphi(m)\, dm$$

or, using $Y_i(m) = y_i(m) \times m$, which are quantities tabulated in Tab. (4.2), by

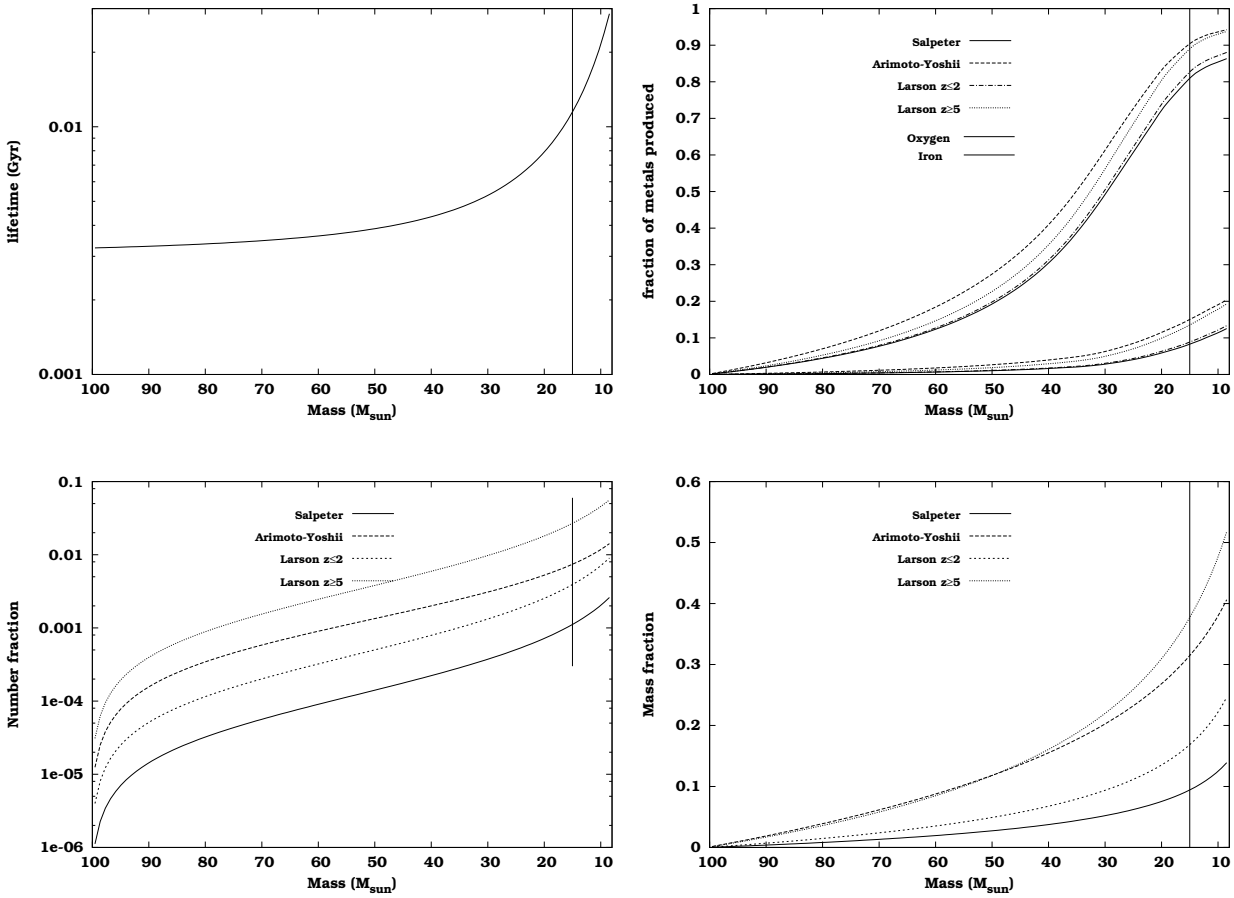

Figure 4.12: The vertical line indicates our choice for $M_{th}^{IRA} = 15\,\mathrm{M}_{\odot}$. [**Panel a**] We remind the lifetimes (using the PM) we are referring to. [**Panel b**] The fraction of Oxygen and Iron produced by stars up to a given mass. [**Panel c**] The number fraction of stars living in the mass range beyond a given mass. [**Panel d**] The mass fraction living in the mass range beyond a given mass.

$$m_{Z_i}^{th} = \int_{M_{th}^{IRA}}^{M_{UP}} Y_i(m)\,\varphi(m)\,dm.$$

Therefore, we must ensure that a Star calculates its evolution starting from M_{th}^{IRA} downto $1\,\mathrm{M}_{\odot}$, in order to avoid that short–lived stars are accounted twice. This is done (1) by delaying the onset of its evolution by τ_{th}^{IRA} and (2) by providing each Star with two different mass attributes. One, namely the initial mass *iMass*, stores the mass with which that SSP was formed, and the second attribute, namely the *mass*, is the actual mass the Star has at a given time. This actual mass keeps trace of the SSP evolution, decreasing as stars die and eject material. Therefore, when a Star Particle is created, its mass will be $f_{th} \times iMass$ if f_{th} is the mass fraction living beyond M_{th}^{IRA}.

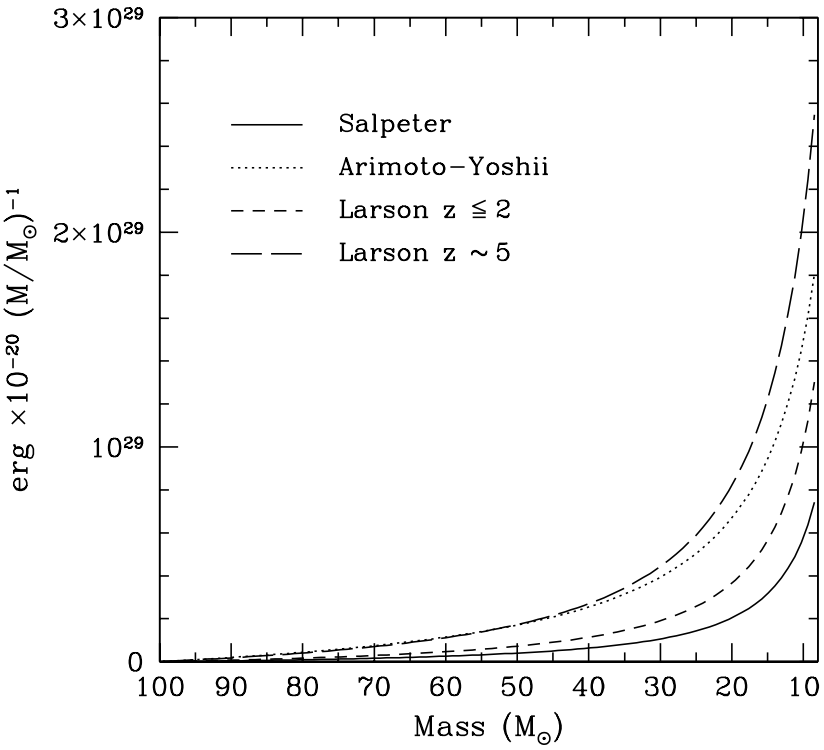

Figure 4.13: The energy released by the explosion of short–living stars as a function of M_{th}^{IRA}. The vertical line indicates the value of $15\,\mathrm{M}_\odot$ we used in simulations.

The metal abundance of a Star is equal to the abundance of the GP from which it has formed. Then, the metal content of the Star and the GP is proportional to the respective masses. In other words, if $m_{Z_i}^g$ is the mass of element i present in the gas at the moment of Star creation, and m_{Z_i} is the mass of the same element produced by the short–living stars, the Star will have a mass $m_{Z_i}^\star = m_{Z_i}^g \times M_\star/M_{gas}$ and the Gas Particle will have a mass $m_{Z_i}^g = m_{Z_i}^g \times (1 - M_\star/M_{gas}) + m_{Z_i}$.

In Fig. (4.12) we show the lifetime of a star as a function of its mass (upper left panel), and, for all stars living in the mass range beyond a given mass, the produced Oxygen and Iron (top right panel), the number fraction (bottom left panel) and the mass fraction (bottom right panel). Fig. (4.13) plots the energy per solar mass of stars formed which is promptly injected in the hot phase as M_{th}^{IRA} varies. These figures give an immediate impression about the fraction of mass, metals and energy that we are instantaneously recycling as a function of M_{th}^{IRA}.

Vertical lines shows the values at $M_{th}^{IRA} = 15\,\mathrm{M}_\odot$ that we choose to run our simulations. This choice was simply a compromise among different needs. From the one

hand, it is necessary to ensure a sufficient energy budget to the effective model in order to ensure the self–regulation of the star formation. On the other hand, we are working to avoid the IRA, so that we should push this value as higher as possible. The choice of $15\,\mathrm{M}_\odot$ keeps about half of the energy due to SnII in the instantaneous recycling approximation.

The parameter M_{th}^{IRA} affect the definition of fundamental quantities of the effective model through Eq. (3.71), Eq. (3.73) and Eq. (3.80) together with its equilibrium solution Eq. (3.81) (see Sec. (3.4.5)).

The dependence in Eq. (3.71) holds formally in order to obtain the heating of hot–gas heating by supernovae (see Eq. (3.72)). Nevertheless, when calculating the star mass using Eq. (4.1), we drop the factor $(1-\beta)$ as we do not need to model the mass loss in such a way. This dropping propagate also to Eq. (4.7) and (4.8).

The β parameter coincide with the mass fraction plotted in the bottom right panel of Fig. (4.12), and the u_{SN} parameter is related to both β and the energy per solar mass of stars formed, as shown in Fig. (4.13). Hence, the lower is the value of M_{th}^{IRA}, the lower are β and u_{SN}. As discussed in Sec. (3.4.5), Eq. (3.80), which described the evolution of the hot phase energy density, tends to an equilibrium solution, which is reached within some decaying time–scale. This time–scale, which is given by Eq. (3.82), tends to increase as β decreases. The mass–fraction β is now smaller, owing to the higher IRA mass–threshold, but just by a factor ~ 2. Furthermore, this decrease of β is somehow compensated by a shorter time–scale of star–formation, $t_\star$, due to the more efficient metal cooling. Therefore, we do not expect the decaying time for reaching the equilibrium solution to be now significantly different from that of the original effective model by Springel & Hernquist (2003a).

The two most crucial parameter which are affected by the choice for M_{th}^{IRA} are the value of density threshold ρ_{th} for the onset of star formation and the value of winds' velocity. Higher values of M_{th}^{IRA} gives a smaller energy budget. This leads to lower values for ρ_{th} thus causing star formation to start at higher redshift and to continue until very late times. The dependence of the wind velocity on M_{th}^{IRA} is shown in Fig. (4.14). This velocity is proportional to $(\epsilon_{SN})^{1/2}$ (see Eq. (3.92)). As it is proportional to the number fraction of short–living stars, plotted in the bottom left panel of Fig. (4.12), the value of v_w is rapidly declining as the the mass threshold grows from very low ($\sim 8\,\mathrm{M}_\odot$) values to extremely high ones ($\lesssim 100\,\mathrm{M}_\odot$). For this reason, we used instead a slightly different formula, calculating the winds' velocity as

$$v_w^2 \propto \frac{\beta_8}{(1-\beta_8)} u_{SN}.$$

instead of

$$v_w^2 \propto \frac{\beta}{(1-\beta)} u_{SN} = \epsilon_{SN}$$

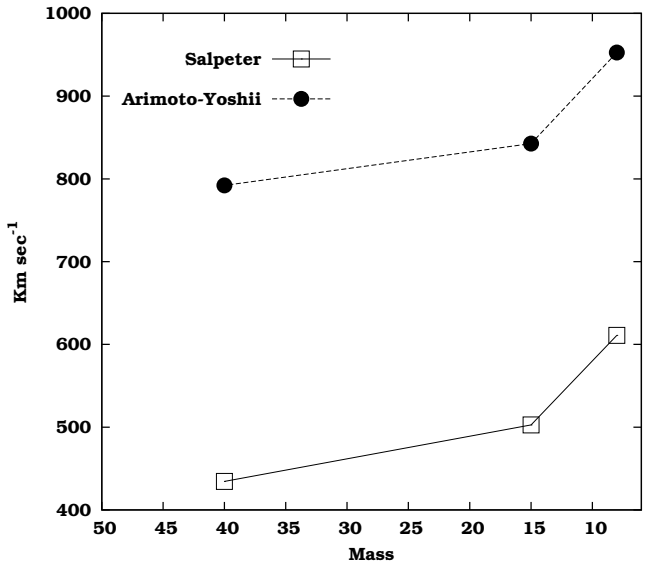

Figure 4.14: The different values our v_w will take as M_{th}^{IRA} range over $m > 8\,\mathrm{M}_\odot$. Continuous line refer to a Salpeter IMF and dashed lines to an Arimoto–Yoshii one.

In the above Eq. (4.8), β_8 is the value of β for $M_{th}^{IRA} = 8\,\mathrm{M}_\odot$. Accordingly, v_W changes now in a much narrower interval. Indeed v_w changes (for a Salpeter IMF) by about 40% when the threshold value varies from $40\,\mathrm{M}_\odot$ to $8\,\mathrm{M}_\odot$. Hence, we can increase IRA limiting mass while still having a reasonable winds' velocity.

We postpone to section Sec. (4.8) a more detailed discussion about how the results change varying M_{th}^{IRA}.

4.9 The Energy from Supernovae

When the supernovae explode they eject a large amount of energy along with metals and non–processed gas. Although several uncertainties in the modelization of supernovae explosions, a general consensus has been reached about a fiducial value of the energy $e_{SN} \sim 10^{51} erg$ due to a single supernova event. Since long time many different papers have been published on how this energy interacts with the Inter–Stellar Medium and deposits therein. However no firm conclusion has been reached so far (e.g. Thornton et al. 1998). From a numerical point of view, several attempts have also been made to model properly the feedback energy settlement into the gas. Basically, these models consist of mixed flavours of two main routes; the first, more simple, is to let the energy to be promptly thermalized, then suddenly raising the adiabat of the gas. The second route makes a fraction α of energy to end in bulk kinetic energy or in kinetic pressure, instead of thermal pressure, then calculating the thermodynamical quantities using

only the remaining $(1-\alpha)$ fraction. In this way, also "cold" gas may be sustaneid by pressure against gravitational collapse. More sophisticated models try to describe the multi–phase nature of the gas and have proven to give very interesting results as for the self–regulation of the star formation without reverting to artificial tricks ().

Within the framework of the multi–phase model implemented in GADGET , we modify the equations that define the model so as to include the extra–energy from the delayed supernovae explosions as an external energy source.

We remind that the code is fully adaptive also in time–stepping, so that each particle has its own timing as for the evolution and only few of them are evolving at each time–step; then we denote as *active* those particles which are evolving in a given time–step. When a Star evolves and spreads the produced metals and energy on the surrounding gas, the involved GPs are not in general active at the same time of the Star. Therefore, the thermodynamics of those GPs is not affected by this extra–energy that has to be stored in a reservoir. Thus, we add such a reservoir of energy to each gas particle, and we sum therein the contribution from all the interacting Stars until the Particle become active. Let us label as e_e this "external energy".

When the code handles the thermodynamics of a Gas Particles, it has to decide whether it is a multi–phase, star–forming particle or not. If conditions for the onset of thermal instability and multi–phase are not fulfilled (see Sec. (3.4.5)), the code reverts to a simple cooling routine. We choose to add the energy of the reservoir once the cooling has been done. In this respect, we tried different schemes, by adding energy before the cooling or half before and half after, and quite reassuringly, no differences are found. Instead, if the conditions for the on–set of star formation are satisfied, the code performs all the calculations described in Sec. (3.4.5). As we have to work with units of specific energy, while the reservoir has units of ergs, in the following we label the specific energy from the external source with $\epsilon_e = e_e/M$, being M the mass of the Gas Particle. This energy both heats the hot gas and evaporates cold clouds. Since we ignore the internal structure of the multi–phase gas, the best hypothesis we can do is that the specific energy amount pertaining to each phase is proportional to the mass in that phase. Therefore, if $M = M_{clouds} + M_{hot}$ is the total mass and x is the fraction of mass in clouds, $x\,\epsilon_e$ is the fraction of energy that evaporates clouds and $(1-x)\epsilon_e$ is the energy that heats the gas. Simply following the same line of reasoning as in Sec. (3.4.5), we must account for the external specific energy ϵ_e in the change of internal energy u_h of the hot phase. To this purpose, we rewrite Eq. (3.72) as

$$\left.\frac{\mathrm{d}}{\mathrm{d}t}(\rho_h u_h)\right|_{SN} = \epsilon_{SN}\frac{\mathrm{d}\,\rho_\star}{\mathrm{d}t_\star} + (1-x)\rho_h\frac{\epsilon_e}{\delta t} \tag{4.55}$$

where δt is the time interval during which the energy is deposited in the reservoir.We can re–interpret the added energy as if it were produced by some additional amount of supernovae. Then, the density of star formation rate which would be required is

$$\frac{(1-x)\epsilon_e}{\epsilon_{SN}} \cdot \frac{\rho_h}{\delta t} = \frac{\delta \rho^e_\star}{\delta t} \tag{4.56}$$

Since $\rho_c = x/(1-x)\rho_h$, the previous equation can be expressed in terms of $d\,\rho_c/dt$ as

$$\frac{\mathrm{d}\,\rho^e_\star}{\mathrm{d}\delta t} = \frac{(1-x)\epsilon_e}{\epsilon_{SN}} \cdot \frac{\rho_h}{\delta t}\frac{x}{1-x} = \frac{x\epsilon_e}{\epsilon_{SN}} \cdot \frac{\rho_c}{\delta t} \tag{4.57}$$

Therefore, the equation for the change of the energy density of the hot–gas is

$$\begin{aligned}
\left.\frac{\mathrm{d}}{\mathrm{d}t}(\rho_h u_h)\right|_{SN} &= \epsilon_{SN}\frac{\mathrm{d}\,\tilde{\rho}_\star}{\mathrm{d}t_\star} && (4.58)\\
&= \epsilon_{SN}\left(\frac{\mathrm{d}\,\rho_\star}{\mathrm{d}t_\star} + \frac{\mathrm{d}\,\rho^e_\star}{\mathrm{d}t_\star}\right) && (4.59)\\
&= \beta\, u_{SN}\frac{\rho_c}{t_\star}\left(1 + \frac{x}{(1-\beta)} \cdot \frac{\epsilon_e}{\epsilon_{SN}} \cdot \frac{t_\star}{\delta t}\right) && (4.60)\\
&= \beta\, \tilde{u}_{SN}\frac{\rho_c}{t_\star}. && (4.61)
\end{aligned}$$

As for Eq. (3.73) that describes the evaporation of clouds, its r.h.s term has the dimension of g cm^{-3} sec^{-1}, because the evaporation rate is proportional to the density rate of supernovae explosions. Then we re–write this equation by adding a term given by the rate of supernovae density that would produce the energy density $x\epsilon_e\rho_c$. Keeping the mass fraction of short–living stars equal to β, it is easy to show that this additional term is

$$\frac{x\epsilon_e}{\epsilon_{SN}} \cdot \frac{\rho_c}{\delta t}\beta. \tag{4.62}$$

Therefore, Eq. (3.73) reads now as

$$\left.\frac{\mathrm{d}\,\rho_c}{\mathrm{d}t}\right|_{EV} = A\beta\frac{\rho_c}{t_\star}\left(1 + x\frac{\epsilon_e}{A\epsilon_{SN}} \cdot \frac{t_\star}{\delta t}\right) = A\beta\frac{\rho_c}{t_\star}\Gamma. \tag{4.63}$$

Here $\Gamma > 1$ accounts for the extra energy term from the supernovae explosions originating by long–lived stars. The passages which lead to the energy equations (3.80) are the same as in Sec. (3.4.5) but using $\tilde{u}_{SN}$ instead of u_{SN} and carrying on the factor Γ that we have introduced. Finally, the equation for the evolution of the energy of the hot phase is

$$\rho_h\frac{\mathrm{d}\,u_h}{\mathrm{d}t} = \beta\frac{\rho_c}{t_\star}\left(\tilde{u}_{SN} + u_c - u_h\right) - A\beta\frac{\rho_c}{t_\star}\left(\frac{u_h}{\Gamma} - u_c\right) \tag{4.64}$$

The functional form is exactly the same as that of the original Eq. (3.80). Therefore, also the formal solution is exactly the same, provided that the temperature to which the solution tends is

$$u_h = \frac{\tilde{u}_{SN}}{1 + A/\Gamma} + u_c. \tag{4.65}$$

Nevertheless, the equation (4.64) involves explicitly the cold mass fraction x owing to our hypothesis on the sharing of the energy e_e among the two phases. So that, the only way to reach the equilibrium solution of the previous energy equation is to solve it iteratively using the original "unperturbed" solution of Eq. (3.81) as the initial guess.

The net effect of this "perturbation" is to lower the cloud mass fraction x and to raise the temperature of the hot phase. The importance of this effect is strongly dependent on the local conditions. In order to have some hint, we perform here below an order–of–magnitude estimate of all factors entering in Eq. (4.64).

(1) Taking $\delta t \sim 0.5\,\mathrm{Myr}$ as a mean value for the time–step the ratio $t_\star/\delta t$ can vary by about an order of magnitude, depending on whether we are considering region of strong or mild star formation. Since $t_0^\star$ is equal to 1.5 Gyr, $t_\star/\delta t$ will range in the interval 10^2 - 10^3 Myr. (2) The value of the cloud mass fraction x ranges obviously in the interval [0:1]. A typical value for x in our simulations is 0.8, meaning that a multi–phase Gas Particle has in general a fairly large cold phase. (3) The ratio between the energy in the reservoir and ϵ_{SN} depends strongly on the value of M_{th}^{IRA} and on the time–step we choose for the stellar evolution. A top–heavier IMF and/or a smaller M_{th}^{IRA} will produce a smaller value for this ratio. We plot in Fig. (4.15) this ratio as a function of time during the evolution of a SSP. At each epoch the energy ejected is computed within a time interval $\Delta t \sim 0.1\,t$. Most of the energy produced by SnII. Therefore the fraction of energy that each Star ejects in a time interval Δt much shorter than its lifetime, is small with respect to the energy released by all the short–living stars. This is especially true in the SnIa regime, while SnII would anyway contribute significantly.

Finally, by assembling together all the order–of–magnitude estimates, we do not expect major variations neither in the final energy of the hot phase nor in the cloud mass–fraction x, appreciable changes being expected in strong star–formation regions.

Finally, the energy of the reservoir is also used to raise the velocity of winds of star–forming particles. Taking Eq. (4.8) and adding to it the contribution from the reservoir energy e_e, gives

$$v_w^2 = 2\frac{\chi}{\eta}\,\frac{\beta_8}{(1-\beta_8)} u_{SN} \cdot \left(1 + \frac{\epsilon_e}{u_{SN}} \cdot \frac{(1-\beta_8)}{\beta_8}\right). \tag{4.66}$$

Furthermore, we also introduce the stochastic wind model for non star–forming particles, by selecting the particles which fulfill the two following conditions:

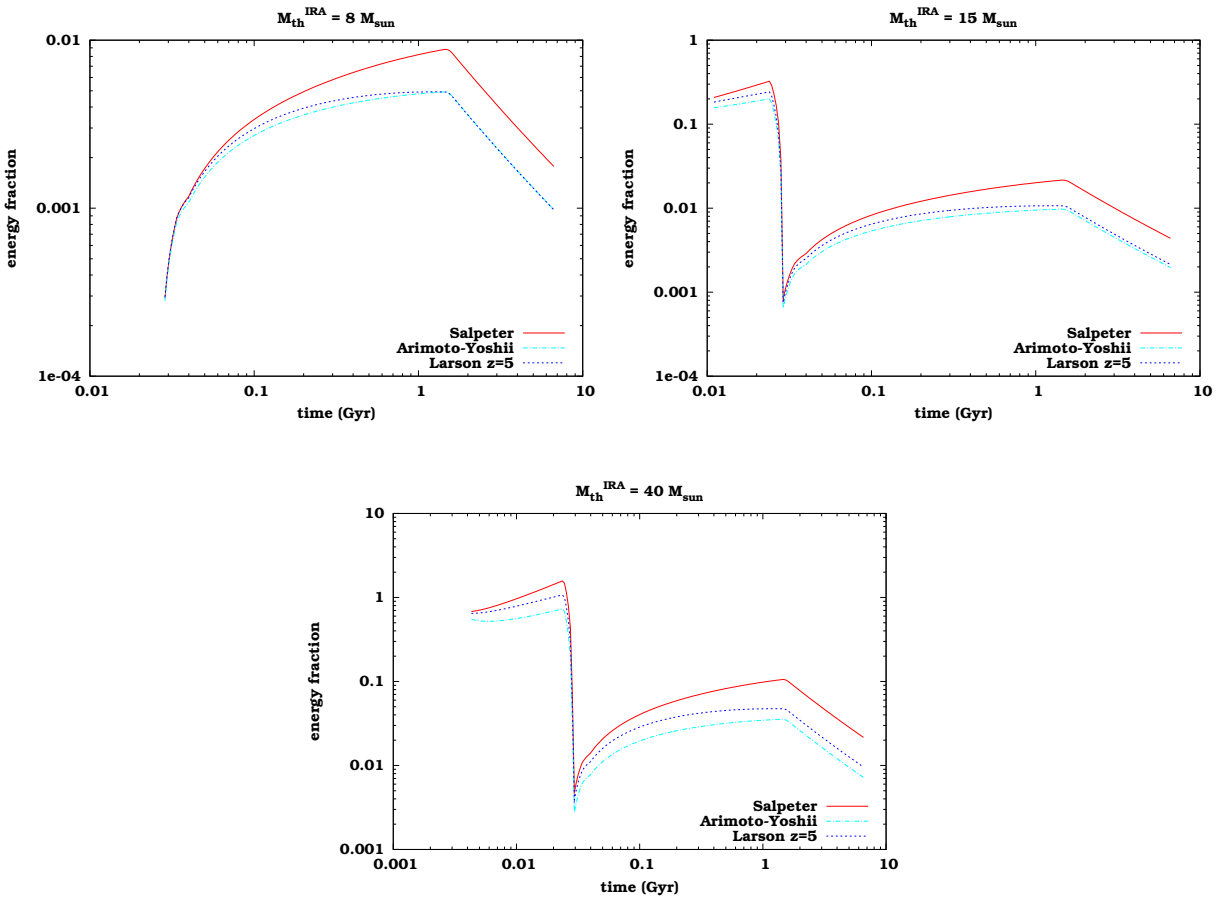

Figure 4.15: The ratio between the energy release by the supernovae of an SSP at a given time and the energy released by the all the supernovae of the same SSP with mass above M_{th}^{IRA}. The Δt of evolution is taken at each time t as $10^{0.85 \log t}$. Continuous line refers to a Salpeter IMF, long–dashed line to an Arimoto–Yoshii IMF and short–dashed line to a Salpeter IMF at redshift 2.

- $\epsilon_e > \frac{1}{2} {v_w^0}^2$
- $p > \eta \frac{\epsilon_e}{\epsilon_{SN}}$

where v_w^0 is the wind velocity due to ϵ_{SN} with no contribution of ϵ_e; $m_\star = e_e/\epsilon_{SN}$ is the mass of stars which would produce the energy e_e, so that the second condition is just the application of the stochastic algorithm. It requires that a randomly drawn number falls above the threshold $\eta \times m_\star/M_g$, where M_g is the mass of the Gas Particle. Basically, the GP eligible to take part of the winds are only those receiving an amount of energy which is comparable to that from short–living (IRA) stars. Therefore, non–star–forming Gas Particles take part to winds, whose energy is given by

$$v_w^2 = 2\frac{\chi}{\eta}\epsilon_e. \tag{4.67}$$

4.10 Summary

In this Chapter we have presented our most advanced implementation for cosmological numerical simulations with metal enrichment. Starting form the code GADGET by Volker Springel (Springel et al. 2001, Springel & Hernquist 2002, Springel & Hernquist 2003a), outlined in Sec. (3.4), we implemented several original features:

[**1**] the full account for the evolution time–scale of stars;

[**2**] the full account for delayed metal and energy production from both SnII and SnIa;

[**3**] the full account for the extra–energy due to supernovae in the thermodynamical equations of the code;

[**4**] the metallicity dependence of the cooling function.

In the next chapter we will present and discuss a number of simulation runs realized with this code.

CHAPTER 5

RESULTS

■ *Chapter Outline*

Here we basically discuss the main results drawn from first simulations run with our "chemical" code. We resume all the parameters and describe all the simulations run; then, we discuss some numerical issues and the general properties of the simulated cluster. Finally, we compare the obtained abundance patterns with those observed.

Introduction

In this chapter we present the results obtained from the analysis of the simulations performed with the code described in Chap. (4). First, we review all the code parameters and give a synoptic table of their values for all runs. After this introduction, we proceed with the discussion as follows. We are interested in studying both the numerical and the physical effects of the parameters' choice as numerical side–effect must be under control in order to be "masked" when conclusions on the physics are drawn. Therefore we distinguish two types of parameters upon which final results are sensitive: parameters that only concern numerical issues and should not affect the physics and

parameters that instead have a physical meanings.
The issues we include in the first group, which basically account for the "numerical stability", are :

[**1**] The spreading technique

- $1.a\cdot$ using an SPH Kernel or a Top–Hat Kernel
- $1.b\cdot$ the number of neighbours over which s Star Particle distribute the produced energy and metals.

[**2**] The mass segregation dependence on the number of stellar generations $N_G^\star$

[**3**] The value of the time–step of stellar evolution.

Item 1 has been already discussed in Sec. (4.6). The TH Kernel proves to be more stable than the SPH one, in the sense that both metal abundance profiles and the mass–metallicity distribution are less sensitive to the value of $N_G^\star$ when using it. Furthermore, both are nearly identical to the ones obtained with eight–times–better mass resolution. As we expect this dependence to be exactly related to the mass resolution, we take this as a sign of a better stability. So far, we trust in stability exhibited by high–resolution runs to draw conclusions on physics.

As for parameters that depend instead on the physics of star formation and evolution, the related issues are the following:

[**1**] The dependence of the effective–model on M_{th}^{IRA}.

[**2**] The dependence of the effective–model dependence on metallicity.

[**3**] Additional requirements for a Gas Particle becomes star–forming

[**4**] Changing the IMF,

- $4.a\cdot$ results when having the Arimoto–Yoshii IMF and winds' energy set to the level of a Salpeter IMF;
- $4.b\cdot$ results having the Arimoto–Yoshii IMF and auto–consistent winds;
- $4.c\cdot$ results having the Larson IMF and winds' energy set to the level of a Salpeter IMF;
- $4.d\cdot$ results having the Larson IMF and auto–consistent winds;

[**5**] Once an IMF has been set, what is the effect of

- $5.a\cdot$ changing lifetimes
- $5.b\cdot$ changing the fraction oAf binary system giving raise to SnIa.

Name	meaning	*reference*
IMF	the Initial Mass Function	Sec. (4.4)
x	the exponent of the IMF	"
$\tau(m)$	the lifetime function stars	"
M_U	the upper mass for IMF normalization	"
M_{inf}	the minimum mass for IMF normalization	"
M_{up}	the minimum mass for a star to give origin to a SnII	"
M_{Bm}	the minimum mass for a SnIa binary system	"
M_{BM}	the maximum mass for a SnIa binary system	"
A	the fraction of stars living in binary SnIa systems	"
$t_0^\star$	the characteristic time for Star Formation	Sec. (3.4.5)
$N_G^\star$	the number of maximum Star generation for each GP	Sec. (4.1)
N_n	the number of neighbours over which each Star distribute its ejecta	Sec. (4.6)
M_{th}^{IRA}	the minimum mass for SnII to be considered short–living	Sec. (4.8)
e_{SN}	the energy produced by a Sn explosion (the same for both SnIa and SnII)	Sec. (4.4)
N_t^{Ia}	the number of steps to calculate the entire evolution of SnIa	Sec. (5.3)
N_t^{II}	the number of steps to calculate the entire evolution of SnII	Sec. (5.3)
η	the efficiency of winds' mass selection	Sec. (3.4.6)
χ	the fraction of energy from short–living stars used to raise winds	"

Table 5.1: List of significant parameters.

From *these* issues we expect to arrive to some conclusions on the physics that is actually acting in Clusters of Galaxies. Finally, we compare simulation results to observations so as to highlight successes and shortcomings of our numerical modelling of the thermodynamical properties of the ICM.

Throughout the Chapter, we focus mainly on chemical properties of the simulated objects, whereas we discuss more briefly the analysis of the signature of chemical enrichment on the thermodynamics of clusters. As for the graphview on abundance profiles, we always rescale the x–axis in units of R_{180} (see below for the definition) in order to compare with observational data from De Grandi & Molendi (2001).

5.1 The Simulation Runs

In this Section we report on all the parameters that we have discussed and that influence the code behaviour. For each parameter we give the reference of the Section where it has been introduced or discussed. Then, we report the value of the parameter set for all the simulation runs.

The simulations that we present in this Chapter have been run with the code

described in Chap. (4), which is a far more advanced and refined version of the one with which we run the simulations presented in Chap. (2). However, we used the same initial conditions as for those simulations. In this way it is easier to realize how the new physics is acting.
In summary, we re–simulate two lagrangian regions taken from a large cosmological simulation. We choose the first one in order to have a single object with a virial mass of about $4 \times 10^{14}\,\mathrm{M}_{\odot}$, that we label as "Cluster", and the second box so as to encompass three smaller halos with mass in the range $(2-6) \times 10^{13}\,\mathrm{M}_{\odot}$, that we label as "Group" 1, 2 and 3. We have simulated these objects at two different mass resolution, corresponding to $m_{\rm gas} \simeq 2.5 \times 10^{9}\,\mathrm{M}_{\odot}$ and $3.2 \times 10^{8}\,\mathrm{M}_{\odot}$, respectively. Nevertheless, in this Chapter we will discuss only the simulations of the cluster. In the following we indicate with the pedex L and H the low– and high–resolution simulations, respectively.
In order to discuss the elements enumerated in the previous Section, we run several simulations, varying the values of crucial parameters. Low–resolution results are mostly devoted to study numerical effects, whereas the high–resolution ones are more reliable to study the physical effects of algorithms.
In the following tables we provide a synoptical view of all simulations presented here and the values of all significant parameters for each of them. We also give to every run a label with which it will be referred in the following. Basically, the pedex indicate the resolution (H or L), while the apex gives more informations about the relevant physics. The meanings of apexes are the followings:

- [*numbers*] the number refer to the value of N_n;
- [*TH*] it means that the Sn ejecta are distributed using a Top Hat Kernel;
- [*IRA-number*] the number report the value of M_{th}^{IRA};
- [*w*] it means that the wind's velocity has been fixed to the same value as for $S_{L/H}$ simulations, i.e. the value it gets for a Salpeter IMF with $M_{th}^{IRA} = 15\,\mathrm{M}_{\odot}$;
- [†] simulations for which the dependence of the effective model on the gas metallicity and M_{th}^{IRA}, introduced in this work, has been switched off;
- [*Sn.t.*] a simulation with different values as for the number of time–steps adopted to follow the evolution of different Sn progenitor, N_t^{II} and N_t^{Ia};
- [*c.t.*] a simulation with two additional requirements on physical conditions suitable for a Gas Particle to become multi–phase.

In Figures (5.1) trough (5.4) we show quantities which will be used throughout the Chapter for all simulations in both low and high resolution. Fig. (5.1) and Fig. (5.2)

show low–resolution results, whereas Fig. (5.3) and Fig. (5.4) show high–resolution results. In Fig. (5.1) and Fig. (5.3) we plot the total gas mass and the baryonic fraction within the virial radius in units of the same quantities obtained in the S_H run (Top Left Panel), the star final fraction, defined as $M_\star/(M_\star + M_{gas})$ (Top Right Panel), the mean temperature within the virial radius in keV (Bottom Left Panel) and the cold gas fraction, defined as $M_{cold}/(M_{cold} + M_{hot})$ (Bottom Right Panel). In Fig. (5.2) and Fig. (5.4) we plot the mean metallicity for each element, both emission and mass weighted (Bottom Left and Right Panel), the fraction of metals which is retained by the gas (Bottom Left Panel) and the mass–weighted Fe abundance within virial radius and in all volume (Bottom Right Panel).

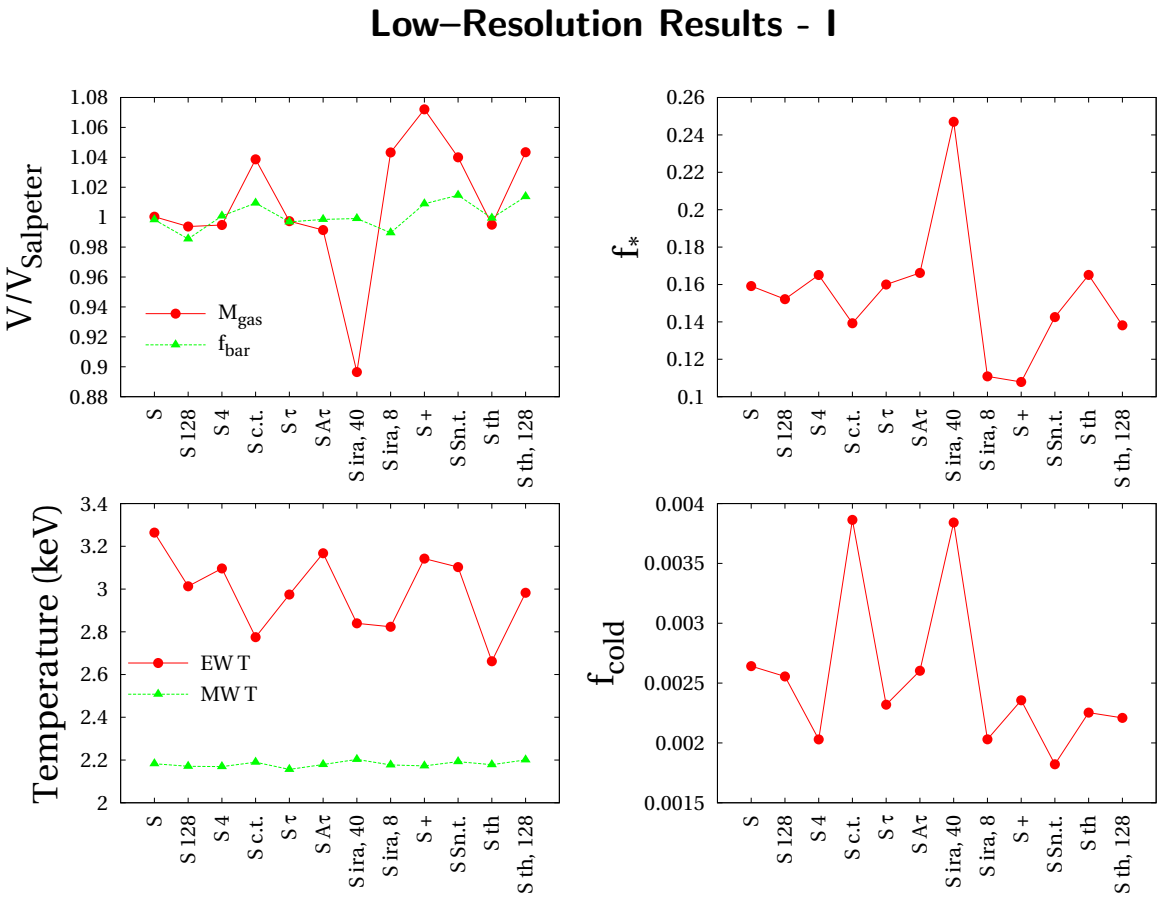

Figure 5.1: Thermodynamical properties (within $R_{\rm vir}$) of all low–resolution simulations. [**Upper Left Panel**] Gas masses (circles) and barynic fractions (triangles) in units of S_L simulation. [**Upper Right Panel**] Star fraction $f_\star = M_\star/(M_{\rm gas} + M_\star)$. [**Bottom Left Panel**] Temperature weighted by mass (triangles) and by emissivity (circles). [**Bottom Right Panel**] The fraction of mass in cold clouds, $f_{\rm cold} = M_{\rm cold}/(M_{\rm hot} + M_{\rm cold})$.

Low–Resolution Runs

Mass of a Gas Particle $= 0.177 \times 10^{10}\,\mathrm{M}_{\odot}$

Label	Obj	IMF	$\tau(m)$	A	M_{th}^{IRA}	χ	η	K	N_n
S_L	CL	Salpeter	PM	0.07	15	1	2	SPH	32
S_L^{128}	CL	Salpeter	PM	0.07	15	1	2	SPH	128
S_L^{4}	CL	Salpeter	PM	0.07	15	1	2	SPH	4
S_L^{TH}	CL	Salpeter	PM	0.07	15	1	2	TH	32
$S_L^{TH,128}$	CL	Salpeter	PM	0.07	15	1	2	TH	128
S_L^{τ}	CL	Salpeter	MM	0.07	15	1	2	SPH	32
$S_L^{A\tau}$	CL	Salpeter	MM	0.1	15	1	2	SPH	32
$S_H^{ira,40}$	CL	Salpeter	MM	0.07	40	1	2	SPH	32
$S_H^{ira,8}$	CL	Salpeter	MM	0.1	8	1	2	SPH	32

High–Resolution Runs

Mass of a Gas Particle $= 0.0221 \times 10^{10}\,\mathrm{M}_{\odot}$

Label	Obj	IMF	$\tau(m)$	A	M_{th}^{IRA}	χ	η	K	N_n
S_H	CL	Salpeter	PM	0.07	15	1	2	SPH	32
S_H^{128}	CL	Salpeter	PM	0.07	15	1	2	SPH	128
$S_H^{TH,32}$	CL	Salpeter	PM	0.07	15	1	2	TH	32
$S_H^{TH,128}$	CL	Salpeter	PM	0.07	15	1	2	TH	128
$S_H^{IRA,40}$	CL	Salpeter	MM	0.07	40	1	2	SPH	32
$S_H^{IRA,8}$	CL	Salpeter	MM	0.1	8	1	2	SPH	32
AY_H	CL	Arimoto–Yoshii	PM	0.07	15	1	2	TH	32
AY_H^{w}	CL	Arimoto–Yoshii	PM	0.07	15	0.3	2	SPH	32
V_H	CL	Larson	PM	0.07	15	1	2	SPH	32
V_H^{w}	CL	Larson	PM	0.07	15	*var*	2	SPH	32
S_H^{gr}	Gr	Salpeter	PM	0.07	15	1	2	SPH	32
AY_H^{gr}	Gr	Arimoto–Yoshii	PM	0.07	15	1	2	TH	32
AY_H^{gr-w}	Gr	Arimoto–Yoshii	PM	0.07	15	0.3	2	SPH	32

Table 5.2:

Special Low– and High– Resolution Runs

Label	description
$S_L^{\dagger}$	same as S_L but with effective–model not dependent on both gas metallicity and M_{th}^{IRA}
$S_L^{Sn.t.}$	same as S_L but with $N_t^{Ia} = 12$ and $N_t^{II} = 4$
$S_L^{c.t.}$	same as S_L but with more requirements to be fullfilled in order to elect a GP into multi–phase regime

Values of parameters common to all simulations

Parameter	Value	*reference*
$t_0^{\star}$	$1.5\,\mathrm{Gyr}$	Sec. (3.4.5)
M_{inf}	$0.1\,\mathrm{M}_{\odot}$	Sec. (4.4)
M_U	$100\,\mathrm{M}_{\odot}$	Sec. (4.4)
M_{up}	$8\,\mathrm{M}_{\odot}$	Sec. (4.4)
M_{Bm}	$3\,\mathrm{M}_{\odot}$	Sec. (4.4)
M_{BM}	$16\,\mathrm{M}_{\odot}$	Sec. (4.4)
N_t^{Ia}	125	Sec. (5.3)
N_t^{II}	40	Sec. (5.3)
$N_G^{\star}$	3	Sec. (3.4.5), Sec. (4.1)
e_{SN}	$10^{51}\,\mathrm{erg}$	Sec. (4.4)

Table 5.3:

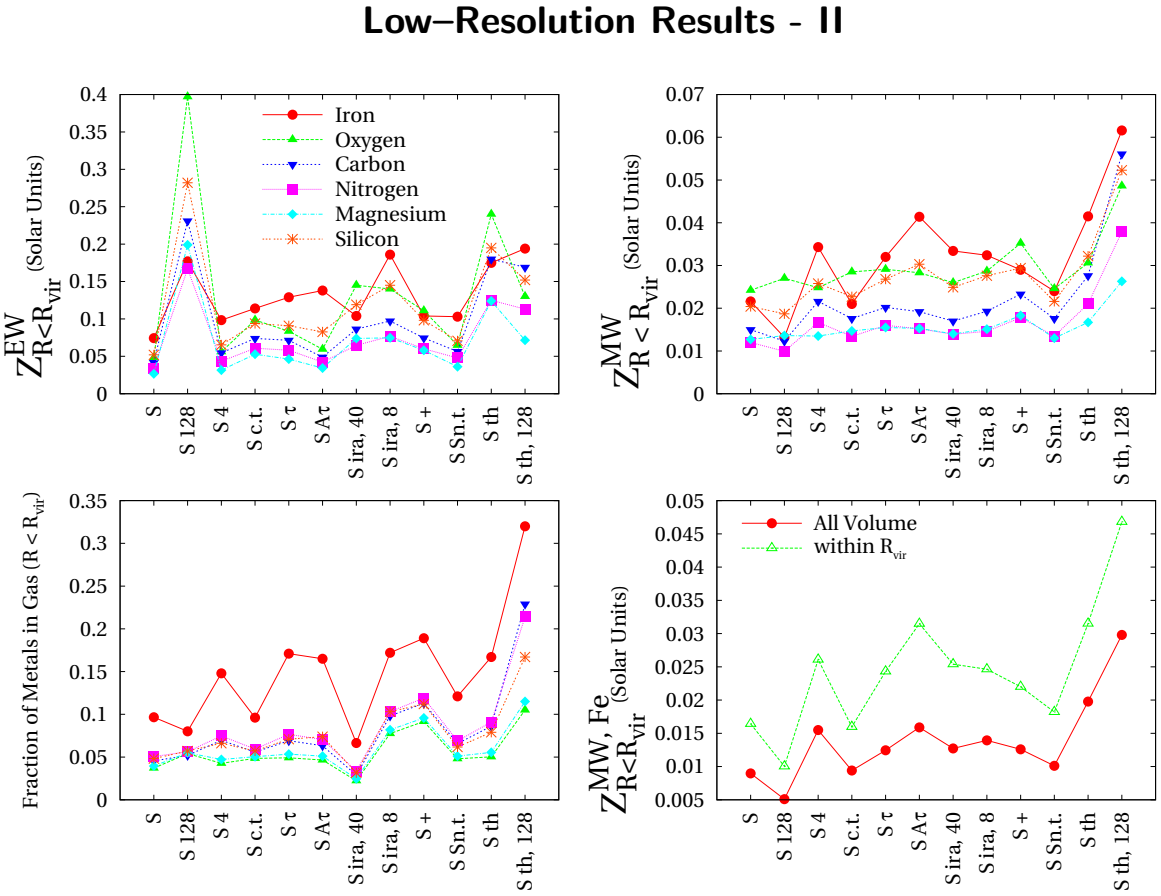

Figure 5.2: Metallicity–related properties (within $R_{\rm vir}$) of all low–resolution simulations. [**Upper Left Panel**] Emission–weighted metallicity for all simulated elements. Symbol are as in Left Panel.[**Upper Right Panel**] Mass–weighted metallicity for all simulated elements. [**Bottom Left Panel**] Fraction of metals retained by gas. Symbols are as in Upper Left Panel. [**Bottom Right Panel**] Mass–weighted Fe metallicity within $R_{\rm vir}$ (circles) and in all the simulated region (triangles).

■ Technical Notes

We focus mainly on results about chemistry of galaxy clusters, so that we avoid describing pure technical issues about the analysis of simulations. We start our analysis with the identification of the centre coordinates for the cluster. To this end, we first apply a friends-of-friends halo finder to the distribution of DM particles, with a linking length equal to 0.15 times their mean separation. For each group of linked particles with more than 500 members, we identify the particle having the minimum value of the gravitational potential. This particle is then used as a starting point to run a spherical overdensity algorithm, which determines the radius (*virial* radius hereafter) around the target particle that encompasses an average density equal to the virial density for the adopted cosmological model, $\rho_{vir}(z) = \Delta_c(z)\rho_c(z)$, where $\rho_c(z) = [H(z) = H0]^2\rho_{c,0}$ is

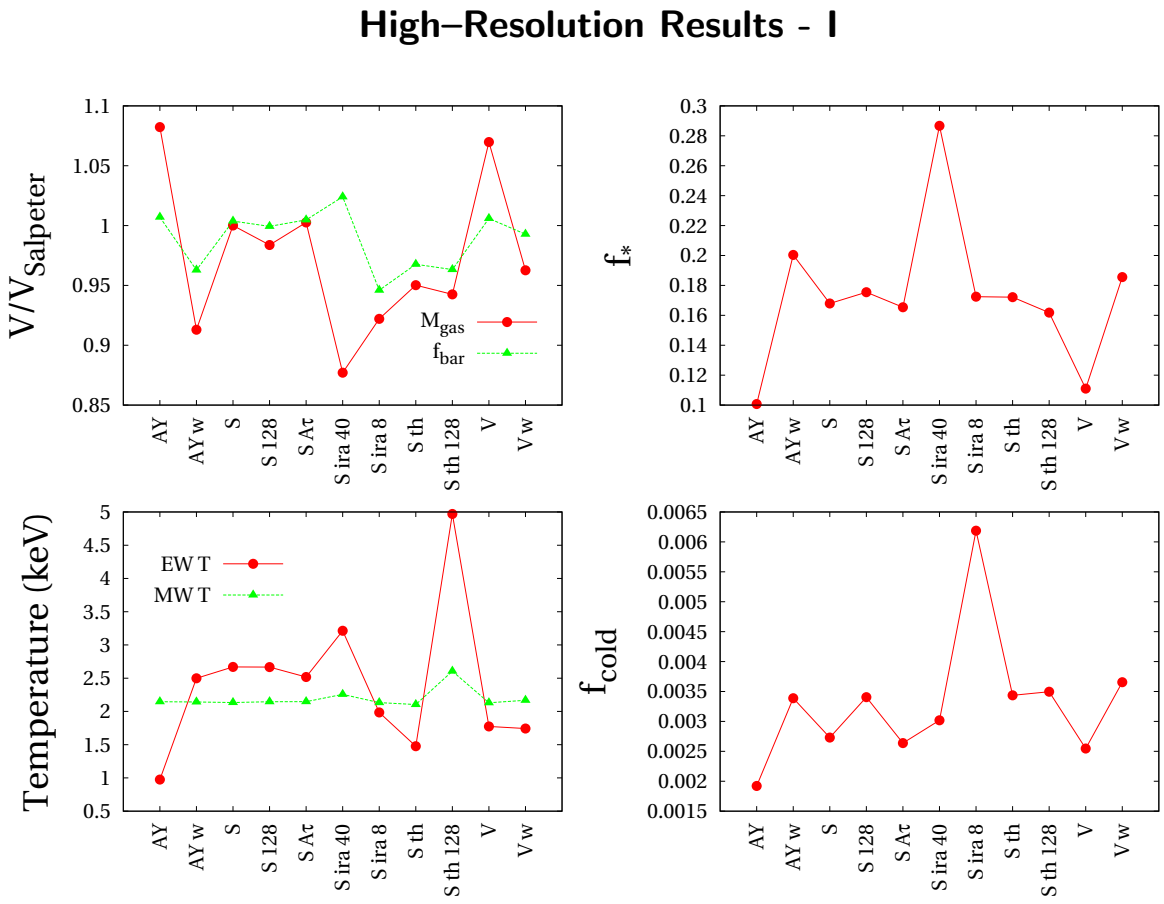

Figure 5.3: The same as Fig. (5.1) for all high–resolution results.

the critical density at redshift z, and the overdensity $\Delta_c(z)$ for virialization under the assumption of spherical model is computed as described in Eke, Cole & Frenk (1996). Then, we always rescale the x–axis when plotting profiles in unit of the virial radius (which is the radius encompassing the virial overdensity computed for the simulated cosmology; e.g. Eke et al. 1998). The only exception is when we plot abundance profiles. Since we refer to data on Iron abundance profiles by De Grandi & Molendi (2001), we rescale the x coordinate in units of R_{180}, as the reference data are given in such units. We define R_{180} as the radius encompassing an average density equal to $180\rho_c(z)$. Finally, all densities reported in graphviews are in units of $f_{bar}\rho_{vir}(z)$, where f_{bar} is the cosmic baryon fraction. If not otherwise stated, we adopt solar abundances by Grevesse & Sauval (1998).

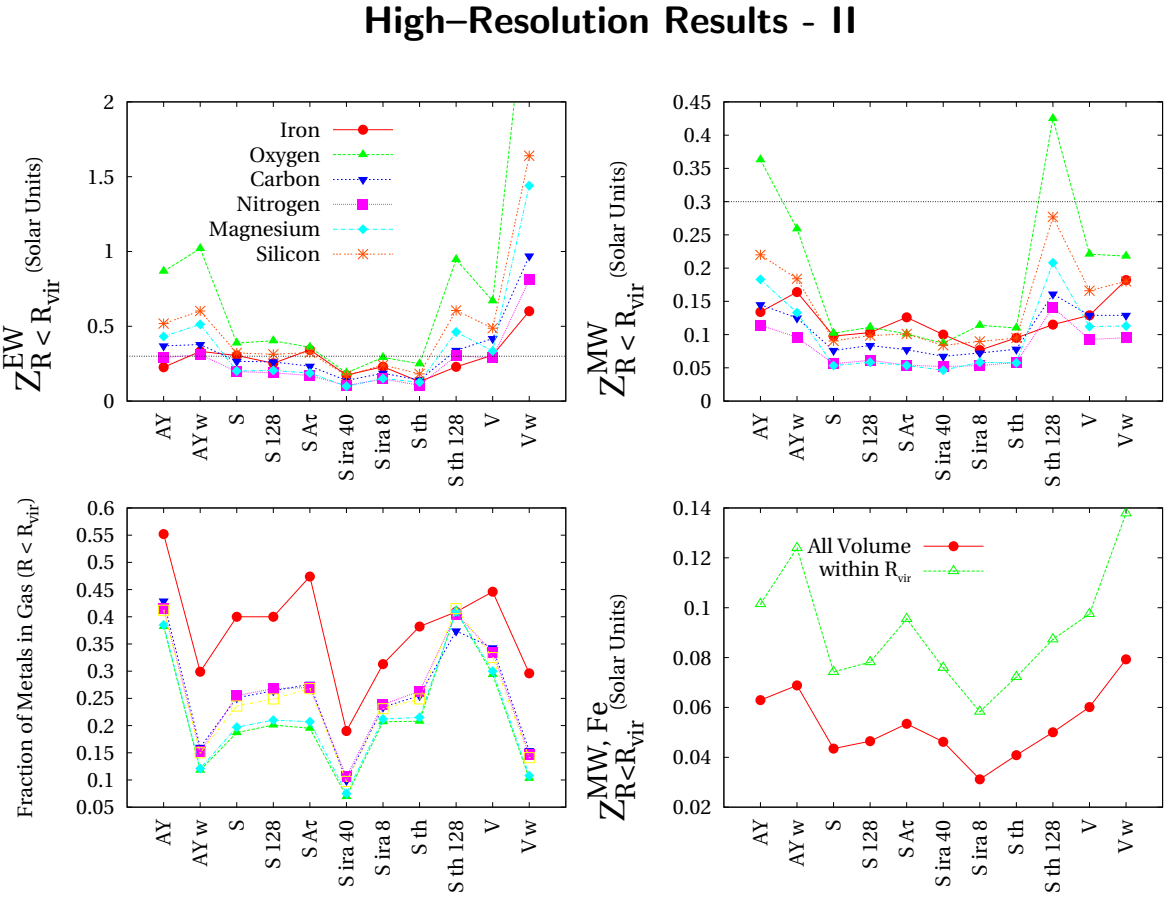

Figure 5.4: The same as Fig. (5.2) for all high–resolution results.

5.2 The Mass Segregation

The mass segregation is defined as particles of different masses settling on a phase–space volume that depends on the masses themselves by purely numerical effects like, e.g, the two–body heating. This artificial dynamical effect is highly undesirable as it would alter the true dynamics. It is likely to arise mostly when the range of particle mass is fairly large, resulting in heavier particles being settled towards the bottom of the gravitational potential well and lighter ones being kicked towards the outskirts. Due to the star–formation algorithm we use, Gas Particles (GP) reduces their mass by $m_0/N^{\star}_G$ each time a Star Particles is spawned. Furthermore, the mass of a GP increases every time it receives ejecta from supernovae while a Star Particle consumes its mass during the stellar evolution. Hence, we will have GP with masses in the range $[\lesssim m_0/N^{\star}_G : \gtrsim m_0]$ and Star Particles with masses scattering around $m_0/N^{\star}_G$. Since the mass of our particles varies by a factor of ~ 3, it is worth to check if some segregation effect is at work.

A rigorous study would require dynamical tracing of orbits; nevertheless, we accomplish the task in a much simpler way. We divide the mass range in a number of bins, then counting the number of Particles which fall in each of them; then, in case of severe mass segregation effect, we would expect that the way particles of each mass distribute radially from the centre of the object will clearly show some trend. If it were not, we are authorized to conclude that non significant mass segregation is present in our simulations.

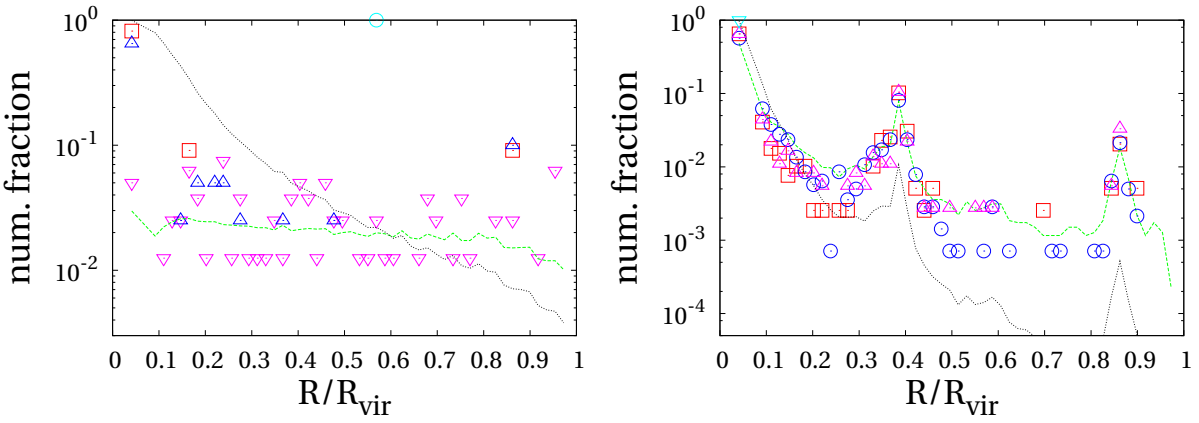

Figure 5.5: The relative radial distribution of Gas (**Left Panel**) and Star (**Right Panel**) Particles. Light–Dotted black lines are the gas and star mass density profiles respectively. Dashed lines refer to the bin within which fall most of the particles. Each pair (symbol, color) refers to a mass bin as follows (masses are expressed in units of $10^{10}\,M_{\odot}$). (*Left Panel*) squares: 0.053 ¡ m ¡ 0.081; triangles down: 0.081 ¡ m ¡ 0.086; triangles up: 0.086 ¡ m ¡ 0.17; circles: 0.17 ¡ m ¡ 0.33. (*Right Panel*) squares: 0.035 ¡ m ¡ 0.052; circles: 0.07¡ m ¡ 0.082; triangles down: 0.082 ¡ m ¡ 0.085; triangles up: 0.085 ¡ m ¡ 0.123.

In fact, no signature of mass–dependent radial distribution appears in Fig. (5.5) where we plot how particles with different masses are distributed. Instead, the lightest particles are more concentrated in inner regions, at odds with what we expect in case of two–body heating. This concentration is due to the recent intense star–formation activity which in our simulations is on–going until late times in the cluster centre; so that GP are spawning more than one Star and, having been much enriched, many of them are right above the value $3/2\,m_0^*$ that is the threshold for the whole Gas Particle to become a Star. Therefore, they are allowed to spawn up to $N_G^\star$ Stars and to have then a minimum mass $m < m_0/N_G^\star$.

■ Summary

We define the mass segregation as particles of different mass systematically ending in different regions, the same for particles of equal mass. To check whether this effect is

present in our simulations, we have studied how particles of different mass distribute radially from the centre and found no significative trends.

5.3 The Supernova Time–Stepping

In Sec. (4.4.1) and Sec. (4.4.2) we have described the equations governing the supernovae explosion both for Type II and Type Ia. In order to apply them to a Star Particle, we calculate in advance a discrete subdivision of the lifetime for each type requiring that the same amount of energy is ejected in each time interval. This amount to require that the same number of supernovae events occurs per subdivision, as long as we assume that $e_{Sn} = e_{SnII} = e_{SnIa}$. Therefore we have about $N_t^{II} + N_t^{Ia}$ steps for each Star Particle to account for all SnII and SnIa respectively (a tolerance of the 5% is used when calculating the subdivision). This should be a purely numerical parameter. Still, it controls the amount of energy that is spread over the neighbouring gas particles; as this energy will enter in the effective–model and winds' velocity calculations, it may influence the way the feedback is released.

Thermodynamical calculations are performed once per each GP time–step, so that as long as the supernovae time–step is short compared to the gas one this problem is not present. In that case, in fact, the Sn energy is stacked in the reservoir, prompt to be used in when the GP becomes active. Since the neighbouring GP tend to have very similar time–steps, probably the best strategy would be to assign this same time–step (or a multiple of it) to the Stars embedded in that gas. We did not yet implement such an algorithm, having instead a fixed time subdivision per each Star, starting from its formation time and delayed by τ_{th}^{IRA}.

One may suppose that the more suitable stepping for Stars is the one which makes the stars evolving accordingly to the time–step of neighbouring GPs. If the time–step of the GPs falls below $\sim 1\,\mathrm{Myr}$ the energy contribution from supernovae would be negligible while the computational cost is greatly increased. Moreover, given that the life–time of SnIa is about $1 - 10\,\mathrm{Gyr}$, this would result in an extremely large number of stellar time–steps. Therefore, in tracing the stellar evolution we choose a compromise between the computational constraints and the accuracy. The values for N_t^{II} and N_t^{Ia} are given by the requirement that 2.5% and 0.8% of SnII and SnIa respectively explode in each time–step. To check how this affect the results, we run a Low–Resolution simulation having $N_t^{II} = 4$ and $N_t^{Ia} = 12$, i.e. a ten times worse stellar–time resolution. In the rest of this Section we refer to the simulation run with finer stepping as "FS" (fine–stepping Simulation) and to the other as "CS" (coarse–stepping Simulation).

The comparison is shown in Fig. (5.6) and Fig. (5.7). The former figure shows the comparison between quantities which concern the effective–model, while the second one shows physical quantities. The two simulations differ in several details but no major changes appear to be in place. As it is expected, the energy received by each GP from

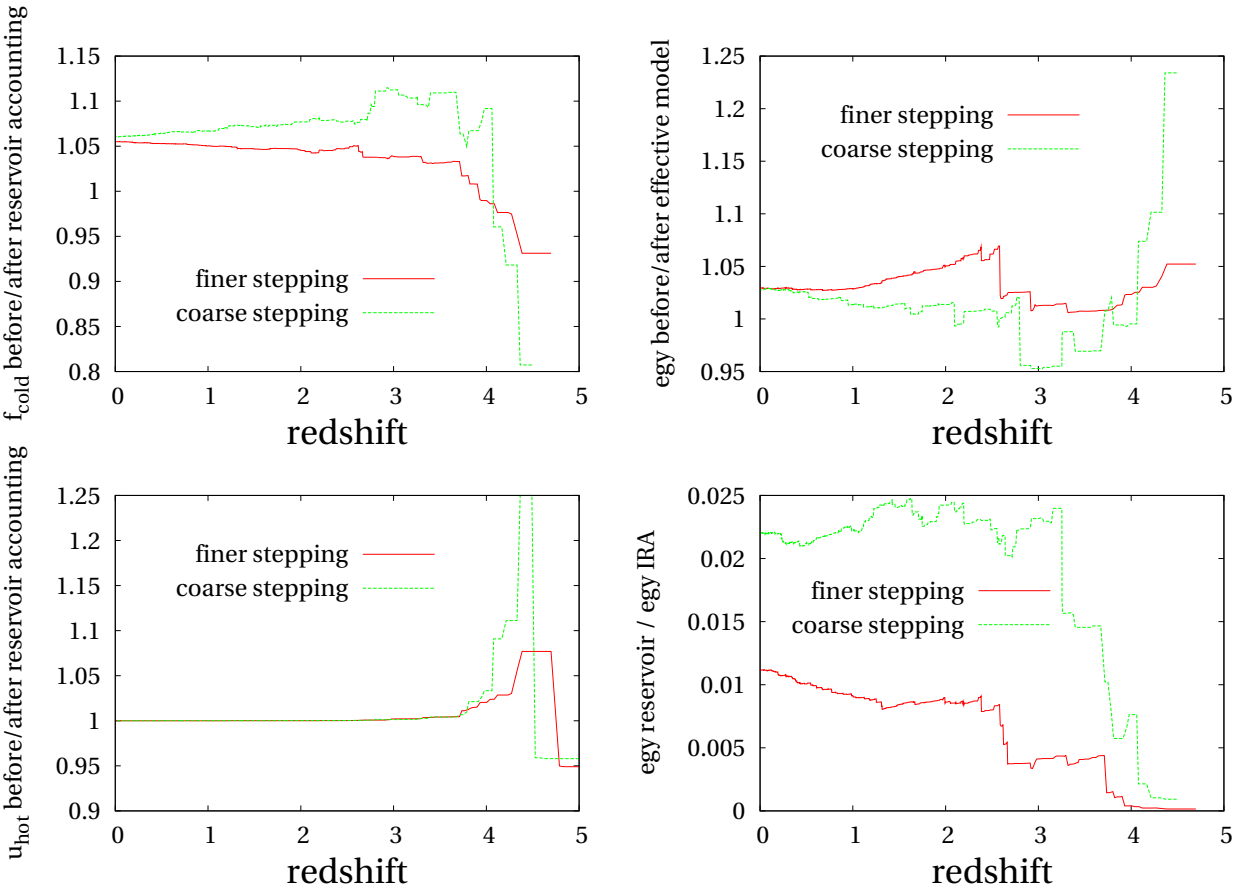

Figure 5.6: [**Top Left**] The mean ratio between the cold fraction before and after the `reservoir` energy accounting. [**Top Right**] The mean ratio between the energy before and after the effective model calculations. [**Bottom Right**] The mean ratio between the `reservoir` energy and the *IRA* energy. [**Bottom Left**] The mean ratio between the hot–phase energy before and after the `reservoir` energy had been accounted.

the interacting Stars is higher when more supernovae explode at a time; in the Bottom Left Panel of Fig. (5.6) we show the ratio between that energy and the energy from IRA stars, that in CS is higher than in FS by about a factor of 2. Accordingly, the cold fraction in CS (Top Left Panel of Fig. (5.6)) is slightly lower and the total energy (Top Right Panel, same figure) of the gas larger. The energy of the hot phase is unaffected from $z = 4$ on, as all the energy of supernova is employed to evaporate clouds in both simulations. As for physical quantities, in the Top Left Panel of Fig. (5.7) we plot the history of the Star Formation Rate for both simulations. Owing to the more efficient evaporation of the cold clouds, the star formation activity at high redshift ($z \lesssim 2$) is suppressed by $30 - 40\%$ in CS with respect to FS. The amount of Iron and Oxygen is larger by 10% in CS than in FS, owing to a less efficient locking of metals in Stars. This is due to the larger amount of supernoave energy that lead to an higher pressure

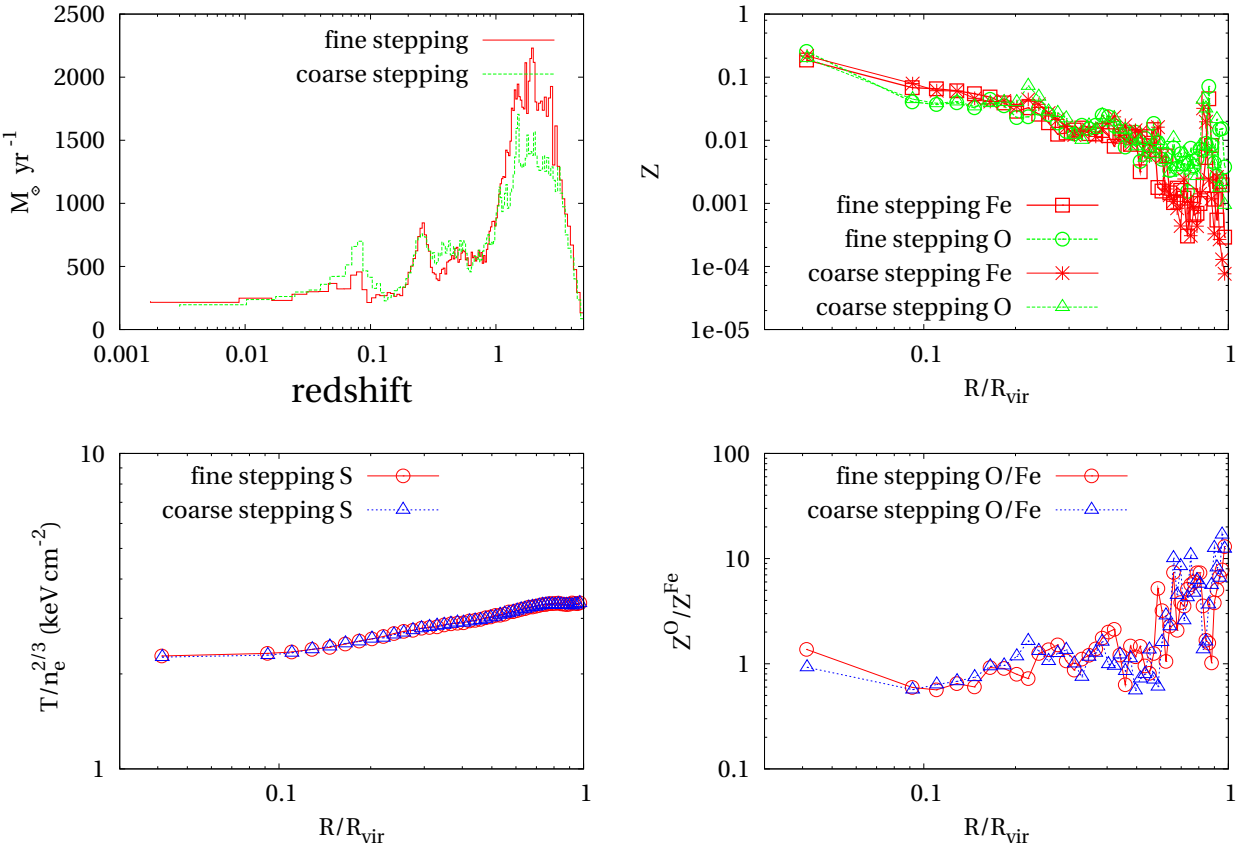

Figure 5.7: In all panels the *red continuous lines* and the *green dashed ones* refer respectively to our standard choice and the more coarse–grained one. [**Top Left**] The Star Formation Rate as a function of redshift. [**Top Right**] Oxygen (light lines) and Iron (bold lines) radial profiles. [**Bottom right**] The radial profile for O/Fe ratio. [**Bottom Left**] The entropy radial profiles.

support. Still, differences are fairly small. Also, the differences in the star formation history reflect the changes in dynamical history; for instance the little starburst at $z \sim 0.1$ in CS has no correspondent in FS, and provides some more Iron at $z \sim 0$.

■ Summary

We found several differences when changing the stellar evolution time–stepping. Even so, all differences exhibit a trend that is reasonably expected and none of them is a major variation witnessing severe dependence of final results on this choice for th Sn time–stepping accuracy.

5.4 The IRA Threshold

The value of $M_{th}^{IRA}$is certainly a rather arbitrary parameter. As we discuss in Sec. (4.8), this parameter sets the extent to which the energy of firstly formed stars in a given star–forming region interferes at later times with the star formation in that same region. Since the details of the star formation process are not understood with great precision the common way to account for the SnII energy is to suppose that some fraction of it is released instantly. What this fraction is, this remains a matter of opinion. Even more, there's nothing special in $\sim 30\,\mathrm{Myr}$, so that one may also conjecture that some fraction of SnIa could be also be treated in the IRA. In this work we limit the M_{th}^{IRA}parameter to SnII.

We have run two simulations with M_{th}^{IRA}set to $40\,\mathrm{M}_{\odot}$ and $8\,\mathrm{M}_{\odot}$ both in Low– and High–Resolution, so as to check to what extent our results are sensitive to this mass scale. The ways in which this parameter directly affects the code behaviour are basically two. The first one is in determining the hot–phase equilibrium temperature in the effective model (see (3.80) and (3.81)); this mostly affect the ICM thermodynamics. The second one is in changing the fraction of metals that are immediately assigned to the Gas Particle which is hosting the star formation, instead of being subsequently spread by a Star Particle; this affects how the metals are distributed and how they are shared among gas and stars. Furthermore, as the value of M_{th}^{IRA}changes, also the values of ρ_{th} changes, owing to the variation of u_{SN}: the larger is the energy amount U_{SN} the larger is the density needed for the collapse to take place, as that energy provides thermal pressure which counteracts the collapse. Fig. (5.17) shows the values of the density threshold for different values of both M_{th}^{IRA} and the gas metallicity. The two simulations with $M_{th}^{IRA} = 8\,\mathrm{M}_{\odot}$ and $40\,\mathrm{M}_{\odot}$ ('$40\,\mathrm{M}_{\odot}$ ' and '$8\,\mathrm{M}_{\odot}$ ' hereafter) exhibit the largest and the lowest values of ρ_{th} respectively; in fact, the energy of IRA SnII is respectively the largest ($\sim 3.7 \times 10^{15}\mathrm{erg}/\,\mathrm{M}_{\odot}$) and the lowest ($\sim 3.1 \times 10^{14}\mathrm{erg}/\,\mathrm{M}_{\odot}$) among the IRA energies of all simulations presented in this Chapter.

The difference in the amount of energy promptly available in the effective model reflects clearly in the star formation rate history of each simulation, as shown in Fig. (5.8). The simulations with the lowest value of $M_{th}^{IRA} = 8\,\mathrm{M}_{\odot}$ has in turn the largest amount of energy suddenly injected in the gas at the moment of star formation; so that, it exhibits a greatly suppressed SF Rate at high redshift (Upper Panels, the Left one reports the Low-Resolution results and the Right one the High–Resolution ones) and an overall shift towards redshift $z \sim 1$ of the epoch of maximum SFR. This delay is evident also in the SnIa rate curve (Bottom Panels). At the opposite, the simulation with $M_{th}^{IRA} = 40\,\mathrm{M}_{\odot}$ has an enhanced star formation activity both at high and low redshifts. Hence, one would expect the final amount of stars and Supernovae to be much lower for smaller values of M_{th}^{IRA}. At odds with this expectation, the simulation with $M_{th}^{IRA} = 8\,\mathrm{M}_{\odot}$ has fairly more (HR) or equal (LR) SnIa explosions at late times

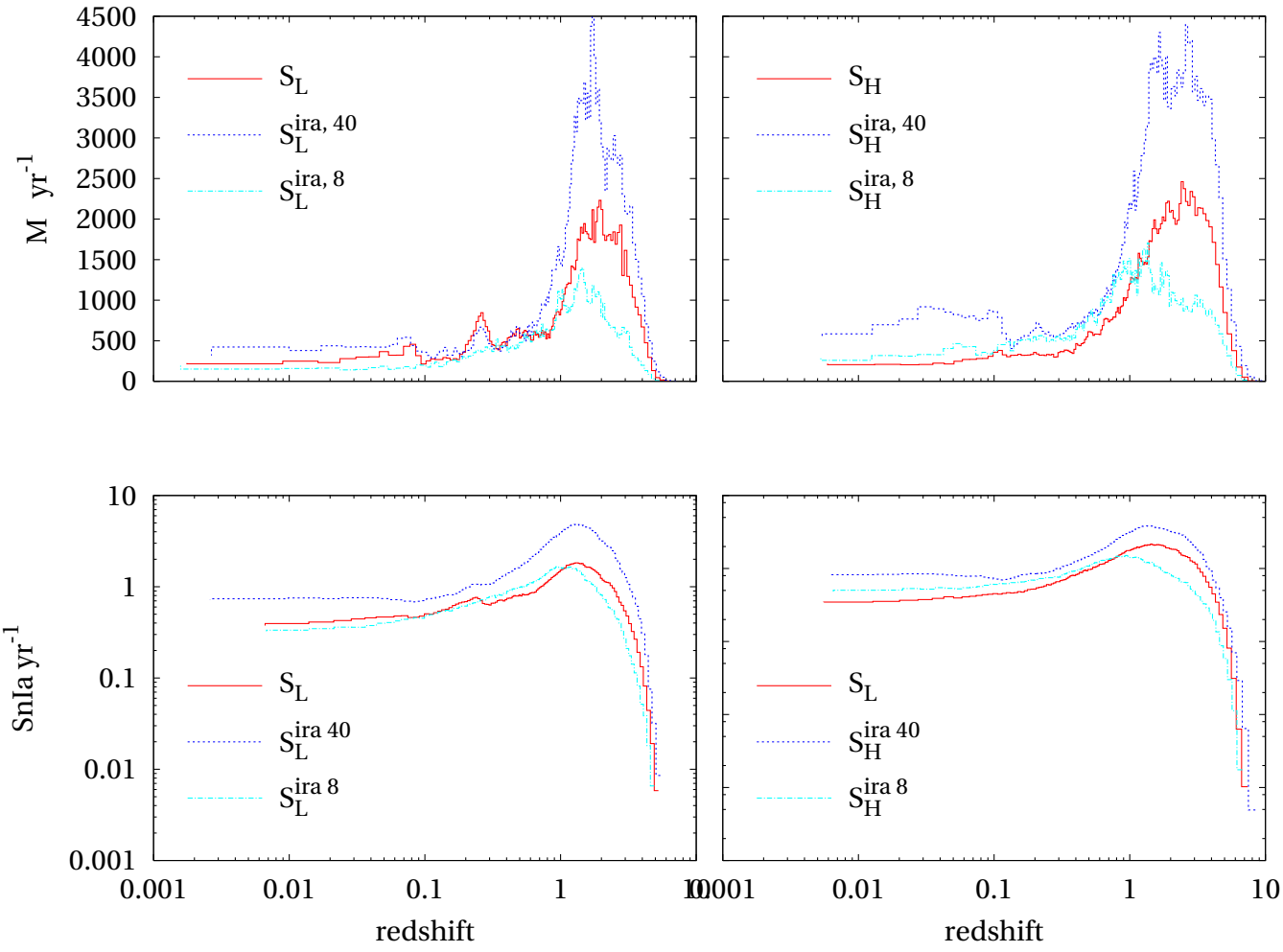

Figure 5.8: In the **Left** and **Right Column** are plotted respectively the Low– and the High–resolution results. The **Upper Row** shows the Star Formation Rate History. Continuous lines indicate S_L and S_H. Dot-Dashed lines indicate S_L^{ira8} and S_H^{ira8}. Dotted line indicate S_L^{ira40}. The **Bottom Row** shows the SnIa Rate History. Lines are coded as for the upper row.

than our 'standard' choice simulation $M_{th}^{IRA} = 15\,\mathrm{M}_{\odot}$. This is due to the fact that the pressure supplied by the IRA energy prevent the gas collapse but is not sufficient to also inflate it significantly, so that the density continues to grow and more gas ends in the cold phase. As the gas become more and more enriched, and thus the cooling become more efficient and the threshold for star formation become lower, the IRA energy no longer succeed in preventing the collapse.

Figures 5.1 – 5.4 show that the simulation with $M_{th}^{IRA} = 40\,\mathrm{M}_{\odot}$ produces a far larger amount of stellar mass, both in Low– and High– Resolution as well as the smallest

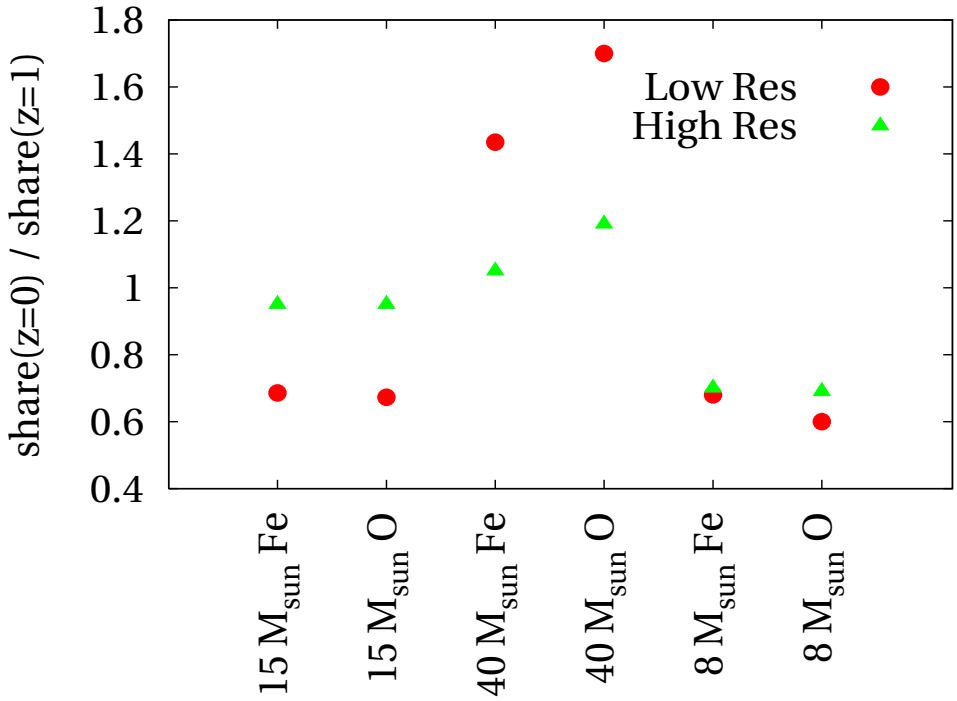

Figure 5.9: The ratio between the fraction of metals in gas at $z = 0$ over the one at $z = 1$, both for Iron and Oxygen (reported on x–axis) and Low– and High–resolution (circles and triangles respectively).

fraction of metals into the gas. The $8\,M_\odot$ case has not such a regular behaviour when the resolution increases. The stellar fraction is significantly larger in the High–Resolution run than in the Low–Resolution one. When the resolution increases, also does the efficiency of cooling and, in fact, the star formation begin quite earlier (see Fig. (5.8)); thus, the lower the resolution, the higher is the efficiency of heating. The difference between Low– and High–Resolution results would have been much larger if the star formation were been treated by a more traditional algorithm, not accounting in any way for the multi–phase nature of the ICM. In the $S_H^{IRA,8}$ run the gas is heated so that the star formation at high redshift ($z \gtrsim 1$) is suppressed by a factor of 2 with respect to the S_H simulation. Nevertheless, the net effect is just to shift the star formation peak down to redshift 1 and to flatten the rate curve. Therefore, the Star Formation rate of $S_H^{IRA,8}$ remains above the S_H rate for $z \lesssim 1$, so as to produce at $z = 0$ a comparable amount of stars. In fact, the amount of cold clouds, that are the reservoir for star formation, in $S_H^{IRA,8}$ is twice as large compared to S_H both, at $z = 1$ and at $z = 0$. As a consequence, at $z = 1$, the mass of stars in $S_H^{IRA,8}$ is 76% of the mass in S_H, while at $z = 0$ the same ratio is 0.95. The winds' velocity in $S_H^{IRA,8}$ is larger by a factor $\sqrt{2}$, owing to the larger amount of energy available. Therefore, the winds are more effective in removing hot gas from the innermost regions. This leads the

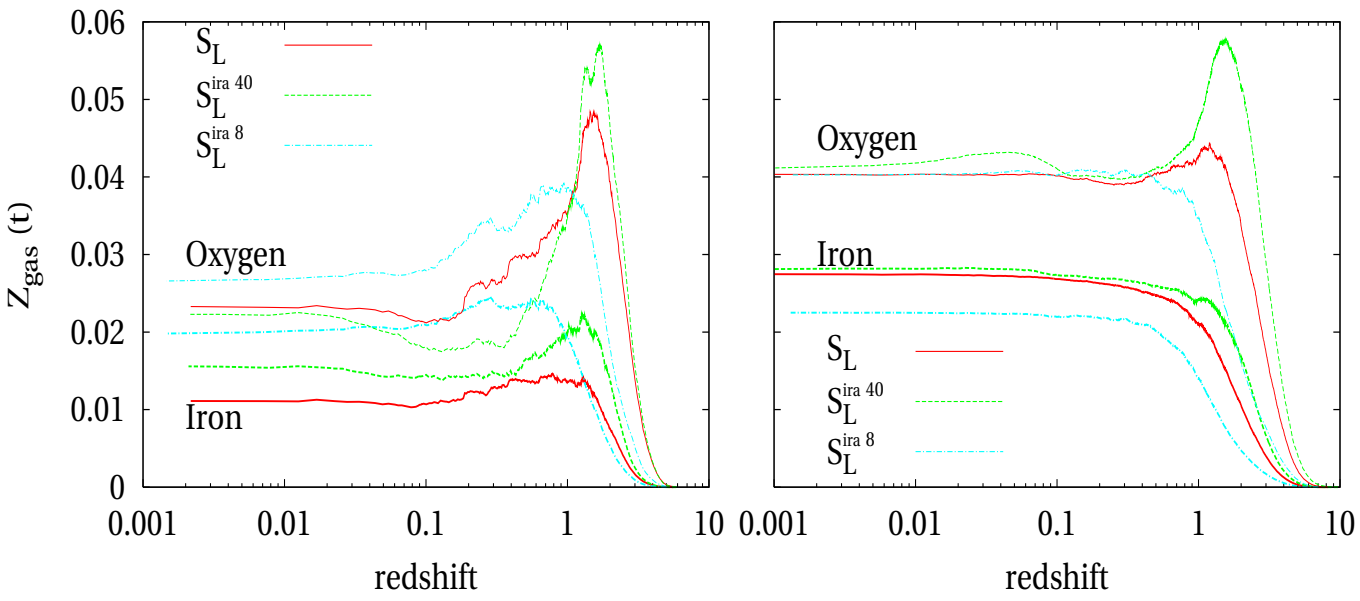

Figure 5.10: Mean Iron and Oxygen abundance of the gas as a function of redshift. [**Left Panel**] shows the low–resolution results. *Bold lines* show the Oxygen data and *thin lines* the Iron ones. Continuous, dotted and dot–dashed lines plot respectively the S_L, S_L^{ira40} and S_L^{ira8} simulations. [**Right Panel**] contains the high–resolution results. Line codes are the same as for the Left Panel.

baryonic fraction in the virial region in $S_H^{IRA,8}$ being about 90% of the same quantity in S_H. Thus, the star mass fraction, i.e. the ratio between the star mass over the total baryonic mass, is slightly higher in $S_H^{IRA,8}$ than in S_H.

From observations (e.g. 2004) we know that the cluster galaxies are preferentially old passive–evolving ellipticals and, hence, no sign of recent star formation has ever been detected. Having an on–going star formation at low redshifts ($z \lesssim 1$) is then at odds with observations. This is a result that holds for all the simulations that we present here, and it is also a common problem of numerical results; possibly this points towards a lack of physical contents in the star formation models. Either some physics in the interaction of feedback energy with the gas is missed, or even major astrophysical processes, that we neglect here, play an important role in regulating the star formation. We expect that such processes to prevent the collapse of gas in dense compact objects, either raising the gas entropy or even wiping out the gas from overdense regions. We note that our on–going star formation mostly takes place in the inner regions of the cluster. Hence, we expect that the AGN activity from the central CD galaxy or past cosmic heating from an earlier QSOs population can be crucial further ingredient in the cauldron of cluster and galaxy evolution. Furthermore, as we know that black holes are harbored at the centre of massive CDs in the innermost part of clusters, a possible conjecture is to imagine that the gas collapse that we found could be a “mass

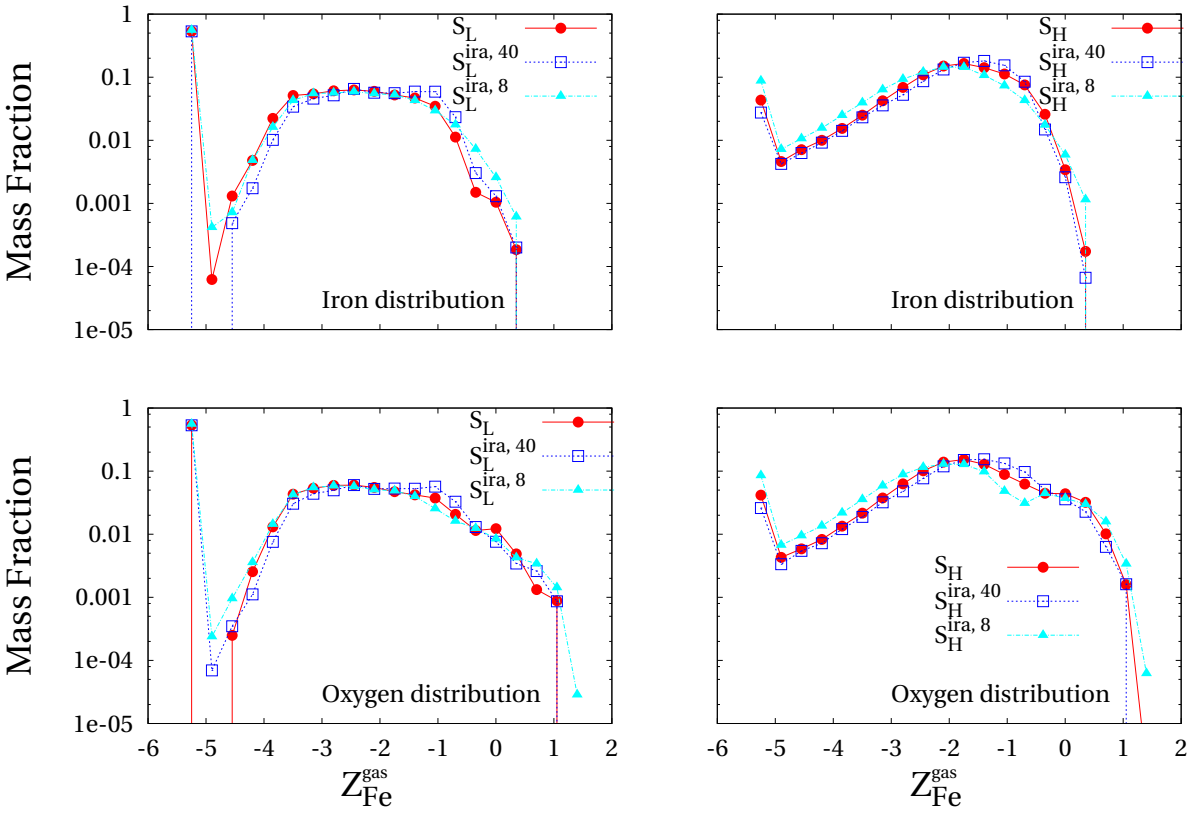

Figure 5.11: The distribution of Iron and Oxygen abundance in the gas. **Left** and **Right Column** show respectively the low– and high–resolution results, **Upper** and **Bottom line** show respectively the distribution of Iron and Oxygen. Continuous line with filled-circles indicates the $S_{L/H}$ simulations, short–dashed filled-square line indicates the $S_{L/H}^{ira40}$ run and dot–dashed filled–triangles line indicates the $S_{L/H}^{a\tau}$ runs.

deposition" to such an object; in fact, this is becoming the most accounted hypothesis to explain the "cool core" structure of galaxy clusters.

Recently formed stars, besides ejecting heavy elements in the ICM, also lock the metals that already were in the gas, as they basically form in enriched environments. Thus, having a significant star formation for $z \lesssim 1$ greatly affects the final amount of metals in a non trivial way. Bottom Right Panels of Fig. (5.2) and Fig. (5.4) show, for each element, the mass fraction which ends in the hot phase at $z = 0$, whereas Fig. (5.10) shows the value of mean Iron and Oxygen abundance of gas as a function of redshift. Several interesting details can be drawn from these figures. We first note that α elements and Iron–peak elements exhibit a different behaviour, owing to the different timescales of their respective release (accordingly, elements like the Silicon, which are produced significantly by both SnII and SnIa, behave in an intermediate way). It turns out that the Iron is the more distributed in the hot gas, while Oxygen (that we take

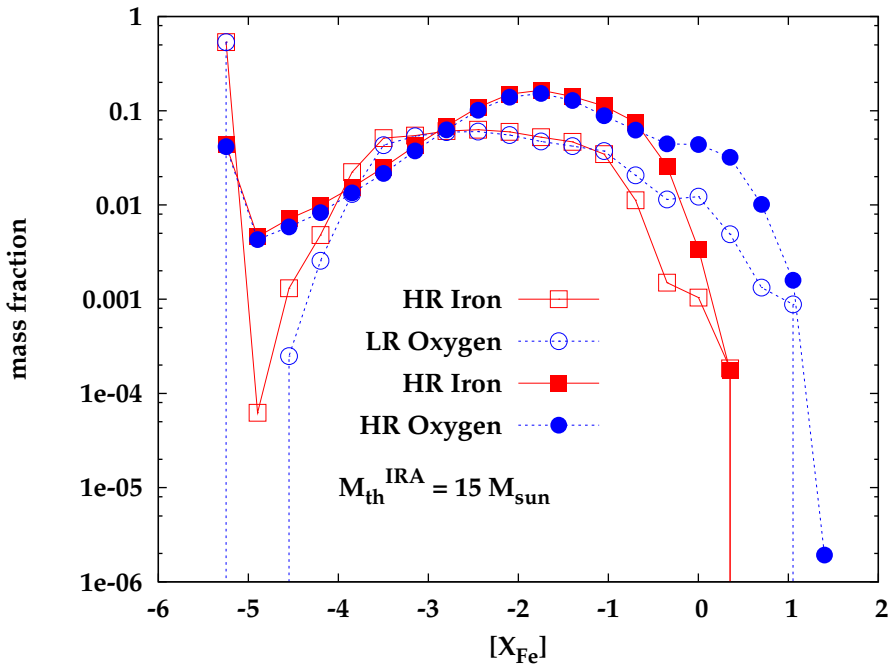

Figure 5.12: We plot here the abundance of Iron and Oxygen in $M_{th}^{IRA} = 15\,M_{\odot}$ simulation both for Low– and High–Resolution. This is to make clearer the difference between the two elements and between the two resolutions.

as a prototype of α elements) is more locked in stars. Oxygen is produced basically by SnII and about 30% of it is synthetized by stars more massive than $40\,M_{\odot}$ (see Sec. (4.4.5)), while $\sim 80\%$ of the total amount is ejected by stars more massive than $15\,M_{\odot}$. Then, the Oxygen is ejected over a timescale that is comparable to the timescale of Star Particle creation, so that the gas dynamics or winds' onset are likely to have no time to displace the enriched gas from the region of strong star formation. Hence, Oxygen is promptly locked in subsequent star formation events. All this does not hold for the Iron; due to its delayed production, its deposition is more determined by gas and stellar dynamics rather than by instantaneous environmental conditions.

Besides this general trend, which holds for all the simulations that are discussed in the Chapter, important differences arise among different simulations.
Similarly to the SFR, Low–Resolution results are affected by the coarser sampling due to the larger size of mass of the single particle. Thus, the sharing of metals between stars and gas is more unfavourable to the gas than in High–Resolution results. This is not due to the larger mass of stars but rather to the mass of gas particles. To check this we run a Low-Resolution simulation, like the $S_L^{IRA,15}$ one, but with 12 stellar generation (i.e. $N_G^{\star} = 12$). If the trends that we described before was depends mostly on this parameter we would expect some major changes in this second run. Instead, the differences are quite negligible and the most relevant ones arise in the sharing of

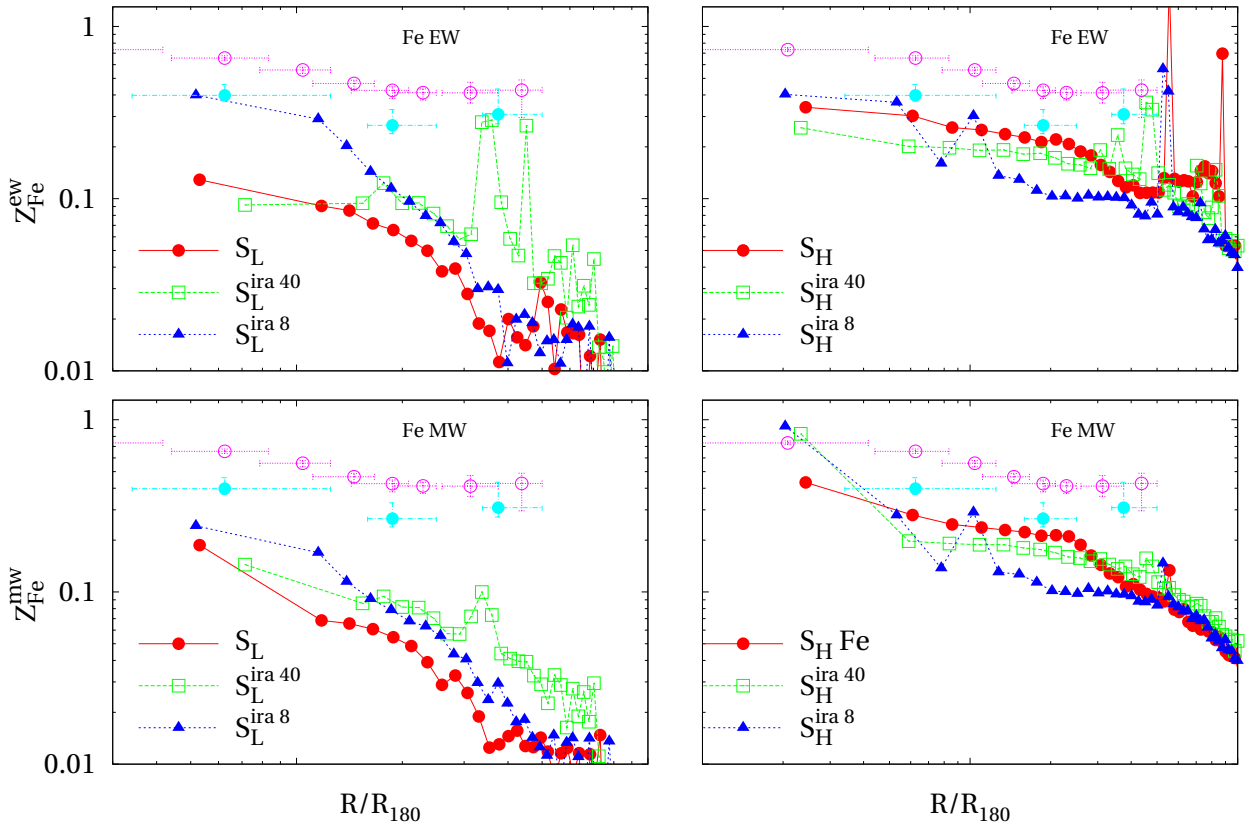

Figure 5.13: Radial profiles of Iron abundance. **Left Column** shows the Low–Resolution results, whereas the **Right Column** shows the High-Resolution ones. The S_L and S_H runs are plotted with filled circles, while the simulations having $M_{th}^{IRA} = 8\,M_\odot$ and $M_{th}^{IRA} = 40\,M_\odot$ are plotted with empty squares and filled triangles respectively. In the **Upper Row** we plot the emission-weighted profiles and in the **Bottom Row** we plot the mass-weighted ones.

Iron and Oxygen. We just mention, without reporting any viewgraph, that the Iron fraction which remains in gas raises from ~ 0.096 up to ~ 0.11 ($\sim 13\%$ variation), whereas the Oxygen mass fraction in gas raise from ~ 0.037 up to ~ 0.044 ($\sim 24\%$). Rather than witnessing an increasingly important role played by the Star Particle's mass, this underlines the different behaviour of these two elements as for their final destination. Having a four times larger number of stellar generations makes higher the probability of Star Particle creation for a given a star formation rate, so that also Gas Particles which do not have the a strong star formation activity are involved. This amounts to enhance the accuracy with which the Star formation process describes the star formation activity in a given volume. Somehow, also the "time resolution" of Star formation is enhanced: having a higher value of $N_G^\star$ leaves more time to a Gas

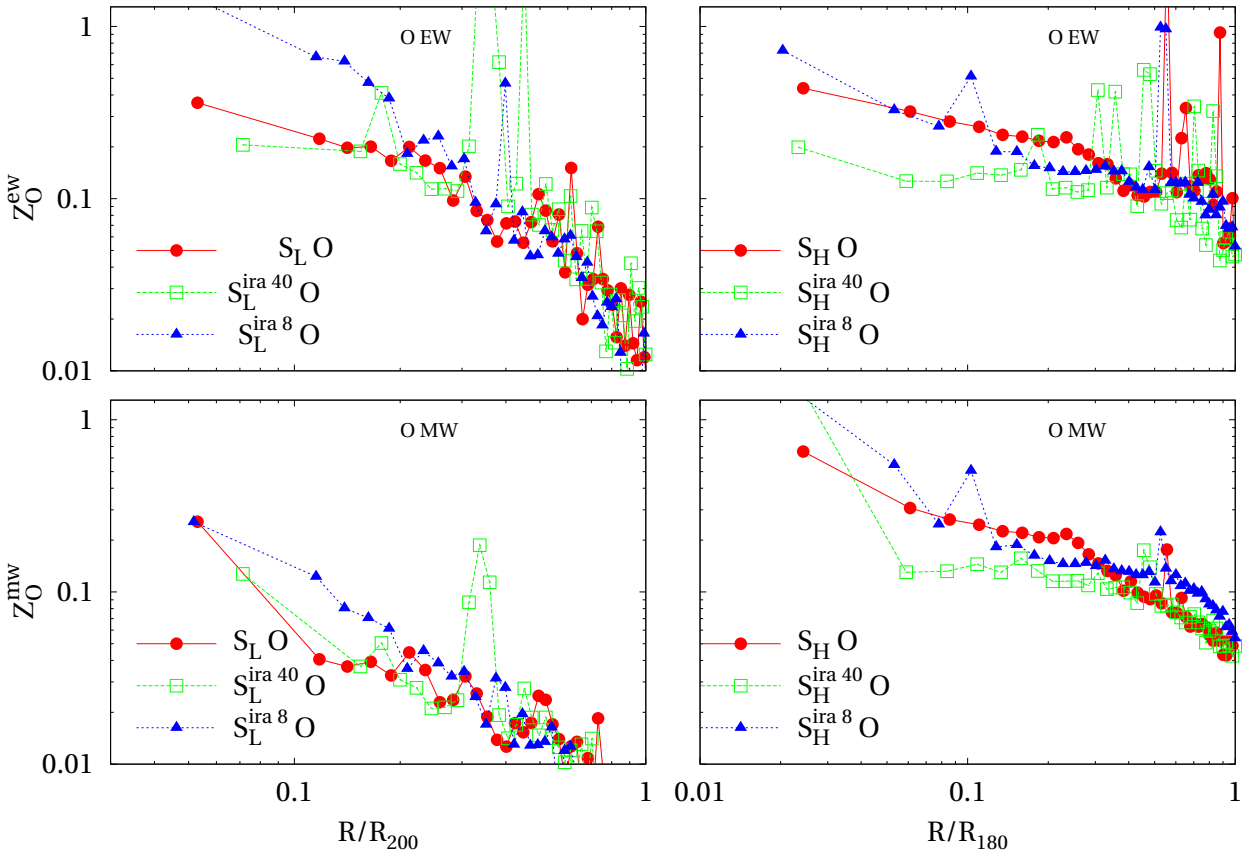

Figure 5.14: Radial profiles of Oxygen abundance. Colors and symbols are the same than in Fig. (5.13)

Particle to receipt the local thermodynamical conditions before letting a non–negligible fraction of its mass to transfer into the stellar phase. Still, in this simulation differences are not dramatic. From them we can draw the conclusions that: (1) the mass of gas particle drives what we can call the "enrichment resolution", (2) using $N_G^\star = 3$ is fairly adequate to the gas mass we have and (3) the rate at which the gas is locked in Star Particles affects significantly the relative amounts of quickly produced elements, like Oxygen, present in gas and stars.

We also note that raising the mass resolution largely increases the presence of metals in the gas. While both the star mass and the Iron mass within the virial radius do not change by more than 10%, the mass fractions of Iron and Oxygen which remains in the gas grow by up to a factor of 5. Fig. (5.11) shows how much mass has a given Iron and Oxygen abundance and how this distribution changes when the mass resolution increases. We take the $M_{th}^{IRA} = 15\,\mathrm{M}_\odot$ simulations as an example (the other two cases exhibit the same behaviour). The fraction of mass which is not enriched (we include on

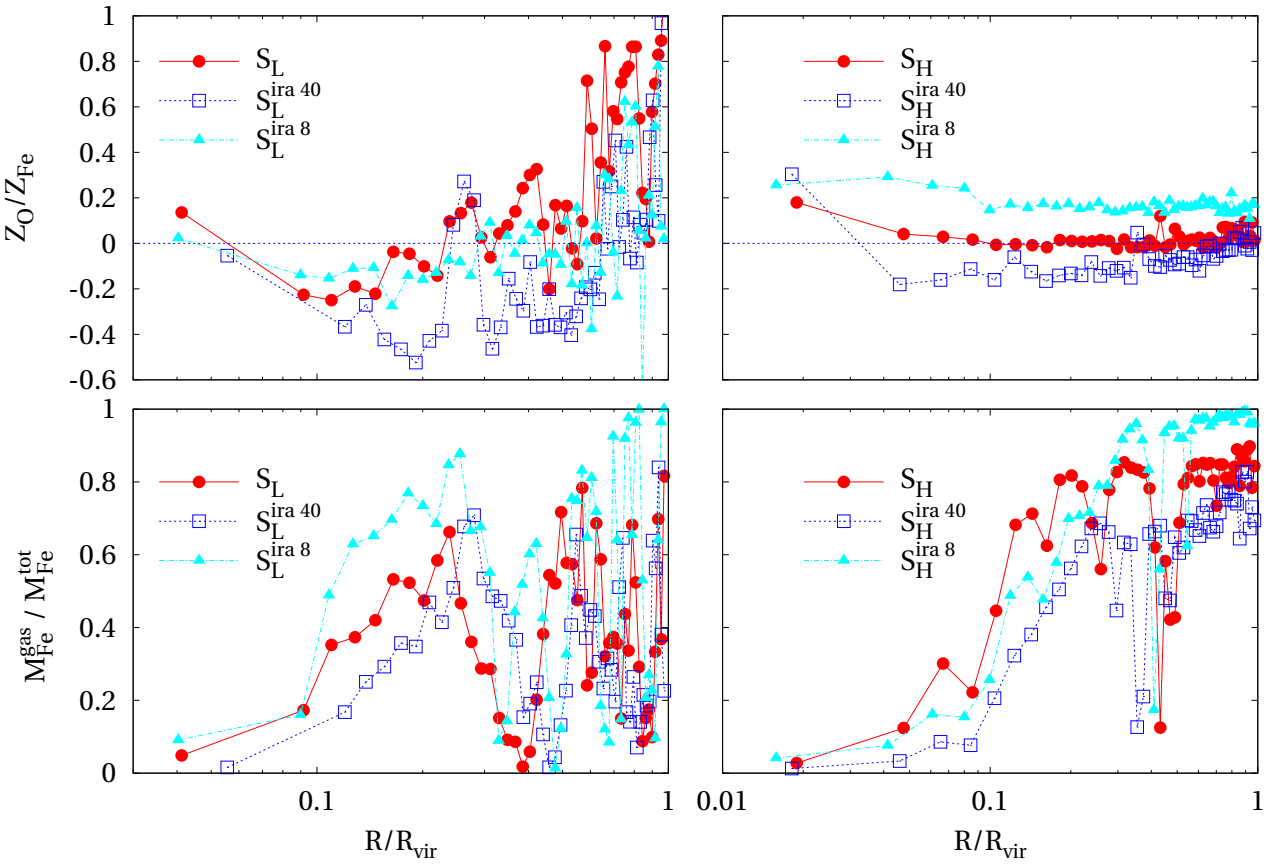

Figure 5.15: Low– and high–resolution results are plotted respectively in **Left** and **Right Column**. [**Upper Row**] The Oxygen over Iron abundance ratio in log–solar units. Straight dotted line indicates the solar value. Continuous line with filled circles stands for $S_{L/H}$ runs, dotted empty–squares line stands for $S_{L/H}^{ira40}$ and dot-dashed filled–triangles line indicates the $S_{L/H}^{ira8}$ run. [**Bottom Row**] The mass fraction of Iron harbored in the ICM as a function of distance from centre. Lines are coded as for the Upper Row.

the last bin in Fig. (5.11) all the gas particles having $[X/H] \leq -5$, where X indicates for either Fe or O) shrinks by an order of magnitude in High–Resolution simulations, and becomes less than 10%. Furthermore, the fraction of gas at moderate or high metallicities ($[X/H] \gtrsim -2$) is larger by a factor of two or three. In Fig. (5.10) it is evident how the mean metallicity of the gas in Low–Resolution runs shrinks after the epoch of strong star formation (note how this effect is much more pronounced for the Oxygen). High–Resolution simulations suffer for the same loss of Oxygen content only mildly and not at all as for the Iron. Considering what we discussed before, we interpret this fact as the signature of a higher accuracy in the resolution of the Star formation in High–Resolution simulations.

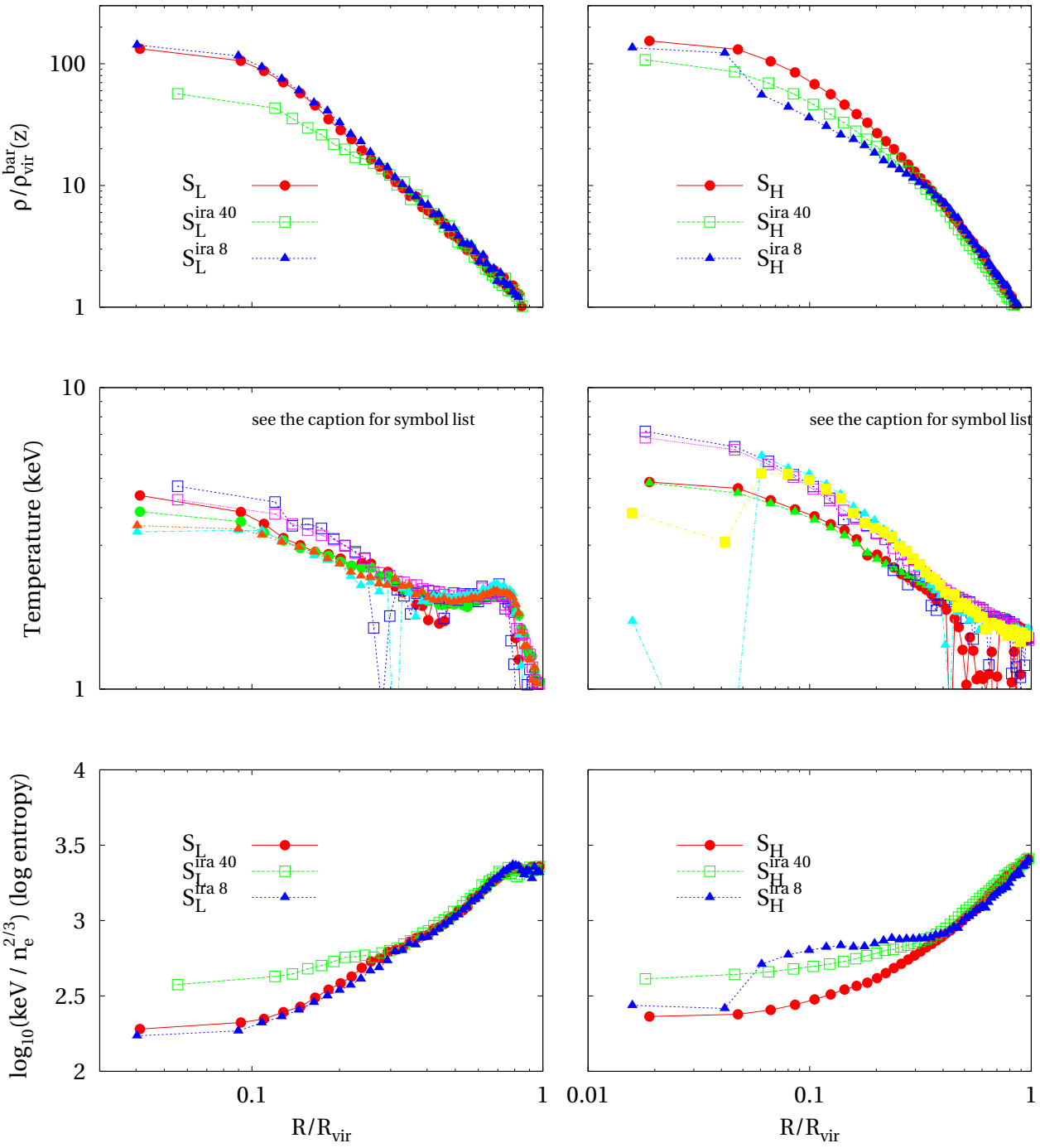

Figure 5.16: Thermodynamical properties in $S_{L/H}$, $S^{ira8}_{L/H}$ and $S^{ira40}_{L/H}$ simulations.

Figures (5.13), (5.14) and (5.15) are helpful to obtain insights about the differences among the three simulations that are discussed here. The bottom Panels of Figures (5.13) and (5.14) show the abundance profiles of Iron and Oxygen respectively, while the upper rows of the same Figures show the emission–weighted abundances. These are defined for each element species as

$$Z^{ew} = \frac{\sum_{i=1}^{N} \tilde{\Lambda}_i \rho_i^2 X_{s,i}}{\sum_{i=1}^{N} \tilde{\Lambda}_i \rho_i^2} \tag{5.1}$$

where sums are over the interested volume. This quantity is more related to the observed abundance as the regions whose emissivity is larger will be correspondingly more weighted. In the following we consider the mass–weighted profiles as they directly reflect the underlying radial distribution of elements. We also refer to High–Resolution results if not explicit stated otherwise.

We observe that the Low–Resolution simulations exhibit a far too low Iron abundance (see Fig. (5.13), filled circles with errorbars are obervations by (De Grandi & Molendi 2001)) due to the large fraction of metals locked in stars. Anyway, also the High–Resolution runs do not succeed in reproducing the correct amount of Iron, though the $M_{th}^{IRA} = 15\,\mathrm{M}_{\odot}$ simulation is very close to the abundance level of non cooling core clusters. It turns out that a value of about $\sim 15\,\mathrm{M}_{\odot}$ as for the threshold M_{th}^{IRA}, maximize the deposition of metals into the gas. The $M_{th}^{IRA} = 40\,\mathrm{M}_{\odot}$ exhibits the flatter profiles both for Iron and for Oxygen abundances, whereas steeply raising in the innermost region.

As for the relative abundances of Iron and Oxygen (Fig. (5.15), Upper Panels), the higher the value of M_{th}^{IRA}, the higher is the $[O/Fe]$ ratio. In the very centre of cluster all simulations exhibit the same value $[O/Fe] \simeq 0.2$, as the recent star formation that take place in those regions makes the quickly formed Oxygen to dominate the metal budget. What is interesting is that the $S_H^{IRA,15}$ simulation reproduce the same relative abundance of the sun apart very closely to the centre as we have just mentioned, while lowering or raising the value of M_{th}^{IRA}produce systematically values larger and smaller by about $\sim 0.2\,\mathrm{dex}$. All Low–Resolution simulations have an undersolar value of $[O/Fe]$ within half of the virial radius whereas having a rather oversolar (up to 10 times) at larger radii. Nevertheless, Low–Resolution profiles exhibit a large scatter, so that no well–defined trend can be inferred from them. Both in Low– and High–Resolution simulations, the ratio between the mass fractions of Iron and Oxygen present in the gas is larger than unity (about 2–2.5 in the central region and 1.5 in the innermost part) and approaches unity in the outskirts. Low–Resolution simulations have larger values of this ratio, and both in Low– and High–Resolution runs the $M_{th}^{IRA} = 40\,\mathrm{M}_{\odot}$ has the highest values and $M_{th}^{IRA} = 8\,\mathrm{M}_{\odot}$ the lowest. Differences between simulations with different values of M_{th}^{IRA}relate to the different star formation histories, while the tendency to approach unity in the outermost regions is mainly due to the fact that

here the star formation activity stopped at earlier times, so that a greater fraction of Oxygen is still hosted by gas and has not been locked in stars. This is witnessed also by the fraction of Iron mass (bottom panels of Fig. (5.15)) present in gas, approaching the highest value for $r/r_{\rm vir} \sim 1$
Since the relative abundance of elements in the gas is a key factor in order to decide whether an IMF may reproduce or not the star formation in clusters, this reveals to be an important effect to be taken under control. Alternatively, instead of a purely numerical issue, it may be taken as a warning that changing the physical conditions of star formation environment (namely how much energy is effectively recycled in the process) has a large impact on final results.

Finally, we note from Fig. (5.16) that the choice for M_{th}^{IRA}also affects significantly the thermodynamics of the ICM, though it is quite difficult to trace the complete history of each change due to non trivial interplay among different physical effects.

■ Summary

We have shown the effect of changing the threshold of M_{th}^{IRA}parameter for the three different value $40\,{\rm M}_\odot$, $15\,{\rm M}_\odot$ and $8\,{\rm M}_\odot$, which correspond to consider as promptly available in the effective model $\sim 8\%$, $\sim 40\%$ and 100% of the energy coming from SnIIrespectively. We stress that this parameter should not be considered as purely numerical, as it roughly includes in our models the interaction between the energy of exploding supernovae with the star forming gas. From our results we can draw the following conclusions:

[**1**] The Mass resolution is one key ingredient in order to properly describe the star formation process and the distribution of metals between the gas and the star phase;

[**2**] The value of M_{th}^{IRA}turns out to have an important impact on the final results, above all on the relative abundances between α elements and Iron–peak elements;

[**3**] The first way in which the value of M_{th}^{IRA}affects the results is influencing the star formation history. Basically, the higher its value, the weaker the feedback on the gas, thus, the higher is the star formation rate;

[**4**] An higher star formation rate does not lead to a higher enrichment level; rather, it ends up in a larger fraction of metals to be locked in stars. This is mainly due to the fact that the star formation will continue significantly also at low redshift;

[**5**] The value of M_{th}^{IRA}affects the amount of metals that are immediately assigned to gas particles of being spread by a Star Particle. This is reflected on the distribution of these elements in the gas;

[**6**] The choice $M_{th}^{IRA} \simeq 15\,\mathrm{M}_{\odot}$ tends to maximize the amount of Iron and Oxygen in the gas.

As a word of caution, we stress that in the simulations presented in this Section the velocity of winds, v_w, changes together with the value of M_{th}^{IRA}. According to Eq. (4.8), the value of v_w depends on both the value of β, which is the mass fraction of stars with mass $m > M_{th}^{IRA}$, and u_{SN}, which is proportional to the energy per gram due to IRA SnII, namely ϵ_{SN}. This means that here we are not disentangling the effect of having stronger or weaker winds from that of having a larger or smaller energy available in the effective model. Since winds can strongly affect the patterns of both star formation and enrichment (see Sec. (5.9)), in order to better understand how the value of M_{th}^{IRA}influences the results it would be necessary to run the same simulations discussed above but keeping v_w to the same value for all simulations. In Sec. (5.8), we present simulations with different IMFs and the same value as for v_w. Changing the IMF implies changing of ϵ_{SN} as well as M_{th}^{IRA}. Nevertheless, we show in that discussion that the pattern of star formation is not affected by a larger value of ϵ_{SN} as much as in $S_H^{IRA,15}$. Hence, we close this summary by outlining that what we have presented here are the combined effects of a larger (smaller) ϵ_{SN} and larger (smaller) wind's velocity.

5.5 The Metal–Dependent Effective Model

In Sec. (4.7) we have mentioned the importance of making the star formation process sensitive to the metal content of the gas. Here we further discuss the same topic, giving more details on our implementation; results will be shown from two Low–Resolution simulations having this dependence set on and off.

Since we choose to use the Sutherland & Dopita (1993) cooling function, our cooling is actually dependent on the Iron content of the gas through the value of $[Fe/H]$; throughout this Section, we refer to this value as the "metallicity" Z of the gas.

We have changed several details in the original effective model by Springel & Hernquist (2003a) in order to make it sensitive to the additional physics that we have implemented. In the following we discuss all such changes:

[**1**] Following (McKee & Ostriker 1977) the evaporation efficiency A in Eq. (3.73) is calculated as

$$A = A_0 \cdot \left(\frac{\rho}{\rho_{th}}\right)^{-4/5}. \tag{5.2}$$

The value of A_0 is fixed by requiring that at the onset of the star formation ($\rho = \rho_{th}$) the thermal instability is operating. This amounts to require that the temperature at which the star formation sets on is exactly the temperature at which the thermal instability also begins to operate. Such a temperature is the

$[Fe/H]$	$T_{\rm Th.Inst.}$
-4.0	$10^{4.9}$
-3.0	$10^{4.9}$
-2.0	$10^{4.95}$
-1.5	$10^{5.35}$
-1.0	$10^{5.35}$
-0.5	$10^{5.35}$
0	$10^{5.35}$
0.5	$10^{5.35}$

Table 5.4: The temperature $T_{\rm Th.Inst.}$ values for the onset of thermal instability for different values of the Fe abundance.

one at which the derivative of the cooling function becomes negative. For the standard cooling function due to a pristine gas made by 76% of H and 24% of He, the thermal instability starts at $T_{th.inst.} \sim 10^5\,{\rm K}$. Therefore, we require

$$T_{SN}/A_0 = 10^5\,{\rm K}$$

where u_{SN} is interpreted as a "supernova temperature" $T_{SN} = 2\mu\,u_{SN}/(3k) \sim 10^8\,{\rm K}$. This results in

$$A_0 = 1000 \tag{5.3}$$

that is the value set by Springel & Hernquist (2003a).
When we consider the metal–dependent cooling function, the point for the onset of the thermal instability shifts towards higher temperatures, as can be seen in Fig. (4.11). In Tab. (5.4) we report the values we choose. Note that we do not use $T = 10^5\,{\rm K}$ any longer also for zero–metallicity gas.

[**2**] As it is argued by Springel & Hernquist (2003a), the value for ρ_{th} is given by imposing the pressure to be a continuous function of the density at the edges of the regime of the self–regulated star formation. The gas just below the threshold cools down to $10^4\,{\rm K}$, as long as we ignore further cooling due to molecules. Therefore, requiring that $u_{eff}(\rho_{th}) = u_4$ where u_{eff} is the effective energy density from Eq. (3.83) and u_4 is the energy density corresponding to a temperature of $10^4\,{\rm K}$, gives

$$\rho_{th} = \frac{x_{th}}{(1-x_{th})^2}\frac{\beta\,u_{SN} - (1-\beta)\,u_c}{t_0^\star\,\Lambda(U_{SN}/A_0)} \tag{5.4}$$

where $x_{th} \sim 1 - A_0\,u_4/u_{SN}$ is the mass fraction in clouds at the threshold and $\Lambda(\rho,u) = \Lambda_{net}(\rho,u)/\rho^2$.

[**3**] By the discussion at the point (1), A_0 in the previous equation has already been made dependent on the metallicity; β and u_{SN} depend on the value of M_{th}^{IRA}, and Λ is an explicit function of $[Fe/H]$.

Therefore, by computing the values for ρ_{th} using Eq. (5.4), we obtain the density threshold as a function of metallicity. Fig. (5.17) shows these values for different IMFs and choices for M_{th}^{IRA}.

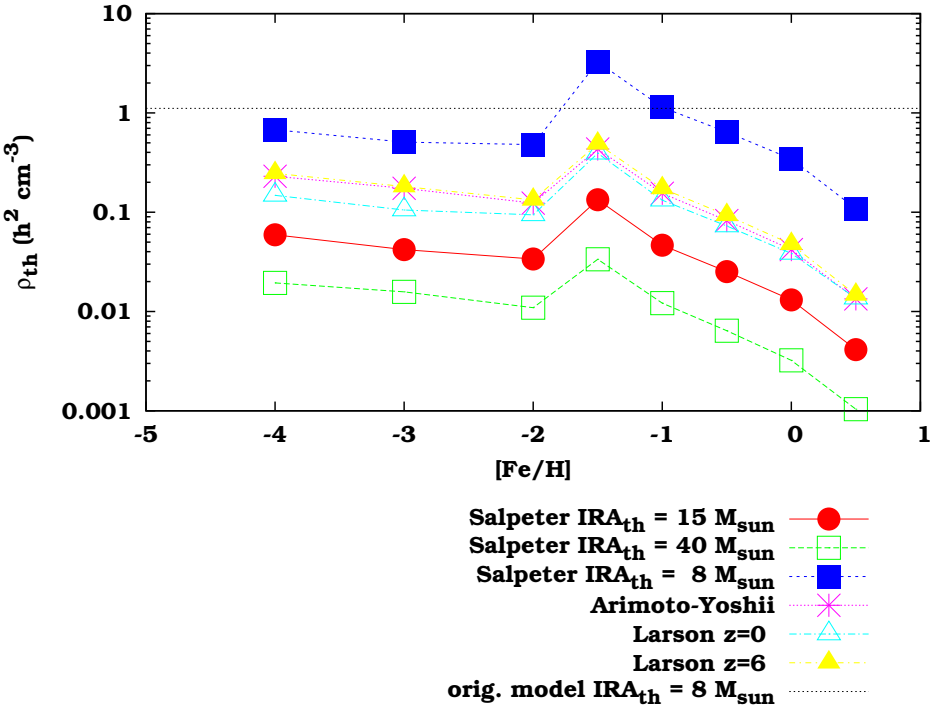

Figure 5.17: The density threshold for the onset of multi–phase model of star formation. *Dotted Line* shows the value obtained without dependence on gas metallicity and having all the SnII promptly recycled in the star formation. Other lines indicate the threshold values as a function of the gas metallicity, for different IMFs and choices of M_{th}^{IRA}. *Filled Circles, Empty* and *Filled Squares* indicate the Salpeter IMF with respectively M_{th}^{IRA}= $15\,M_\odot$, $40\,M_\odot$, $8\,M_\odot$. *Stars* indicate the Arimoto–Yoshii IMF whereas *Empty* and *Filled Triangles* show the Larson IMF at respectively $z = 0$ and $z = 5$. For the Arimoto–Yoshii and Larson IMF the value of $M_{th}^{IRA}$is $15\,M_\odot$.

The dotted line shows the ρ_{th} value when all the described dependencies are switched off. Instead, the filled-square line is obtained for $M_{th}^{IRA} = 8\,M_\odot$, so as the u_{SN} and β parameters have the same value as in the previous case. Therefore, the comparison between the dotted and the filled–square lines gives the importance of the metal cooling as for the onset of star formation, with no other factors playing any role. Note that the value for $Z = -4$ of the filled-square line is only $\sim 60\%$ of the one in the original case (dotted line); this is the effect of having fixed the thermal instability onset temperature

for $Z = -4$ to $10^{4.9}$ instead of 10^5 as in the original formulation. The sudden increase of ρ_{th} at $Z = -1.5$ is due to the growth of $T_{th.inst.}$ from $10^{4.9}$ to $10^{5.35}$.

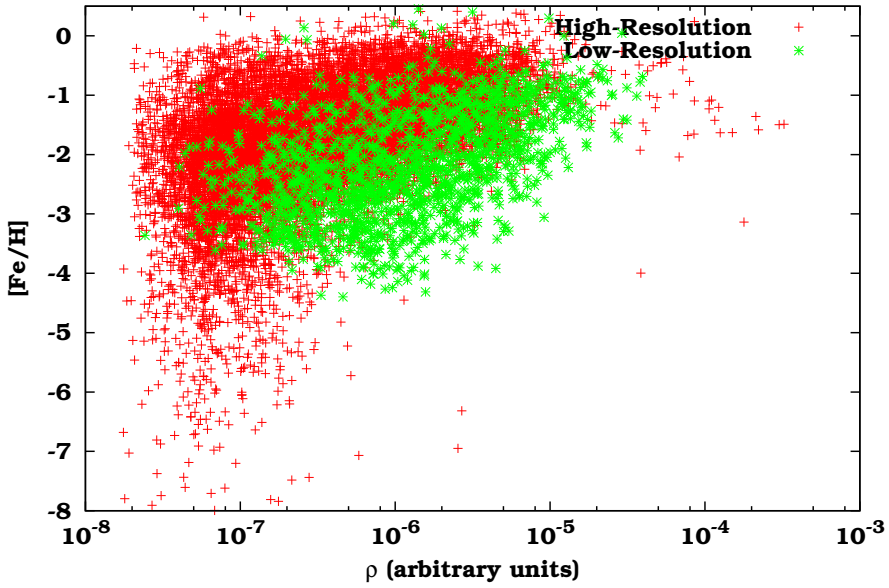

Figure 5.18: The distribution of the Iron content with the density of the gas for the S_L (*asteriscs*) and S_H (*crosses*) simulations. One point every 20 and one point every 5 has been plotted for respectively the High–Resolution and the Low–Resolution run.

Apart from the presence of this barrier, the trend is that the density threshold decreases as the metallicity, and thus the cooling efficiency, increases. For all plotted curves, the variation of ρ_{th} from the lower Z to the higher metallicity is of about one order of magnitude or, meaning that the star formation would occur in regions with lower and lower densities as they become more and more enriched. Nevertheless, the high metallicities are reached mostly in very high density regions, as it is shown in Fig. (5.18), so that no run–away process takes place.

The second important note is that the density threshold decreases or increases as the energy amount from short–living stars respectively is reduced or increased, as effect of both lowering or raising $M_{th}^{IRA}$and changing the IMF. This is the reason why the curve corresponding to $M_{th}^{IRA} = 40\,\mathrm{M}_\odot$ with a Salpeter IMF (empty-square) has the lowest values, whereas both the Arimoto–Yoshii (starred symbols) and the Larson (empty and filled triangles) IMFs show the largest values among the simulations with $M_{th}^{IRA} = 15\,\mathrm{M}_\odot$.

We run the $S_L^\dagger$ simulation having ρ_{th} set at the level of dotted line in Fig. (5.17) to

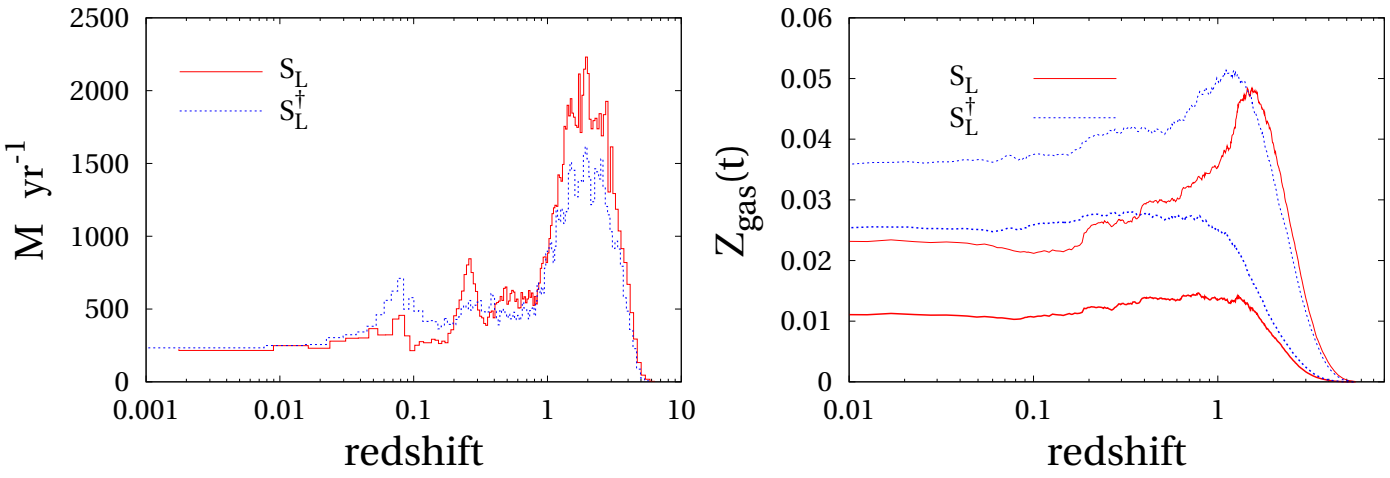

Figure 5.19: [**Left Panel**] The history of star formation rate. Continuous line indicates the S_L run. [**Rigth Panel**] The mean Iron (heaviest lines) and Oxygen (lightest lines) abundance of gas in both S_L (continuous line) and $S_L^\dagger$ (dotted line).

understand how results change when the dependency of ρ_{th} both on $M_{th}^{IRA}$and on gas metallicity is set off.

Figures (5.19), (5.1) and (5.2) anticipate how final results differ from S_L. Having a higher density threshold and a larger energy from supernovae suppress the star formation at high redshift in the $S_L^\dagger$ run (see Left Panel of Fig. (5.19)) so that the star fraction is about 13% smaller than in S_L. The locking of both Iron and Oxygen in stars is then less efficient (Right Panel of Fig. (5.19)) and the mass fractions of Ion and Oxygen in the hot gas are respectively $\sim 50\%$ and $\sim 250\%$ higher in $S_L^\dagger$ than in S_L. In turn, overall mass–weighted metallicities of gas within the virial radius are respectively $\sim 30\%$ and 100% higher. The graphviews in the Upper Row of Fig. (5.21) show that changes in the mass–metallicity distribution involve only the very high metallicity bins, whose population grows by a factor of $2-3$ in $S_L^\dagger$ with respect to S_L. The Bottom Right Panel of the same figure shows that the fraction of Iron which remains in the gas is generally larger in $S_L\dagger$. Instead, the ratio $[O/Fe]$ (Bottom Left Panel, same figure) does not appreciably change. The radial abundance profiles shown in Fig. (5.21) exactly reflect what we discussed so far. As we expected, all the relevant thermodynamical properties do not change significantly (see Fig. (5.22)).

■ Summary

We have compared the results form the S_L simulation with those of $S_L^\dagger$ having the value of ρ_{th} which is independent of the gas metallicity and of M_{th}^{IRA}. The higher

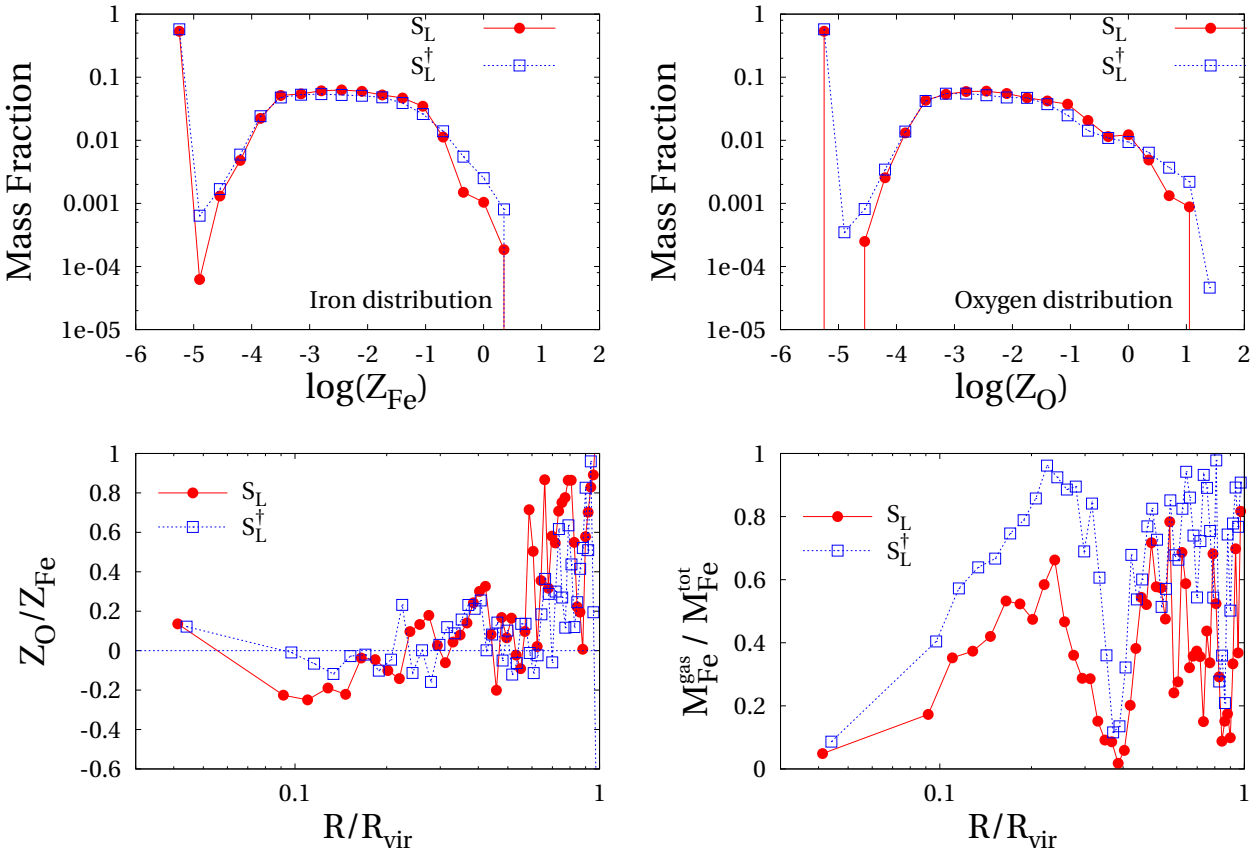

Figure 5.20: ,
Fraction of Fe locked in the ICM with and without the Metallicity–Dependence of the EM for SF] [**Top Left Panel**] The distribution of Iron–abundance. [**Top Right Panel**] The distribution of Oxygen–abundance. [**Bottom Left Panel**] The radial profile of $[O/Fe]$. [**Bottom Right Panel**] The fraction of Iron resident on the gas as a function of the radius.

value of the density threshold in $S_L^\dagger$ leads to a suppression of star formation and to an enhancement of the mass fraction of metals (Iron and Oxygen) resident in the hot–phase. Accordingly, the radial abundance profiles reach slightly higher values than in S_L.

5.6 Changing the Criteria of Star Formation

In the original GADGET code the only condition for the onset of Star Formation is given by the requirement that the density of the gas is larger than a physical threshold value. This might appear as not adequate to capture the complexity of physical processes at

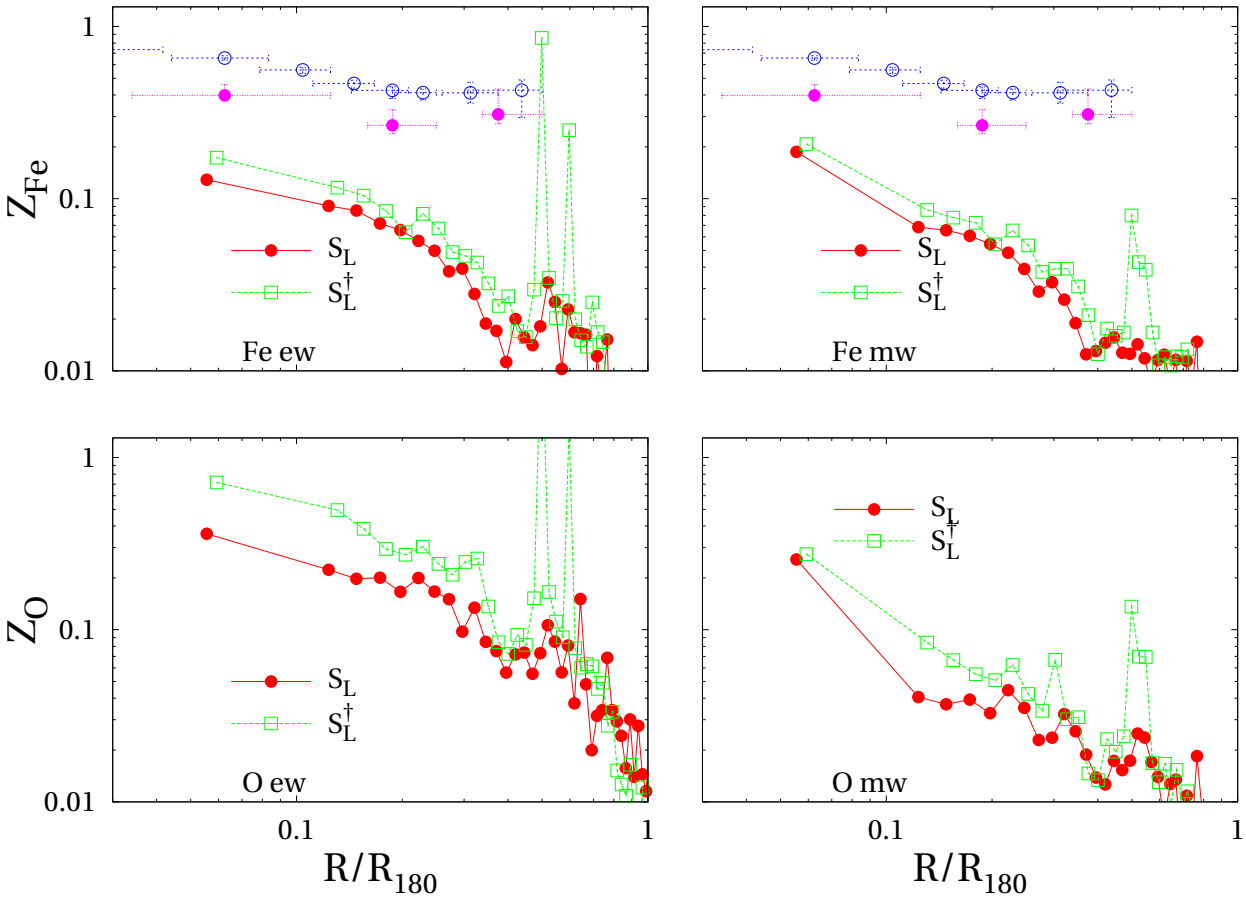

Figure 5.21: [**Top Left Panel**] The radial profile of emission–weighted Iron abundance. [**Top Right Panel**] The radial profile of mass–weighted Iron abundance. [**Bottom Left Panel**] The radial profile of emission–weighted Oxygen abundance. [**Bottom Right Panel**] The radial profile of mass–weighted Oxygen abundance.

work is considered. Thus, we have added two more constraints that must be fulfilled in order to let a Gas Particle becoming a multi–phase, star–forming particle. These conditions are the following:

[**1**] The gas *cooling time* is defined as $\epsilon\rho/(\Lambda n^2)$, where ϵ and ρ are the gas specific energy and density respectively, $\Lambda = \Lambda_{net}/n^2$ is the emissivity and n is the number density of hydrogen atoms. This quantity measure essentially the time–scale over which the entire energy of the gas would be radiated by a constant emissivity Λ. Then, we require that this time–scale is shorter than the *sound–crossing time*, that is defined as the time a pressure wave employs to cross the volume enclosing the same gas.
This basically means that the pressure support due to the internal energy of the

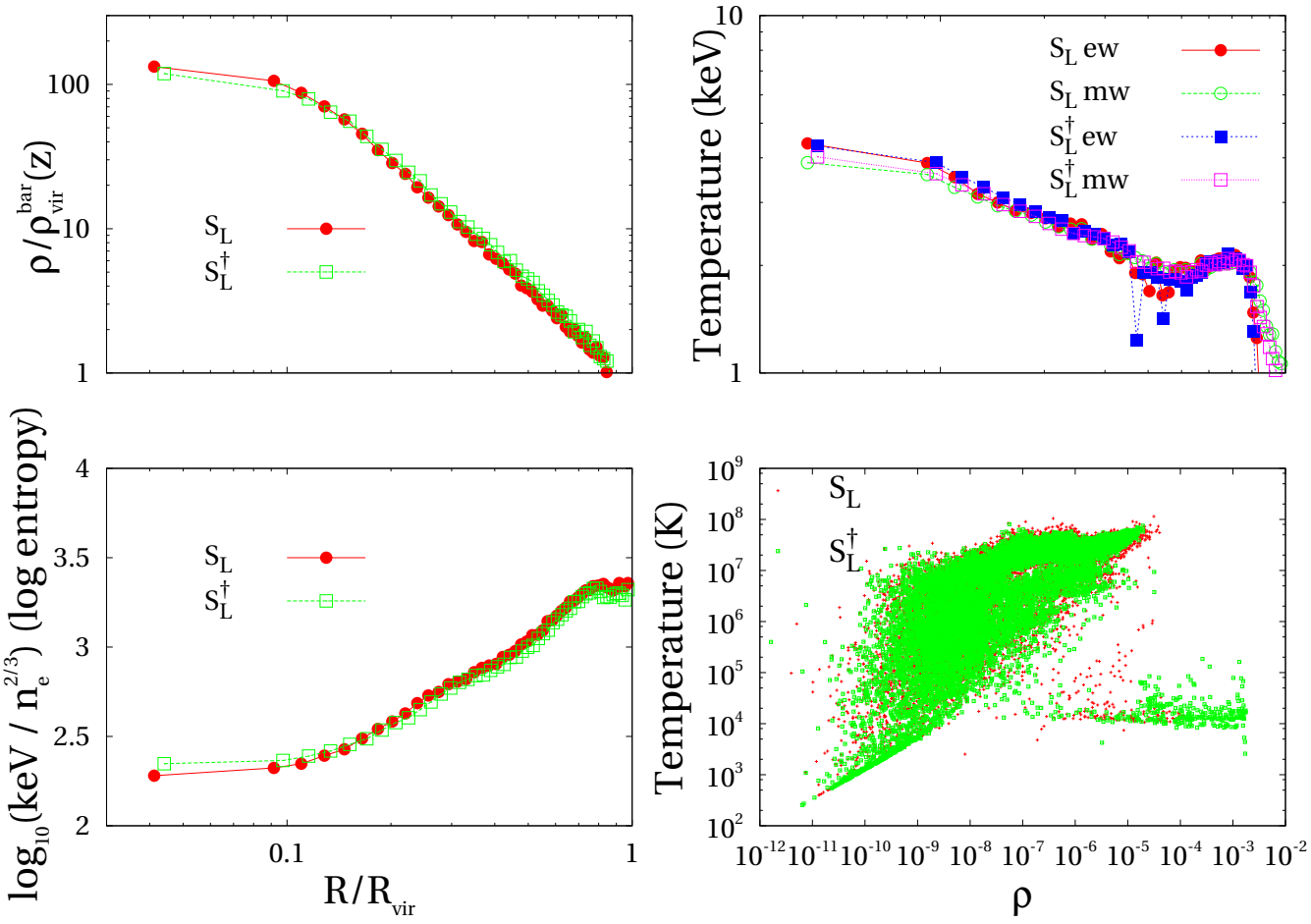

Figure 5.22: Thermodynamical properties of S_L and $S_L^\dagger$ simulations. Filled circles and empty squares indicate respectively the S_L and $S_L^\dagger$ simulation. [**Top Left Panel**] Radial density profile. [**Top Right Panel**] Emission–weighted (filled symbols) and mass-weighted (empty symbols) temperatures for both S_L (circles) and $S_L^\dagger$ (squares). [**Bottom Left Panel**] The radial entropy profile. [**Bottom Right Panel**] The ρ–T phase space for the hot–phase.

gas does not have time to counteract the compressional effect due to the energy loss. As the sound speed is equal to $(\gamma P/\rho)^{1/2}$, where P is the pressure and γ is the adiabatic index, this conditions reads as

$$t_{cool} < \left(\frac{m}{\rho}\right)^{1/3} / \sqrt{\gamma \frac{P}{\rho}}. \tag{5.5}$$

We estimate the scale–length of the volume occupied by the Gas Particle by using $(m/\rho)^{1/3}$.

[**2**] The second condition requires that the *free-fall time* is shorter than the *sound–crossing time*, i.e. the diem for gas collapse is shorter than the time that a pressure wave take to supply the internal support of the gas. This reads as

$$\frac{1}{\sqrt{G\,\rho}} < \left(\frac{m}{\rho}\right)^{1/3} / \sqrt{\gamma \frac{P}{\rho}}. \tag{5.6}$$

We have implemented this further two conditions in the code and let them to be either enabled or disabled. We run only a low–resolution simulation with them, the one labelled as $S_L^{c.t.}$.
The effectiveness of such conditions depends strongly on the metallicity of the gas, as the cooling rate will be much enhanced by the presence of heavy elements. In Fig. (5.23), the Top Right panel shows which particles fulfill each request.
The Bottom Right panel shows the particles which fulfill both (*dots*) and the particles having $\rho > \rho_{th}$ which do not (*filled triangles*). This latter panel, also shows (*empty squares*) the values for the hot–phase density and temperature of all particles with $\rho > \rho_t h$. The Bottom Left Panel shows what would have been the hot phase of th particles plotted with filled triangles in the Right Panel.
Condition [2] turns out to be more restrictive than Condition [1]; all GPs fullfilling the former also satisfy the condition on cooling time, whereas the opposite is not true, as can be seen in the Top Right panel of Fig. (5.23).

Only 2.3% of GPs fullfill both conditions (1) and (2). Nevertheless, we are not interested on all particles but just on those eligible to enter in the multi–phase star–forming regime. Of such particles, 66.7% fullfill both (1) and (2) while 33.3% satisfy (1) but not (2). These last particles are shown as filled triangles in the Bottom Right Panel of figure Fig. (5.23). They are prevented to collapse from keeping a large pressure support from the surrounding gas. The hot phase of gas taking part to the Star Formation is plotted in the same Panel with empty squares. If particles with $\rho > \rho_{th}$ are considered as multi–phase particles, their hot phase will result as in the Bottom Left Panel. Overall 29 particles, about 5%, which would all have $x \gtrsim 0.9$ are excluded from star formation.
In Fig. (5.24) we plot the SFR of both the S_L and the $S_L^{c.t}$ simulations. The net effect of including the constraints of Eq. (5.5) and Eq. (5.6) is to prevent gas having a strong pressure supply to form stars at high redshifts, while storing it in a warm/hot very dense phase that collapses at later time.

At $\mathbf{z = 2}$ the cold fraction of the proto–cluster in th S_L run is $\sim 20\%$ higher than in $S_L^{c.t.}$, and the star fraction is $\sim 45\%$ higher as well. Nevertheless, at $\mathbf{z = 0}$ the cold fraction of the cluster is higher by $\sim 45\%$ in the $S_L^{c.t.}$ simulation, whereas the star fraction is still larger by $\sim 15\%$ in S_L. Again this is due to the fact that $S_L^{c.t.}$ produces, at $z = 0$, slightly less star mass, while having a cold fraction twice as large as S_L

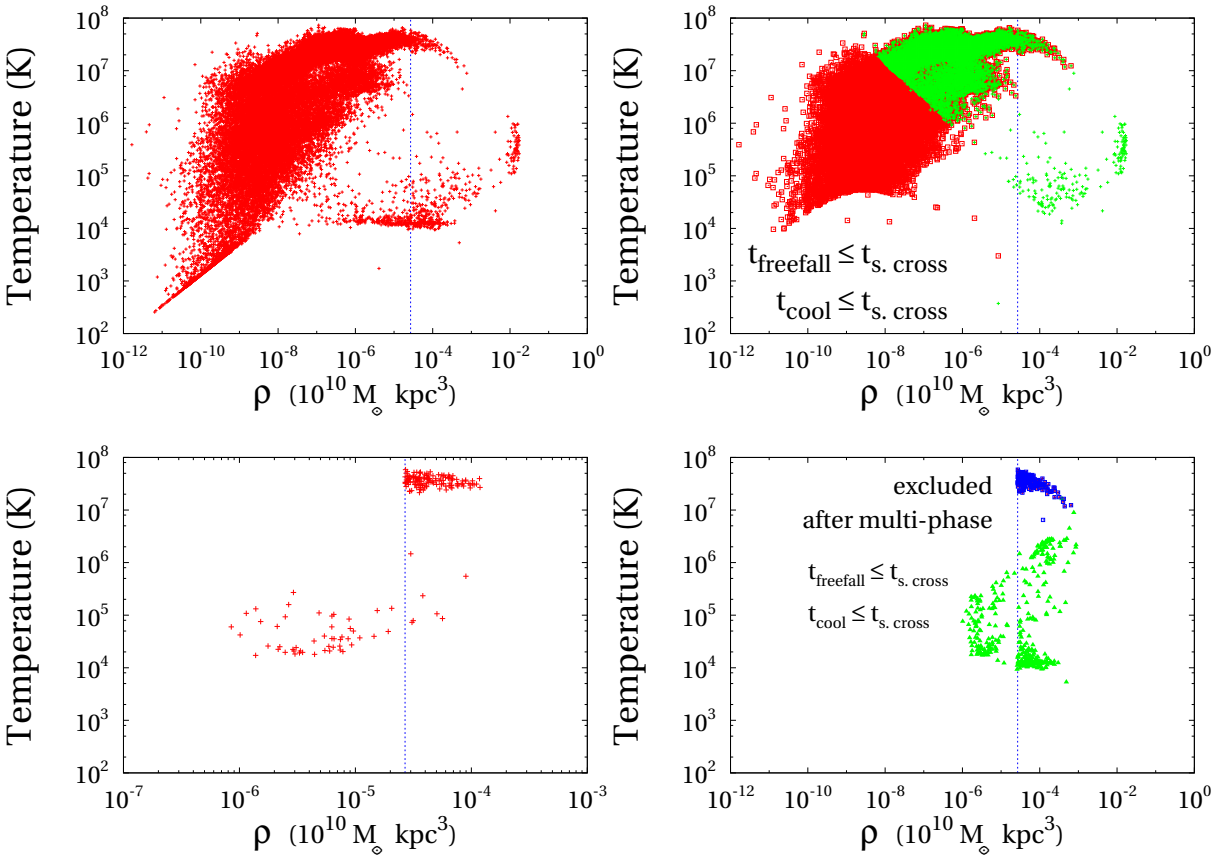

Figure 5.23: [**Top Left Panel**] The $\rho - T$ plane for the simulation $S_L^{c.t.}$ before the multi–phase algorithm is applied to particles. [**Top Right Panel**] Particles in $\rho - T$ plane which have a cooling–time t_{cool} shorter than their sound–crossing–time t_{sc} are shown with *dots*, whereas particles which have a free–fall time $t_{\rm ff}$ shorter than t_{sc} are shown with *empty squares*. [**Bottom Left Panel**] Phase diagram of particles having $\rho > \rho_{th}$ which do not satisfy either $t_{cool} \leq t_{sc}$ or $t_{\rm ff} \leq t_{sc}$. [**Bottom Right Panel**] Particles in $\rho - T$ plane with $\rho > \rho_{th}$ having both $t_{cool} \leq t_{sc}$ and $t_{\rm ff} \leq t_{sc}$, before (*little dots*) and after (*empty squares*) the multi–phase decomposition have been applied to them. Particles eligible to be multi–phase which do not satisfy one of the two conditions are plotted with filled triangles. – All data are taken from the snapshot at $z = 0$.Vertical dotted line shows the ρ_{th} for $[Fe/H] = 0.5$, which is the lowest ρ_{th} below which the multi–phase model switch off.

do. This also results in a lower mass-weighted temperature inside the virial radius. This can be inferred from Fig. (5.25) where we have plotted the hot and cold phases of gas for both S_L and $S_L^{c.t.}$ at $z = 2$ and $z = 0$ respectively in the Left and Right Panel. At high redshifts the "phase decomposition" of the two simulations is quite indistinguishable , while at late times much more gas has been pushed towards very high densities or high temperatures in the modified algorithm run.

In Fig. (5.26) we plot the radial profiles of some interesting thermodynamical and chemistry–related quantities; Top Left and Right Panels, Middle Left and Right

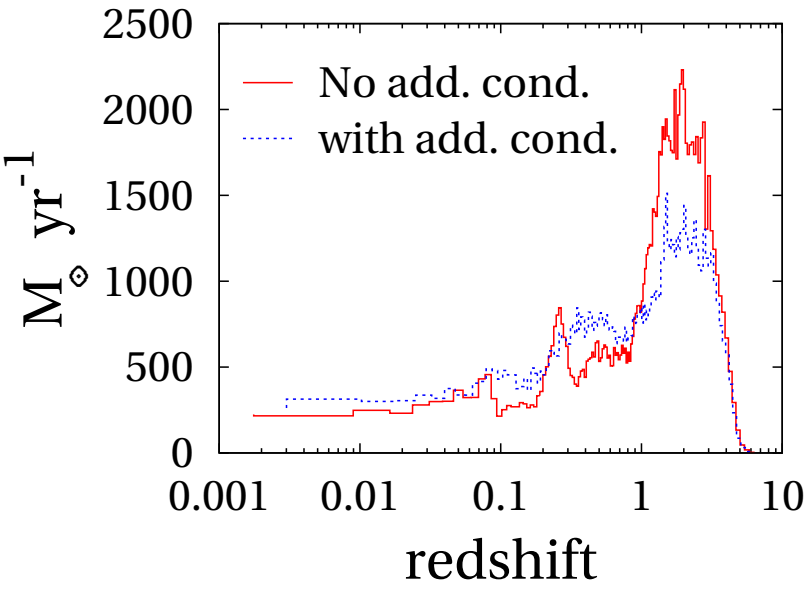

Figure 5.24: The Star Formation History of S_L (*continuous line*) and of $S_L^{c.t.}$ (*dashed line*).

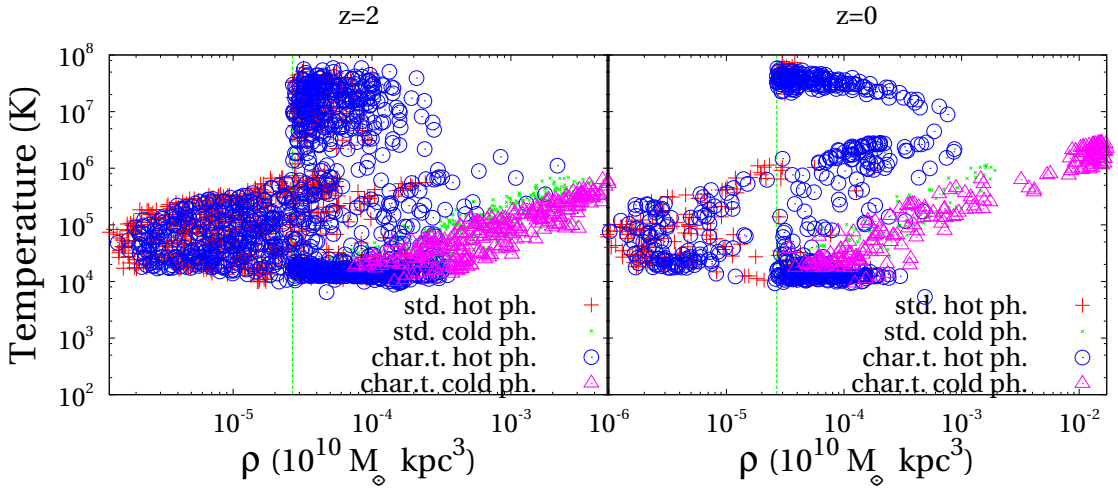

Figure 5.25: Hot and Cold Phase for multi–phase particles at $z = 2$ [**Left Panel**] and $z = 0$ [**Right Panel**]. Hot and cold phases for S_L run are plotted respectively with crosses and points, whereas those for $S_L^{c.t.}$ run are plotted using respectively empty circles and triangles. The vertical dashed line indicates the vale of ρ_{th} for $[Fe/H] = 0.5$.

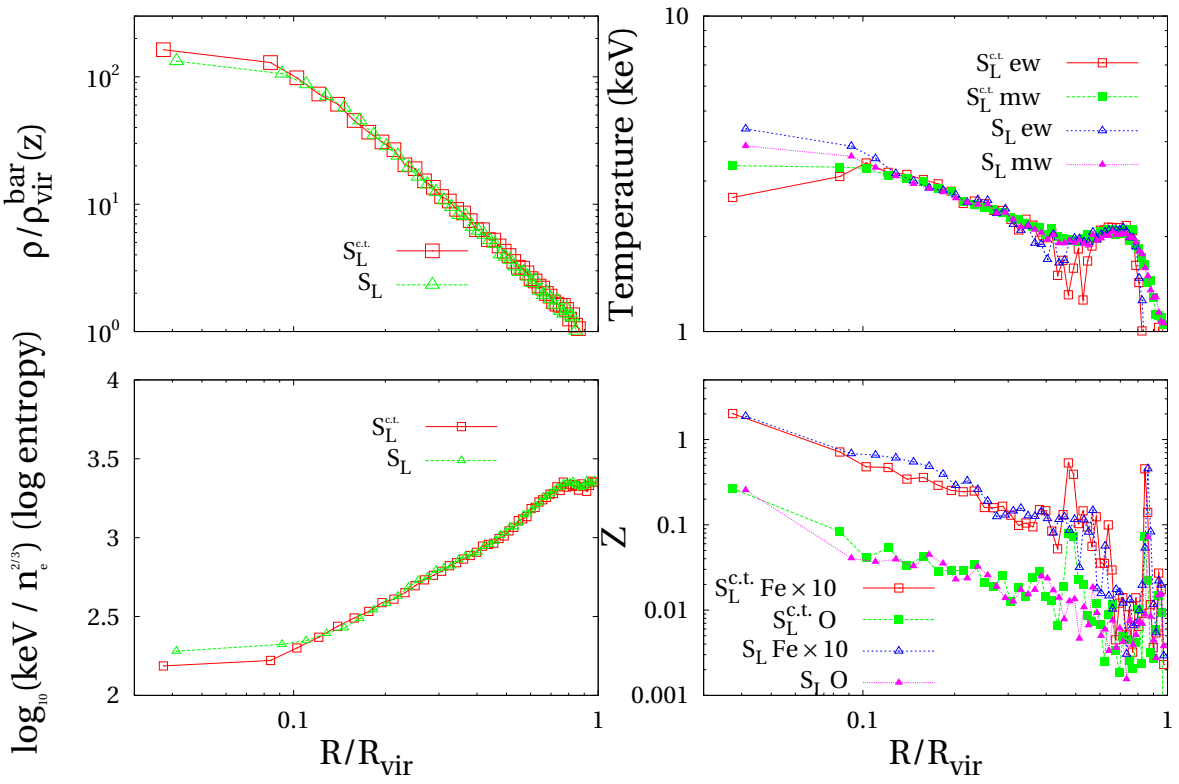

Figure 5.26: In all Panels the x–axis report the distance from cluster's centre in units of the virial radius. Scale is indicated on x–axis of the bottom panels. In all Panels, squares and triangles indicate respectively $S_L^{c.t.}$ and S_L data. [**Top Left Panel**] The density profiles. Density is in units of the baryonic virial density. [**Top Right Panel**] The temperature (in keV) both mass (*filled symbols*) and emission weighted (*empty symbols*). [**Bottom Left Panel**] The "entropy" profiles. [**Bottom Right Panel**] The radial abundace profiles for Iron (*empty symbols*) and Oxygen (*filled symbols*). Iron profiles have been magnified by a factor of ten for clarity. Units are solar abundances. indicates $X_O/X_{Fe} = solar$.

Panels, Bottom Left and Right Panels show respectively the hot gas density, the hot gas temperature, the entropy (defined as $T/n_e^{2/3}$ where n_e is the free electron number), the Iron and Oxygen abundances, the fraction of all metals locked in gas and the ratio between Iron and Oxygen abundances. No major differences can be seen in the graphviews. Density and entropy profiles of $S_L^{c.t.}$ are, respectively, a bit lower and a bit higher in the innermost region with respect to those of S_L. This is expected, since S_L has a lower fraction of cold, low entropy clouds. This also leaves an interesting signature on the temperature profile: $S_L^{c.t.}$ exhibits a fairly decreasing temperature in the centre.

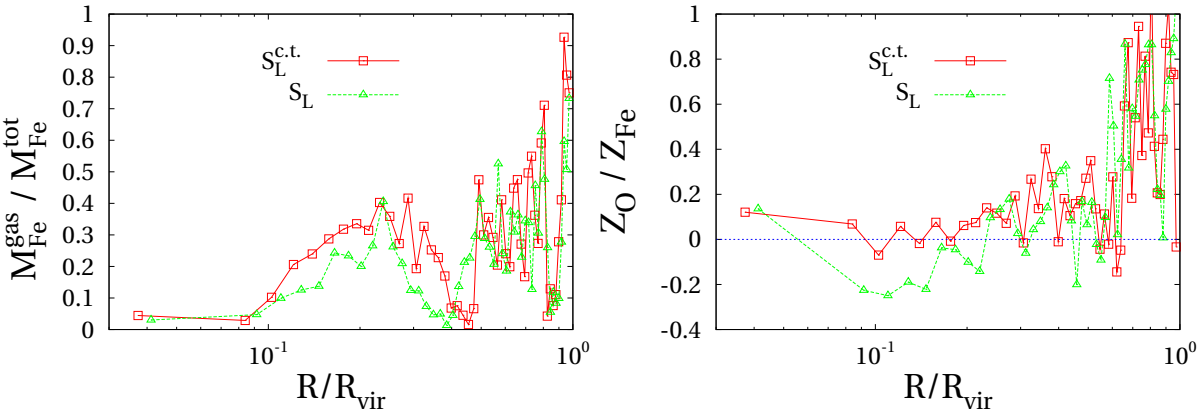

Figure 5.27: The x–axis report the distance from cluster's centre in units of the virial radius. Squares and triangles indicate respectively $S_L^{c.t.}$ and S_L data. [**Left Panel**] The fraction of all metals locked in gas as a function of radial distance. [**Right Panel**] The radial profile of ratio $[X_O/X_{Fe}]$ in units of the solar ratio. Straight dotted line indicates $X_O/X_{Fe} = solar$.

■ Summary

Introducing futher requirements of Eq. (5.5) and Eq. (5.6) in order to allow a Gas Particle to become multi–phase and star–forming one does not have a major quantitative impact on final results, though from a qualitative viewpoint we obtain somewhat interesting trends. What is probably missed is an effective way to provide the gas which collapse with the energy supply coming from the star–forming neighbourhood. Thus it is not effectively re-heated, and its collapse is only delayed to lower redshifts. Having a high star formation rate at $z < 1$ in galaxy clusters is not a good result, as it has not observational counterparts. This is a common problem in numerical simulation of galaxy clusters, witnessing that some physics is missed either in the Sn–feedback or in accounting for extra–energy surces. However, introducing the new requirements that we discussed in this Section does not tend towards the right direction or, at least, enhances this lack of physics. Moreover, besides the fact that we are only roughly modelling the estimates of characteristic time–scales $t_{\rm ff}$ and $t_{s.c.}$, we also do not really resolve the inner structure of the gas phases. A more refined numerical description of the pressure support against the collapse may be appropriate when the mass resolution increases.

5.7 Changing the Lifetimes and the Fraction of Binary Systems

The Initial Mass Function (IMF, see Sec. (4.3.5)) is one of the key ingredients for a chemical evolution model. During the lifetime of a galaxy or of a galaxy cluster, many

subsequent stellar generations born and the masses of their stars distribute according to the IMF. How the stars' mass distributes over the mass range (usually [0.1-100] $M_\odot$ is considered) characterizes the resulting stellar population, whose composition determines the global properties of chemical enrichment. Once an IMF has been chosen, several other physical quantities remain to be fixed; the most important ones are the stellar lifetimes as a function of the stars' mass, the yields for the nucleosynthesis of heavy elements and the details of stellar evolution. In this work, we choose to keep constant both the yields and the stellar evolution model. Instead, we test how results change when varying the IMF or the lifetime function of stars; moreover, we also change only the fraction A of stars ending in binary systems which give raise to SnIa.

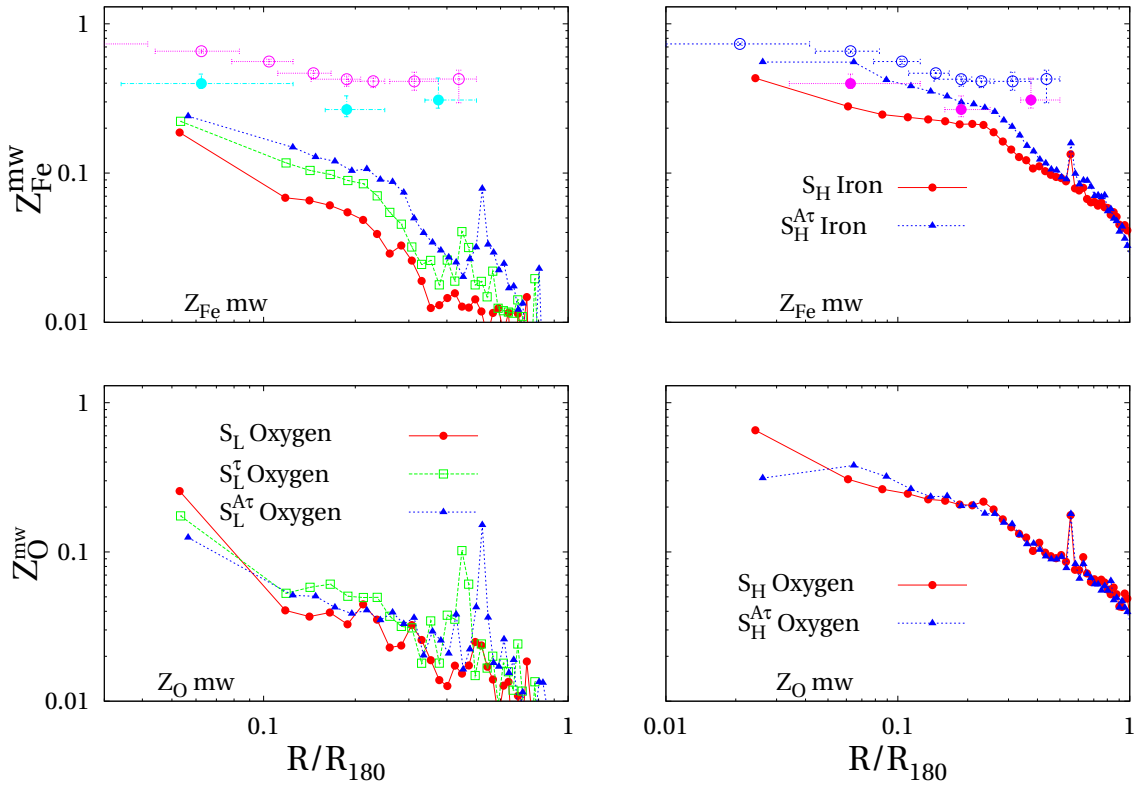

Figure 5.28: Radial profiles of Iron and Oxigen emission–weighted abundance. **Left Column** shows the Low–Resolution results, whereas the **Right Column** shows the High-Resolution ones. The S_L and S_H runs are plotted with empty triangles, the simulations with MM lifetimes and increased A fraction are plotted with empty and filled squares. In the **Upper Row** we plot the Iron profiles and in the **Bottom Row** we plot the Oxygen ones. Simulation data in **Top Left Panel** are coded as in the Bottom Left Panel.

In the following, we fix the IMF to be the Salpeter one and we vary the lifetime function and the parameter A. In the following Section, we do the opposite, keeping constant both the lifetime and all stellar parameters and varying the IMF.

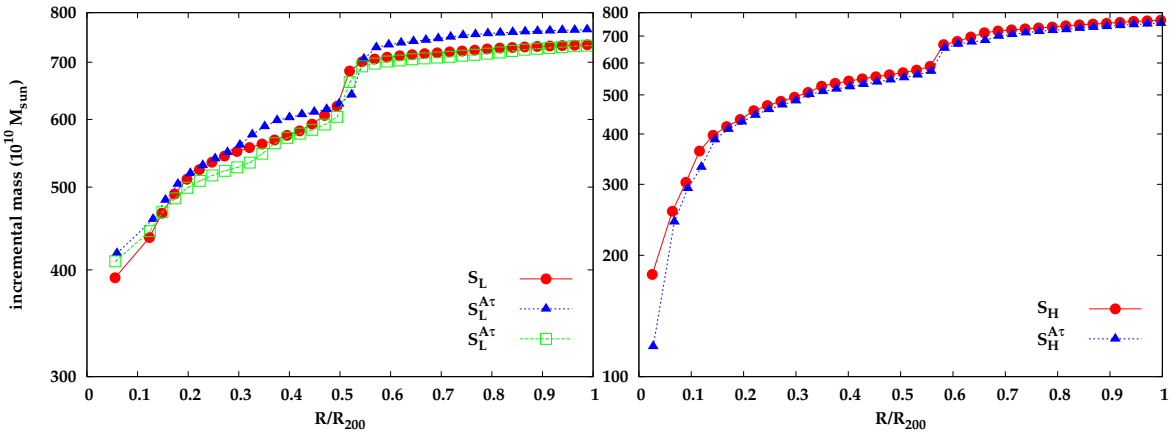

Figure 5.29: The total **star** mass within a given radius as a function of radius (in units of R_{200}).

As an example of lifetimes different than our reference one (given by Padoani & Matteucci (Padovani & Matteucci 1993), see Sec. (4.4)) we choose the function by Maeder & Meynet (MM), which has already been described in Sec. (4.4). We run a simulation, both in Low– and High– Resolution, labelled $S^{A\tau}_{L/H}$ using such lifetimes and raising A from 0.07 to 0.1. Furthermore, we present a Low–Resolution simulation having $A = 0.07$ and using MM lifetimes. This latter run is referred as S^{τ}_{L}. As the parameter A enters in our adopted stellar model as a multiplicative constant, raising it increases the number of SnIa produced by a stellar population. Therefore, a simulation using MM lifetimes and $A = 0.07$ is useful to check to what extent changes are due to different lifetimes or instead to the larger number of SnIa. We expect that such a simulation lives somehow 'in between' the simulation using PM lifetimes and that one with MM lifetimes and $A = 0.1$; to save computational time we choose to run such a simulation only in Low–Resolution.

Fig. (5.28) shows the radial abundance profiles for these simulations. Looking at High–Resolution results, $S^{A\tau}_{H}$ exhibits higher values as for the Iron contents which bring the abundance profile up to the observed level in the inner regions ($r \lesssim 0.3 r_{200}$). Changing the lifetimes roughly does not affect the overall production of metals, once a given total stellar mass has formed; therefore, as for $S^{A\tau}_{H}$ one would naively expect a total amount of Iron $\sim 40\%$ higher than in S_H (i.e. $\sim 0.1/0.07 - 1$), since the total stellar mass in the two simulations is nearly equal ($\sim 7\%$ larger in S_H). Nevertheless, we can infer from the Star Formation History, shown in Fig. (5.30), that about 20% of the stellar mass in $S^{A\tau}_{H}$ has formed after redshift $z \sim 0.25$, i.e. less than ~ 3 Gyr ago. Looking at Fig. (4.2) we know that the MM lifetimes for SnIa are $\sim 80\%$ of PM lifetimes until about ~ 3 Gyr by the formation time of a given stellar population. Hence, we are missing a substantial fraction of the total amount of Iron, since not all SnIa had time to explode. Taking all data into account, we would expect at maximum only $\lesssim 20\%$

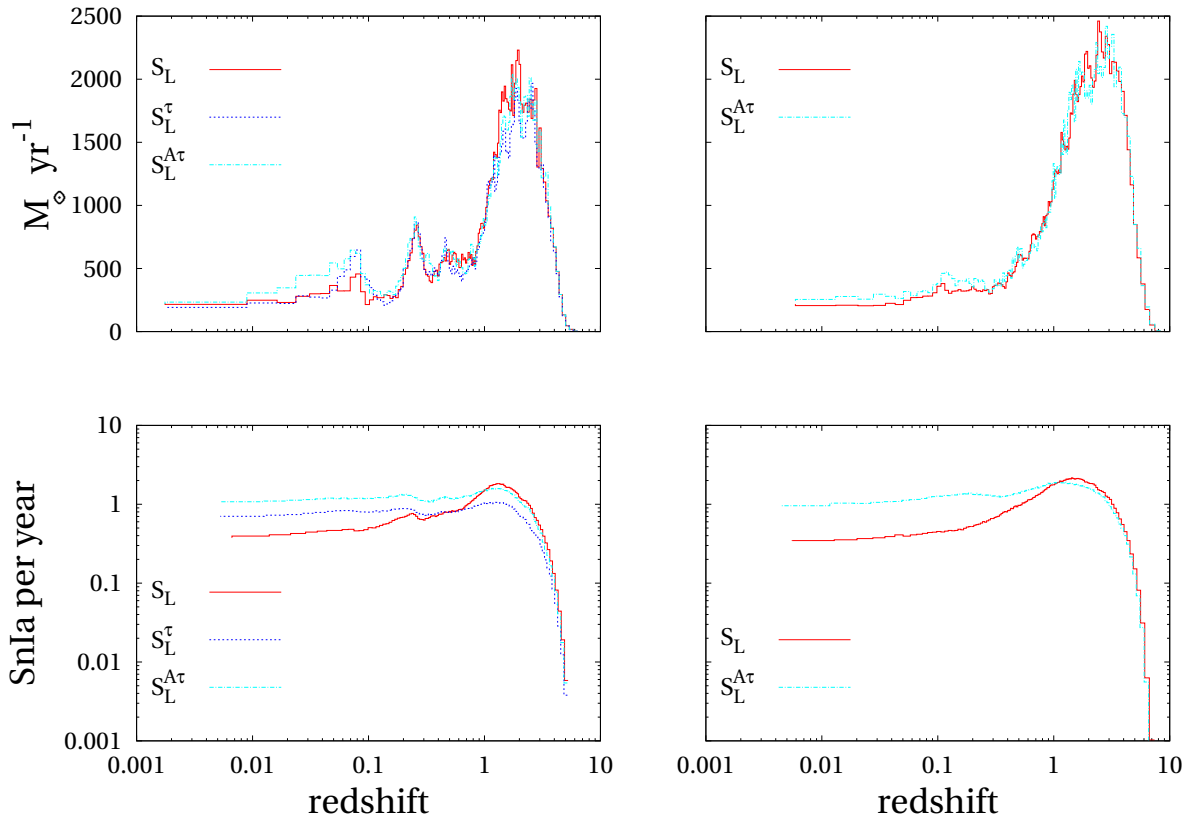

Figure 5.30: In the **Left** and **Right Column** are plotted respectively the Low– and the High–resolution results. The **Upper Row** shows the Star Formation Rate History. Continuous lines indicate S_L and S_H. Dot-Dashed lines indicate $S_L^{A\tau}$ and $S_H^{A\tau}$. Dotted line indicate S_L^{τ}. The **Bottom Row** shows the SnIa Rate History. Lines are coded as for the upper row.

more Iron in $S_H^{A\tau}$ than in S_H if all SnIa events were occurred. Actually, we obtain just $\sim 9\%$ more Iron within the virial radius in $S_H^{A\tau}$ than in S_H. The profiles plotted in the Top Right Panel of Fig. (5.28) present two features that is worth explaining; the first is the flattening in the innermost region and the second is the coincidence of abundance out of $R/R_{180} \gtrsim 0.5$. Fig. (5.29) shows the total stellar mass within a given radius, as a function of radius. An inspection of High–Resolution results (Right Panel) reveals that in $S_H^{A\tau}$ there are much more stars in the second distance bin with respect to the first one than in S_H. Moreover, there are more stars younger than 3 Gyr than in S_H. This causes that flattening of abundance profile, as well as the the higher abundance of Oxygen for S_H in the innermost bin, which is visible in the Bottom Right Panel. The similarity of abundances beyond $R/R_{180} \gtrsim 0.5$ turns out to be a sort of conspiracy. In these regions the stellar mass is the same for both simulations within $\sim 1\%$, so that we would expect a much higher Iron content in $S_H^{A\tau}$. Nevertheless, in this latter run

$\sim 35\%$ more stars than in S_H run are younger than $\sim 3\,\mathrm{Gyr}$, so by the same reasoning as before the total ejected Iron is less than naively expected. The fact this turns in the same amount of Iron is just a coincidence.

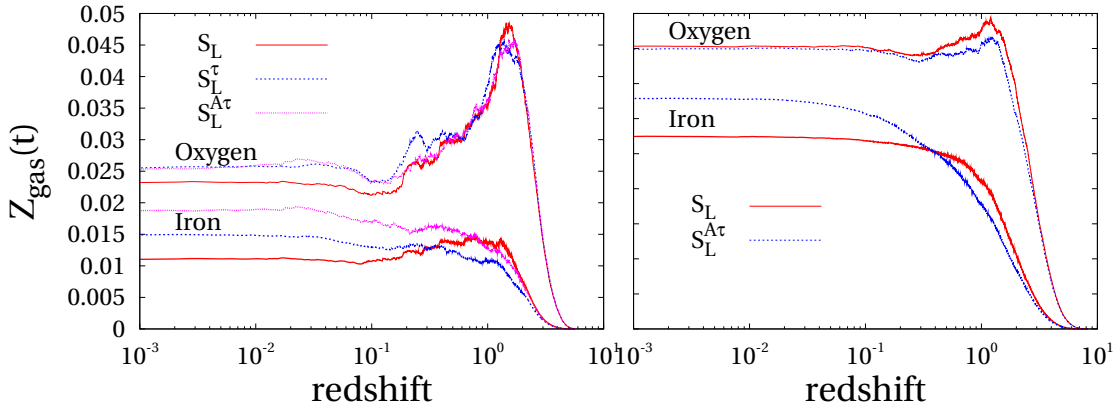

Figure 5.31: Mean Iron and Oxygen abundance of the gas as a function of redshift. [**Left Panel**] shows the low–resolution results. *Bold lines* show the Oxygen data and *thin lines* the Iron ones. Continuous, dotted and dot–dashed lines plot respectively the S_L, S_L^{τ} and $S_L^{A\tau}$ simulations. [**Right Panel**] contains the high–resolution results. Line codes are the same as for the Left Panel.

The same interpretation applies to Low–Resolution results. The Iron profiles are as we expected they to be, being $S_L^{A\tau}$ and S_L respectively the highest and the lowest one with S_L^{τ} in the middle. Instead, once the Left Panel of Fig. (5.29) has been considered, it appears that the Oxygen profiles disagree with the interpretation that we have drawn right above. What is playing a role here is the different fraction of Oxygen locked in stars. Looking at the Top Left Panel in Fig. (5.30) we infer that both in S_L^{τ} and $S_L^{A\tau}$ more stars than in S_L have formed very recently. Most of them are located in the cluster's centre, so that the fraction of Oxygen which reside in the hot–phase is $\sim 2.7\%$, $\sim 1.9\%$ and $\sim 1.3\%$ respectively for S_L, S_L^{τ} and $S_L^{A\tau}$. This is the reason why the $S_L^{A\tau}$ simulation exhibit the lowest Iron content in the centre though it has the largest stellar mass.

The enrichment history plotted in Fig. (5.31) clearly shows that the mean gas Iron abundace of both S_L^{τ} and $S_L^{A\tau}$ grows slowly than in S_L and, instead of declining at low redshifts ($z \lesssim 1$) continues to grow due to the Iron produced by those SnIa which are not allowed to explode in S_L. The same reasoning holds as for the enrichment history of High–Resolution simulations.

The ratios between the Oxygen and Iron metallicities (see Fig. (5.32)) exhibit fairly different behaviours accordingly to abundance profiles of Fig. (5.28), so as $S_H^{A\tau}$ has values of $[O/Fe]$ much lower than S_H and the same holds as for $S_L^{A\tau}$ and S_L, S_L^{τ} and S_L. Though in the central region the signature of different lifetimes is clear, in the outer regions ($R \gtrsim 0.3 R_{vir}$) the profiles of all simulations aremuch more similar as for

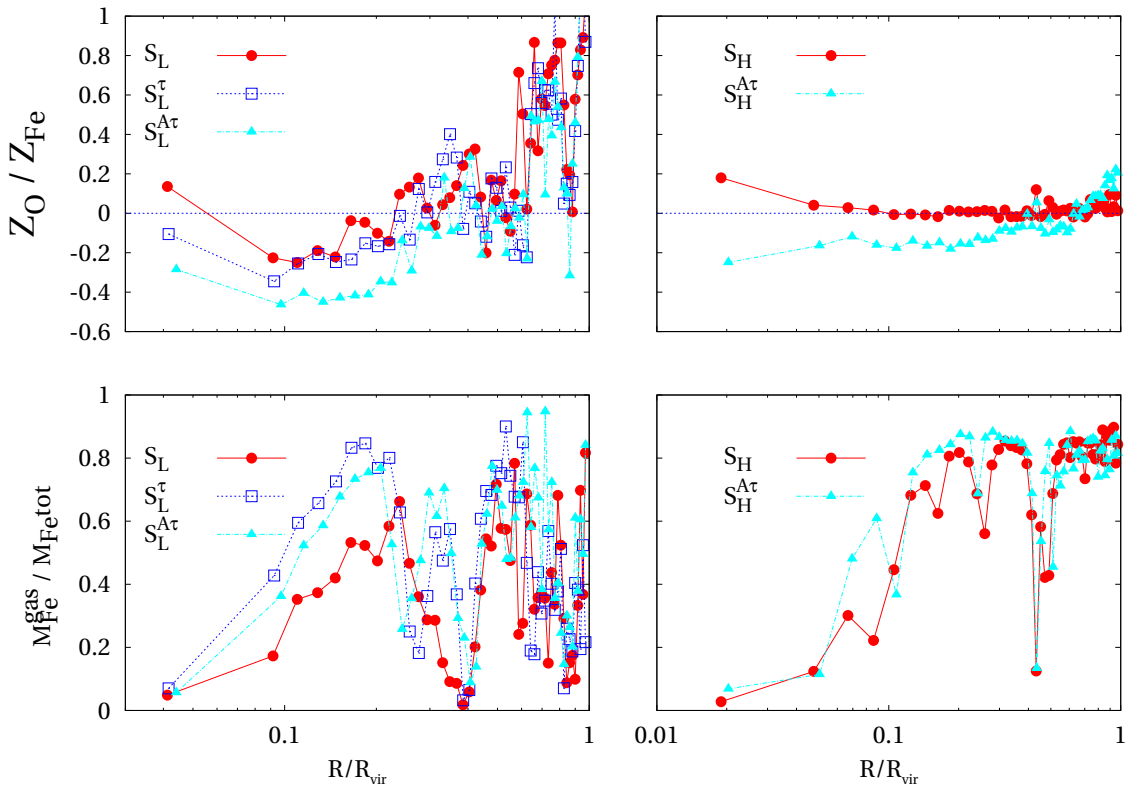

Figure 5.32: Low– and High–Resolution results are plotted respectively in **Left** and **Right Column**. [**Upper Row**] The Oxygen over Iron abundance ratio in log–solar units. Straight dotted line indicates the solar value. Continuous line with filled circles stands for $S_{L/H}$ runs, dotted empty–squares line stands for S_L^τ and dot-dashed filled–triangles line indicates the $S_{L/H}^{A\tau}$ run. [**Bottom Row**] The mass fraction of Iron harbored in the ICM as a function of distance from centre. Lines are coded as for the Upper Row.

both the abundance ratios and the mass fraction of metals harbored in the gas (bottom row in Fig. (5.32).

■ Summary

We changed one of the key ingredients for the chemical enrichment, namely the lifetime function for stars. Also, we vary the fraction of mass ending in binary systems from which SnIaoriginate.

The Thermodynamical properties (Fig. (5.33)) are not significantly affected by neither changing lifetimes nor changing the bynary system fraction A. Changing the lifetimes affects mostly the intermediate and low–mass stars, so, as for the energy, it amounts to vary the energy injection rate by SnIa. Changing A turns in having more (larger A) or less (smaller A) SnIa events, and this again reflects on the total amount

of energy available from this source. The stability of the thermodynamical properties when varying both the lifetimes and A argues against a major role played by the SnIa energy.

As for the metal enrichment, changing both the lifetimes and A makes important differences both in the Iron abundance profile and in the abundance ratio between α and Iron–peak elements. Iron abundance becomes larger in the inner regions ($R \lesssim 0.3R_{200}$), arriving at the observed enrichment level (De Grandi & Molendi 2001). The $[O/Fe]$ ratio is significantly undersolar (~ -0.2 dex) out to $R \sim 0.3R_{vir}$ while remaining unaltered (slightly suprsolar) for $R \sim 0.5R_{vir}$. The SnIa explosion rate is strongly affected, and together with abundance ratios it can be a key test in order to obtain constraints on the star formation history in galaxy clusters.

5.8 Changing the Initial Mass Function

In the previous Section we kept fixed the IMF of stars while varying their lifetimes. In the following we show the effect of assuming different IMFs, namely the Arimoto–Yoshii IMF (Arimoto & Yoshii 1987) and the Larson IMF (Larson 1998), which is also varying with time. We label these simulation as AY_H^w and V_H^w respectively. We have already introduced the Arimoto–Yoshii IMF and the Larson IMF in Sec. (4.5).

In Sec. (3.4.6) we described how the energy due to SnII is also employed to supply kinetic energy to gas particles having a strong star formation activity. This is what we call 'winds' as the net effect of this energy supplying is an outflow of gas from star–forming regions. As we've already described, if $\dot{m}_w$ is the rate of gas ouflow from winds and $\dot{M}_\star$ is the rate at which the gas convert into stars, the wind's energy equation is given by

$$1/2\dot{m}_w v_w^2 = \chi \epsilon_{SN} \dot{M}_\star$$

so that the wind's velocity is given by the equation

$$v_w^2 = 2\frac{\chi}{\eta}\epsilon_{SN}.$$

We remind that ϵ_{SN} is the energy per gram per solar mass of stars formed due to the SnII having mass larger than M_{th}^{IRA}, and that both χ and η are parameters of the code. The first one defines the fraction of energy ϵ_{SN} which give raise to winds and the second controls how much efficiently a gas particle is selected to take part to the wind.

The IMF determines the number of both SnII and SnIa that a stellar population provides during its lifetime. Hence, by changing the IMF we also change the total amount of energy provided by Sn. In turn, this affects the value of the wind velocity, once χ, η and M_{th}^{IRA}have been fixed. This can have a significant impact on the evolution of the cluster we are simulating. In this section we focus on the effect that

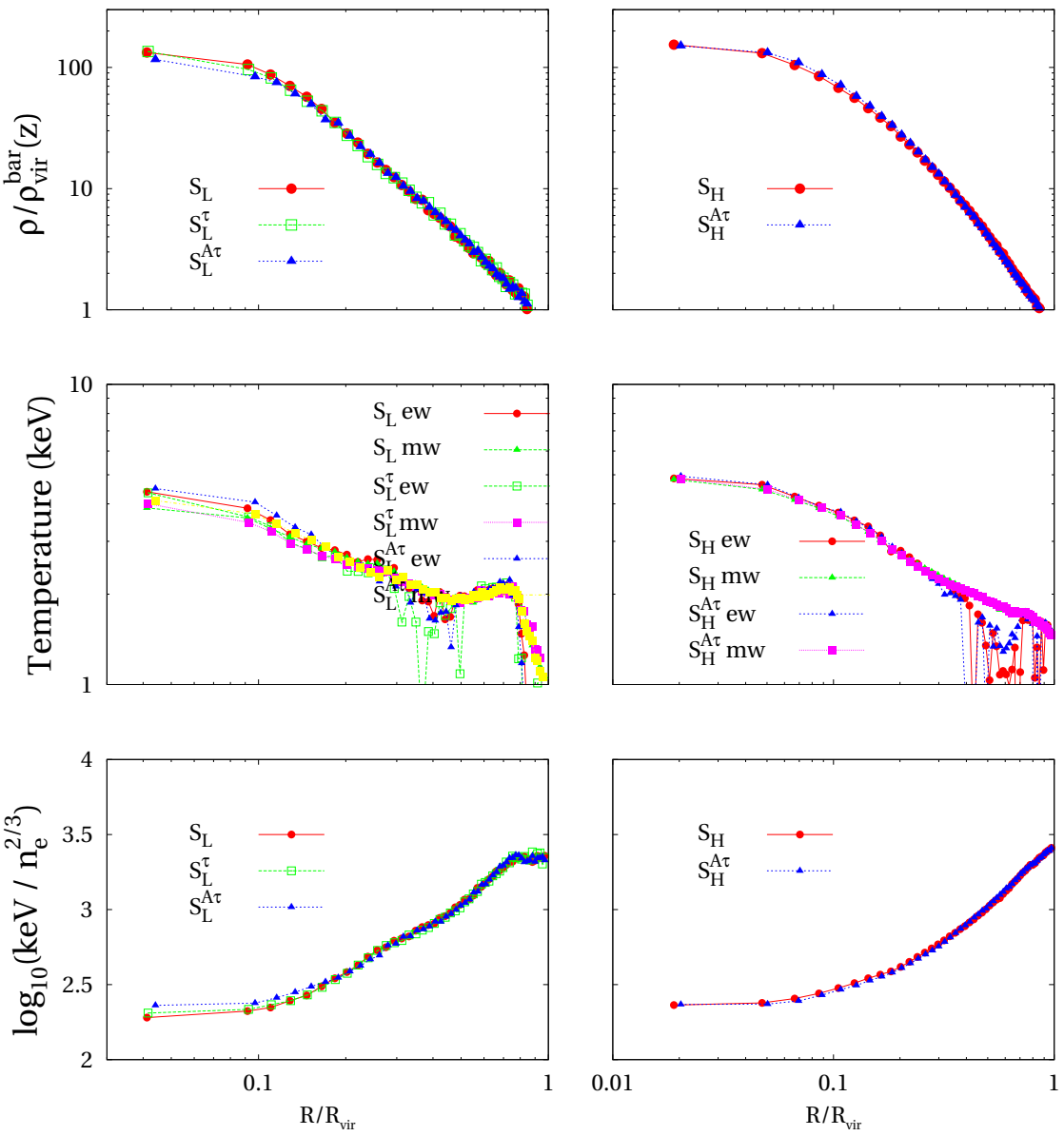

Figure 5.33: Thermodynamical properties in $S_{L/H}$, $S^{A\tau}_{L/H}$ and S^{τ}_{L} simulations. [**Upper Row**] Density profiles. [**Middle Row**] Temperature profiles, both mass– and emisison– weighted. [**Bottom Row**] Entropy profiles.

varying the mass distribution of stars has on both the production of elements and the thermodynamical history of gas; then, we set the winds's velocity to the value it has using a Salpeter IMF and $M^{IRA}_{th} = 15\,\mathrm{M}_{\odot}$, that is $v_w \simeq 500\,\mathrm{km\ s^{-1}}$. In the next Section we let the wind's velocity to change.

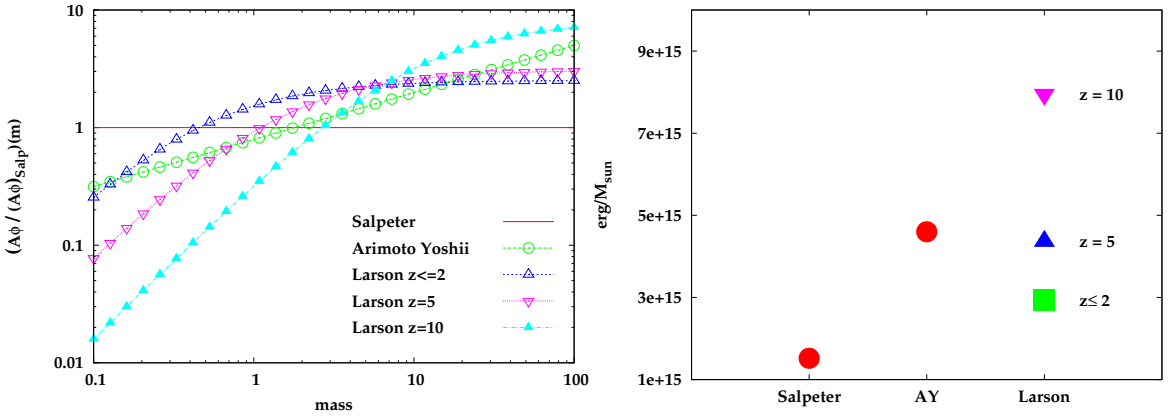

Figure 5.34: [**Left Panel**] The relative weight of Arimoto–Yoshii and Larson IMFs relatively to the Salpeter one. *Open circles* indicate the ratio between the Arimoto–Yoshii and the Salpeter IMFs, the *Triangles* indicate the ratio between the Larson IMF at different redshift (see the legend) and the Salpeter IMF. [**Right Panel**] The energy due to SnII having mass $m > M_{th}^{IRA} = 15\,\mathrm{M}_{\odot}$ for the IMF we use. This energy is that one which is immediately incorporated in the star formation algorithm.

The Left Panel of Fig. (5.34), which reports the relative weights of the Arimoto–Yoshii and the Larson IMFs with respect to the Salpeter IMF, gives us an insights on how each IMF will drive the chemical enrichment (compared with the Salpeter IMF). Firstly, the mass at which these IMFs are equal to the Salpeter one are in the range of low–mass stars; even, the Larson IMF after $z = 2$ crosses the Salpeter IMF in the region of stars that never die. Since above this mass all the IMFs are higher than the Salpeter IMF, we expect that both the Arimoto–Yoshii and the Larson IMFs produce an amount of heavy elements larger than the Salpeter IMF. Next, we remind that the very low mass stars are the main responsibles for the locking of metals in the stellar phase; then, as both Arimoto–Yoshii and Larson distribution functions have much less stars of small mass than the Salpeter function, we expect the gas metallicity in AY_H^w and V_H^w to be enhanced also by a smaller enrichment of the stellar phase.

Surprisingly, the star formation rate is not strongly suppressed when a top–heavier IMF is adopted. Fig. (5.35) shows the rates of star formation as a function of time: the feature common to AY_H^w and V_H^w is the shift of the SFR peak towards $z \sim 1$, whereas the rate of S_H peaks $Z \sim 2 - 3$. From Fig. (5.34), we know that the energy provided by IRA SnII in AY_H^w and V_H^w is quite similar (or even larger in V_H^w for $z \gtrsim 2$) to the energy in S_H^{IRA8}. Therefore, considering Fig. (5.8), besides this shift of the maximum of star formation, one would have also expected a significative suppression of the rate itself. In the summary of Sec. (5.4), we stressed that in the results presented in that Section we did not disentangled the effect of changing the wind's velocity accordingly to the value of M_{th}^{IRA}. Having fixed the value of v_w for all the simulations, here we are somehow separating these two effects since changing the IMF amounts also to change

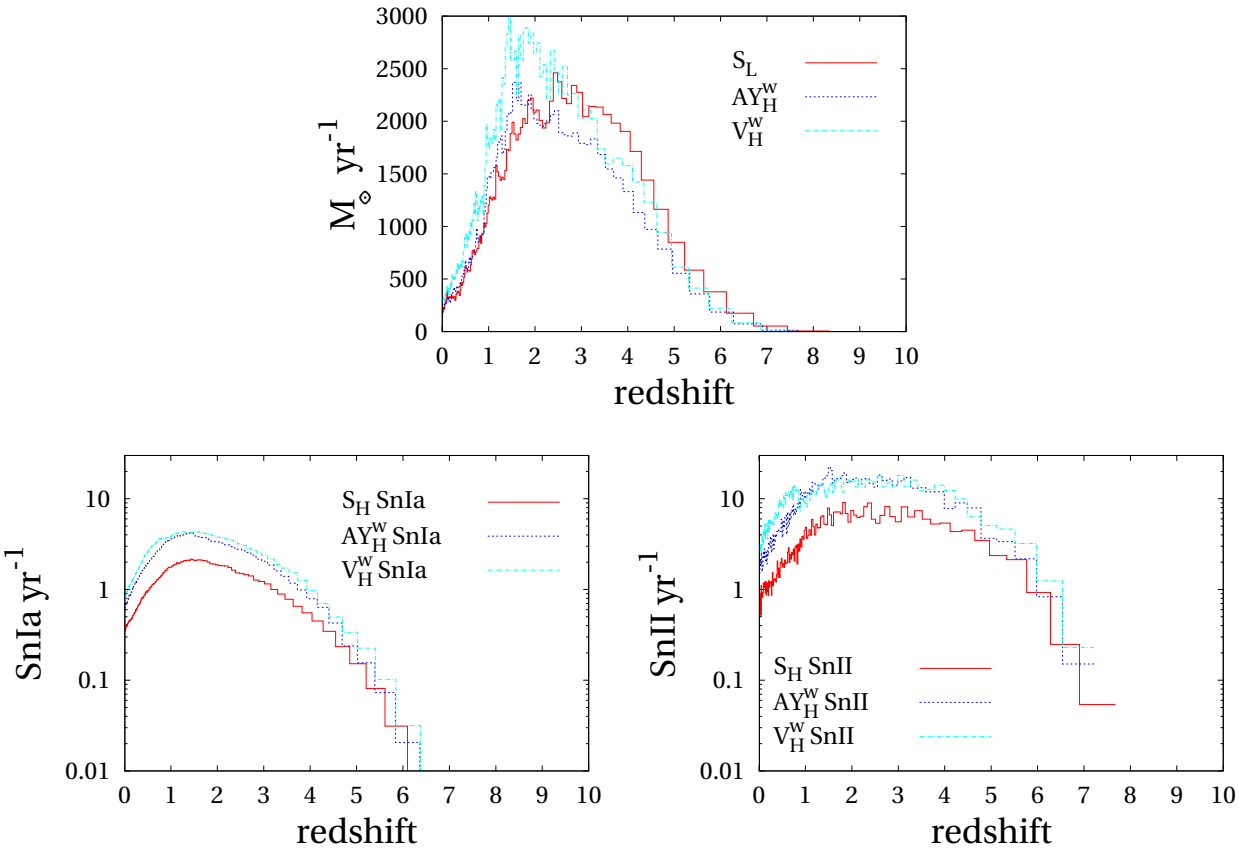

Figure 5.35: [Upper Panel] The star formation rate history and the related SnIa and SnII explosion rates (respectively **Bottom Left**) and **Bottom Right**.

the value of ϵ_{SN}.

The plot shown in Fig. (5.34) have a rather straightforward interpretation. The Arimoto–Yoshii IMF produces slighlty more Oxygen and significatively less Iron than the Larson–Variable IMF. In fact, Fig. (5.34) shows that in the high–mass range the Arimoto–Yoshii function dominates over the Larson IMF at $z < 10$, whereas the Larson IMF is always higher than Arimoto–Yoshii IMF for masses $\lesssim 10\,M_\odot$. The final amount of Iron within the virial radius in S_H is about one half the total quantity in AY_H^w and $\sim 40\%$ of the amount in V_H^w; the Oxygen mass within the virial radius in S_H run is $\sim 27\%$ and $\sim 29\%$ of the Oxygen mass present in respectively AY_H^w and V_H^w. This difference in the metal budget is also an increased population of the very high metallicity tail, as shown in the bottom row of Fig. (5.38).

As for the abundance profiles (Fig. (5.37)), both the AY_H^w and the $V_H^{,w}$ reach the observed levels. Nevertheless, Iron profiles of both simulations exhibit a too steep shape if compared with the observational data; they reach the abundance level of non–cooling

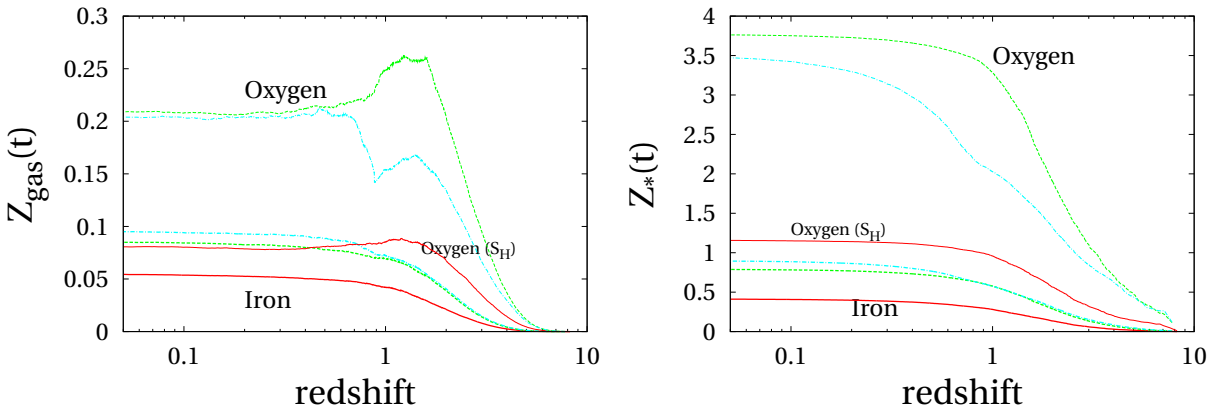

Figure 5.36: The mean Oxygen (thin lines) and Iron (thick lines) content of gas (**Left Panel**) and stars (**Right Panel**) as function of redshift. S_H simulation data are plotted with continuous lines, AY_H^w data are plotted with short–dashed lines and V_H^w data are plotted with dot–dashed lines.

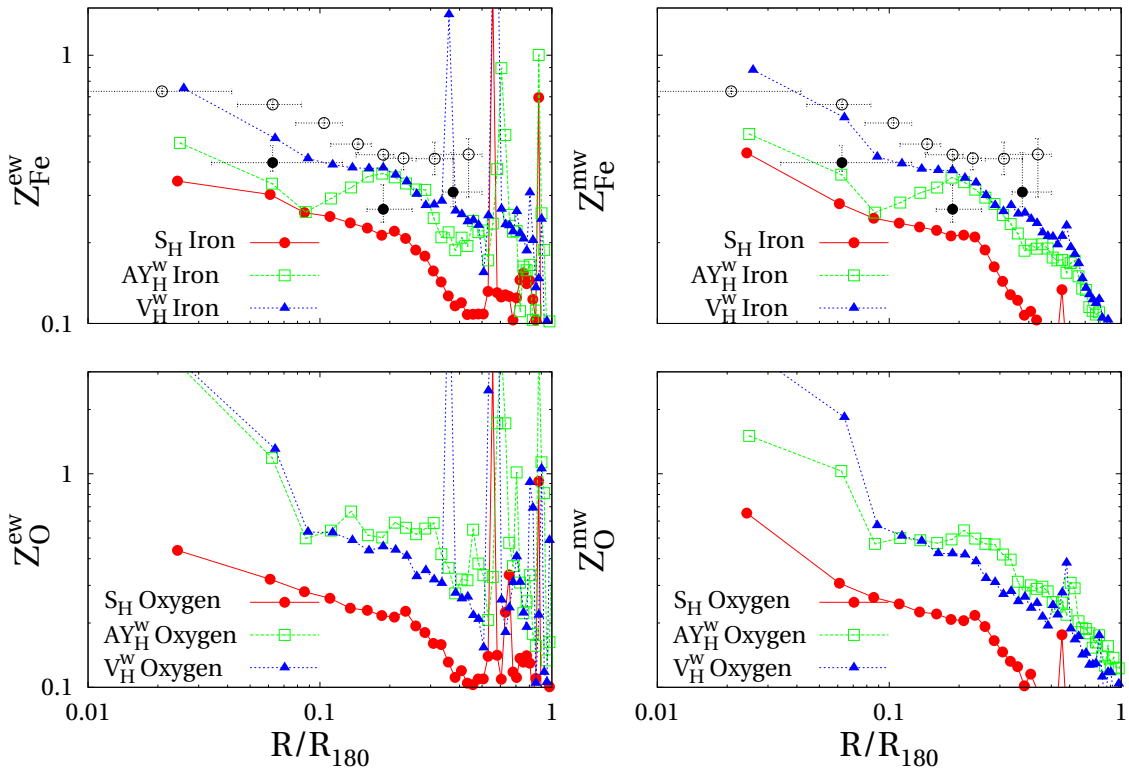

Figure 5.37: Radial abundances profiles for the hot gas. Both Fe (*Upper Row*) and O (*Bottom Row*) are shown. On the *Left Hand Side* we plot emission weighted abundances and on the *Right Hand Side* we plot the mass-weighted abundances.

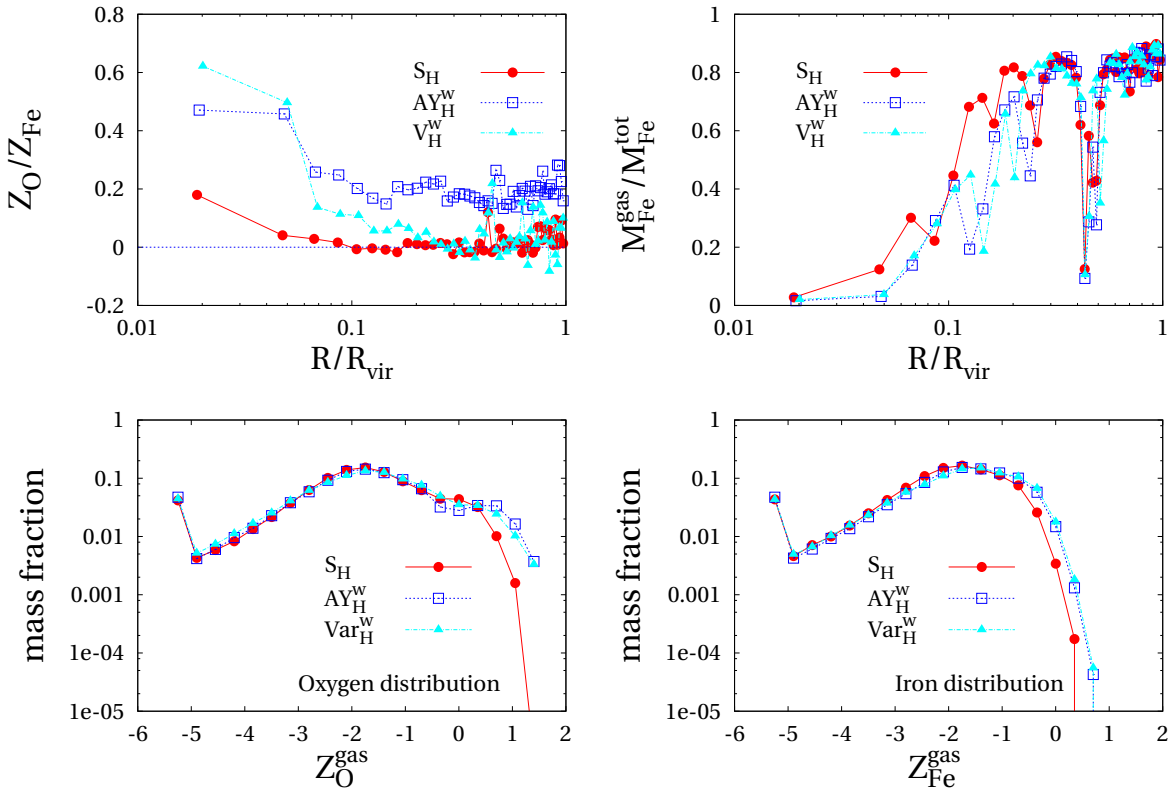

Figure 5.38: [**Upper Left Panel**] The radial profiles of O/Fe gas abundances. [**Upper Rigth Panel**] The radial variance of the fraction of Fe retained by gas. [**Bottom Left Panel**] [**Bottom Right Panel**] The gas mass distribution vs Fe and O abundances, respectively.

core clusters only at $R \sim 0.3R_{200}$, while steeply declining in outer regions. The very steep raising of the Oxygen profiles in the innermost regions is due to the recent star formation activity. This recent enrichment affects also the radial profile of $[O/Fe]$ ratio (Top Left Panel of Fig. (5.38)).

Thermodynamical properties are mildly affected by changing the IMF, as shown in Fig. (5.39). The temperature of V_H^w in the inner regions ($R \lesssim 0.2R_{vir}$) is $\sim 15\%$ higher than in the other two simulations, which is indeed a poor result if we remind that the total energy released by Sn in this simulation is about $\sim 300\%$ and $\sim 28\%$ larger than that released respectively in S_H and AY_H^w.

■ Summary

In this Section we described the effect of changing the IMF on the chemical properties of our simulated cluster. We run simulations using three different IMFs: the Salpeter IMF, the Arimoto–Yoshii IMF and the time–dependent Larson IMF. As result, we

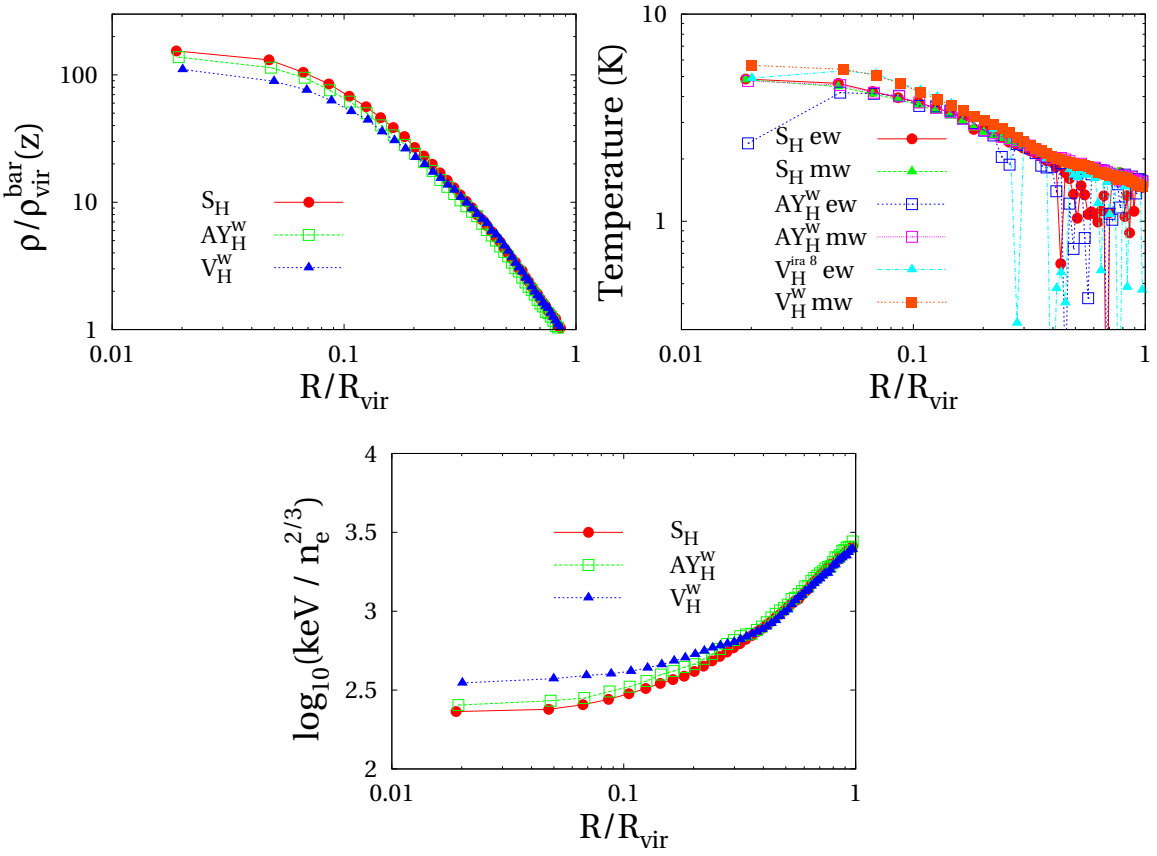

Figure 5.39: [**Upper Panel**] The density radial profile of hot gas. [**Bottom Right Panel**] The hot gas entropy radial profile. [**Bottom Left Panel**] The temparature profiles for the hot gas are shown both emission–weighted and mass-weighted.

find a large difference in the total amount of produced metals arise when an heavier IMF is adopted. This difference reflects also in the radial abundance profiles, which reach higher values in the central part ($R \lesssim 0.3 R_{vir}$) of the cluster. Nevertheless, our profiles are somewhat steeper than the observed ones.
The main signature of using different IMFs is in the $[O/Fe]$ profiles. All simulations give a supersolar value in the innermost part of the cluster, owing to the very recent star formation. For this reason we consider the third distance bin as an estimate of a more representative value that we can expect once this bias has been taken into account. The Salpeter IMF exhibits solar values down to the very inner regions ($R \lesssim 0.05 R_{vir}$), where it become mildly supersolar. The Arimoto–Yoshii IMF produces instead a fairly constant $[O/Fe] \sim 0.2$ profile, slightly higher towards the centre; finally, the results from V_H^w are very similar to those from S_H down to $R \sim 0.3 R_{vir}$, then raising and reaching in the centre values similar to those of AY_H^w.

The minor changes in the profiles of the thermodynamical properties of the gas, as in Sec. (5.7), against a major role of supernovae in determining the global properties of galaxy clusters. This suggest that while Sn have a crucial role in determining the pattern ic the ICM chemical enrichment, the details of dtar formation model hardly reflect in the global thermal properties of the ICM.

5.9 Changing the Wind's Velocity

In Sec. (5.8) we discussed the link between the IMF and the wind's velocity; changing the IMF amounts to change how many stars form with $m \geq M_{th}^{IRA} \geq 8\,\mathrm{M}_{\odot}$. In our star formation model these stars provide, as SnII, the energy available to achieve the self–regulation of the star formation itself. This same energy is assigned as kinetic energy to the gas particles tha form the winds (see Sec. (3.4.6)). The velocity which is assigned to such particles is proportional to the square root of the energy provided by short–living stars. Hence, changing the IMF turns in modifying the velocity assigned to wind particles. In our implementation of stellar evolution, we let the energy deposited on a Gas Particle by nearby supernovae to be involved in the computation of the winds' velocity (see Eq. (4.8)). As a consequence, the velocity calculated using the energy from short–living stars represents the minimum velocity of winds in that simulation.

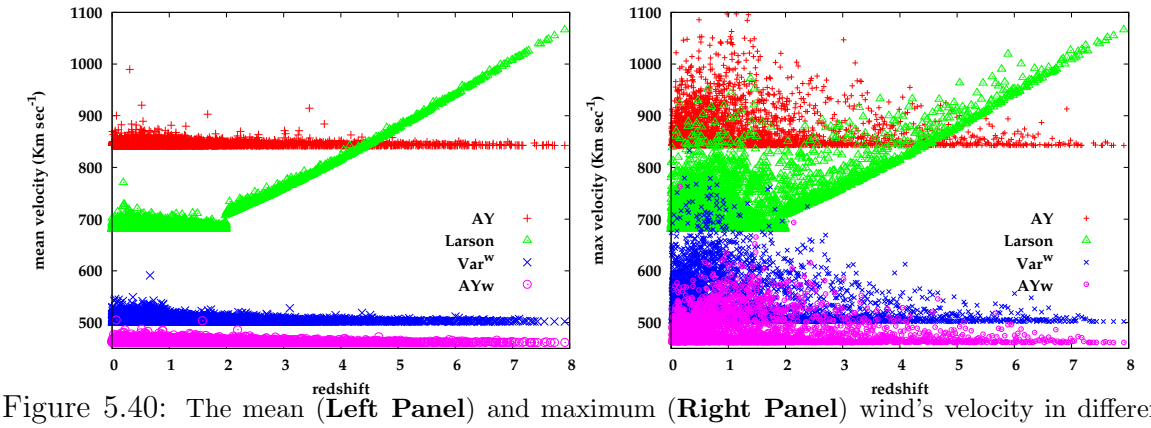

Figure 5.40: The mean (**Left Panel**) and maximum (**Right Panel**) wind's velocity in different runs. We remind that the apex w label those simulations having a fixed value of v_w. The spread is due to the contribution from Sn not in IRA.

Since we are interested in disentangling the effect of a larger energy available in the thermodynamics and of an higher wind velocity, in Sec. (5.8) we fix this value for all simulations. Instead, here we present the results from the same simulations AY_H^w and V_H^w discussed above, compared with two simulations AY_H and V_H which are equal to the formers but for the wind's velocity being calculated accordingly to the actual energy provided by short–living stars.

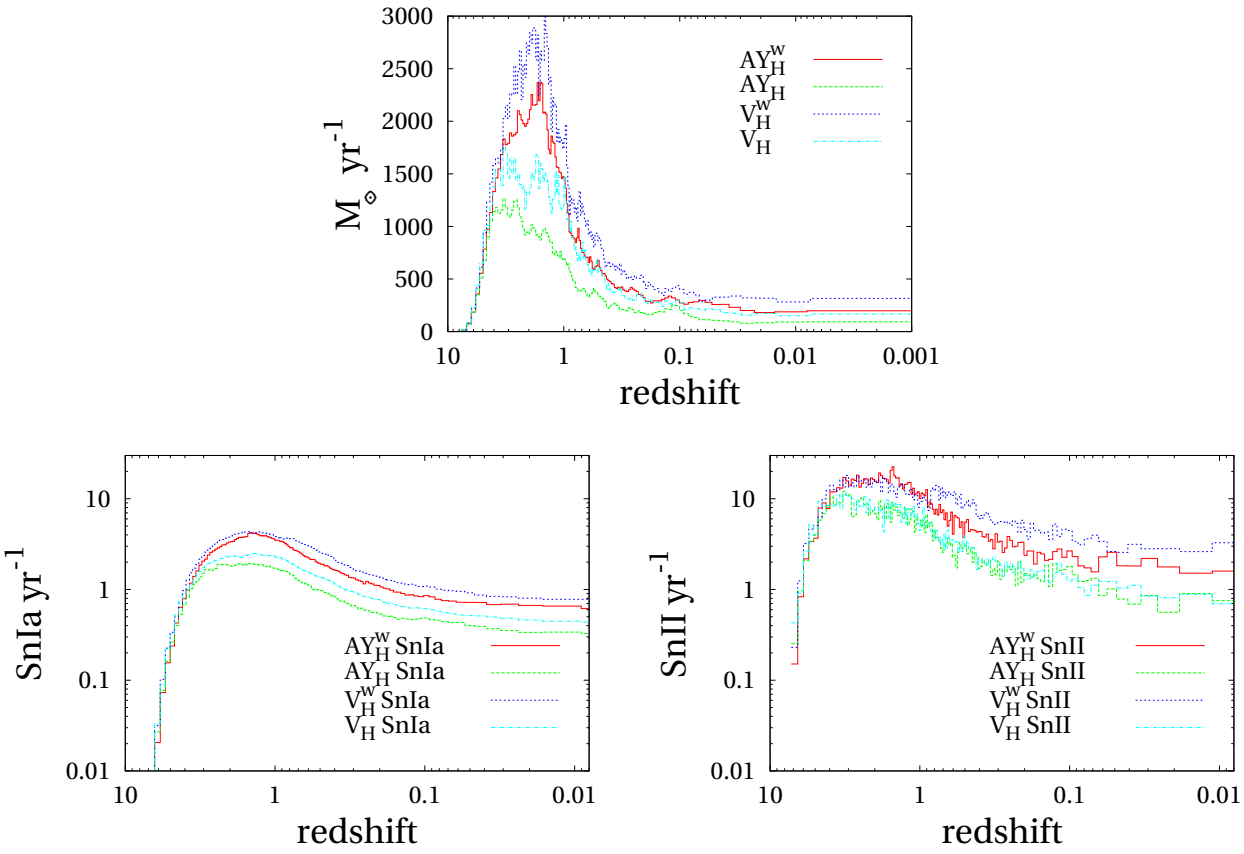

Figure 5.41: [**Upper Panel**] The star formation rate history for top–heavier IMFs with strong and 'standard' winds. In the bottom row we show the the underlying SnIa explosion rate [**Bottom Left Panel**] and SnII explosion rate [**Bottom Right Panel**].

Hence, both AY_H^w and V_H^w have $v_w \simeq 500\,\mathrm{km\ sec^{-1}}$, while v_w in AY_H is about $\sim 840\mathrm{Km\ sec^{-1}}$. The Larson IMF is time–depdendent so that we have to recalculate all related quantities at each time. Since the number of short–living stars formed changes, also the value of v_w evolves in time.
Fig. (5.40) shows the mean and the maximum velocity of winds (respectively in the Left and the Right Panel) as a function of redshift. On average, the energy that nearby supernovae deposit on Gas Particles gives an average contribution to the wind's velocity of about $5-10\%$; in some case (see the Right Panel), the contribution is more substantial, reaching the $\sim 40\%$ level.
Anyway, the main results from this figure are that (1) the velocities change considerably from one simulation to another and (2) the first star–forming regions at early times in V_H suffer for the presence of a strong wind.

Fig. (5.41) and Fig. (5.42) explicitly show the effects of wind on the patterns of star

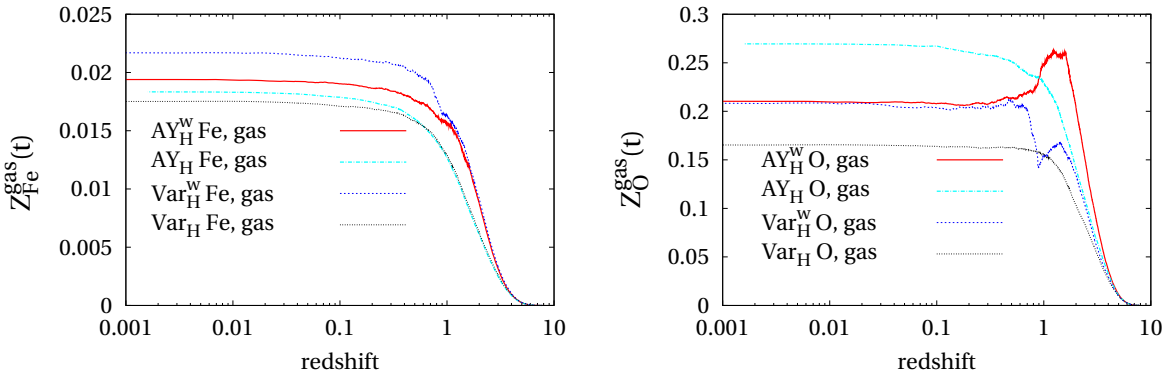

Figure 5.42: The mean Oxygen (**Right Panel**) and Iron (**Left Panel**) content of gas as function of redshift. AY_H and AY_H^w data are plotted with heavier lines. AY_H^w is plotted with a continuous line, AY_H with a dot–dashed line, V_H^w with a short–dashed line, V_H with a dotted line.xs

formation and metal enrichment. Bearing in mind that the Gas Particles which take part to the wind are those having a strong star formation activity (and which are not been turned in Star Particles), the Upper Panel of Fig. (5.41) clearly shows the effect of giving to such particles enough energy to escape from the dense clouds in the potential well where they are bounded. Both simulations with the most energetic winds exhibit a strong suppression of the star formation rate once the number of star–forming Gas Particles become high enough to make the winds effective in removing a considerable gas mass (see Sec. (3.4.6) as for the algorithm used to model the winds). The Bottom Panels of the same figure show the consequences on the supernovae explosion rates. It is worth underlining two interesting features shown by the star formation rate and the enrichment history (see Fig. (5.42)).

Firstly, though for $z \leq 2$ the difference between the value of v_w in V_H^w (AY_H^w) and in V_H is is comparable with the difference between the velocity in V_H and AY_H, V_H does not fall somehow in between AY_H and V_H^w (AY_H^w). Instead, its pattern of star-formation rate is very similar to the one of AY_H, some difference being appreciable by $z = 2$ (since at $z \lesssim 4$ v_w in V_H is smaller than in AY_H, coeherently the rate of V_H is slightly higher than that of AY_H by this time). This means that the wind feedback at high redshift (when v_w in V_H is quite extreme) determines the subsequent pattern of star formation and that a larger effect appears when the wind velocity exceeds the typical esape velocity of the galaxy–sized halos, where star formation takes place. This may appear as a trivial point, as certainly the escape velocity is the threshold which define wheter a wind is 'strong' or not. However, since we are not currently able to model winds carefully and in a fully physical–grounded way, we can not neglect that fixing the velocity wind above or below that threshold may changes results.

The second feature which is worth noting, is that removing the gas from the dense star–forming regions prevents the severe locking of metals into stars. We know from

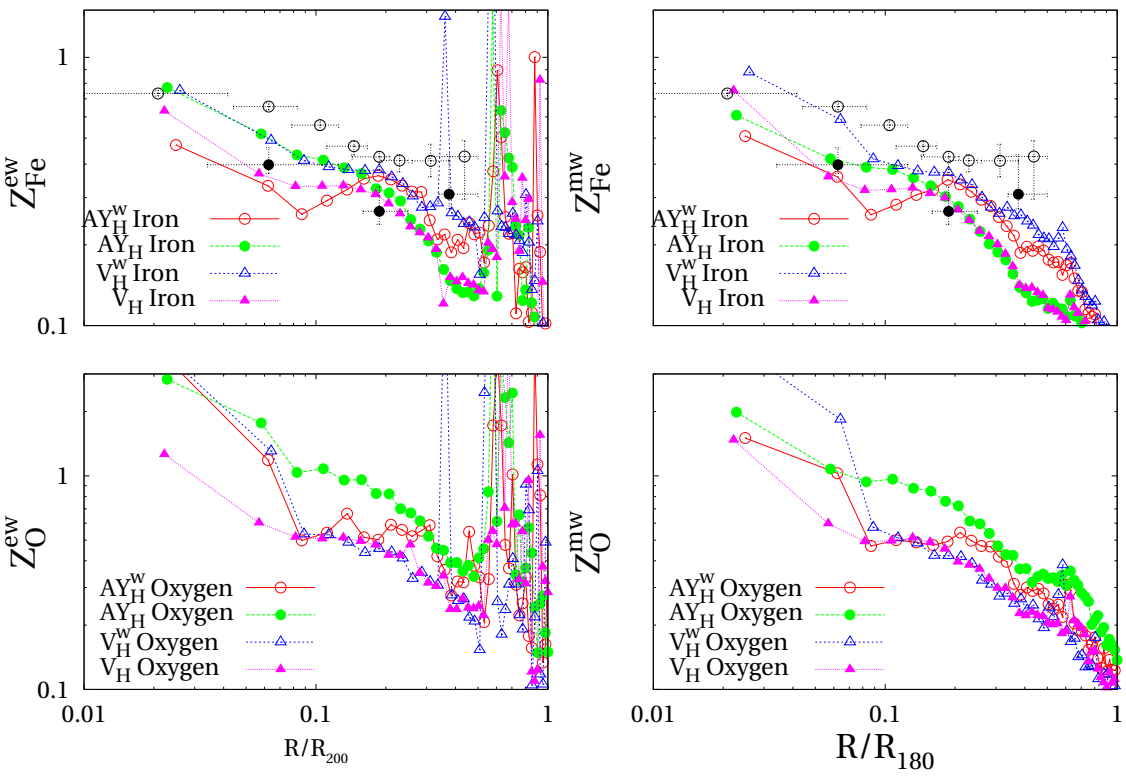

Figure 5.43: Radial abundances profiles for the hot gas. Both Fe (*Upper Row*) and O (*Bottom Row*) are shown. On the *Left Hand Side* we plot emission weighted abundances and on the *Right Hand Side* we plot the mass-weighted abundances.

previous discussions that the Oxygen is the most affected by this process, since it is mainly produced by massive stars which make it very quickly available in the surrounding, star–forming, gas. The Right Panel of Fig. (5.42) clearly shows this process acting in AY_H^w and V_H^w simulations: as the star formation rate is suppressed, the Oxygen production becomes smaller than its 'capture' by newly formed stars (basically for $z \lesssim 1.5$ for both AY_H^w and V_H^w). Instead, neither V_H nor AY_H exhibit such a decreasing of the mean Oxygen content of the gas, instead having a continuous enriching. The final effect on the metal sharing is shown, as for the Iron, in the Top Right Panel of Fig. (5.44); in the central region, where the recent star formation is strong, the gain of Iron mass fraction retained in the gas is substantial (up to a factor of ~ 2).

For the sake of clarity we report in Fig. (5.45) data which are plotted also in Fig. (5.4); it is shown that AY_H and V_H produce the lowest amount Iron and Oxygen, while substantially higher mass fractions of heavy metals enrich the gas. Radial abundance profiles, shown in Fig. (5.43), reflect the same effect. In that figure open symbols stands for simulations having v_w *a priori* determined. Triangles are used to plot simu-

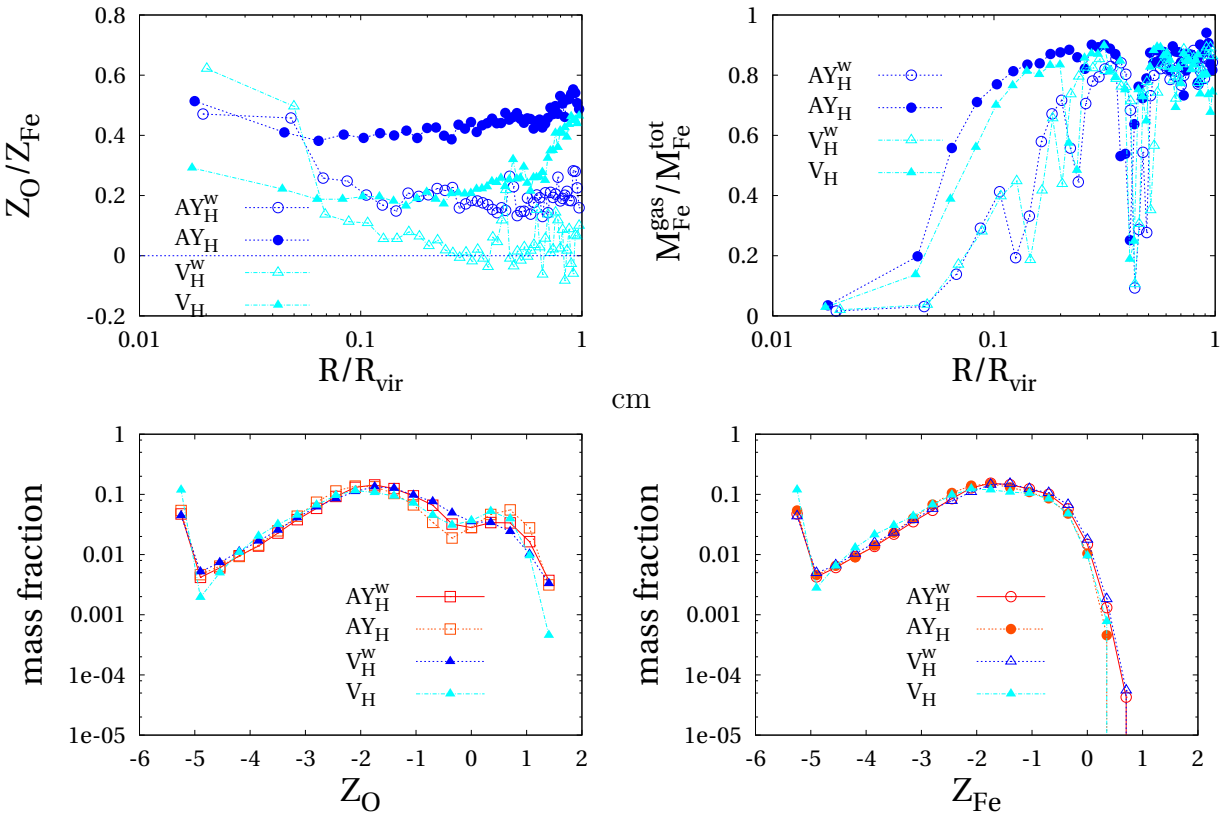

Figure 5.44: [**Upper Left Panel**] The radial profiles of O/Fe gas abundances. [**Upper Rigth Panel**] The radial variance of the fraction of Fe retained by gas. [**Bottom Left Panel**] [**Bottom Right Panel**] The gas mass distribution vs Fe and O abundances respectively.

lations with the Laron IMFand circles to plot simulations with Arimoto–Yoshii IMF. Although AY_H produces much less stars, and then metals, than AY_H^w, the higher mass fraction of metals in the gas makes its abundance profiles to be larger than those of AY_H^w. As for the Iron, this happens only in the central region of the cluster ($R \lesssim 0.2R_{200}$), whereas for the Oxygen the abundance profile of AY_H lives above th one of AY_H^w along all the cluster. In the outer regions, the Iron sharing between gas and star phases is about the same in the two simulations, so that the smaller stellar density in AY_H makes the Fe profile to lie below the AY_H^w one. Instead, the fraction of Oxygen resident in the gas phase is still higher by $15-20\%$ in AY_H than in AY_H^w, and, as we mentioned, the two Oxygen profiles become similar. On the other hand, V_H provides a too small star mass and although the fraction of Iron resident in the gas is much higher than in V_H^w, the Iron abundance profile stands significantly below the profile of V_H^w. Instead, the Oxygen abundance profiles reach the same levels downto $R \sim 0.1R_{200}$, where the larger rate of recent star formation in V_H^w determines the amount of Oxygen

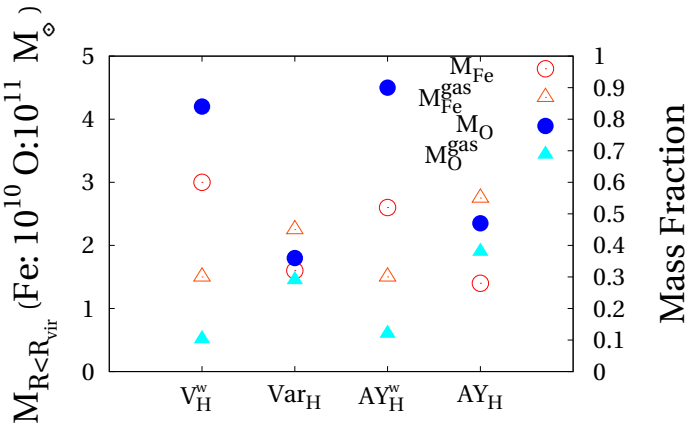

Figure 5.45: Oxygen and Iron Masses and fraction in gas, within virial radius. Triangles refer to mass fractions (right y–axis) and Circles refer to masses (left y–axis). Open symbols refer to Iron and filled symbols refer to Oxygen. Iron masses are reported by a factor 10^{10}, while Oxygen masses by a factor 10^{11}.

ejected in the gas.

A very interesting consequence of making v_w consistent with ϵ_{SN}, are the changes in the radial profile of $[O/Fe]$ ratio. Arimoto–Yoshii runs stand well above sola values, AY_H being fairly constant and AY_H^w growing as we noted in Sec. (5.8). The runs with the Larson IMF follow instead the opposite behaviour. V_H is declines from AY_H–like values in the outskirts downto ~ 0.2 dex values in the centre; V_H^w givea nearly solar values downto $R \sim 0.2 R_{200}$ and thereafter grows steeply up to ~ 0.6 dex in the centre.

The impact on the profiles of thermodynamical properties is quite more significant than seen previous Sections. Besides having a much smaller star fraction, both AY_H and V_H simulations have a higher central density; they also appear to have very similar entropy and temperature profiles. All emission–weighted temperature profiles exhibit a mild decline in the innermost regions; however, this is still highly unsufficient in order to recover the observed profiles (see Chap. (2)).

5.10 Comparing metallicities with observations

In this Section we explicitly plot observational results superimposed to our findings from simulations. As we do not have a large ensemble of objects, we can not discuss interesting observational data such as the dependence of central sbundances on the mass of the system or namely on its baryonic fraction. Instead, we concentrate on the single–object properties.

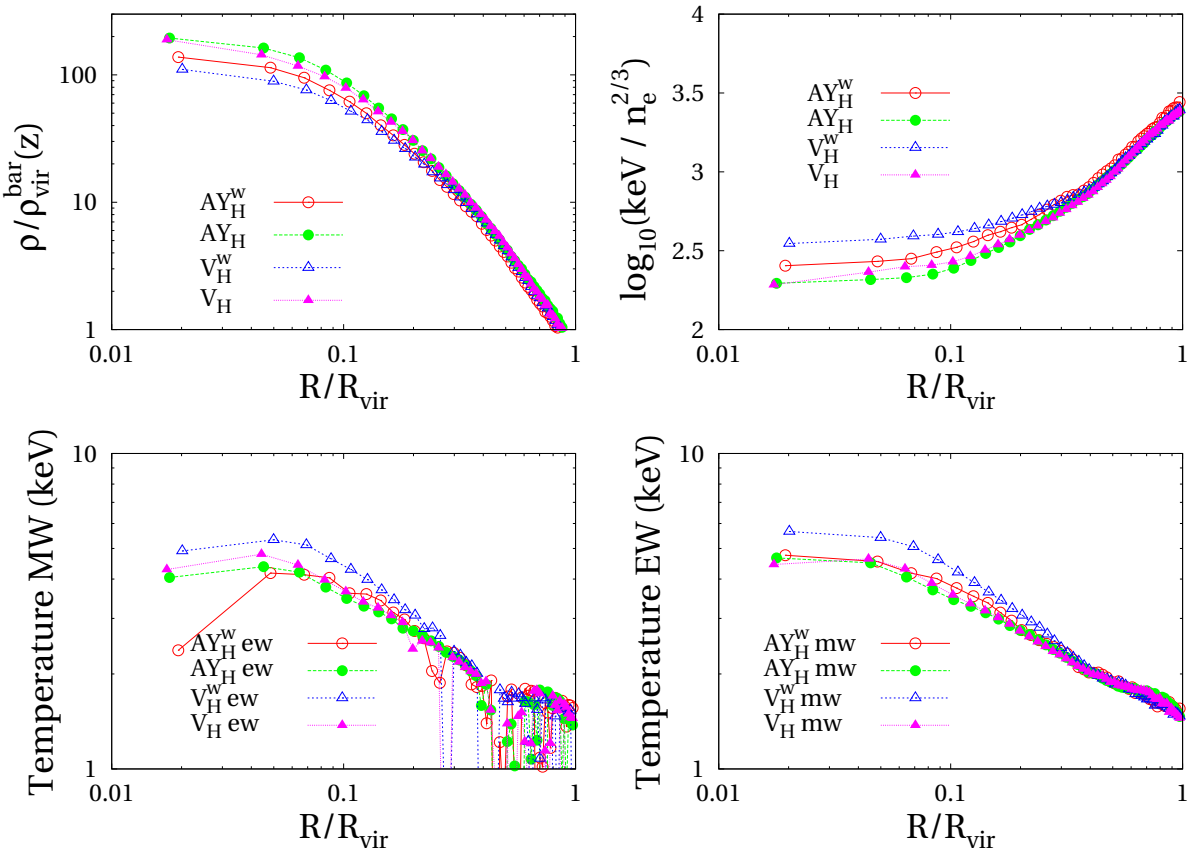

Figure 5.46: [**Upper Left Panel**] The density radial profile of hot gas. [**Upper Right Panel**] The hot gas entropy radial profile. [**Bottom Left Panel**] The emission–weighted temparature profile for the hot gas [**Bottom Right Panel**]
The mass–weighted temparature profile for the hot gas.

We focus our attention on a subset of our high–resolution simulations, chosen so as to account for the physics that we have so far introduced in the code. Besides the 'standard' simulation S_H and its variant $S_H^{A\tau}$, the most interesting cases may be the simulations performed with top–heavier IMFs. Since the winds velocity has proven to be a fundamental factor, we include simulations AY_H^w and V_H^w, which have $v_w = v_w^{S_H}$, as well as AY_H and V_H, whose value of v_w is instead calculated accordinlgy with the actual value of SnII energy available in the IRA regime.

As first we compare with the result from *BeppoSAX* observations by De Grandi & Molendi (2001). Data and simulated profiles are given in Fig. (5.47). As we noted in previous sections, our simulations fairly reproduce in the central region both the abundance and the shape of data (we remind that plotted points are the stacking result of several objects). Since reliable observations of abundances in the outskirts of

galaxy clusters are yet missed, we do not have clues on the shape of Fe abundance in the outermost regions. Although observed profiles exhibit different behaviours, from a very steep decline to a shallower shapes, the general inference is that SnIa products are very centrally concentrated. Hence, the steepness of our profiles starting at about $R \sim 0.4 R_{180}$ may not witness some serious problem, given that we are dealing with a single object.

Accordingly with a priori order–of–magnitude reasonings, top–heavier IMFs reach the highest abundances and, above all, are in fair agreement with data out to larger radii than other IMF. Also, we infer that strong winds may play a crucial role in depleting the central Iron abundance. It is remarkably that also the Salpeter IMF is able to produce high abundance levels if lifetime of Maeder & Meynet (1989) are

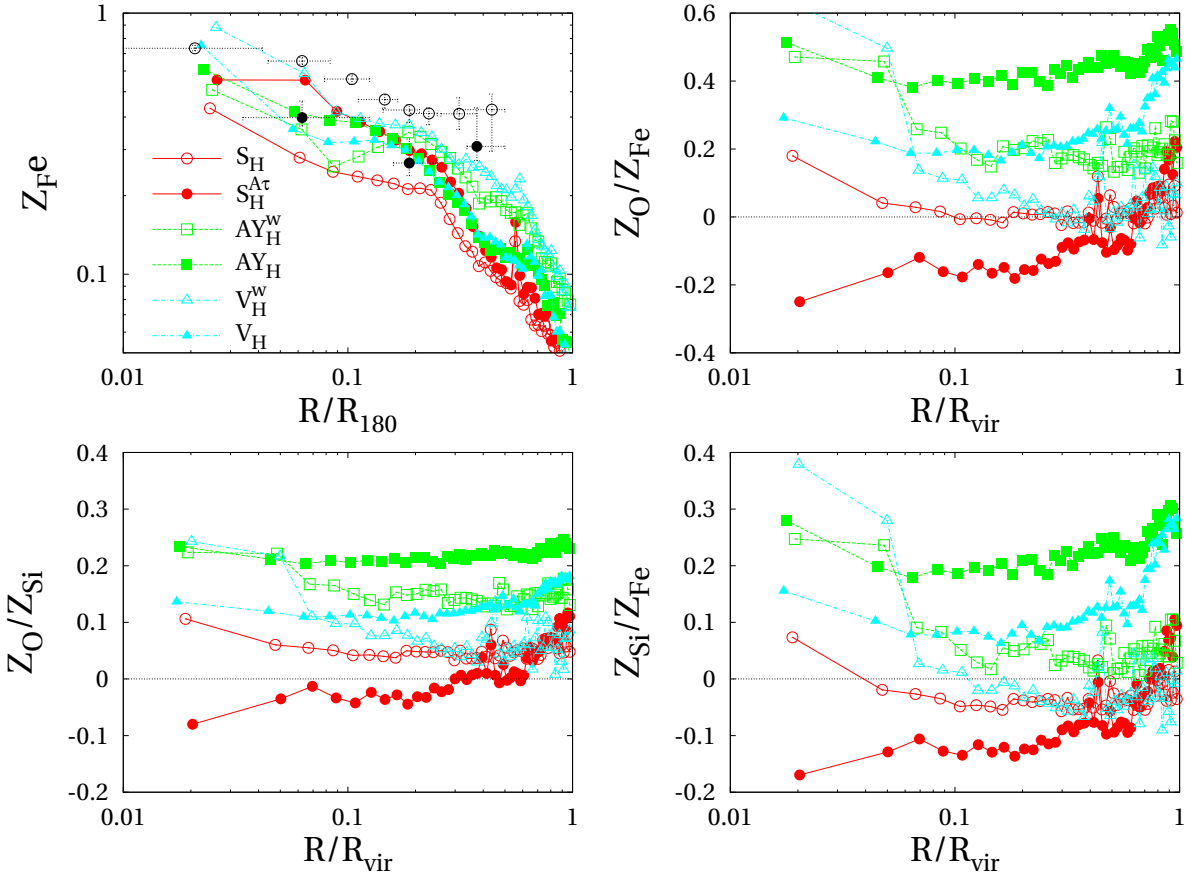

Figure 5.47: We plot radial profiles for abundances and abundance ratios for all the discussed simulations. Z_{Fe} is in solar value (Grevesse & Sauval 1998). Circles are data from De Grandi & Molendi (2001); empty circles refer to *Cooling–Core* clusters whereas filled ones refer to *non Cooling–Core* objects. [**Upper Left Panel**] Fe abundance profiles. [**Upper Right Panel**] O/Fe profile. [**Bottom Left Panel**] O/Si [**Bottom Right Panel**] Si/Fe profile.

assumed. To what extent using such lifetimes has been an exercise is unclear as we do not have measures of SnIa rates in galaxy clusters. Nevertheless, Chiappini (2004, private communication) find that shorter timescales for SnIa arising from low–mass binary systems may be a key ingredient in solving the G–dwarf problem in the Milky Way. Moreover, deferring to late times the ejection of a sizeable fraction of Fe would enhance the fraction of this element which is retained in the gas ($S_H^{A\tau}$ obtain the second higher fraction of Iron in the ICM). Since it is commonly thought that this fraction must be quite large ($> 50\%$, see Renzini 2004), this would be a a way out for saving also the Salpeter IMF that seems not to be best suited to account for chemical enrichment in galaxy clusters (e.g. Larson 1998, Moretti et al. 2003). We also note that the $S_H^{A\tau}$ simulation is the only one achieving negative central values as for the [O/Fe] ratio.

Observations of M87 in the centre of the Virgo cluster (e.g. Gastaldello & Molendi 2002, Matsushita et al. 2003) found undersolar O/Fe and slightly oversolar values for Si/Fe. Also, the raising of both Iron–peak elements and α–elements in interpreted as the signature of recent star formation. Although we have a star–forming central region, no one of our simulation can reproduce such a pattern; either both O and Si are undersolar with respect to Fe (the case of $S_H^{A\tau}$) or both increases towards the centre, even if solar or slight undersolar value are reached at larger radii (S_H and V_H^w). Hence, either a complete different star formation history has take place in our cluster and in M87, or possibly different nucleosynthetic channels are acting in the two. This also can be invoked to explain opposite trend which are shown by S and Si in some clusters.

Finoguenov, David & Ponman (2000b) find in clusters a strong evidence of an increasing role of SnII when moving towards the external regions. We also find a noticeable dependence on the radius for the Si/Fe ratio, which is fairly traced by O/Fe ratio. Finoguenov et al. found solar value in the very centre of systems and supersolar value ($[Si/Fe] \sim 0.6$) in the outskirts. We find very different behaviours, as shown in the bottom right panel of Fig. (5.47). Nevertheless, our results are biased by a strong recent production of α elements which pushes to high values the Fe/α ratios; it is not unlikely that top–heavier IMFs would produce Si/Fe profiles once the star formation at low redshift is inhibited.

Very recently, Tamura et al. (2004) have anlyzed a sample of 19 nearby clusters observed with *XMM–Newton* . We plot their binned profile in Fig. (5.48). Observations concern only the inner $\sim 500\,\mathrm{kpc}$. Although we should normalize the profiles on a characteristic scale (e.g. the virial radius; not provided by the authors) to highlight the peculiar properties of the objects, such a rough comparison is sufficient to confirm us that the general trend of our results is basically correct; this is mostly evident when comparing the Fe profile or the Si/Fe profile, whilst the O/Fe seems to be not in a good agreement. Nevertheless, the obtained error bars (which we do not show for clarity) are quite large and no strict conclusions can be drawn.

Fig. (5.49) shows data on Si/Fe from the *ASCA* database as reported by Baumgartner et al. (2003). The empty circles represent the point which is closer to our cluster

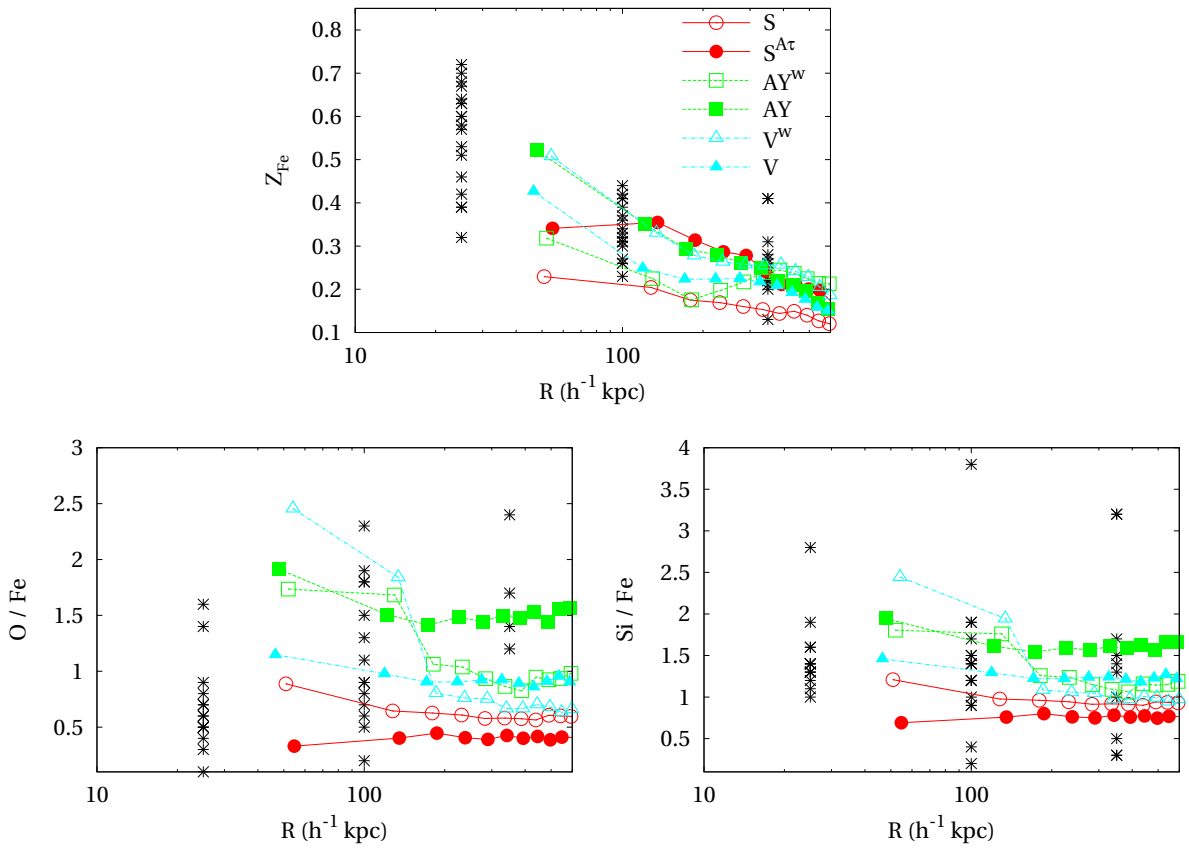

Figure 5.48: We plot our result making a comparsion with recent observations of Tamura et al. (2004). Note that only innermost regions are reported. A really meaningfull comparison should be made among profiles normalized to the virial radius, or a given fraction of it; nervertheless, we find quite interesting to compare with data in central regions, exactly where we have major biases from recent star formation. [**Upper Panel**] The Fe abundance in the central region. Abundance ratios for O/Fe and Si/Fe are plotted in [**Bottom Left Panel**] and [**Bottom Right Panel**] respectively. Data are expressed in units of abundances by Anders & Grevesee 1989.

as for the temperature. Hence, All our simulations, except V_H^w, seems to produce a relative amount of Silicon which agrees with observations. Since a fair correlation between Fe abundance and ICM temperature is now well established, we would expect that taking the filled point as a reference, our simulations produce a similar amount of Iron. Instead, we find that our runs produce less Fe than observed.

We do not show here the redshift evolution of the metallicity for our cluster as the modelled physics changes; however, it can be straightforwardly estimated from the evolution of the mean ICM metallicity that we have plot for all simulations. In all cases there is no significant evolution out to redshift $z \sim 1$, in rough agreement with observation. The only exception is the case for $S_H^{A\tau}$ whose increasing rate of

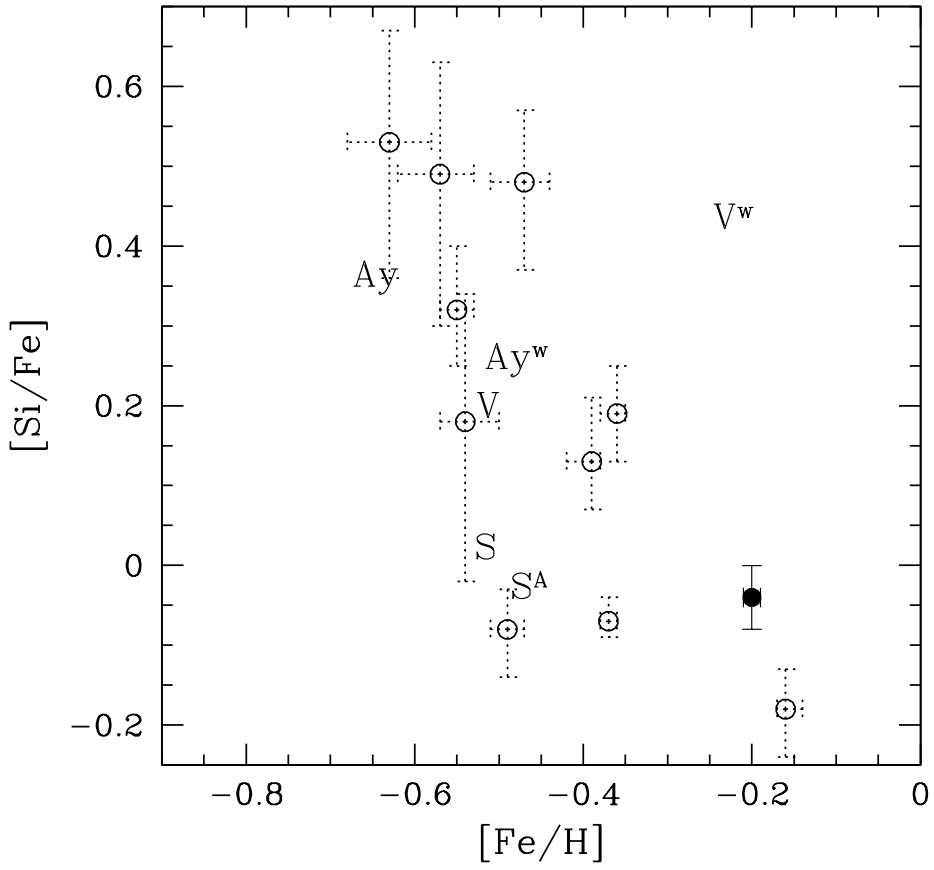

Figure 5.49: We report the correlation between the Si/Fe ratio and the Fe/H abundance. Empty points are taken from Baumgartner et al. 2003; the filled point is the most close to our Virgo–like clusters among data from Baumgartner et al. Note that quantities are reported in dex. We assume solar abundance by Grevesse & Sauval 1998.

SnIamakes Z_{Fe}^{ICM} also increasing with time down to $z \sim 0.1$, which is at odds with observations. Nevertheless, this is in turn caused by the non–negligible recent star formation activity.

CHAPTER 6

CONCLUSIONS AND FUTURE WORK

This Section is devoted to draw the conclusions of the work presented in the previous Chapters. We discuss them in the following Section, whereas in the last one we outline future prospects and developments.

6.1 Discussion and Conclusions

Galaxy Clusters play a key role in modern Cosmology in many respects; since they are the most massive virialized objects in the universe, they witness the history of baryons on large scales and, in general, they are very useful probes for the large scale structure and for the structure formation theories. In the last decades, more and more accurate and deep observations have revealed that Galaxy Clusters have a very intense life both within their virial radius and in the outskirts; most of them are far from being relaxed and quiescent systems, as analytical modelling has so far assumed. Instead, the last generations of X–ray satellites (*ROSAT* , *Chandra* , *ASCA* , *BeppoSAX* , *XMM–Newton*) have shown very complex features in maps of density, temperature, and metallicity.
Therefore, we know that complex physical processes are acting and play a major role in determining the overall properties of the ICM; nevertheless, not only their highly complex interplay is far to be completely understood, but also the influence of each single physical process is not yet firmly clarified.

In this thesis we resorted to advanced numerical methods to achieve some more understanding on a number of these physical processes and on the way they interact with each other. We used the code GADGET [1] that has been kindly provided us in its most advanced version by its author, Volker Springel. We introduced several important

[1] www.mpa-garching.mpg.de/galform/gadget/index.shtml

changes in this code, as discussed in Chap. (2) and Chap. (4).

■ Cooling and heating the ICM

In the **first part** (Chap. (2)) of this work we have studied how radiative cooling and non–gravitational heating influence the relations between fundamental properties of the ICM, namely the link between the X–ray luminosity and the temperature ($L_X - T$) and the relation between the mass and temperature ($M - T$). The results presented here have been published in Tornatore et al. (2003) and Finoguenov et al. (2003a). We remind that the code used to perform the simulations presented in Chap. (2) did not include neither self–consistent supernovae explosions nor the effective star–formation model.

In Chap. (2), we presented high–resolution simulations (up to $3.9 \times 10^7\,\mathrm{M}_\odot$ as for gas particles) of a Virgo–like clusters ($M_{\rm vir} \sim 4 \times 10^{14}\,\mathrm{M}_\odot$) and three poor groups of galaxies ($M_{\rm vir}$ from 2 to 6 $\times 10^{13}\,\mathrm{M}_\odot$), aimed to follow in detail the pattern of gas cooling and its effect on X–ray properties of the ICM. In detail, we study the effect of different energy injection prescriptions coupled with radiative cooling and star formation. On the one hand we model the supernovae explosions by a Semi–Analytical Model (Menci & Cavaliere 2000). Energy from supernovae is distributed on gas particles having density larger than given thresholds, such as to mimic the fact that stars form in dense environment. On the other hand, we simply impose either an energy floor or an entropy floor to gas particles at different redshifts, such as to mimic different energy sources.

The key results from Chap. (2) can be summarized as follows:

[**1**] Our star fraction $f_\star$ ranges in the interval $0.25-0.35$, reproducing the well–known 'overcooling' problem (Balogh et al. 2001). Observations (e.g. Lin et al. 2003) set this fraction at about ~ 0.1 for massive clusters, with a possible slight increase for groups; we know that a more advanced treatment of thermodynamics and star formation succed in lowering the fraction of the star component; Borgani et al. (2004) obtain a fraction of about 20% which, being too high yet, is not likely to increase with resolution, as demonstrated by Springel & Hernquist (2003b). Introducing the extra–heating reduces $f_\star$ by an amount which depends on feedback energy, on the epoch of injection and on the overdensity of targeted gas. Impulsive injection at high–redshift is very effective in bringing the value of $f_\star$ below 10% for the cluster with a strong suppression of the star formation rate until very late times, a result which is higly discrepant with observations (Kodama & Bower 2001). A similar result is achieved by a supernovae energy input for an IMF heavier than that by Salpeter (1955).

[**2**] The entropy profiles of simulations are in general agreement with the profiles very recently reported by Piffaretti et al. (2004) for nearby cooling flow clusters. Our profile show the expected icreasing in the central regions; nevertheless, we have not yet performed a quantitative comparison with available data (Ponman et al. 2003, Arnaud et al. 2004).

[**3**] Heating at $z = 3$ with $E \sim 0.75\,\mathrm{keV/part}$ is shown to produce scaling of X–ray luminosity, mass and entropy vs. temperature which agree in general with observations. This hold independently of wheter an entropy floor is created or an equal amount of energy is assigned to each particle. A similar agreement is also found using a Semi–Analitycal Modelling for supernovae which assumed a Salpeter–like IMF.

[**4**] Many attempts to recover the observed scaling relations for X–Ray luminosity and mass vs. temperature have been presented in literature (see references above). Besides the details of each model, all works agree in finding that cooling and star formation, removing the low–entropy gas, succed in raising temperature in central regions (Voit & Bryan 2001). This tends to reconcile the simulated $M-T$ relation with the observed one, but steepens irremediably the temperature profiles. We find this same result, as we obtain temperature profiles which do not have any evidence of declining at small cluster–centric distances. Although the 'adiabatic' simulation exhibits a temperature drop in the centre, this starts in the very inner region $R \lesssim 0.1 R_{\rm vir}$ whereas the declining trend is expect starting from about $\sim 0.3 R_{\rm vir}$. Thermal conduction has been also invoked in the past as a possible solution for this puzzling question (e.g. Zakamska & Narayan 2003, Ruszkowski & Begelman 2002). Since both small–scale temperature variations (Markevitch et al. 2003) and the magnetic fields (Brighenti & Mathews 2003) can suppress the thermal conduction, wheter or not the effective conductivity can reach a sizeable fraction of the spitzer conductivity is highly uncertain. Dolag et al. (2004) find that, using a conductivity $\kappa = \kappa_{Sp}/3$, thermal conduction is able to reproduce an isothermal core in massive clusters, whereas in poor groups it fails due to the temperature dependence of the conductivity; hence, it does not lead to the self–similar temperature profiles which are suggested by observations.

[**5**] Combining heating and cooling in such a way that overcooling is avoided while simultaneously providing a good fit to the X ray scaling relations, is not an obvious task. Our simplified models for pre–heating are probably not realistic; in literature one may find several model wich implement ad–hoc schemes in order to reproduce single observations. Although all these attempts are aimed at obtaining hints about the actual physical processes, it is certainly preferrable that the solution arises quite naturally from the simulations. From the simulations

presented in Chap. (2), we infer that a careful self–consistent treatment of supernovae evolution is needed. As of today, it is still not clear wheter or not the supernovae can provide enough energy to account for the thermodynamical history of the ICM (e.g. Renzini 1997, Finoguenov et al. 2001a, Pipino et al. 2002). Several feedback sources have been proposed, the most natural being AGN and PopIII stars. The latter are unlike to have contributed significantly given the constraints on the pristine enrichment of gas that they would have caused; nevertheless, large uncertainties on their IMF and on the energetics of very supermassive stars make this topic still rather unclear (Loewenstein 2001). As for AGN (Valageas & Silk 1999b, Wu et al. 2000, Cavaliere et al. 2002), their energy budget is surely large enough, although the energy deposition mechanism, and hence its efficiency, is yet to be clarified.

■ The Chemical Enrichement of Galaxy Clusters

In Chap. (4) and Chap. (5) we report results on what is probably the most accurate numerical description of chemical enrichment of galaxy clusters presented so far. Our code allows us to follow in a self–consistent way the evolution of stellar populations which form during the simulation, also accounting for the finite lifetime of stars of different masses. Then, both energy and metals are deposited in gas surrounding stars. We account for the metal dependence of the cooling function and for the extra–energy in the effective model for star–formation.
Early results have been published in Tornatore et al. (2004). We stress that the challenging task of implementing the stellar evolution and chemical enrichment in numerical simulations is an ongoing project, whose technical aspects are given in Chap. (4). Currently we have extensively tested our code and established its robustness. First results from these tests are then discussed in Chap. (5).
Our chemical code (Chap. (4)), besides involving the entropy–based equations and the effective star formation model (Sec. (3.3.6) and Sec. (3.4.5)) by Springel & Hernquist (2002, 2003a), features full–consistent SnII and SnIa energy treatment as well as the effect of metallicity on the cooling function; simulations of this kind have not yet been performed extensively by any other group, and it would be of extreme interest to check what is the effect on the mentioned scaling relations. At the time of writing we did not yet run simulations for a statistical ensemble of galaxy clusters spanning a large range of masses with this advanced version of GADGET .

In order to test our code, we run an extended suite of simulations aimed to check possible numerical effects on the results. Also, we run and discuss several simulations aimed to explore ...

Our key results are summarized as follows:

[**1**] In simulations performed with this advanced version of GADGET we obtain values for $f_\star$ which live in the range $\sim 0.1- \sim 0.3$, with a mean value of ~ 0.17. Simulations AY_H and V_H involve two top–heavier IMFs and have an energy budget similar to simulations of Chap. (2) run with the highest values of energy feedback from Sn. The net result in both AY_H and V_H is to lower $f_\star$ down to ~ 0.11 while not suppressing the star–formation rate as dramaticly as in the discussed case and, moreover, without shifting the maximum of rate below redhift ~ 2. Besides the self–consistency of supernovae accounting, a key aspect that makes the difference in AY_H and V_H with respect to the mentioned simulations of Chap. (2) is the onset of winds, that are instead absent in simulations of Chap. (2). We also stress that simulations AY_H^w and V_H^w are not so effective in reducing $f_\star$, the only difference from AY_H and V_H being the value of the velocity of galactic winds; v_w is much larger in AY_H and V_H than in AY_H^w and V_H^w (we remind that in these latter simulations it is fixed to $\sim 500\,\mathrm{Km\ sec^{-1}}$, whereas in the former ones it depends on the actual energy available from SnII above $M = 15\,\mathrm{M}_\odot$). Therefore, to reduce $f_\star$ without an exceeding suppression of the star formation, we need (1) an heat source which acts starting from an high enough redshift and which provide enough energy per gram; and (2) an effective removal of gas from dense star–forming regions which is possibly triggered by the same energy source.

[**2**] As discussed above, simulations involving IMFs top–heavier than that by Salpeter ($\mathrm{d}\,n/\mathrm{d}\log m \propto m^{-1.35}$), and with winds' velocity according to the SnII available energy, better succed in reproducing the observed $f_\star$; at the same time, they have neither an exceedingly suppressed star formation nor a maximum of star formation rate shifted towards too low redshifts. Nevertheless, all simulations producing $f_\star \sim 0.15 - 0.20$ are not ruled out. In fact, the accepted estimate of $f_\star \sim 0.1$ is just a lower limit (see Borganiet al. (2004) for a discussion), as, for instance, the stars which do not lie in galaxies may amout to 20% of the total star mass (e.g. Arnaboldi 2003, Murante et al. 2004).

[**3**] While providing emission–weighted Iron abundances within the virial radius that are in fair agreement with the observed level $\sim 0.3 X_{Fe}^{\odot}$ (e.g. Renzini 2004, Baumgartner et al. 2003), the Salpeter IMF can hardly account for the observed abundance profiles (e.g. De Grandi & Molendi 2002). This discrepancy comes from the fact that the emission–weighted estimates are dominated by the innermost region, where the abundance reaches the observed level. As argued by (Portinari et al. 2004), the total amount of Fe produced by the Salpeter IMF would be sufficient to enrich gas to the required level provided that all the Iron ever produced and not locked in stars is expelled in the ICM. In this case, significantly undersolar values for $[\alpha/Fe]$ ratios are obtained, which is at odds with observations (e.g. Tamura et al. 2004; see also Pipino et al. 2002).

[**4**] A fundamental bias that affects our results is that the star formation rate of the simulated clusters remains very high ($\gtrsim 10^2\,\mathrm{M}_\odot$ per year) down to redshift zero, in contraddiction with observations (e.g. Balogh et al. 1997, Balogh et al. 1998). This points toward a lack of physics in modelling either the feedback processes or the star formation below redshift ~ 1. The net effect of such star formation is twofold; on the one hand, it locks a significant amount of metals in stars. On the other hand, newborn stellar populations produce SnII which explode quite rapidly, then enhancing the α element abundance of the ICM. Which one of these two aspects is dominating depends on the IMF: the top–heavier it is, the more α elements are ejected with respect to those locked in stars. At the same time, stars born until $z \sim 0.1$ also produce a significant amount of Iron, as the SnIa of such stellar populations have enough time to explode. What is the resulting balance is difficult to be predicted a priori.

[**5**] Although observations of element abundances in the ICM are now available for extended ensembles of clusters(e.g. Loewenstein 2004), only a general trend can be drawn from them, and a satisfaying theoretical model is far to be achieved. Generally, α elements distribute quite uniformly along the radial direction (e.g. Tamura et al. 2001, Finoguenov et al. 2000b, Gastaldello & Molendi 2002, Peterson et al. 2003) while Iron–peak products exhibit a clear steep declining in the outer regions. No combination of standard SnIa and SnII can accounts for the observed pattern (Finoguenov et al. 2000b, Finoguenov et al. 2003c, Baumgartner et al. 2003, Loewenstein 2004). Our Simulations produce ratios of overall Si/Fe and O/Fe vs. Fe/H which are roughly in the ranges taken from respectively Baumgartner et al. (2003) and Peterson et al. (2003). Nevertheless, our radial abundance ratios are hardly in agreement with observations. Finoguenov et al. (2000b) report for a radial profile of $[Si/Fe]$ which strongly increase with radius, starting from solar values in the centre. The raise is so steep that at about $\sim 0.2R_{\rm vir}$ the Si/Fe ratio is 4 times the solar values. No one of our $[Si/Fe]$ can fit such a behaviour, although our values of overall $[Si/Fe]$ vs $[Fe/H]$ match those found by Finoguenov et al. However, our radial profiles of relative abundance are likely to be strongly affected by the ongoing star formation that we mentioned in the previous point; in fact, the bulk of newly formed stars are harbored in the innermost region; hence, the net effect is to increase the α–elements abundance within $R < 0.1R_{\rm vir}$. This is clearly visible in the S_H simulations, which involve a standard Salpeter IMF. At the opposite, the $S_H^{A\tau}$ run exhibit an opposite trend, owing to the large number of SN that are exploding at redshift $z \lesssim 0.1$ as a consequence of having assumed the shorter stellar lifetimes by Maeder & Meynet (1989).

[**6**] One of the key signature that an IMF leaves is the pattern of relative abundance

ratios (Larson 1998, Larson 2003, Portinari et al. 2004). Wheter the Salpeter IMF is able to reproduce the observed metal pattern in clusters (e.g. Renzini 1997, Renzini 2004, Wyse 1997, Ishimaru & Arimoto 1997) or not (e.g. Portinari et al. 2004, Finoguenov et al. 2000b, Loewenstein 2001, Baumgartner et al. 2003, Finoguenov et al. 2003c) is an highly debated issue. Larson (1998) suggests his IMF arguing that at high redshift an IMF top–heavier than at present time is likely to be more realistic. It also argues that it would account for several observed properties of galaxy clusters. Looking at the radial profiles of relative abundances, as well as at the radial Fe profile, is seems that, in fact, his IMF is that which better behaves, once the biasing of the recent star formation has been taken into account.

[**7**] Our star formation is also likely to affect the so–called *chemical asimmetry*, as the Iron is incorporated into stars as much as α elements. This effect proves to be less severe in AY_H^w and V_H^w, since the strong winds which develop in these two simulations are effective in bringing enriched material out of the densest regions. In any case, we are still far from reaching the metal sharing between stars and gas suggested by Renzini (1997, 2004). He infers that Iron in ICM must be about twice that in stars, while our typical prediction is that between 30% and 50% of Iron lives in the gas.

6.2 Future Perspectives

[**1**] As the scaling relations discussed above are one of the key test for the studying of galaxy clusters, our first aim is to run a complete suite of single–object simulations, spanning mass the range from groups to very rich galaxy clusters.

[**2**] The problem of an ongoing star formation at low redshifts is almost certainly related to an insufficient modelling of both the ICM and star formation process. However, it appears reasonable to conjecture that its solution lies in missing physical effects. One important lack in our simulations are the energy inputs from AGN (e.g. Wu et al. 2000, McNamara et al. 2000, Cavaliere et al. 2002). Owing to the large quantity of ejected energy, they can act so as to 'estinguish' residual star formation at low redshift, mainly by sweeping away the dense clouds from the neighbourhood of central cD which harbour them. One of the key perspectives is exactly that of developing and implementing a model for AGN in cosmological simulations.

[**3**] We plan to compute luminosities in different optical bands from the stellar populations found in simulations by means of photometric evolutionary codes.
This estimates are important in several respects. (1) The $M_\star/L_B$ ratio is a key

quantities which determines measures and estimates of the metal sharing between gas and stars (see Portinari et al. (2004) for a discussion). (2) The Mass–to–Light ratio is an unvaluable test to quantify the metal–retainment capacity of the ICM. Having estimates of this quantity from numerical simulations, where IMF and star formation histories are well–determined, may provide useful hints about the interpretation of observational results. (3) Knowing the emission in different bands makes straightforwad to study the photometric evolution and color relations of cluster galaxies, which are both useful quantities in order to understand how the galaxy clusters formed.

Bibliography

Abel, T., Anninos, P., Zhang, Y., & Norman, M. L.: 1997, Modeling primordial gas in numerical cosmology, *New Astron.* 2, 181–207

Abell, G. O.: 1958, The Distribution of Rich Clusters of Galaxies., *Astrophys. J. Supp.* 3, 211–+

Abell, G. O., Corwin, H. G., & Olowin, R. P.: 1989, A catalog of rich clusters of galaxies, *ApJS* 70, 1–138

Aguirre, A., Hernquist, L., Schaye, J., Weinberg, D. H., Katz, N., & Gardner, J.: 2001a, Metal Enrichment of the Intergalactic Medium at z=3 by Galactic Winds, *Astrophys. J.* 560, 599–605

Aguirre, A., Hernquist, L., Schaye, J., Weinberg, D. H., Katz, N., & Gardner, J.: 2001b, Metal Enrichment of the Intergalactic Medium at z=3 by Galactic Winds, *Astrophys. J.* 560, 599–605

Alimi, J.-M., Serna, A., Pastor, C., & Bernabeu, G.: 2003, Smooth particle hydrodynamics: importance of correction terms in adaptive resolution algorithms, *J. Comput. Phys.* 192, 157–174

Allen, S. W. & Fabian, A. C.: 1994, A ROSAT PSPC Investigation of the Centaurus Cluster of Galaxies, *Mon. Not. R. Astron. Soc.* 269, 409–+

Allen, S. W. & Fabian, A. C.: 1998, The relationship between cooling flows and metallicity measurements for X-ray-luminous clusters, *Mon. Not. R. Astron. Soc.* 297, L63–L68

Allen, S. W., Fabian, A. C., Johnstone, R. M., Arnaud, K. A., & Nulsen, P. E. J.: 2001a, ASCA and ROSAT observations of nearby cluster cooling flows, *Mon. Not. R. Astron. Soc.* 322, 589–613

Allen, S. W., Schmidt, R. W., & Fabian, A. C.: 2001b, The X-ray virial relations for relaxed lensing clusters observed with Chandra, *Mon. Not. R. Astron. Soc.* 328, L37–L41

Anders, E. & Grevesse, N.: 1989, Abundances of the elements - Meteoritic and solar, *gc.a.* 53, 197–214

Arimoto, N. & Yoshii, Y.: 1987, Chemical and photometric properties of a galactic wind model for elliptical galaxies, *Astron. Astrophys.* 173, 23–38

Arnaboldi, M.: 2003, Intracluster Stellar Population, in *AU Symp. 217 "Recycling*

intergalactic and interstellar matter", ASP

Arnaud, M.: 2004, How Evolution Can Affect the Use of Clusters As Cosmological Probes. XMM-Newton Observations of Distant Galaxy Clusters, in *The Riddle of Cooling Flows in Galaxies and Clusters of galaxies*

Arnaud, M. & Evrard, A. E.: 1999, The L_X-T relation and intracluster gas fractions of X-ray clusters, *Mon. Not. R. Astron. Soc.* 305, 631–640

Arnaud, M., Pratt, G. W., & Pointecouteau, E.: 2004, Structural and scaling properties of galaxy clusters: probing the physics of structure formation, *Memorie della Societa Astronomica Italiana* 75, 529–+

Böhringer, H., Matsushita, K., Churazov, E., Ikebe, Y., & Chen, Y.: 2002, The new emerging model for the structure of cooling cores in clusters of galaxies, *Astron. Astrophys.* 382, 804–820

Bahcall, N. A. & Bode, P.: 2003, The Amplitude of Mass Fluctuations, *Astrophys. J. Lett.* 588, L1–L4

Balogh, M. L., Morris, S. L., Yee, H. K. C., Carlberg, R. G., & Ellingson, E.: 1997, Star Formation in Cluster Galaxies at 0.2 L_X–T Z L_X–T 0.55, *Astrophys. J. Lett.* 488, L75+

Balogh, M. L., Pearce, F. R., Bower, R. G., & Kay, S. T.: 2001, Revisiting the cosmic cooling crisis, *Mon. Not. R. Astron. Soc.* 326, 1228–1234

Balogh, M. L., Schade, D., Morris, S. L., Yee, H. K. C., Carlberg, R. G., & Ellingson, E.: 1998, The Dependence of Cluster Galaxy Star Formation Rates on the Global Environment, *Astrophys. J. Lett.* 504, L75+

Balsara, D. S.: 1995, von Neumann stability analysis of smooth particle hydrodynamics–suggestions for optimal algorithms, *J. Comput. Phys.* 121, 357–372

Barkana, R. & Loeb, A.: 2001, In the beginning: the first sources of light and the reionization of the universe, *Phys. Rep* 349, 125–238

Barnes, J. & Hut, P.: 1986, A Hierarchical O(NlogN) Force-Calculation Algorithm, *Nature* 324, 446–449

Baumgartner, W. H., Loewenstein, M., Horner, D. J., & Mushotzky, R. F.: 2003, Intermediate Element Abundances in Galaxy Clusters

Bennett, C. L., Halpern, M., Hinshaw, G., Jarosik, N., Kogut, A., Limon, M., Meyer, S. S., Page, L., Spergel, D. N., Tucker, G. S., Wollack, E., Wright, E. L., Barnes, C., Greason, M. R., Hill, R. S., Komatsu, E., Nolta, M. R., Odegard, N., Peiris, H. V., Verde, L., & Weiland, J. L.: 2003, First-Year Wilkinson Microwave Anisotropy Probe (WMAP) Observations: Preliminary Maps and Basic Results, *Astrophys. J. Supp.* 148, 1–27

Benoît, A. & coauthors, .: 2003, Cosmological constraints from Archeops, *Astron. Astrophys.* 399, L25–L30

Boesgaard, A. M. & Steigman, G.: 1985, Big bang nucleosynthesis - Theories and observations, *Annu. Rev. Astron. Astrophys.* 23, 319–378

Bond, J. R. & Efstathiou, G.: 1984, Cosmic background radiation anisotropies in universes dominated by nonbaryonic dark matter, *Astrophys. J. Lett.* 285, L45–L48

Borgani, S.: 2004, Galaxy Clusters As Cosmological Tools and Astrophysical Laboratories, in *The Riddle of Cooling Flows in Galaxies and Clusters of galaxies*

Borgani, S., Governato, F., Wadsley, J., Menci, N., Tozzi, P., Lake, G., Quinn, T., & Stadel, J.: 2001a, Preheating the Intracluster Medium in High-Resolution Simulations: The Effect on the Gas Entropy, *Astrophys. J. Lett.* 559, L71–L74

Borgani, S., Governato, F., Wadsley, J., Menci, N., Tozzi, P., Quinn, T., Stadel, J., & Lake, G.: 2002, The effect of non-gravitational gas heating in groups and clusters of galaxies, *Mon. Not. R. Astron. Soc.* 336, 409–424

Borgani, S. & Guzzo, L.: 2001, X-ray clusters of galaxies as tracers of structure in the Universe, *Nature* 409, 39–45

Borgani, S., Murante, G., Springel, V., Diaferio, A., Dolag, K., Moscardini, L., Tormen, G., Tornatore, L., & Tozzi, P.: 2004, X-ray properties of galaxy clusters and groups from a cosmological hydrodynamical simulation, *Mon. Not. R. Astron. Soc.* 348, 1078–1096

Borgani, S., Rosati, P., Tozzi, P., Stanford, S. A., Eisenhardt, P. R., Lidman, C., Holden, B., Della Ceca, R., Norman, C., & Squires, G.: 2001b, Measuring $Omega_m$ with the ROSAT Deep Cluster Survey, *Astrophys. J.* 561, 13–21

Bower, R. G., Benson, A. J., Lacey, C. G., Baugh, C. M., Cole, S., & Frenk, C. S.: 2001, The impact of galaxy formation on the X-ray evolution of clusters, *Mon. Not. R. Astron. Soc.* 325, 497–508

Brighenti, F. & Mathews, W. G.: 2001, Entropy Evolution in Galaxy Groups and Clusters: a Comparison of External and Internal Heating, *Astrophys. J.* 553, 103–120

Brighenti, F. & Mathews, W. G.: 2003, Feedback Heating in Cluster and Galactic Cooling Flows, *Astrophys. J.* 587, 580–588

Brookshaw, L.: 1985, A method of calculating radiative heat diffusion in particle simulations, *Proceedings of the Astronomical Society of Australia* 6, 207–210

Brookshaw, L.: 1994, Solving the Heat Diffusion Equation in SPH (Invited paper), *Mem. Soc. Astr. It.* 65, 1033–+

Bryan, G.: 1996, The Numerical Simulation of X-ray Clusters, *Ph.D. Thesis*

Bryan, G. L. & Norman, M. L.: 1998, Statistical Properties of X-Ray Clusters: Analytic and Numerical Comparisons, *Astrophys. J.* 495, 80–+

Buote, D. A.: 2000, X-ray evidence for multiphase hot gas with nearly solar Fe abundances in the brightest groups of galaxies, *Mon. Not. R. Astron. Soc.* 311, 176–200

Burles, S. & Tytler, D.: 1998, On the Measurements of D/H in QSO Absorption Systems Closing in on the primordial abundance of deuterium, *Space Science Reviews* 84, 65–75

Carlstrom, J. E., Holder, G. P., & Reese, E. D.: 2002, Cosmology with the Sunyaev-Zel'dovich Effect, *Annu. Rev. Astron. Astrophys.* 40, 643–680

Cavaliere, A. & Fusco-Femiano, R.: 1976, X-rays from hot plasma in clusters of galaxies, *Astron. Astrophys.* 49, 137–144

Cavaliere, A., Lapi, A., & Menci, N.: 2002, Quasar Feedback on the Intracluster Medium, *Astrophys. J. Lett.* 581, L1–L4

Cavaliere, A., Menci, N., & Tozzi, P.: 1998, Diffuse Baryons in Groups and Clusters of Galaxies, *Astrophys. J.* 501, 493–+

Cen, R.: 1992, A hydrodynamic approach to cosmology - Methodology, *Astrophys. J. Supp.* 78, 341–364

Cen, R. & Ostriker, J. P.: 2000, Physical Bias of Galaxies from Large-Scale Hydrodynamic Simulations, *Astrophys. J.* 538, 83–91

Ciardi, B. & Ferrara, A.: 2004, The First Cosmic Structures and their Effects

Coles, P.: 2000, Large-Scale Structure, in *Perspectives on Radio Astronomy: Science with Large Antenna Arrays, Proceedings of the Conference held at the Royal Netherlands Academy of Arts and Sciences in Amsterdam on 7-9 April 1999. Edited by M. P. van Haarlem. Published by ASTRON. ISBN: 90-805434-1-1, 340 pages, 2000, p.53*, pp 53–+

Coles, P.: 2001, Large-Scale Structure, Theory and Statistics

Coles, P. & Lucchin, F.: 1995, *Cosmology. The origin and evolution of cosmic structure*, Chichester: Wiley, —c1995

Cox, D. P. & Tucker, W. H.: 1969, Ionization Equilibrium and Radiative Cooling of a Low-Density Plasma, *Astrophys. J.* 157, 1157–+

Davé, R., Katz, N., & Weinberg, D. H.: 2002, X-Ray Scaling Relations of Galaxy Groups in a Hydrodynamic Cosmological Simulation, *Astrophys. J.* 579, 23–41

David, L. P., Nulsen, P. E. J., McNamara, B. R., Forman, W., Jones, C., Ponman, T., Robertson, B., & Wise, M.: 2001, A High-Resolution Study of the Hydra A Cluster with Chandra: Comparison of the Core Mass Distribution with Theoretical Predictions and Evidence for Feedback in the Cooling Flow, *Astrophys. J.* 557, 546–559

De Grandi, S. & Molendi, S.: 2001, Metallicity Gradients in X-Ray Clusters of Galaxies, *Astrophys. J.* 551, 153–159

De Grandi, S. & Molendi, S.: 2002, Temperature Profiles of Nearby Clusters of Galaxies, *Astrophys. J.* 567, 163–177

de Plaa, J., Kaastra, J. S., Tamura, T., Pointecouteau, E., Mendez, M., & Peterson, J. R.: 2004, X-ray spectroscopy on Abell 478 with XMM-Newton

Dolag, K., Bartelmann, M., & Lesch, H.: 2002, Evolution and structure of magnetic fields in simulated galaxy clusters, *Astron. Astrophys.* 387, 383–395

Dolag, K., Jubelgas, M., Springel, V., Borgani, S., & Rasia, E.: 2004, Thermal Conduction in Simulated Galaxy Clusters, *Astrophys. J. Lett.* 606, L97–L100

Dupke, R. A. & White, R. E.: 2000a, Constraints on Type IA Supernova Models from X-Ray Spectra of Galaxy Clusters, *Astrophys. J.* 528, 139–144

Dupke, R. A. & White, R. E.: 2000b, Metallicity Gradients in the Intracluster Gas of

Abell 496, *Astrophys. J.* 537, 123–133

Efstathiou, G., Davis, M., White, S. D. M., & Frenk, C. S.: 1985, Numerical techniques for large cosmological N-body simulations, *Astrophys. J. Supp.* 57, 241–260

Eke, V. R., Cole, S., & Frenk, C. S.: 1996, Cluster evolution as a diagnostic for Omega, *Mon. Not. R. Astron. Soc.* 282, 263–280

Ellis, J.: 2003, Dark matter and dark energy: summary and future directions, *Royal Society of London Philosophical Transactions Series A* 361, 2607–2627

Ettori, S., De Grandi, S., & Molendi, S.: 2002a, Gravitating mass profiles of nearby galaxy clusters and relations with X-ray gas temperature, luminosity and mass, *Astron. Astrophys.* 391, 841–855

Ettori, S., Fabian, A. C., Allen, S. W., & Johnstone, R. M.: 2002b, Deep inside the core of Abell 1795: the Chandra view, *Mon. Not. R. Astron. Soc.* 331, 635–648

Ettori, S., Tozzi, P., Borgani, S., & Rosati, P.: 2004, Scaling laws in X-ray galaxy clusters at redshift between 0.4 and 1.3, *Astron. Astrophys.* 417, 13–27

Evrard, A. E.: 1997, The intracluster gas fraction in X-ray clusters - Constraints on the clustered mass density, *Mon. Not. R. Astron. Soc.* 292, 289–+

Evrard, A. E. & Henry, J. P.: 1991, Expectations for X-ray cluster observations by the ROSAT satellite, *Astrophys. J.* 383, 95–103

Fabian, A. C.: 1994, Cooling Flows in Clusters of Galaxies, *Annu. Rev. Astron. Astrophys.* 32, 277–318

Fabian, A. C., Mushotzky, R. F., Nulsen, P. E. J., & Peterson, J. R.: 2001, On the soft X-ray spectrum of cooling flows, *Mon. Not. R. Astron. Soc.* 321, L20–L24

Finoguenov, A., Arnaud, M., & David, L. P.: 2001a, Temperature and Heavy-Element Abundance Profiles of Cool Clusters of Galaxies from ASCA, *Astrophys. J.* 555, 191–204

Finoguenov, A., Borgani, S., Tornatore, L., & Böhringer, H.: 2003a, Reproducing the entropy structure in galaxy groups, *Astron. Astrophys.* 398, L35–L39

Finoguenov, A., Burkert, A., & Böhringer, H.: 2003b, Role of Clusters of Galaxies in the Evolution of the Metal Budget in the Universe, *Astrophys. J.* 594, 136–143

Finoguenov, A., Burkert, A., & Böhringer, H.: 2003c, Role of Clusters of Galaxies in the Evolution of the Metal Budget in the Universe, *Astrophys. J.* 594, 136–143

Finoguenov, A., David, L. P., & Ponman, T. J.: 2000a, An ASCA Study of the Heavy-Element Distribution in Clusters of Galaxies, *Astrophys. J.* 544, 188–203

Finoguenov, A., David, L. P., & Ponman, T. J.: 2000b, An ASCA Study of the Heavy-Element Distribution in Clusters of Galaxies, *Astrophys. J.* 544, 188–203

Finoguenov, A. & Ponman, T. J.: 1999, Constraining the role of Type IA and Type II supernovae in galaxy groups by spatially resolved analysis of ROSAT and ASCA observations, *Mon. Not. R. Astron. Soc.* 305, 325–337

Finoguenov, A., Reiprich, T. H., & Böhringer, H.: 2001b, Details of the mass-temperature relation for clusters of galaxies, *Astron. Astrophys.* 368, 749–759

Fukazawa, Y., Makishima, K., Tamura, T., Ezawa, H., Xu, H., Ikebe, Y., Kikuchi, K.,

& Ohashi, T.: 1998, ASCA Measurements of Silicon and Iron Abundances in the Intracluster Medium, *pasj* 50, 187–193

Fukazawa, Y., Ohashi, T., Fabian, A. C., Canizares, C. R., Ikebe, Y., Makishima, K., Mushotzky, R. F., & Yamashita, K.: 1994, Metal concentration and X-ray cool spectral component in the central region of the Centaurus cluster of galaxies, *PasJ* 46, L55–L58

Gastaldello, F. & Molendi, S.: 2002, Abundance Gradients and the Role of Supernovae in M87, *Astrophys. J.* 572, 160–168

Giacconi, R., Branduardi, G., Briel, U., Epstein, A., Fabricant, D., Feigelson, E., Forman, W., Gorenstein, P., Grindlay, J., Gursky, H., Harnden, F. R., Henry, J. P., Jones, C., Kellogg, E., Koch, D., Murray, S., Schreier, E., Seward, F., Tananbaum, H., Topka, K., Van Speybroeck, L., Holt, S. S., Becker, R. H., Boldt, E. A., Serlemitsos, P. J., Clark, G., Canizares, C., Markert, T., Novick, R., Helfand, D., & Long, K.: 1979, The Einstein /HEAO 2/ X-ray Observatory, *Astrophys. J.* 230, 540–550

Giacconi, R., Murray, S., Gursky, H., Kellogg, E., Schreier, E., & Tananbaum, H.: 1972, The UHURU catalog of X-ray souces., *Astrophys. J.* 178, 281–308

Gibson, B. K., Loewenstein, M., & Mushotzky, R. F.: 1997, Supernovae Types Ia/II and intracluster medium enrichment, *Mon. Not. R. Astron. Soc.* 290, 623–628

Gingold, R. A. & Monaghan, J. J.: 1977, Smoothed particle hydrodynamics - Theory and application to non-spherical stars, *Mon. Not. R. Astron. Soc.* 181, 375–389

Gingold, R. A. & Monaghan, J. J.: 1982, Kernel estimates as a basis for general particle methods in hydrodynamics, *J. Comput. Phys.* 46, 429–453

Greggio, L. & Renzini, A.: 1983, The binary model for type I supernovae - Theoretical rates, *Astron. Astrophys.* 118, 217–222

Grevesse, N. & Sauval, A. J.: 1998, Standard Solar Composition, *Space Science Reviews* 85, 161–174

Guth, A. H. & Pi, S.-Y.: 1982, Fluctuations in the new inflationary universe, *Physical Review Letters* 49, 1110–1113

Henriksen, M. J. & Mushotzky, R. F.: 1986, The X-ray spectrm of the Coma Cluster of galaxies, *Astrophys. J.* 302, 287–295

Hernandez, X. & Ferrara, A.: 2001, Cosmological origin of the lowest metallicity halo stars, *Mon. Not. R. Astron. Soc.* 324, 484–490

Hernquist, L.: 1993, Some cautionary remarks about smoothed particle hydrodynamics, *Astrophys. J.* 404, 717–722

Hernquist, L. & Katz, N.: 1989, TREESPH - A unification of SPH with the hierarchical tree method, *Astrophys. J. Supp.* 70, 419–446

Hockney, R. W. & Eastwood, J. W.: 1981, *Computer Simulation Using Particles*, Computer Simulation Using Particles, New York: McGraw-Hill, 1981

Hubble, E. & Humason, M. L.: 1931, The Velocity-Distance Relation among Extra-Galactic Nebulae, *Astrophys. J.* 74, 43–+

Hwang, U., Mushotzky, R. F., Burns, J. O., Fukazawa, Y., & White, R. A.: 1999, Mass and Metallicity of Five X-Ray-bright Galaxy Groups, *Astrophys. J.* 516, 604–618

Iben, I. & Renzini, A.: 1983, Asymptotic giant branch evolution and beyond, *Annu. Rev. Astron. Astrophys.* 21, 271–342

Ikebe, Y., Reiprich, T. H., Böhringer, H., Tanaka, Y., & Kitayama, T.: 2002, A new measurement of the X-ray temperature function of clusters of galaxies, *Astron. Astrophys.* 383, 773–790

Irwin, J. A. & Bregman, J. N.: 2000, Radial Temperature Profiles of 11 Clusters of Galaxies Observed with BEPPOSAX, *Astrophys. J.* 538, 543–554

Irwin, J. A. & Bregman, J. N.: 2001, Iron Abundance Profiles of 12 Clusters of Galaxies Observed with BeppoSAX, *Astrophys. J.* 546, 150–156

Ishimaru, Y. & Arimoto, N.: 1997, Roles of SN IA and SN II in ICM Enrichment, *PASJ* 49, 1–8

Jeans, J. H.: 1928, *Astronomy and cosmogony*, Cambridge [Eng.] The University press, 1928.

Jubelgas, M., Springel, V., & Dolag, K.: 2004, Thermal conduction in cosmological SPH simulations, *Mon. Not. R. Astron. Soc.* 351, 423–435

Kaastra, J. S., Ferrigno, C., Tamura, T., Paerels, F. B. S., Peterson, J. R., & Mittaz, J. P. D.: 2001, XMM-Newton observations of the cluster of galaxies Sérsic 159-03, *Astron. Astrophys.* 365, L99–L103

Kahn, S. M., Behar, E., Kinkhabwala, A., & Savin, D. W.: 2002, X-ray spectroscopy of astrophysical plasmas, *Royal Society of London Philosophical Transactions Series A* 360, 1923–+

Kaiser, N.: 1986, Evolution and clustering of rich clusters, *Mon. Not. R. Astron. Soc.* 222, 323–345

Katz, N. & Gunn, J. E.: 1991, Dissipational galaxy formation. I - Effects of gasdynamics, *Astrophys. J.* 377, 365–381

Katz, N., Weinberg, D. H., & Hernquist, L.: 1996, Cosmological Simulations with TreeSPH, *Astrophys. J. Supp.* 105, 19–+

Kawata, D. & Gibson, B. K.: 2003, GCD+: a new chemodynamical approach to modelling supernovae and chemical enrichment in elliptical galaxies, *Mon. Not. R. Astron. Soc.* 340, 908–922

Kay, S. T., Pearce, F. R., Frenk, C. S., & Jenkins, A.: 2002, Including star formation and supernova feedback within cosmological simulations of galaxy formation, *Mon. Not. R. Astron. Soc.* 330, 113–128

Kay, S. T., Thomas, P. A., & Theuns, T.: 2003, The impact of galaxy formation on X-ray groups, *Mon. Not. R. Astron. Soc.* 343, 608–618

Kennicutt, R. C.: 1998, The Global Schmidt Law in Star-forming Galaxies, *Astrophys. J.* 498, 541–+

Kodama, T. & Bower, R. G.: 2001, Reconstructing the history of star formation in rich cluster cores, *Mon. Not. R. Astron. Soc.* 321, 18–36

Kravtsov, A. V., Klypin, A. A., Bullock, J. S., & Primack, J. R.: 1998, The Cores of Dark Matter-dominated Galaxies: Theory versus Observations, *Astrophys. J.* 502, 48–+

Kravtsov, A. V. & Yepes, G.: 2000, On the supernova heating of the intergalactic medium, *Mon. Not. R. Astron. Soc.* 318, 227–238

Landau, L. D. & Lifshitz, E. M.: 1959, *Fluid mechanics*, Course of theoretical physics, Oxford: Pergamon Press, 1959

Landau, L. D. & Lifshitz, E. M.: 1969, *Statistical physics. Pt.1*, Course of theoretical physics - Pergamon International Library of Science, Technology, Engineering and Social Studies, Oxford: Pergamon Press, and Reading: Addison-Wesley, —c1969, 2nd rev. - enlarg.ed.

Larson, R. B.: 1998, Early star formation and the evolution of the stellar initial mass function in galaxies, *Mon. Not. R. Astron. Soc.* 301, 569–581

Larson, R. B.: 2003, The Stellar Initial Mass Function and Beyond (Invited Review), in *Astronomical Society of the Pacific Conference Series*, pp 65–80

Larson, R. B. & Dinerstein, H. L.: 1975, Gas loss in groups of galaxies, *pasp* 87, 911–915

Lia, C., Portinari, L., & Carraro, G.: 2002, Star formation and chemical evolution in smoothed particle hydrodynamics simulations: a statistical approach, *Mon. Not. R. Astron. Soc.* 330, 821–836

Lin, Y., Mohr, J. J., & Stanford, S. A.: 2003, Near-Infrared Properties of Galaxy Clusters: Luminosity as a Binding Mass Predictor and the State of Cluster Baryons, *Astrophys. J.* 591, 749–763

Lloyd-Davies, E. J., Ponman, T. J., & Cannon, D. B.: 2000, The entropy and energy of intergalactic gas in galaxy clusters, *Mon. Not. R. Astron. Soc.* 315, 689–702

Loewenstein, M.: 2001, The Contribution of Population III to the Enrichment and Preheating of the Intracluster Medium, *Astrophys. J.* 557, 573–577

Loewenstein, M.: 2004, Chemical Composition of the Intracluster Medium, in *Origin and Evolution of the Elements*, pp 425–+

Lombardi, J. C., Sills, A., Rasio, F. A., & Shapiro, S. L.: 1999, Tests of Spurious Transport in Smoothed Particle Hydrodynamics, *J. Comput. Phys.* 152, 687–735

Lucy, L. B.: 1977, A numerical approach to the testing of the fission hypothesis, *Astron. J.* 82, 1013–1024

Maeder, A. & Meynet, G.: 1989, Grids of evolutionary models from 0.85 to 120 solar masses - Observational tests and the mass limits, *Astron. Astrophys.* 210, 155–173

Markevitch, M., Forman, W. R., Sarazin, C. L., & Vikhlinin, A.: 1998, The Temperature Structure of 30 Nearby Clusters Observed with ASCA: Similarity of Temperature Profiles, *Astrophys. J.* 503, 77–+

Markevitch, M., Mazzotta, P., Vikhlinin, A., Burke, D., Butt, Y., David, L., Donnelly, H., Forman, W. R., Harris, D., Kim, D.-W., Virani, S., & Vrtilek, J.: 2003, Chandra Temperature Map of A754 and Constraints on Thermal Conduction, *As-*

trophys. J. Lett. 586, L19–L23

Martin, C. L.: 1999, Properties of Galactic Outflows: Measurements of the Feedback from Star Formation, *Astrophys. J.* 513, 156–160

Matsumoto, H., Pierre, M., Tsuru, T. G., & Davis, D. S.: 2001, ASCA observations of massive medium-distant clusters of galaxies. II., *Astron. Astrophys.* 374, 28–35

Matsumoto, H., Tsuru, T. G., Fukazawa, Y., Hattori, M., & Davis, D. S.: 2000, Gas, Iron, and Gravitational Mass in Galaxy Clusters: The General Lack of Cluster Evolution at z L_X–T 1.0, *PasJ* 52, 153–+

Matsushita, K., Finoguenov, A., & Böhringer, H.: 2003, XMM observation of M 87. II. Abundance structure of the interstellar and intergalactic medium, *Astron. Astrophys.* 401, 443–461

Matteucci, F.: 2003, *The Chemical Evolution of the Galaxy*, The Chemical Evolution of the Galaxy. By Francesca Matteucci, Department of Astronomy, University of Trieste, Italy. Astrophysics and Space Science Library Volume 253 reprint Kluwer Academic Publishers, Dordrecht

Matteucci, F. & Padovani, P.: 1993, Chemical Evolution of Galaxies and Quasar Metallicities, *Astrophys. J.* 419, 485–+

Matteucci, F. & Recchi, S.: 2001, On the Typical Timescale for the Chemical Enrichment from Type Ia Supernovae in Galaxies, *Astrophys. J.* 558, 351–358

McHardy, I. M., Lawrence, A., Pye, J. P., & Pounds, K. A.: 1981, The Ariel V /3 A/ catalogue of X-ray sources. II - Sources at high galactic latitude /absolute value of B greater than 10 deg/, *Mon. Not. R. Astron. Soc.* 197, 893–919

McKee, C. F. & Ostriker, J. P.: 1977, A theory of the interstellar medium - Three components regulated by supernova explosions in an inhomogeneous substrate, *Astrophys. J.* 218, 148–169

McNamara, B. R., Wise, M., Nulsen, P. E. J., David, L. P., Sarazin, C. L., Bautz, M., Markevitch, M., Vikhlinin, A., Forman, W. R., Jones, C., & Harris, D. E.: 2000, Chandra X-Ray Observations of the Hydra A Cluster: An Interaction between the Radio Source and the X-Ray-emitting Gas, *Astrophys. J. Lett.* 534, L135–L138

Mellier, Y., van Waerbeke, L., Bertin, E., Tereno, I., & Bernardeau, F.: 2002, Wide-field cosmic shear surveys, in *Astronomical Data Analysis II. Edited by Starck, Jean-Luc; Murtagh, Fionn D. Proceedings of the SPIE, Volume 4847, pp. 112-122 (2002).*, pp 112–122

Menci, N. & Cavaliere, A.: 2000, The history of cosmic baryons: X-ray emission versus star formation rate, *Mon. Not. R. Astron. Soc.* 311, 50–62

Mitchell, R. J., Culhane, J. L., Davison, P. J. N., & Ives, J. C.: 1976, Ariel 5 observations of the X-ray spectrum of the Perseus Cluster, *Mon. Not. R. Astron. Soc.* 175, 29P–34P

Monaghan, J. J.: 1982, *SIAM J. Sci. Stat. Comput.* 3, 422

Monaghan, J. J.: 1992, Smoothed particle hydrodynamics, *Annu. Rev. Astron. Astrophys.* 30, 543–574

Monaghan, J. J.: 2002, SPH compressible turbulence, *Mon. Not. R. Astron. Soc.* 335, 843–852

Monaghan, J. J. & Lattanzio, J. C.: 1985, A refined particle method for astrophysical problems, *Astron. Astrophys.* 149, 135–143

Monaghan, J. J. & Pongracic, H.: 1984, *IMACS* 1, 187

Moretti, A., Portinari, L., & Chiosi, C.: 2003, Chemical evolution of the intra-cluster medium, *Astron. Astrophys.* 408, 431–453

Morris, J. P. & Monaghan, J. J.: 1997, A Switch to Reduce SPH Viscosity, *J. Comput. Phys.* 136, 41–50

Muanwong, O., Thomas, P. A., Kay, S. T., & Pearce, F. R.: 2002, The effect of cooling and preheating on the X-ray properties of clusters of galaxies, *Mon. Not. R. Astron. Soc.* 336, 527–540

Muanwong, O., Thomas, P. A., Kay, S. T., Pearce, F. R., & Couchman, H. M. P.: 2001, The Effect of Radiative Cooling on Scaling Laws of X-Ray Groups and Clusters, *Astrophys. J. Lett.* 552, L27–L30

Mulchaey, J. S. & Zabludoff, A. I.: 1998, The Properties of Poor Groups of Galaxies. II. X-Ray and Optical Comparisons, *Astrophys. J.* 496, 73–+

Murante, G., Arnaboldi, M., Gerhard, O., Borgani, S., Cheng, L. M., Diaferio, A., Dolag, K., Moscardini, L., Tormen, G., Tornatore, L., & Tozzi, P.: 2004, The Diffuse Light in Simulations of Galaxy Clusters, *Astrophys. J. Lett.* 607, L83–L86

Mushotzky, R.: 2002, Clusters of galaxies: a cosmological probe, *Royal Society of London Philosophical Transactions Series A* 360, 2019–+

Mushotzky, R. F.: 1984, X-ray emission from clusters of galaxies, *Physica Scripta Volume T* 7, 157–162

Mushotzky, R. F.: 2004, Clusters of Galaxies: An X-ray Perspective, in *Clusters of Galaxies: Probes of Cosmological Structure and Galaxy Evolution*, pp 124–+

Mushotzky, R. F. & Loewenstein, M.: 1997, Lack of Evolution in the Iron Abundance in Clusters of Galaxies and Implications for the Global Star Formation Rate at High Redshift, *Astrophys. J. Lett.* 481, L63+

Navarro, J. F., Frenk, C. S., & White, S. D. M.: 1995, The assembly of galaxies in a hierarchically clustering universe, *Mon. Not. R. Astron. Soc.* 275, 56–66

Navarro, J. F., Frenk, C. S., & White, S. D. M.: 1997, A Universal Density Profile from Hierarchical Clustering, *Astrophys. J.* 490, 493–+

Navarro, J. F., Hayashi, E., Power, C., Jenkins, A. R., Frenk, C. S., White, S. D. M., Springel, V., Stadel, J., & Quinn, T. R.: 2004, The inner structure of ΛCDM haloes - III. Universality and asymptotic slopes, *Mon. Not. R. Astron. Soc.* 349, 1039–1051

Navarro, J. F. & Steinmetz, M.: 1997, The Effects of a Photoionizing Ultraviolet Background on the Formation of Disk Galaxies, *Astrophys. J.* 478, 13–+

Nelson, R. P. & Papaloizou, J. C. B.: 1993, Three-Dimensional Hydrodynamic Simulations of Collapsing Prolate Clouds, *Mon. Not. R. Astron. Soc.* 265, 905–+

Nelson, R. P. & Papaloizou, J. C. B.: 1994, Variable Smoothing Lengths and Energy

Conservation in Smoothed Particle Hydrodynamics, *Mon. Not. R. Astron. Soc.* 270, 1–+

Nevalainen, J., Markevitch, M., & Forman, W.: 2000, The Cluster M-T Relation from Temperature Profiles Observed with ASCA and ROSAT, *Astrophys. J.* 532, 694–699

Nomoto, K., Iwamoto, K., Nakasato, N., Thielemann, F.-K., Brachwitz, F., Tsujimoto, T., Kubo, Y., & Kishimoto, N.: 1997, Nucleosynthesis in type Ia supernovae, *Nuclear Physics A* 621, 467–476

Osmond, J. P. F. & Ponman, T. J.: 2004, The GEMS project: X-ray analysis and statistical properties of the group sample, *Mon. Not. R. Astron. Soc.* 350, 1511–1535

Padovani, P. & Matteucci, F.: 1993, Stellar Mass Loss in Elliptical Galaxies and the Fueling of Active Galactic Nuclei, *Astrophys. J.* 416, 26–+

Peacock, J. A.: 2001, Clustering of Mass and Galaxies, in *NATO ASIC Proc. 565: Structure Formation in the Universe*, pp 305–+

Pearce, F. R., Thomas, P. A., Couchman, H. M. P., & Edge, A. C.: 2000, The effect of radiative cooling on the X-ray properties of galaxy clusters, *Mon. Not. R. Astron. Soc.* 317, 1029–1040

Peebles, P. J. & Ratra, B.: 2003, The cosmological constant and dark energy, *Reviews of Modern Physics* 75, 559–606

Peebles, P. J. E.: 1980, *The large-scale structure of the universe*, Research supported by the National Science Foundation. Princeton, N.J., Princeton University Press, 1980. 435 p.

Peebles, P. J. E.: 1993, *Principles of physical cosmology*, Princeton Series in Physics, Princeton, NJ: Princeton University Press, —c1993

Perlmutter, S. & The Supernova Cosmology Project Team: 1999, Measurements of Omega and Lambda from 42 High-Redshift Supernovae, *Astrophys. J.* 517, 565–586

Peterson, J. R., Kahn, S. M., Paerels, F. B. S., Kaastra, J. S., Tamura, T., Bleeker, J. A. M., Ferrigno, C., & Jernigan, J. G.: 2003, High-Resolution X-Ray Spectroscopic Constraints on Cooling-Flow Models for Clusters of Galaxies, *Astrophys. J.* 590, 207–224

Peterson, J. R., Paerels, F. B. S., Kaastra, J. S., Arnaud, M., Reiprich, T. H., Fabian, A. C., Mushotzky, R. F., Jernigan, J. G., & Sakelliou, I.: 2001, X-ray imaging-spectroscopy of Abell 1835, *Astron. Astrophys.* 365, L104–L109

Pierpaoli, E., Borgani, S., Scott, D., & White, M.: 2003, On determining the cluster abundance normalization, *Mon. Not. R. Astron. Soc.* 342, 163–175

Piffaretti, R., Jetzer, P., Kaastra, J. S., & Tamura, T.: 2004, Temperature and entropy profiles of nearby cooling flow clusters observed with XMM–Newton

Pipino, A., Matteucci, F., Borgani, S., & Biviano, A.: 2002, SNe heating and the chemical evolution of the intra-cluster medium, *New Astronomy* 7, 227–247

Ponman, T. J., Cannon, D. B., & Navarro, J. F.: 1999, The thermal imprint of galaxy

formation on X-ray clusters., *Nature* 397, 135–137

Ponman, T. J., Sanderson, A. J. R., & Finoguenov, A.: 2003, The Birmingham-CfA cluster scaling project - III. Entropy and similarity in galaxy systems, *Mon. Not. R. Astron. Soc.* 343, 331–342

Portinari, L., Moretti, A., Chiosi, C., & Sommer-Larsen, J.: 2004, Can a "Standard" Initial Mass Function Explain the Metal Enrichment in Clusters of Galaxies?, *Astrophys. J.* 604, 579–595

Press, W. H. & Schechter, P.: 1974, Formation of Galaxies and Clusters of Galaxies by Self-Similar Gravitational Condensation, *Astrophys. J.* 187, 425–438

Preto, M. & Tremaine, S.: 1999, A Class of Symplectic Integrators with Adaptive Time Step for Separable Hamiltonian Systems, *Astron. J.* 118, 2532–2541

Quilis, V.: 2004, A new multidimensional adaptive mesh refinement hydro + gravity cosmological code, *Mon. Not. R. Astron. Soc.* 352, 1426–1438

Quinn, T., Katz, N., Stadel, J., & Lake, G.: 1997, Time Stepping N-body simulations

Raymond, J. C. & Smith, B. W.: 1977, Soft X-ray spectrum of a hot plasma, *Astrophys. J. Supp.* 35, 419–439

Reiprich, T. H. & Böhringer, H.: 2002, The Mass Function of an X-Ray Flux-limited Sample of Galaxy Clusters, *Astrophys. J.* 567, 716–740

Renzini, A.: 1997, Iron as a Tracer in Galaxy Clusters and Groups, *Astrophys. J.* 488, 35–+

Renzini, A.: 1999, Chemical Evolution on the Scale of Clusters of Galaxies, and Beyond, in *Chemical Evolution from Zero to High Redshift*, pp 185–+

Renzini, A.: 2004, The Chemistry of Galaxy Clusters

Renzini, A. & Voli, M.: 1981, Advanced evolutionary stages of intermediate-mass stars. I - Evolution of surface compositions, *Astron. Astrophys.* 94, 175–193

Riess, A. G. & coauthors, .: 1998, Observational Evidence from Supernovae for an Accelerating Universe and a Cosmological Constant, *Astron. J.* 116, 1009–1038

Rosati, P., Borgani, S., & Norman, C.: 2002, The Evolution of X-ray Clusters of Galaxies, *ARA&A* 40, 539–577

Ruszkowski, M. & Begelman, M. C.: 2002, Heating, Conduction, and Minimum Temperatures in Cooling Flows, *Astrophys. J.* 581, 223–228

Salpeter, E. E.: 1955, The Luminosity Function and Stellar Evolution., *Astrophys. J.* 121, 161–+

Sanderson, A. J. R., Ponman, T. J., Finoguenov, A., Lloyd-Davies, E. J., & Markevitch, M.: 2003, The Birmingham-CfA cluster scaling project - I. Gas fraction and the M-Tx relation, *Mon. Not. R. Astron. Soc.* 340, 989–1010

Sarazin, C. L.: 1988, *X-ray emission from clusters of galaxies*, Cambridge Astrophysics Series, Cambridge: Cambridge University Press, 1988

Scalo, J. M.: 1986, The initial mass function of massive stars in galaxies Empirical evidence, in *IAU Symp. 116: Luminous Stars and Associations in Galaxies*, pp 451–466

Schmidt, M.: 1959, The Rate of Star Formation., *Astrophys. J.* 129, 243–+

Sellwood, J. A.: 2004, What is the Evidence for Dark Matter?, in *IAU Symposium*, pp 27–+

Serlemitsos, P. J., Smith, B. W., Boldt, E. A., Holt, S. S., & Swank, J. H.: 1977, X-radiation from clusters of galaxies - Spectral evidence for a hot evolved gas, *Astrophys. J. Lett.* 211, L63–L66

Serna, A., Alimi, J.-M., & Chieze, J.-P.: 1996, Adaptive Smooth Particle Hydrodynamics and Particle-Particle Coupled Codes: Energy and Entropy Conservation, *Astrophys. J.* 461, 884–+

Shadwick, B. A., Buell, W. F., & Bowman, J. C.: 2000, *Structure Preserving Integration Algorithms*

Sheth, R. K. & Tormen, G.: 2002, An excursion set model of hierarchical clustering: ellipsoidal collapse and the moving barrier, *Mon. Not. R. Astron. Soc.* 329, 61–75

Smith, S.: 1936, The Mass of the Virgo Cluster, *Astrophys. J.* 83, 23–+

Spergel, D. N., Verde, L., Peiris, H. V., Komatsu, E., Nolta, M. R., Bennett, C. L., Halpern, M., Hinshaw, G., Jarosik, N., Kogut, A., Limon, M., Meyer, S. S., Page, L., Tucker, G. S., Weiland, J. L., Wollack, E., & Wright, E. L.: 2003, First-Year Wilkinson Microwave Anisotropy Probe (WMAP) Observations: Determination of Cosmological Parameters, *Astrophys. J. Supp.* 148, 175–194

Spitzer, L.: 1962, *Physics of Fully Ionized Gases*, Physics of Fully Ionized Gases, New York: Interscience (2nd edition), 1962

Springel, V.: 2004, in preparation at the time of writing

Springel, V. & Hernquist, L.: 2002, Cosmological smoothed particle hydrodynamics simulations: the entropy equation, *Mon. Not. R. Astron. Soc.* 333, 649–664

Springel, V. & Hernquist, L.: 2003a, Cosmological smoothed particle hydrodynamics simulations: a hybrid multiphase model for star formation, *Mon. Not. R. Astron. Soc.* 339, 289–311

Springel, V. & Hernquist, L.: 2003b, The history of star formation in a Λ cold dark matter universe, *Mon. Not. R. Astron. Soc.* 339, 312–334

Springel, V., Yoshida, N., & White, S. D. M.: 2001, GADGET: a code for collisionless and gasdynamical cosmological simulations, *New Astron.* 6, 79–117

Steinmetz, M.: 1996, GRAPESPH: cosmological smoothed particle hydrodynamics simulations with the special-purpose hardware GRAPE, *Mon. Not. R. Astron. Soc.* 278, 1005–1017

Sutherland, R. S. & Dopita, M. A.: 1993, Cooling functions for low-density astrophysical plasmas, *Astrophys. J. Supp.* 88, 253–327

Tamura, T., Bleeker, J. A. M., Kaastra, J. S., Ferrigno, C., & Molendi, S.: 2001, MM-Newton observations of the cluster of galaxies Abell 496. Measurements of the elemental abundances in the intracluster medium, *Astron. Astrophys.* 379, 107–114

Tamura, T., Kaastra, J. S., den Herder, J. W. A., Bleeker, J. A. M., & Peterson, J. R.: 2004, Elemental abundances in the intracluster medium as observed with

XMM-Newton, *Astron. Astrophys.* 420, 135–146

Thornton, K., Gaudlitz, M., Janka, H.-T., & Steinmetz, M.: 1998, Energy Input and Mass Redistribution by Supernovae in the Interstellar Medium, *Astrophys. J.* 500, 95–+

Tinsley, B. M.: 1980, Relations between nucleosynthesis rates and the metal abundance, *Astron. Astrophys.* 89, 246–248

Tornatore, L., Borgani, S., Matteucci, F., Recchi, S., & Tozzi, P.: 2004, Simulating the metal enrichment of the intracluster medium, *Mon. Not. R. Astron. Soc.* 349, L19–L24

Tornatore, L., Borgani, S., Springel, V., Matteucci, F., Menci, N., & Murante, G.: 2003, Cooling and heating the intracluster medium in hydrodynamical simulations, *Mon. Not. R. Astron. Soc.* 342, 1025–1040

Tozzi, P., Rosati, P., Ettori, S., Borgani, S., Mainieri, V., & Norman, C.: 2003, Iron Abundance in the Intracluster Medium at High Redshift, *Astrophys. J.* 593, 705–720

Tozzi, P., Scharf, C., & Norman, C.: 2000, Detection of the Entropy of the Intergalactic Medium: Accretion Shocks in Clusters, Adiabatic Cores in Groups, *Astrophys. J.* 542, 106–119

Valageas, P. & Silk, J.: 1999a, The entropy history of the universe, *Astron. Astrophys.* 350, 725–742

Valageas, P. & Silk, J.: 1999b, The reheating and reionization history of the universe, *Astron. Astrophys.* 347, 1–20

Vikhlinin, A., Markevitch, M., Murray, S. S., Jones, C., Forman, W., & Van Speybroeck, L.: 2004, Chandra temperature profiles for a sample of nearby relaxed galaxy clusters

Vikhlinin, A., VanSpeybroeck, L., Markevitch, M., Forman, W. R., & Grego, L.: 2002, Evolution of the Cluster X-Ray Scaling Relations since z ¿ 0.4, *Astrophys. J. Lett.* 578, L107–L111

Voit, G. M., Balogh, M. L., Bower, R. G., Lacey, C. G., & Bryan, G. L.: 2003, On the Origin of Intracluster Entropy, *Astrophys. J.* 593, 272–290

Voit, G. M. & Bryan, G. L.: 2001, Regulation of the X-ray luminosity of clusters of galaxies by cooling and supernova feedback, *Nature* 414, 425–427

Weinberg, S.: 1972, *Gravitation and cosmology: Principles and applications of the general theory of relativity*, New York: Wiley, —c1972

White, D. A.: 2000, Deconvolution of ASCA X-ray data - II. Radial temperature and metallicity profiles for 106 galaxy clusters, *Mon. Not. R. Astron. Soc.* 312, 663–688

Woosley, S. E. & Weaver, T. A.: 1995, The Evolution and Explosion of Massive Stars. II. Explosive Hydrodynamics and Nucleosynthesis, *Astrophys. J. Supp.* 101, 181–+

Wu, K. K. S., Fabian, A. C., & Nulsen, P. E. J.: 2000, Non-gravitational heating in the hierarchical formation of X-ray clusters, *Mon. Not. R. Astron. Soc.* 318, 889–912

Wu, X., Xue, Y., & Fang, L.: 1999, The L_X-T and L_X-σ Relationships for Galaxy Clusters Revisited, *Astrophys. J.* 524, 22–30

Wyse, R. F. G.: 1997, The Intracluster Medium: an Invariant Stellar Initial Mass Function, *Astrophys. J. Lett.* 490, L69+

Xu, H., Kahn, S. M., Peterson, J. R., Behar, E., Paerels, F. B. S., Mushotzky, R. F., Jernigan, J. G., Brinkman, A. C., & Makishima, K.: 2002, High-Resolution Observations of the Elliptical Galaxy NGC 4636 with the Reflection Grating Spectrometer on Board XMM-Newton, *Astrophys. J.* 579, 600–606

Yamada, M. & Fujita, Y.: 2001, The Heating of Intracluster Gas by the Jet Activities of Active Galactic Nuclei: Is the "Preheating" Scenario Realistic?, *Astrophys. J. Lett.* 553, L145–L148

Zakamska, N. L. & Narayan, R.: 2003, Models of Galaxy Clusters with Thermal Conduction, *ApJ* 582, 162–169

Zel'Dovich, Y. B.: 1970, Gravitational instability: an approximate theory for large density perturbations., *Astron. Astrophys.* 5, 84–89

Zwicky, F.: 1937, On the Masses of Nebulae and of Clusters of Nebulae, *Astrophys. J.* 86, 217–+

Zwicky, F., Herzog, E., & Wild, P.: 1966, *Catalogue of galaxies and of clusters of galaxies*, Pasadena: California Institute of Technology (CIT), —c1966